

**ACOUSTIC POWER TRANSFER LEVERAGING PIEZOELECTRICITY AND
METAMATERIALS**

A Dissertation
Presented to
The Academic Faculty

By

Ahmed Allam

In Partial Fulfillment
of the Requirements for the Degree
Doctor of Philosophy in the
School of Mechanical Engineering

Georgia Institute of Technology

August 2021

© Ahmed Allam 2021

ACOUSTIC POWER TRANSFER LEVERAGING PIEZOELECTRICITY AND METAMATERIALS

Thesis committee:

Dr. Alper Erturk, Committee Chair
School of Mechanical Engineering
Georgia Institute of Technology

Dr. Alper Erturk, Advisor
School of Mechanical Engineering
Georgia Institute of Technology

Dr. Karim Sabra, Co-Advisor
School of Mechanical Engineering
Georgia Institute of Technology

Dr. Julien Meaud
School of Mechanical Engineering
Georgia Institute of Technology

Dr. Massimo Ruzzene
Department of Mechanical Engineering
University of Colorado Boulder

Dr. Fabio Semperlotti
School of Mechanical Engineering
Purdue University

Dr. Chengzhi Shi
School of Mechanical Engineering
Georgia Institute of Technology

Date approved: July 16, 2021

ACKNOWLEDGMENTS

I would like to express my deepest gratitude to my supervisors Dr. Alper Erturk and Dr. Karim Sabra for their guidance, and support throughout the stages of this dissertation. I am truly blessed and lucky to have you as my mentors. Thanks to you, I have grown, not only academically, but also as a person. I would also like to thank my committee members Dr. Julien Meaud, Dr. Massimo Ruzzene, Dr. Fabio Semperlotti, Dr. Chengzhi Shi for all their valuable insights and comments. I would also like to extend my gratitude to my fellow friends and labmates at the SSDSL, and at Georgia Tech, who have made my journey fun and enjoyable. Special thanks to Dr. Christopher Sugino and Eetu Khotanen for many useful comments and discussions. I owe special thanks to Dr. Ihab El-kady for his insightful comments and advice on power transfer in metals. I would also like to acknowledge Dr. S. Hales Swift from Sandia and Dr. Jim Martin from Georgia Tech for many fruitful discussions.

I would also like to thank my MSc advisers Dr. Wael Akl, Dr. Adel Elsabbagh, and Dr. Tamer Elnady for guiding me to the exciting fields of acoustics and smart materials.

I would not have made it so far without the love, care, and, support of my parents, my brother Mohamed, and my sister Sama. Thanks for always being there for me.

Last but not least, I would like to thank my beloved wife Mariam. You have filled my life with love and joy, and was always with me when I needed you the most.

This work was supported by U.S. National Science Foundation CMMI Grant No. 1727951, and by the Sandia National Laboratories. Any views and conclusions contained herein are those of the author, and do not necessarily represent the official positions, express or implied, of the funders.

TABLE OF CONTENTS

Acknowledgments	iii
List of Tables	ix
List of Figures	x
Chapter 1: Introduction	1
1.1 Motivation	1
1.2 Opportunities for Ultrasonic Power Transfer	2
1.3 Ultrasonic Power Transfer Challenges	4
1.4 Transducer Modeling and Aspect Ratio Effects	7
1.5 System-Level Analysis and Efficiency	8
1.6 Reducing Beam Divergence in Ultrasonic Power Transfer Systems	10
1.6.1 Phononic Crystals	10
1.6.2 Gradient Index Phononic Crystals in Water	11
1.6.3 Gradient Index Phononic Crystals in Air	12
1.7 Acoustic and Electrical Impedance Matching for Power and Data Transfer .	13
1.8 Dissertation Outline	15
Chapter 2: Aspect Ratio-Dependent Piezoelectric Transmitter and Receiver Dynamics	18

2.1	Thickness-Mode Dynamics of a Piezoelectric Transducer with Circular Cross Section	19
2.1.1	Classical Thin-Rod Model	22
2.1.2	Rayleigh Model	28
2.1.3	Bishop Model	29
2.1.4	Infinite Plate Model	31
2.2	Resulting Dynamics and Comparison of the Analytical Models	33
2.2.1	Numerical Model	33
2.2.2	Experimental Validation	34
2.2.3	Electrical Impedance in Air	35
2.2.4	Electrical Impedance in Oil	37
2.3	Effect of Aspect Ratio on the Performance of a Thickness-Mode Transmitter	39
2.4	Effect of Aspect Ratio on the Performance of a Thickness-Mode Receiver .	42
2.5	Conclusions	48
Chapter 3: System-Level Analysis with a Focus on Power Transfer through Metallic Barriers		50
3.1	Analytical Modeling	50
3.1.1	Modeling Attenuation	55
3.1.2	Performance Metrics	58
3.2	Benchmark System Performance	62
3.2.1	Experimental Validation	62
3.2.2	Numerical Model	64
3.2.3	Benchmark Results and Discussion	65

3.2.4	Maximum Achievable Efficiency	67
3.3	Transducers with Wrap-around Electrodes	69
3.4	Interfacing Circuits	72
3.4.1	AC-to-DC Conversion	73
3.4.2	Power Amplifiers	75
3.4.3	Class E Amplifier Design for UPT	78
3.5	UPT with an Integrated Power Amplifier (DC-to-AC Operation)	80
3.6	Overall System Performance (DC-to-DC Operation)	83
3.7	Dry-coupled Detachable Power Transfer System	87
3.7.1	Experimental Setup	89
3.7.2	Experimental Results	92
3.7.3	Effect of Gluing the Soft Layer to the Transmitter	95
3.7.4	Overall System Performance	97
3.8	Conclusions	100
Chapter 4: Performance Enhancement by Leveraging Phononic Crystals and Wave Focusing		101
4.1	GRIND-PCs for Underwater Focusing	102
4.1.1	Underwater Unit Cell Analysis and Refractive Index Tailoring . . .	102
4.1.2	Underwater Phononic Crystal Lens Design	106
4.1.3	Experimental Validation	109
4.2	Underwater Power Transfer Enhancement Using GRIN-PCs	113
4.3	GRIN-PCs for Focusing in Air	120
4.3.1	In-Air Unit Cell Analysis and Refractive Index Tailoring	120

4.3.2	In-Air Phononic Crystal Lens Design	123
4.3.3	Experimental Results	126
4.4	Sound Power Enhancement using GRIN-PCs	127
4.5	Conclusions	129
Chapter 5: Acoustic and Electrical Impedance Matching for Simultaneous Power and Data Transfer		132
5.1	Modeling Reflection from a Piezoelectric Layer	133
5.2	Acoustic Reflection from a Piezoelectric Transducer	135
5.3	The Smith Chart	139
5.4	Simultaneous Acoustic and Electrical Impedance Matching	141
5.4.1	Single Matching Layer	144
5.4.2	Two-layer Acoustic Impedance Matching	149
5.5	Experimental Verification	151
5.5.1	Transducer fabrication	151
5.5.2	Measuring the Electrical Impedance of the Transducers	153
5.5.3	Setup for Measuring the Acoustic Reflection Coefficient	154
5.6	Impedance Matching for Data Transfer	156
5.7	Impedance Matching for Power Transfer	158
5.8	Simultaneous Power and Data Transfer	161
5.9	Conclusions	163
Chapter 6: Conclusions, Contributions, and Future work		166
6.1	Summary and Conclusions	166

6.1.1	Aspect Ratio-Dependent Piezoelectric Transmitter and Receiver Dynamics	166
6.1.2	System-Level Analysis with Focus on Ultrasonic Power Transfer through Metallic Barriers	167
6.1.3	Performance Enhancement by Leveraging Phononic Crystals and Wave Focusing	168
6.1.4	Acoustic and Electrical Impedance Matching for Simultaneous Power and Data Transfer	169
6.2	Contributions	171
6.3	Future Work	172
References		175

LIST OF TABLES

2.1	Measured/Identified material properties of modified PZT-5	35
3.1	Material properties of Steminc SM111 (modified PZT4)	63
3.2	Material properties used in the transducer 1D model	63
3.3	Dimensions and material properties of elastic layers in the base model . . .	63
3.4	Material properties of elastomer layers used in the study	92
5.1	Material properties of PZT-4 used in the transducer 1D model	136
5.2	Dimensions of the fabricated transducers	151
5.3	Experimentally identified modified PZT-4 material properties from electrical impedance data in air	153

LIST OF FIGURES

1.1	Schematic of a typical wireless UPT system.	4
1.2	Loss mechanisms in ultrasonic power transfer systems (adapted from Ref. [65])	6
2.1	(a) Schematic of a piezoelectric rod transducer, (b) three-port element representation, and (c) incident and reflected voltage and pressure waves on the transducer.	20
2.2	Comparison of the electrical impedance in air for two cylindrical transducers with aspect ratios (a) $\beta = 5$ and (b) $\beta = 1.7$. Experimental results are compared with those estimated numerically using FEM and analytically using thin rod, Rayleigh and Bishop rod theories.	36
2.3	In-air resonance frequency of the first thickness mode of a PZT transducer ($h_p = 12$ mm) versus the aspect ratio β . Frequency values are shown in solid lines, and percentage errors relative to FEM are shown in dashed lines of the same color.	37
2.4	Comparison of electrical impedance in oil for two cylindrical transducers with aspect ratios (a) $\beta=5$ and (b) $\beta=1.7$. Experimental results are compared with those estimated numerically and analytically.	39
2.5	Effect of aspect ratio on the average normal surface velocity of the transducers. The aspect ratio is varied between (a) $\beta = 10$, (b) $\beta = 5$, (c) $\beta = 1$, and (d) $\beta = 0.1$. The insets show surface plots of the distribution of the surface velocity in the axis direction of the transducer (z-direction). In all cases, the applied electric field is the same (1 kV/m).	41
2.6	Effect of aspect ratio on the near field sound pressure level (SPL) generated by the baffled TX estimated using FEM for (a) $\beta = 10$, (b) $\beta = 5$, (c) $\beta = 1$, and (d) $\beta = 0.1$. The color contour inside the transducer represents the normalized velocity in the axial direction.	43

2.7 Effect of the aspect ratio on the power output of RX. The transducers are submerged in water and subjected to incident plane harmonic waves of amplitude (1 kPa) and the power output under different values for the load resistance is estimated using the FEM for (a) $\beta = 10$, (b) $\beta = 5$, (c) $\beta = 1$, and (d) $\beta = 0.1$. The normalized displacement amplitude of the transducers are shown in the insets.	45
2.8 Output power of RX at the optimal load when completely submerged inside the fluid medium versus the flushed case where only the front face of the transducer is coupled to the fluid and the other faces are free. The aspect ratio is varied between (a) $\beta = 10$, (b) $\beta = 5$, (c) $\beta = 1$, and (d) $\beta = 0.1$. The insets show the acoustic intensity stream lines for the submerged case. The normalized displacement amplitude of the transducers are also shown.	46
3.1 Basic configuration of a through-metal UPT system for AC input and AC output.	51
3.2 Transfer matrix parameters for (a) an elastic layer and (b) an electrical circuit. (c) The impedance matrix representation for a piezoelectric transducer. (d) The scattering matrix representation for an elastic layer.	53
3.3 Experimental setup for characterizing the performance of the developed through-metal UPT.	64
3.4 A cross-section in the base UPT FEM model showing Von Mises stress magnitude distribution calculated numerically when the system is excited with a steady-state 10 V sinusoidal voltage at 1.025 MHz.	65
3.5 (a) Voltage FRF between the input and output piezoelectric transducer. (b) Operating (ultrasonic) efficiency of the system. The experimental results are compared to 1D analytical model and numerical model predictions.	66
3.6 (a) Voltage FRF between the input and output piezoelectric transducer. (b) Operating (ultrasonic) efficiency of the system. The experimental results are compared to the 1D analytical model and numerical model predictions over frequencies ranging from 0.5 MHz to 10 MHz.	67
3.7 (a) Operating (ultrasonic) efficiency of the base system obtained numerically compared to the maximum achievable efficiency calculated using Equation (3.39). The frequency range from 0.5 MHz to 2 MHz is shown in (b).	69

3.8 Experimental setup for through-metal UPT systems using circular transducers with dimensions (a) 30 x 2.1 mm, (b) 15 x 1 mm (c) 10 x 0.5 mm, and (d) a rectangular transducer with dimensions 20 x 15 x 2.1 mm.	71
3.9 Experimental (a) voltage FRF and (b) operating efficiency for UPT systems for the transducers shown in Figure 3.8.	72
3.10 A block diagram showing the essential components for a through-metal UPT system and the flow of power between them.	73
3.11 (a) Full bridge AC-to-DC rectifier circuit (b) Half-wave voltage doubler circuit.	74
3.12 Power amplifier design classes depending on how the power transistor is biased and the nature of the excitation signal (sinusoidal vs. square wave). .	77
3.13 A circuit simulation using the harmonic balance method for a class E amplifier connected to the base model shown in Figure 3.1.	79
3.14 The printed circuit board of the designed class E power amplifier with a microcontroller used as a variable square wave generator and the MOSFET driving circuitry. The different components of the circuit are highlighted. .	80
3.15 Simulated and experimental (a) input and (b) output voltage waveforms to and from the ultrasonic system as supplied from the designed power amplifier. The simulation results are obtained from the circuit shown in Figure 3.13.	81
3.16 Experimental MOSFET drain voltage when the amplifier operation is tuned by selecting a proper feed inductor ($4.7\ \mu\text{H}$) versus the detuned operation when a different inductor is used ($10\ \mu\text{H}$ in the case shown).	82
3.17 (a) DC-to-AC experimental system efficiency vs DC input voltage. The efficiency is calculated by dividing AC output power supplied to a $50\ \Omega$ load by the total input DC power. (b) The output power vs the input DC voltage supplied.	83
3.18 Harmonic balance simulation of a complete through-metal DC-to-DC UPT system.	84
3.19 Input voltage (V_i) and output voltage (V_o) waveforms (see Figure 3.18) of the complete DC-to-DC UPT system operated from a 20V power supply. The simulated waveforms obtained using the circuit shown in Figure 3.18 are compared to experimental measurements.	84

3.20 (a) Total experimental system efficiency vs DC input voltage. The efficiency is calculated by dividing output power supplied to a 50Ω load by the total input DC power. (b) The DC output power vs the input DC voltage supplied.	85
3.21 Experimental (a) amplifier drain voltage and (b&c) DC output voltage waveforms when (b) a 50Ω load and (c) a 100Ω loads were used. The waveforms are measured at the DC supply voltage levels shown in the color bar.	86
3.22 Different approaches to achieve ultrasonic coupling at the interface between two rigid solids. The surface roughness of the transducer and metallic enclosure is exaggerated to limelight the contact problem.	89
3.23 Schematic of the proposed dry-coupled detachable through-metal UPT system.	91
3.24 Pulling force between two $1/4'' \times 1/4''$ NdFeB Grade N42 magnets vs separating distance.	91
3.25 Experimental setup for evaluating the electromechanical performance of the developed detachable through-metal UPT system.	92
3.26 (a) Experimental voltage FRF and (b) operating efficiency for the detachable setup with direct contact between the transmitter and the aluminum wall with and without the use of a liquid ultrasonic couplant.	93
3.27 (a) Experimental voltage FRF for the detachable setup with a soft layer of thickness 0.5 mm for the soft materials tested. (b) The operating efficiency of the system.	94
3.28 (a) Experimental voltage FRF for the detachable setup with a soft layer of thickness 1 mm for the soft materials tested. (b) The operating efficiency of the system.	94
3.29 The operating efficiency of the system when a soft layer made of Aqualink100 was used. Results for a 0.5, 1, 2 mm thick layer are shown.	95
3.30 Comparing the performance of the dry-coupled system when the soft layer is glued to the transmitter vs when a liquid couplant is used. The results are shown for (a) Aquasilox 1 mm, (b) Aqualink 1 mm, and (c) Aqualink 2 mm soft layers.	96
3.31 Experimental setup for evaluating the overall performance (DC-to-DC operation) of the developed detachable through-metal UPT system.	98

3.32 Experimental (a) amplifier drain voltage and (b) output voltage waveforms for AC and DC output operation of the dry-coupled system at the DC supply voltage levels shown in the color bar. The operation of the system with the AC-to-DC bridge rectifier is shown using dashed lines and without it using solid lines	98
3.33 (a) Experimental total system efficiency and ultrasonic efficiency vs DC input voltage for the dry-coupled system. (b) The total input and output DC power vs the input DC voltage supplied to the system.	99
4.1 (a) Band structure of the proposed PC for different filling fractions (ϕ) of air volume per unit cell volume (propagation modes of different branches are shown as insets). (b) Frequency dependence of the PC refractive index for different filling fractions.	103
4.2 The effect of including air as an acoustic material on the bandstructure of the proposed unit cell. The bandstructure of the cell with air modeled as an acoustic domain is shown as solid lines while the model assuming air as a free boundary condition is shown as markers.	104
4.3 (a) PC refractive index versus the filling fraction at the target design frequency of 100 kHz. (b) Refractive index profile for a continuous Luneburg lens and the discretized GRIN-PC implementation. Simulations are for waves propagating in the ΓX direction.	105
4.4 Normalized pressure field in the focus region of a sphere-shaped lens design (left column) and a cube-shaped lens design (right column). The pressure is shown in (a&b) the propagation (z) direction and (c&d) the focal plane (x -direction). Two different materials for the lens are considered: an elastic material matched to water ($c_p = 1500 \text{ m/s}$, $c_s = 700 \text{ m/s}$) shown in solid blue and PLA shown in dashed red. For the sphere lens, the pressure field for waves incident in the $\Gamma X \langle 100 \rangle$ direction are compared to $\Gamma R \langle 111 \rangle$ incidence. The internal structures of the lens designs are shown in the insets of (a) and (b).	107
4.5 Cross-sections of the peak pressure field distributions behind the cube and sphere lenses (i.e. in the focus region) are shown for the (a&b) matched material and (c&d) PLA.	108
4.6 (a) X-ray scan of the internal structure at the midsection of the 3D-printed lens. (b) 3D reconstruction of an X-ray scan of the inner 10 cells of the lens.	110

4.7 (a) Overview and (b) close-up view of the experimental setup for plane wave generation and for scanning the pressure field behind the 3D-printed PC lens.	111
4.8 Peak pressure field behind the lens (focus region) revealing a substantial enhancement of the pressure intensity via focusing: (a) Numerical (FEM) simulation, (b) experimental data (via scanning using the hydrophone), and (c) baseline case without the lens (obtained from experiments).	112
4.9 Comparison of the experimental and numerical pressure distributions along the (a) x -axis of the focal plane normal to the propagation direction, and along (b) the z -axis (in the propagation direction). The baseline case without the lens is also shown for reference.	113
4.10 Normalized pressure field at 100 kHz for two GRIN-PC lenses used for enhancing the acoustic power delivered from a point source to a point receiver. The field is obtained numerically using a 2D acoustic FEM. The distance between the point source and the lens is varied between (a) $d_s = 0$, (b) $d_s = 10$ mm, and (c) $d_s = 20$ mm.	114
4.11 Experimental setup for measuring the received power enhancement of a two-lens GRIN-PC power transfer system. (a) Hydrophones are used as a point TX and point RX. (b) Piezoelectric transducers are used as TX and RX.	115
4.12 (a) Power spectrum (power spectral density) of the voltage signal generated by the RX hydrophone when the TX hydrophone was excited by a 10 V voltage Gaussian pulse centered around 90 kHz. (b) The power gain due to the introduction of the lenses with respect to the received power without the lenses. (c) Filtered received voltage pulse showing the gain in amplitude when the lenses were introduced. The received signal was filtered from 85 kHz to 95 kHz to obtain this pulse response.	117
4.13 Normalized pressure field at 100 kHz for (a) the selected piezoelectric transducers without the lens. (b) The effect of introducing the GRIN-PC lenses on the pressure field of the transducers. The field is obtained numerically using a 2D acoustic FEM.	118
4.14 (a) Experimental power spectrum (power spectral density) of the voltage signal generated by the RX piezoelectric transducer when TX was excited by a 200 V voltage Gaussian pulse centered around 90 kHz. (b) The power gain due to the introduction of the lenses. (c) Received voltage signal when TX was excited with a 10% bandwidth Gaussian pulse centered around 90 kHz.	119

4.15 (a) Dispersion plots of a unit cell in the main direction of wave propagation for different volume filling fraction values (ϕ), i.e. different polymer to cubic unit cell volume ratios. (b) The effective refractive index of the PC versus frequency for different ϕ values. (c) Effective refractive index at the design frequency (18 kHz) versus ϕ for different directions. (d) Analytical refractive index profile of an ideal Luneburg lens versus the discretized profile used in the implementation of the GRIN-PC lens for different directions. The effective refractive index in the diagonal $\langle 110 \rangle$ and $\langle 111 \rangle$ directions are also shown.	121
4.16 Experimental setup (a) for measuring the acoustic pressure field of the 3D-printed GRIN-PC lens (microphone mounted on an XYZ stage scans the pressure field) and (b) for measuring the electrical power enhancement of a piezoelectric receiver placed at the focal spot of the GRIN-PC lens.	123
4.17 Normalized peak pressure field behind the lens obtained (a) numerically and (b) experimentally.	124
4.18 (a) Normalized pressure at the focal plane obtained numerically and experimentally. The experimental pressure fields are shown for waves propagating in the directions $\langle 110 \rangle$ and $\langle 100 \rangle$ with respect to the PC lattice. (b) Normalized peak pressure obtained experimentally for different Gaussian pulse center frequencies. The bandwidth was kept constant at 6 kHz. (c) Time series for the pressure at the focal position of the lens compared to its absence. The case shown is for a pulse with 18 kHz center frequency.	125
4.19 Simulated output power of the receiver when subjected to a uniform harmonic pressure of 30 Pa (≈ 120 dB). The power is plotted vs excitation frequency and load resistance.	128
4.20 (a) Experimental peak received electrical power versus load resistance for an incident acoustic plane wave with a peak pressure of 30 Pa (≈ 120 dB) on the lens-receiver system. The output power from a pulse with center frequency $f_c = 15$ kHz and bandwidth BW=4 kHz (wideband) is compared to pulses with narrower bandwidth (BW=500 Hz) and centered around $f_c = 14.5$ kHz and $f_c = 15$ kHz. The baseline case without the lens is also shown for all the pulse shapes considered. (b) The voltage time series obtained experimentally for the maximum power output obtained with a pulse centered at $f_c = 15$ kHz with BW=500 Hz and a load resistance of $R_l = 6$ k Ω connected to the transducer.	130
5.1 Basic implementation of a simultaneous power and data transfer UPT system.	132

5.2	A schematic of a piezoelectric disc transducer represented as a 3-port element connected to arbitrary electrical impedance Z_e and an arbitrary backing layer with mechanical impedance Z_b	134
5.3	(a) Analytical acoustic reflection coefficient of an air-backed 1 MHz piezoelectric transducer submerged in water and connected to a resistive load ranging from 0-10 k Ω . (b) Electrical input impedance of the transducer with the front face submerged in water.	137
5.4	(a) Time history of a normalized broadband ultrasonic Gaussian pulse ($f_c = 998$ kHz, $BW = 50\%$) incident on the front face of an air-backed transducer. The reflected pulse when the transducer is connected to the SC resonance resistance (9 Ω) is compared to that when a 1 M Ω is connected. (b) The acoustic reflection coefficient of the transducer with respect to water when the different electric loads are used. The normalized frequency spectrum of the incident pulse is also shown.	138
5.5	(a) Time history of a normalized narrowband ultrasonic Gaussian pulse ($f_c = 998$ kHz, $BW == 5\%$) incident on the front face of an air-backed transducer. The reflected pulse when the transducer is connected to the SC resistance (9 Ω) is compared to that when a 1 M Ω is connected. (b) The acoustic reflection coefficient of the transducer with respect to water when the different electric loads are used. The normalized frequency spectrum of the incident pulse is also shown.	139
5.6	Acoustic to electric transmission efficiency for an air-backed transducer placed in water and connected to a 9 Ω resistive load.	140
5.7	Fundamentals of the Smith chart.	141
5.8	Smith chart of the air-backed transducer acoustic reflection coefficient S_{11} with respect to water when the electric resistance connected to the transducer varies (a) from 0-75 Ω and (b) from 100-10 000 Ω	143
5.9	Smith chart of the air-backed transducer electric reflection coefficient (S_{22}) with respect to 50 Ω when the acoustic port is in water.	144
5.10	Smith chart of the (a) acoustic and (b) electric reflection coefficients of an air-backed piezoelectric transducer with a single matching layer of impedance $Z_m = (Z_p Z_w)^{1/2}$ with different thickness. The amplitude of the acoustic reflection coefficient is shown in (c).	146

5.11 Smith chart of the (a) acoustic and (b) electric reflection coefficients of an air-backed piezoelectric transducer acoustically matched with a single quarter wavelength matching layer with varying acoustic impedance. The amplitude of the acoustic reflection coefficient is shown in (c).	147
5.12 Effect of using a series inductor on the Smith chart of the (a) acoustic and (b) electric reflection coefficients of an air-backed piezoelectric transducer with a single quarter wavelength matching layer of acoustic impedance 6 MRayl. The amplitude of the acoustic reflection coefficient is shown in (c).	148
5.13 Electrical impedance matching of a transducer with two quarter-wavelength matching layers (quartz glass and epoxy). The effect of using a parallel then series inductor is shown on the Smith chart of the (a) acoustic reflection coefficient and (b) electric reflection coefficient. The electric load connected to the transducer in each case is shown in the legend. (c) The amplitude of the acoustic reflection for the different electric loads. (d) A reflected acoustic pulse from the transducer when using the matching circuit compared to the case when a $1 M\Omega$ load (OC) is used.	150
5.14 (a) Schematic of an air-backed transducer without acoustic matching layers. (b) Construction of the two-layer acoustically matched transducer. (c) Fabricated transducers U1 and M1 before polishing.	152
5.15 Analytical (lines) and experimental (markers) electric impedance underwater for three matched transducers (M1-M3) with different epoxy layer thickness as summarized in Table 5.2. The impedance of a transducer without acoustic matching (U1) is also shown for comparison.	154
5.16 Experimental setup for measuring the acoustic reflection coefficient of the fabricated transducers.	155
5.17 Experimental versus analytical acoustic reflection coefficient for (a) the transducer without acoustic matching (U1), and (b) the two-layer acoustically matched transducer (M3).	156
5.18 Electrical circuit used to achieve a broadband electrical match with the two-layer acoustically matched transducer (M3).	157
5.19 (a) Experimental acoustic reflection coefficient for an electrically and acoustically matched transducer. Broadband electrical matching is shown using the circuit in Figure 5.18 versus when the transducer was open circuit. (b) Time waveform showing the modulation of the reflected pulse by varying electrical circuit connected to the transducer.	158

5.20 Ultrasonic efficiency versus frequency for two air-backed transducers without acoustic impedance matching. The efficiency is shown for a separating distance between the transducers of (a) 10 mm, (b) 50 mm, (c) 100 mm, and (d) 200 mm.	160
5.21 Peak efficiency of the ultrasonic power transfer system without acoustic matching versus the separating distance between the transducers.	160
5.22 (a) Schematic and (b) implementation of an electrical circuit for simultaneous ultrasonic power and data transfer. The circuit routes in incident power and data signals to two separate electrical branches allowing for uninterrupted power flow to an energy harvesting circuit while transmitting backscatter data.	162
5.23 (a) Experimental acoustic reflection coefficient for a transducer connected to the simultaneous power and data transfer circuit shown in Figure 5.18. (b) The spectrum of the signal received by the power branch of the circuit versus that received by the data branch for an incident ultrasonic pulse. (c) Filtered echo signal showing the data bandwidth between 600 kHz and 800 kHz.	164

SUMMARY

Acoustic power transfer, or ultrasonic power transfer (UPT) more specifically, has received growing attention as a viable approach for wireless power delivery to low-power electronic devices. It has found applications in powering biomedical implants, sensors in sealed metallic enclosures, and sensors deep in the ocean. The design of an efficient UPT system requires coupled multiphysics modeling to establish strategies toward maximizing the transferred power. This work, first, investigates different analytical and numerical models to analyze the performance of UPT systems to increase the transferred power. Various electromechanical models are developed to represent the transducer (transmitter or receiver) and overall system dynamics for a broad range of aspect ratios covering the diverse UPT applications. The main challenges that limit UPT system efficiency such as attenuation, power divergence, and reflection due to impedance mismatch issues are investigated using the developed models. These effects are investigated at the system level with an application to transfer power through metallic barriers using bonded piezoelectric disc transducers. A complete system for transferring power from the battery of a transmitter to the DC load of a receiver is designed and simulated, then experimentally tested. The experimental results of the system agree well with the modeling predictions, and the system is able to deliver 17.5 W to a DC load with a total DC-to-DC efficiency of 66%. A second system with a portable and detachable dry-coupled transmitter is also experimentally tested. The dry-coupled system is able to deliver 3 W of DC power with 50% efficiency from a 9 V battery. Novel approaches using acoustic metamaterials/phononic crystals are introduced to enhance the efficiency of UPT through wave focusing. Specifically, two 3D phononic crystal structures based on air in a 3D-printed polymer matrix are introduced to manipulate acoustic waves both under water and in air. Two designs for gradient-index lenses are fabricated and experimentally characterized to focus acoustic waves on a piezoelectric receiver, thereby dramatically enhancing the power output. Fi-

nally, acoustic and electrical impedance matching are investigated for sending both power and data using ultrasonic waves. Several impedance matching techniques are proposed to maximize transducer bandwidth, power efficiency, as well as sensitivity for underwater data transfer. A novel approach is introduced for achieving simultaneous power and data transfer using frequency multiplexing with a single transducer. The introduced designs allow for configurable matching for maximizing power efficiency, maximizing data transfer, or simultaneously sending power to the transducer while receiving data with lower bandwidth.

CHAPTER 1

INTRODUCTION

1.1 Motivation

Smart connected electronic devices are becoming ubiquitous in our everyday lives thanks to developments in ultra-low-power electronic circuits. These circuits allow for the development of wireless devices that are capable of sensing and influencing their environments and communicating their state, all while consuming minimal power. This has motivated their integration into devices deployed in traditionally inaccessible locations such as inside the skull [1], in nuclear waste containers [2] or deep in the ocean [3, 4]. Their presence in such extreme locations prevents powering via wires and requires other practical means for power delivery. Energy harvesting devices could be used to collect energy from their environment and convert it into useful electrical energy [5–10]. However, if the ambient energy is limited, external energy can be supplied using a wireless power transfer system.

Electromagnetic (inductive) wireless power transfer is a popular solution when the separating distance between the transceivers is small and the medium is air [11–13]. However, some environments present a challenge for efficient electromagnetic waves propagation. For example, electromagnetic waves cannot penetrate deep into conductive materials such as metals. They are also not suitable for underwater applications because of high attenuation. In biomedical applications, strict regulations are imposed on the human exposure to electromagnetic waves which restricts their usage [14]. Moreover, the energy transfer efficiency of magnetically coupled transducers decreases drastically with increased separation distance compared to the transceiver size [15].

Acoustic Power Transfer (APT) or Ultrasonic Power Transfer (UPT)¹ systems do not suffer from these limitations and have recently found applications in transmitting energy through metallic walls [16–18], powering wireless sensors along industrial pipelines [19, 20], powering bio-medical implants [21], and powering underwater sensors [3, 4], among others. In each of these applications, ultrasonic waves solve a unique set of challenges for power transfer and communication. The opportunities for UPT in the biomedical, through-metal (aerospace and military), and underwater applications are discussed next.

1.2 Opportunities for Ultrasonic Power Transfer

Biomedical technology researchers have been developing UPT systems for powering and communicating with miniature implanted medical devices (IMDs). Minute ultrasonic-powered devices with (sub)millimeter dimensions are investigated for general health monitoring and rehabilitation [22–27], enhancing tumor treatment [28, 29], for neural recording [1, 30] and stimulation [31–37], realizing a brain-machine interface [38, 39], and retinal stimulation [40] to name a few. Ultrasonic power is being considered since the United States Food and Drug Administration (FDA) limits the electromagnetic power that can be transmitted safely through the human body to 0.1 mW/mm^2 while the limit for ultrasonic waves is much higher at 7.2 mW/mm^2 [41]. Ultrasonic waves also have a much smaller wavelength compared to electromagnetic waves at the same frequency which allows for the use of smaller receivers and thus smaller implants. This allows for transmitting at lower frequencies compared to RF devices which leads to lower attenuation, lower tissue heating and allows for deeper implants [37, 42]. Ultrasonic power delivery and communication could be one of the enabling technologies for concepts such as the body area network (BAN) [43, 44]

¹Between the two naming options, the more general is “acoustic power transfer” to include power transfer systems that use any region of the acoustic frequency spectrum. However, the term “ultrasonic power transfer” is more common since most applications involve frequencies in the ultrasonic regime [15].

Ultrasonic waves are also the only viable approach for deep underwater wireless power and data transfer solutions [45]. While optical and radiofrequency (RF) based solutions exist, their operation is typically limited to short distances on the order of tens of meters due to the large attenuation of electromagnetic waves [45, 46]. Underwater wireless ultrasonic sensor nodes are investigated for ocean monitoring and tracking climate change [47, 48], increasing underwater communication bandwidth [49], tracking marine life [50–52], and as markers for aiding the navigation of autonomous underwater vehicles [53], among other applications. They could also be leveraged for concepts such as the underwater internet of things [54–57]. Most of the devices developed in the underwater literature are battery-powered which limits their lifespan given the difficulties in retrieving and replacing the batteries. Recent efforts have investigated ultrasonic waves for both powering and communicating with underwater sensor nodes [3, 4, 58, 59].

Lastly, ultrasonic (acoustic) waves are used to send power and data to electronics placed inside solid metallic enclosures [60, 61]. Since, sensitive electronics are usually sealed inside metallic enclosures to shield them from electromagnetic interference, the presence of any gaps or slots in the enclosure results in electromagnetic leakage and reduces the shielding performance. Structural gaps are also undesirable to ensure the structural integrity of the metallic enclosure in scenarios such as powering sensors placed on the external surface of an aircraft, spacecraft, or submarine. UPT is also used for supplying power to sensors placed in sealed hazardous environments such as nuclear waste containers. The ability to send power through metals allows for using sealed structures for sealing the hazard eliminating the risk associated with battery replacement. Weather protection and waterproofing are among other benefits of UPT, as charging ports introduce the risk of water damage. Full metal casings coupled with UPT could be a viable approach to remove charging ports while providing maximum structural integrity for the device.

1.3 Ultrasonic Power Transfer Challenges

Most of the UPT systems surveyed (Figure 1.1) consist of a piezoceramic transmitter (TX) connected to an electric power source/circuit, and a piezoelectric receiver (RX) which is integrated into an electronic device to be powered (or to an electrical storage component). TX converts the source electric power into mechanical (elastic/acoustic) waves which can travel through the medium. RX then captures this power and converts it back to usable electric power with the aid of an energy harvesting circuit and power regulation electronics.

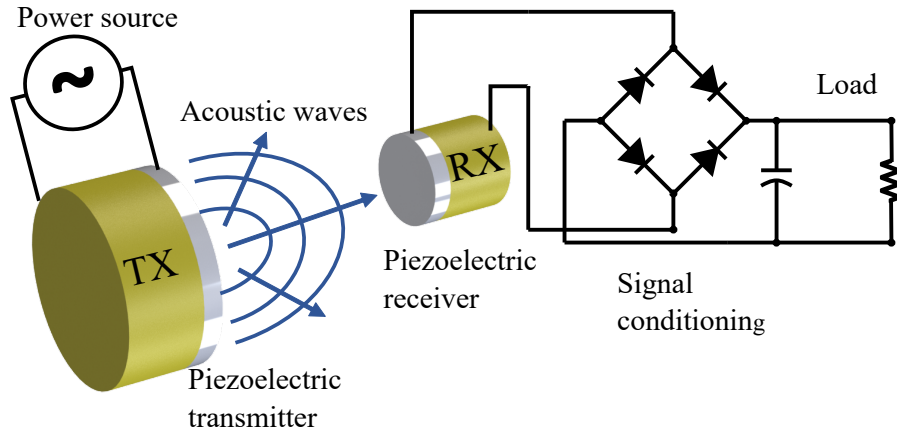


Figure 1.1: Schematic of a typical wireless UPT system.

Several power loss mechanisms reduce the efficiency of UPT systems. The most important factors are summarized in Figure 1.2 and they include:

- **Attenuation:** The amount of power dissipated depends on the medium and the frequency. For example, biological tissue has large attenuation above 60 dB/m at 1 MHz [62].² Metals have an attenuation below 50 dB/m at 1 MHz for many alloys [63] which is higher than water with an attenuation around 0.3 dB/m at 1 MHz [64].

²An attenuation of 3 dB/m means that half of the power is dissipated as the wave travels 1 m in the medium.

- **Beam divergence:** Some of the power generated by TX diverges in the medium and never reaches RX. The amount of divergence depends on the aperture of TX and its size compared to the wavelength which also depends on the frequency. As the frequency of operation increases, a more focused/directional beam can be generated and less power diverges in the medium.
- **Impedance mismatch:** The difference in the acoustic or electrical impedance between any two successive components of a UPT system causes power to be reflected and reduces the system efficiency. For example, the acoustic impedance of PZT, which is the most common material used in piezoelectric transducers (35 MRayl), is comparable to that of metals (15 MRayl to 60 MRayl for common metals); however, it is much higher than that of water and tissues (1.5 MRayl). This reduces the efficiency of the system unless effort is made to acoustically and electrically match the transducer to the medium.

A large portion of the UPT system characteristics depends on its frequency of operation. Given a system with transducers of a fixed size, as the frequency of operation increases, the transducers become more directional (beam divergence losses decrease); however, the power absorbed by the medium increases. The attenuation in the medium is an intrinsic property that cannot be reduced without changing the medium itself. Thus, the attenuation imposes a hard limit on the operating frequency, while the divergence losses impose a softer limit subject to improvement by refocusing the diverged waves. On the other hand, a given transducer can only operate efficiently if driven near its resonance frequency which depends on its thickness. Thus, typically larger transducers are required for exciting lower frequencies efficiently.

The nature of a given UPT application imposes different limitations for UPT system design. Through-metal UPT is usually used for short distances ranging from a few millimeters to a few centimeters with a little restriction on the size of the transducer. This allows for minimizing divergence losses by using transducers with large apertures and op-

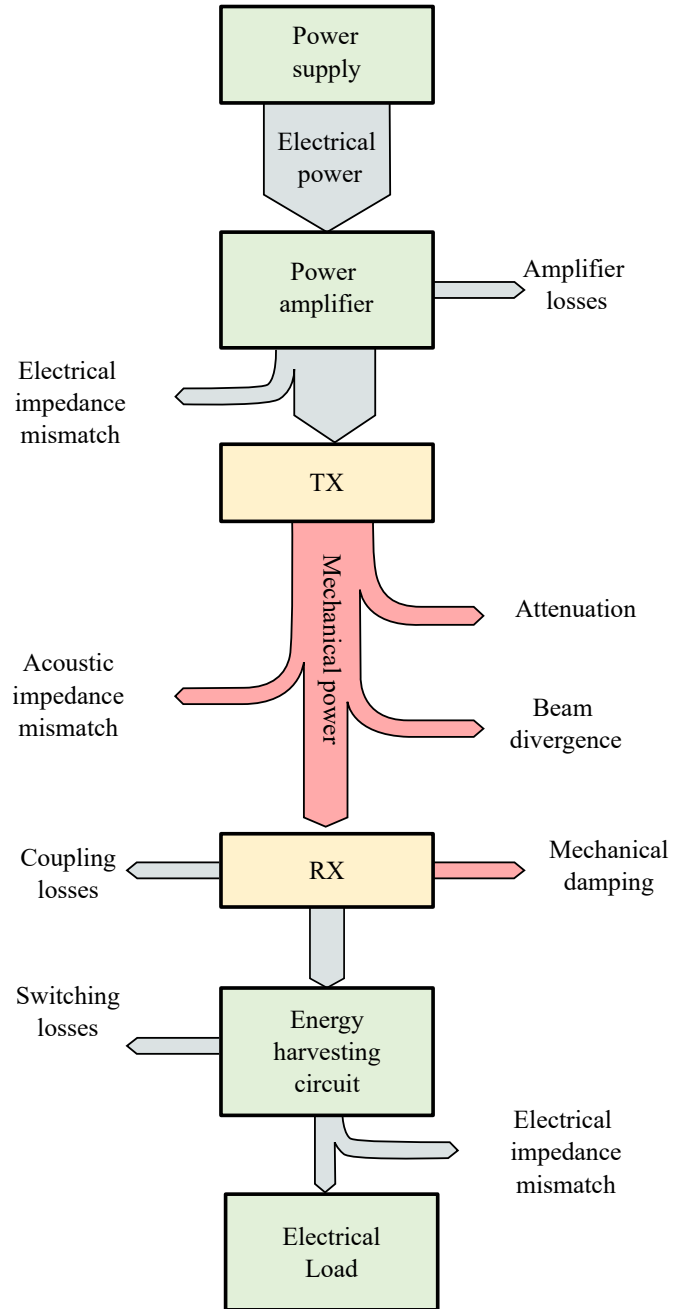


Figure 1.2: Loss mechanisms in ultrasonic power transfer systems (adapted from Ref. [65]).

erating at a high frequency. In biomedical UPT, the attenuation is higher, and the size of RX is restricted depending on the location of the implant, but the power requirements are low. For underwater applications, the attenuation is very low compared to other mediums, and the transducer size is usually unrestricted. However, the distance requirements are large, ranging from a few meters to tens of kilometers which restricts the practical frequency range to lower frequencies to avoid attenuation (typically below 1 MHz down to tens of kHz). The UPT system in this case becomes limited by divergence losses.

The limits imposed by each UPT application on the transducer shape and operating frequency present new challenges for the modeling and design of the UPT system in general, and the transducers in particular. Common analytical models for piezoelectric transducers are derived with certain assumptions about the transducer shape. These assumptions are seldom satisfied in practical UPT applications which makes it important to state them clearly, and use the correct model depending on the transducer shape.

1.4 Transducer Modeling and Aspect Ratio Effects

Several analytical techniques exist in the literature to model piezoelectric transducers. Perhaps the most common are Krimholtz, Leedom, and Matthaei (KLM) and Mason [66] equivalent circuit models. These equivalent circuit models are convenient and can be easily simulated using available circuit analysis tools [67]; however, their accuracy and applicability depend on the dimensions of the transducer, specifically its aspect ratio ($\beta = h/a$ where h is the height or thickness and a is the radius). When derived from first principles (rather than identified from experiments), KLM and Mason models are best suited for extreme aspect ratios: the thickness expander plate (thin infinite plate assumption) which can only be used for very small β , or the length expander bar which is limited to very large β . In practical APT systems, these assumptions are difficult to satisfy due to size limitations on the dimensions of RX. Size and frequency constraints lead to transducers with moderate aspect ratios [68–71].

Analytical models based on the continuum elastodynamics of the transducers have also been investigated [72–75]. While these models offer insights into the factors affecting the power conversion capabilities of the transducers, their applicability is limited to transducers with extreme aspect ratios. To overcome these limitations experimentally, the parameters of both the equivalent circuit and analytical models are usually fit to the response of the actual transducers when they cannot be accurately modeled as a thin bar or a thin plate. This limits the utility of such models when the response of the transducer is critical to UPT system performance and prevents optimization in the design phase. The limits of existing models, as well as new models based on the Rayleigh, and Bishop rod theories are discussed in Chapter 2 [76].

Each application of UPT has a commonly used range for the transducers aspect ratio. Through-metal applications usually use thin-plate transducers operating at high frequencies. Underwater systems, on the other hand, use lower frequencies with moderate aspect ratio transducers while biomedical applications use large plate transducers as transmitters and small moderate aspect ratio transducers as receivers. This introduces a different set of challenges for each system related to either attenuation, divergence, impedance mismatch, or a combination of them. These challenges are analyzed while studying their most relevant applications in the following sections, and throughout the dissertation.

1.5 System-Level Analysis and Efficiency

Through-metal UPT is highly efficient compared to other UPT applications owing to low attenuation in metals and low distance requirements which allow for the use of highly directional thin plate transducers operating at high frequencies (typically in the neighborhood of 1 MHz) for power transfer. These factors facilitate neglecting diffraction losses in the system and allow for using simple 1D models to study its performance. The 1D approximations facilitate studying the interactions between different components of the UPT systems

such as the transducers, the driving circuit, and the energy harvesting circuits which helps in pinpointing the key factors limiting the system efficiency.

Through-metal UPT was first suggested by Hu *et al.* in 2003 [16]. Since then, multiple research groups have investigated its realization albeit with different motivations. The NASA Jet Propulsion Laboratory (JPL) explored supplying high power through titanium barriers for space exploration applications [77]. They were able to power a 100 W incandescent lamp with a peak ultrasonic efficiency of 88% using air-backed piezoelectric transducers operating at 750 KHz [78]. They later demonstrated 1 kW of power transfer with 84% ultrasonic efficiency using a pair of Tonpliz transducers operating at 25 kHz [79]. Researchers from the Rensselaer Polytechnic Institute focused on simultaneously transmitting power and data transfer through thick steel barriers (submarine steel) [80, 81]. They demonstrated simultaneous 50 W (@1MHz) power transfer and 17.37 Mbps (@4MHz) data transfer using two separate transducers mounted on the same 2.5" thick steel wall [2]. They also tested the limits of power transfer using 2.5 cm diameter piezoelectric tiles operating at 1 MHz and demonstrated 141 W power transfer with an ultrasonic efficiency of 67% before failure [82].

Most of the surveyed through-metal UPT literature only reported the measured ultrasonic (AC-to-AC) efficiency from simulations [16, 78, 83–85] or experiments [77, 82, 86, 87]. Attempts to compare experimental to simulated AC-to-AC efficiency showed significant discrepancies [88, 89]. Moreover, only a few publications discussed the efficiency of the system with energy harvesting electronics. Lawry *et al.* [2], Yang *et al.* [90] and Tseng *et al.* [91] reported the AC-to-DC efficiency by including a full-bridge rectifier in their experiments; however, they did not report the overall DC-to-DC efficiency which includes the driving electronics.

The research discussed so far has focused on permanently bonded systems in which both the transmitting and the receiving transducers are meant to remain adhered to the metallic enclosure. For charging portable devices, and for other devices that do not require

continuous power delivery, it is useful to have a detachable charger which is only used when the device needs to be supplied with power. Moss *et al.* [92] developed a detachable UPT system that uses attracting magnets to hold the transducers while in operation. Their design, however, required the use of a liquid couplant which is inconvenient since it contaminates the surface, or dries out and requires frequent reapplication. An approach for simulating, realizing, and characterizing a complete through-metal UPT system with dry coupling is discussed in Chapter 3.

1.6 Reducing Beam Divergence in Ultrasonic Power Transfer Systems

The efficiency and range of a UPT system can be improved through innovative solutions aiming to improve the directivity of TX and focus energy on RX while operating at lower frequencies. This is particularly useful for underwater applications to power wireless nodes placed deep in the ocean, for example. Phononic crystals (PCs) and metamaterial-based approaches have shown promising results for controlling acoustic waves in space, and are investigated for enhancing UPT in Chapter 4 [93, 94].

1.6.1 Phononic Crystals

PCs are ordered engineered structures consisting of a periodic array of inclusions in a homogeneous background [95]. The inclusions are usually made from materials that have a large impedance contrast with respect to the background medium. The periodicity of the inclusions introduces wave bandgaps due to destructive interference of the scattered wave which is known as Bragg scattering. The first Bragg bandgap happens when the wavelength of the incident waves is twice the scattering periodicity. For larger wavelengths, the PC can be considered as a homogeneous material with effective properties that depend on the shape and size (their volumetric filling fraction) of the inclusions in addition to the material properties of both the background medium and the inclusions. PCs are studied by considering a unit cell of the crystal and assuming periodic boundary conditions. The

effective crystal properties (wave speed and acoustic impedance) can be deduced by solving an eigenvalue problem associated with the periodic boundaries. These properties could then be engineered to desirable values by changing the shape and size of the inclusions.

1.6.2 Gradient Index Phononic Crystals in Water

Gradient-Index Phononic Crystals (GRIN-PCs) allow for engineered control of wave propagation beyond what could be achieved using traditional materials. In GRIN-PCs, the effective refractive index profile is varied in space by gradually adjusting the lattice structure of the material, thereby steering the direction of propagating waves. Since the effective acoustic impedance usually follows the gradual variation of the refractive index, reflections that might arise from the steering process can be minimized. Different designs for gradient-based and gradient-index materials have been suggested to guide [96, 97], mode-convert[98–100], focus [101–107], compress [108], absorb [109–111], transmit [112] and retroreflect [113] elastic and acoustic waves, in addition to other exotic applications such as realizing acoustic black holes [114] and asymmetric transmission [115]. Practical realizations of GRIN-PCs have focused on 2D devices as in Lamb [116–118] and Rayleigh [99, 119] waves. Other realizations involved 2.5D approaches in which the variation of the refractive index occurs in a single plane [120–125].

In underwater acoustic applications, metals are commonly used to construct PCs [103, 125–129]. Since manufacturing metals into complex 3D structures is a challenging task, most of the literature has been limited to 2.5D realizations in the form of ordered metallic rods or shells. Additive manufacturing presents a viable approach for fabricating ordered 3D structures; however, 3D printing complex metallic structures is still a challenging task [130].

In-air realization of acoustic GRIN-PCs has been recently reported for sonic frequencies [131]. The large impedance contrast between 3D-printed polymers and air was used to achieve the gradient-index variation required to enable a GRIN-PC Luneburg lens. The

same approach, however, cannot be easily applied to GRIN-PCs for underwater applications, since the impedance contrast between polymers and water is relatively small. A new design for underwater GRIN-PCs using 3D-printed polymers as the background material and air as the inclusion material is discussed in Chapter 4 with application towards enhancing the performance of an underwater UPT systems.

1.6.3 Gradient Index Phononic Crystals in Air

A few publications [15, 132] have looked into using acoustic power to transfer power through air mainly due to the huge impedance mismatch between air and piezoelectric materials which reduces the efficiency of the system significantly. Nevertheless, the efficiency of in-air power transfer systems could be significantly enhanced by focusing the transmitted waves at RX [133, 134]. Moreover, audio-frequency acoustic waves, i.e., sound waves, are abundantly available in everyday life, they exhibit a low power density, which has limited the power harvested from air-borne sound to mostly nano-Watt level [135]. To efficiently convert acoustic energy to electrical power, sound needs to be focused and localized at RX location. A GRIN-PC solution for focusing sound waves in air could thus be used for enhancing both energy harvesting systems and power transfer systems.

While the literature on acoustic power transfer in air is limited, many researchers have looked into focusing acoustic waves for enhancing the performance of sound energy harvesters. For example, Helmholtz resonators with energy harvesters built into their cavity walls have been proposed to localize airflow energy with various configurations [136–139]. Other forms of resonators, such as tube and quarter-wave resonators, have also been used to harvest acoustic energy by combining them with piezoelectric diaphragms [140, 141]. Acoustic/elastic phononic crystals (PCs) and metamaterials have also been proposed to enhance the performance of energy harvesters by focusing or localizing acoustic/elastic wave energy at the harvester location [142–145]. Other effort includes the use of metasurfaces

by coiling up space for the confinement and enhanced harvesting of acoustic energy [146] as well as spatial grading to trap and harvest elastic wave energy [147].

GRIN-PCs have also been used to focus acoustic waves [148]. Climente et al. [102] fabricated a 2D gradient index sonic crystal lens based on the hyperbolic secant profile to focus airborne sound. More recently, along with advancements in 3D printing technology, Xie et al. [131] succeeded in fabricating 2.5D and 3D Luneburg lenses capable of focusing acoustic waves in air. The circular/spherical (in 2D/3D) profile of the Luneburg lens allows incident plane waves to be focused on the other side of the lens regardless of their direction. This was exploited to enhance the performance of ultrasonic imaging using a 2.5D lens operating around 40 kHz [131]; however, no numerical or experimental results were reported for the 3D Luneburg lens. Hyun et al. [149] designed a 2.5D GRIN-PC lens made of 3D-printed ABS cylinders to focus acoustic waves between 250 Hz and 1 kHz on an energy harvester (receiver) with a peak observed in an acoustic duct system.

In-air implementations of GRIN-PC lenses for enhancing sound energy harvesting and power transfer are discussed in Chapter 4.

1.7 Acoustic and Electrical Impedance Matching for Power and Data Transfer

Power reflection due to impedance mismatch should be minimized in order to maximize the system efficiency. However, if the power reflection is controlled (modulated) through varying the electrical impedance connected to RX, it could be used to transmit data back to the source. This is known as impedance modulation or backscatter communication, and it has been investigated by researchers from different disciplines simultaneously with UPT [1, 3, 37, 91, 150–152].

The simultaneous power and data transfer ultrasonic systems in the literature included a PZT transmitter which is connected to an electrical power source (power amplifier) and sends power to a piezoelectric receiver which is either connected to a sensor for collecting data or an actuator for providing some stimulation to its environment. Depending on

the system complexity, communication between the two devices could be designed so that data is only sent from TX to the RX (downlink communication), i.e., for sending excitation commands [2, 31, 32, 34, 36, 153], or from RX to TX only (uplink communication) to transmit sensor data and device status [1, 4, 22, 24, 26, 27, 30, 91, 154–157], or in both directions either simultaneously (full-duplex) [81, 158] or in turns (half-duplex/time multiplexing) [37, 80, 83, 159–161]. Downlink communication can be as simple as switching between turning TX on and off, i.e., on-off keying (OOK) [32], or the data could be packed in narrow frequency communication channels such as orthogonal frequency division multiplexing (OFDM) for a higher throughput [2].

Uplink communication has more restrictions compared to downlink since the power available to the wireless node is limited. While active approaches (exciting the transducer to send data) have been proposed for uplink communication, their realization usually involves toggling between storing enough power and transmitting the uplink data [4, 24]. This limits the uplink throughput since no communication occurs while the wireless node is being charged. It also requires the use of a large capacitor or a battery to store the data which might not be feasible in space-limited applications such as in biomedical implants.

Ultrasonic backscatter is a passive uplink communication approach in which the reflected ultrasonic signal from RX is modulated to send the uplink data. Backscattering works by changing the electrical impedance connected to the piezoelectric receiver which in turn changes its acoustic impedance and the amplitude of the reflected ultrasonic signal. By switching between absorbing and reflecting the ultrasonic waves, uplink communication could be established with minimal power from RX. Only a low-power single transistor with a driving circuit is required to establish uplink communication using backscatter which greatly reduces the hardware complexity compared to active approaches. The majority of the surveyed literature incorporated some variation of backscattering in their simultaneous ultrasonic power and data transfer system designs [26, 58, 81, 159].

A fundamental limitation in state-of-the-art simultaneous power and backscatter systems is that for communication to happen, incident ultrasonic power intended for powering the system needs to be reflected. This reduces the power available to the wireless device, limiting its range and throughput. Ozeri et al. [155] attempted to address this by imposing a small change in the load connected to the transducer instead of completely shorting it. However, this approach only offers a compromise between communication sensitivity and power harvesting.

Another limitation commonly acknowledged in the biomedical literature is the use of commercial ultrasound transducers as power and data transmitters for convenience [34, 37, 59, 161]. Since commercial transducers are usually optimized for bandwidth (for imaging and NDT applications), their sensitivity and power conversion efficiency is much lower than those of a transducer optimized for low loss applications. The performance of the developed simultaneous power and backscatter systems could thus benefit from optimizing the transmitter for simultaneous power and data transfer operation.

Acoustic and electrical impedance matching for simultaneous power transfer and backscattering communication is discussed in Chapter 5.

1.8 Dissertation Outline

The rest of the dissertation is organized as follows. First, the background, opportunities, and challenges for using acoustic waves to transfer energy through the human body, through metals, and underwater are presented in Chapter 1.

In Chapter 2, standard theories for modeling thickness-mode piezoelectric transducers are reviewed. Models based on the Rayleigh and Bishop rod theories are then developed to analyze transducers (transmitter or receiver) with various aspect ratios. Results from these models are compared with experimental data and finite-element analysis to determine the range of aspect ratios in which they are valid. In addition, fluid loading effects on the predictions of all models are investigated. The resulting models are used to analyze the

effect of aspect ratio on the performance of the transducer when operated as TX or RX in an UPT setting.

Chapter 3 covers a system-level study of ultrasonic power transfer through metals in which power is delivered from an electrical DC source to a DC load. The chapter covers a typical configuration in which the transducers are bonded to the metallic barrier, as well as a new design for achieving efficient power transfer with a detachable dry-coupled transmitter. Transmission line 1D models based on the transfer matrix method are developed for analyzing the performance of the ultrasonic system. The analytical predictions of key system parameters such as the ultrasonic efficiency and voltage transfer function are compared to experimental results and numerical simulations. The efficiency of the different electrical and mechanical components of the system are discussed, as well as, the overall DC-to-DC efficiency of the system, highlighting bottlenecks in system performance. A dry-coupled detachable through-metal UPT is also developed to provide efficient power transfer without the need for a liquid couplant. Low attenuation soft elastomers are experimentally tested with a magnetic setup to evaluate the dry-coupled efficiency. Samples with different materials and thicknesses are tested to select the best configuration for the dry-coupling. A portable/battery-operated detachable power transmitter is then fabricated, and the DC-to-DC operation of the system is characterized experimentally to find the power transfer levels as well as the total system efficiency.

Chapter 4 is dedicated to the reduction of divergence losses through wave focusing and collimation. Two designs for a phononic crystal based lens for in-air and underwater operation are introduced to enhance the power output of a UPT system. An acoustic phononic crystal based on structured air inclusions in a 3D-printed polymer is introduced for focusing ultrasonic waves under water. The GRIN-PC lens is simulated using the finite element method, 3D-printed, then experimentally verified. Two lenses are used at the transmitter and receiver of an underwater UPT system to enhance its performance. A second GRIN-PC targeting in-air operation in the audio frequency range is designed and simulated using the

finite element method. The 3D printed lens is experimentally tested to validate its design. It is then used to enhance the performance of a piezoelectric diaphragm receiver placed at its focal point. The output power enhancement due to the introduction of the lens is experimentally verified for different resistor values.

Chapter 5 studies the effect of acoustic and electrical impedance matching on the performance of an ultrasonic system designed for simultaneous power and data transfer using impedance modulation. The factors affecting power/signal reflection due to impedance mismatch are analyzed analytically. The effect of using one and two acoustic matching layers on the bandwidth and sensitivity of RX are compared analytically. An approach for simultaneous acoustic and electrical impedance matching is introduced to maximize the bandwidth of the transducer. Several air-backed underwater transducers with no acoustic matching and with two-layer acoustic matching are fabricated. Their electrical and acoustic reflection as well as their electrical impedance are experimentally measured and compared to analytical predictions. The effect of varying the acoustic matching layers' thickness on the electrical impedance is also determined. A circuit for maximizing the bandwidth and sensitivity of the transducer for data transfer is then tested experimentally. Another circuit for achieving uninterrupted simultaneous power and data transfer using a single transducer is also implemented and tested.

Finally, Chapter 6 discusses the main conclusions of this work. The main contributions to the literature are highlighted, and potential future work is outlined.

CHAPTER 2

ASPECT RATIO-DEPENDENT PIEZOELECTRIC TRANSMITTER AND RECEIVER DYNAMICS

The design of an efficient UPT system requires accurate models to describe its individual components as well as the interaction between them. Most of the available analytical models for the bulk piezoelectric transducers used in UPT are limited to either thin rod or thin plate transducers. However, transducers with moderate aspect ratios are often used, especially at the receiver end.

In this chapter, several continuum analytical models are derived from first principles to approximate the response of a thickness-mode piezoelectric transducer, where each model is applicable within a specific range of aspect ratios. The validity range of the models are investigated by comparing their numerical predictions to the values obtained using finite element method (FEM) simulations as well as experimental measurements of the impedance of thickness-mode PZT transducers. The introduced models are represented in S-parameters (i.e. scattering parameters) matrix form [162–164], which can be easily imported to the abundantly available circuit simulators such as those used in Chapter 3. This facilitates integrating their design in conjunction with other electrical components involved in the UPT system. The analytical and numerical methods are then used to analyze the effect of aspect ratio on the generated pressure from the transducers when used as TX and on the generated electrical power when used as RX.

In the following, dynamics of thickness-mode piezoelectric transducers (TX or RX) are studied analytically, and transducer models based on the thin rod, Rayleigh (also known as Rayleigh-Love), Bishop (also known as Rayleigh-Bishop) and thin plate assumptions are derived using energy approaches in Section 2.1. The electrical impedance of select transducers is measured experimentally and compared to the analytical predictions and to

numerical simulations in Section 2.2. The effect of transducer's aspect ratio on its performance is analyzed when used as a TX in Section 2.3 and as an RX in Section 2.4. A summary of the findings of the work and concluding remarks are presented in Section 2.5.

2.1 Thickness-Mode Dynamics of a Piezoelectric Transducer with Circular Cross Section

A continuum of piezoelectric material is governed by the piezoelectric constitutive equations, which are given in their stress-charge form by:

$$T = \mathbf{C}^E S - \mathbf{e}^T E \quad (2.1)$$

$$D = \mathbf{e} S + \epsilon^S E \quad (2.2)$$

where T and S are the mechanical stress and strain vectors, E and D are the electric field and electric displacement vectors respectively, \mathbf{C}^E is the stiffness matrix at constant electric field, ϵ^S is the electric permittivity matrix at constant strain and \mathbf{e} is the piezoelectric coupling matrix. Structural (mechanical) and dielectric losses are considered in the form of complex elastic and dielectric constants:

$$\begin{aligned} \mathbf{C}^E &= \mathbf{C}_{\text{undamped}}^E (1 + j\gamma), \\ \epsilon^S &= \epsilon_{\text{undamped}}^S (1 + j\delta) \end{aligned} \quad (2.3)$$

where γ and δ are the structural and dielectric loss factors.

A cylindrical piezoelectric transducer with height h and radius a is considered (Figure 2.1a). The transducer is poled in the longitudinal (z) direction, and thin metallic electrodes are deposited on its circular faces. The lateral components of the electric field and the electric displacement vanish; therefore, Equation (2.1) and Equation (2.2) can be expanded

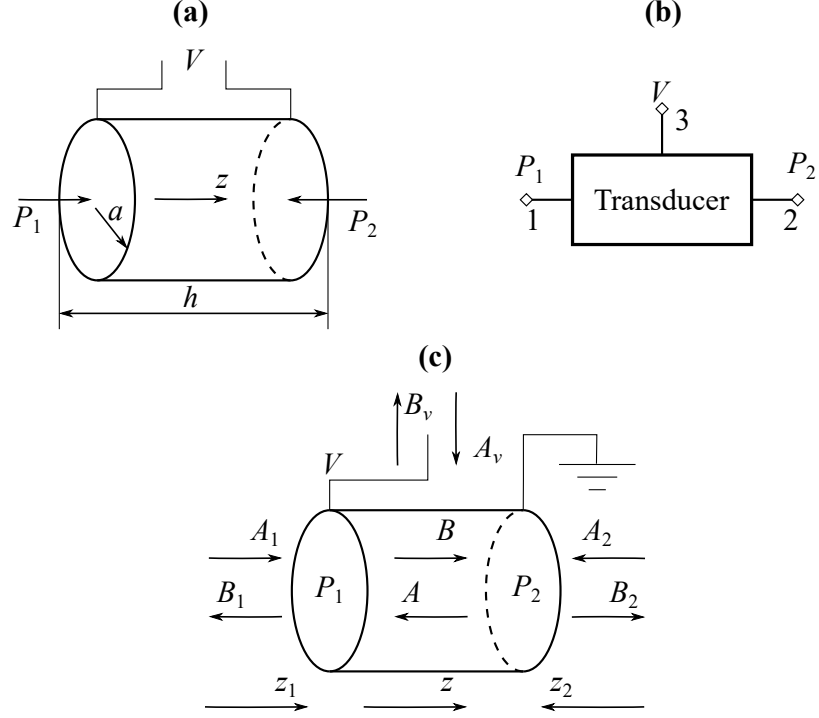


Figure 2.1: (a) Schematic of a piezoelectric rod transducer, (b) three-port element representation, and (c) incident and reflected voltage and pressure waves on the transducer.

and simplified to:

$$T_1 = C_{11}S_1 + C_{12}S_2 + C_{13}S_3 - e_{31}E_3 \quad (2.4)$$

$$T_2 = C_{12}S_1 + C_{22}S_2 + C_{13}S_3 - e_{31}E_3 \quad (2.5)$$

$$T_3 = C_{13}S_1 + C_{13}S_2 + C_{33}S_3 - e_{33}E_3 \quad (2.6)$$

$$T_4 = C_{44}S_4 \quad (2.7)$$

$$T_5 = C_{44}S_5 \quad (2.8)$$

$$T_6 = \frac{C_{11} - C_{12}}{2}S_6 \quad (2.9)$$

$$D_3 = e_{31}S_1 + e_{31}S_2 + e_{33}S_3 + \epsilon_{33}E_3. \quad (2.10)$$

where the index 3 indicates the polarization direction, and (1,2) indicate the directions normal to the polarization vectors. Indices (4-6) follow Voigt notation to represent shear stresses and strains. In the cylindrical coordinates (r, θ, z) , the mechanical strain is related

to the displacement field by [165]:

$$\begin{aligned} S_1 &= \frac{du_r}{dr}, & S_2 &= \frac{1}{r} \left(\frac{du_\theta}{d\theta} + u_r \right), & S_3 &= \frac{du_z}{dz}, \\ S_4 &= \frac{1}{r} \frac{du_z}{d\theta} + \frac{du_\theta}{dz}, & S_5 &= \frac{du_r}{dz} + \frac{du_z}{dr} \\ S_6 &= \frac{1}{r} \left(\frac{du_r}{d\theta} - u_\theta \right) + \frac{du_\theta}{dr} \end{aligned} \quad (2.11)$$

where u_r , u_θ and u_z are the displacements in r , θ and z directions respectively. The modified Hamilton's principle for a piezoelectric volume is given by [166, 167]:

$$\int_{t_1}^{t_2} \delta (\bar{T} - U + W_e + W_{nc}) dt = 0 \quad (2.12)$$

where \bar{T} is the total kinetic energy, U is the total potential (elastic) energy, W_e is the electric energy stored in the transducer, and W_{nc} is the work due to the non-conservative forces acting on the rod including the external mechanical and electrical forces. These terms are given by:

$$\bar{T} = \frac{1}{2} \int_{\bar{V}} \rho (\dot{u}_r^2 + \dot{u}_\theta^2 + \dot{u}_z^2) d\bar{V} \quad (2.13)$$

$$U = \frac{1}{2} \int_{\bar{V}} \sum_{i=1}^6 T_i s_i d\bar{V} \quad (2.14)$$

$$W_e = \frac{1}{2} \int_{\bar{V}} E_3 D_3 d\bar{V} \quad (2.15)$$

$$W_{nc} = \int_S (\bar{t}_r u_r + \bar{t}_\theta u_\theta + \bar{t}_z u_z - \bar{q} \phi) dA \quad (2.16)$$

where ρ is the mass density, \bar{V} is the volume, S is the external surface of the transducer, \bar{t} is the external traction acting on the surface of the transducer, \bar{q} is the external surface charge density, and ϕ is the electric potential applied to the surface.

The response of the transducer cannot be estimated analytically unless certain assumptions are made regarding the displacement fields inside it. These assumptions can be made

when the aspect ratio ($\beta = h/a$) of the transducer is very high (thin rod, Rayleigh, and Bishop theories) or very low (thickness vibration of an infinite plate).

2.1.1 Classical Thin-Rod Model

For a symmetric thin rod transducer, the lateral and shear stresses are assumed to be very small i.e.,:

$$T_1 = T_2 = T_4 = T_5 = T_6 = 0 \quad (2.17)$$

The longitudinal displacement u_z is assumed to have the form:

$$u_z = u(z, t) \quad (2.18)$$

and the electric potential $\phi(z, t)$ is related to the electric field E_3 by:

$$E_3 = -\frac{\partial \phi}{\partial z}. \quad (2.19)$$

Substituting Equation (2.17) - Equation (2.19) into Equation (2.11) and Equation (2.4) - Equation (2.10) yields:

$$T_3 = C_{33}u^{(1,0)}(z, t) + e_{33}\phi^{(1,0)}(z, t) - \frac{2C_{13}(C_{13}u^{(1,0)}(z, t) + e_{31}\phi^{(1,0)}(z, t))}{C_{11} + C_{12}} \quad (2.20)$$

$$D_3 = e_{33}u^{(1,0)}(z, t) - \epsilon_{33}\phi^{(1,0)}(z, t) - \frac{2e_{31}(C_{13}u^{(1,0)}(z, t) + e_{31}\phi^{(1,0)}(z, t))}{C_{11} + C_{12}} \quad (2.21)$$

where the superscript (m, n) indicates the m^{th} derivative with respect to z and the n^{th} derivative with respect to t . Substituting Equation (2.17) - Equation (2.21) in Equation (2.13) - Equation (2.16) and neglecting the lateral inertia terms ($\dot{u}_r = \dot{u}_\theta = 0$) yield the formula for the conservative energies inside the rod in terms of the longitudinal displacement $u(z, t)$

and electric potential $\phi(z, t)$:

$$\bar{T} = \frac{1}{2} \int_{\bar{V}} \rho (u^{(0,1)}(z, t)^2) d\bar{V} \quad (2.22)$$

$$U = \frac{1}{2} \int_{\bar{V}} \left(\left(C_{33} - \frac{2C_{13}^2}{C_{11} + C_{12}} \right) u^{(1,0)}(z, t)^2 + \left(e_{33} - \frac{2C_{13}e_{31}}{C_{11} + C_{12}} \right) \phi^{(1,0)}(z, t) u^{(1,0)}(z, t) \right) d\bar{V} \quad (2.23)$$

$$W_e = \frac{1}{2} \int_{\bar{V}} \left(\left(\epsilon_{33} + \frac{2e_{31}^2}{C_{11} + C_{12}} \right) \phi^{(1,0)}(z, t)^2 - \left(e_{33} - \frac{2C_{13}e_{31}}{C_{11} + C_{12}} \right) u^{(1,0)}(z, t) \phi^{(1,0)}(z, t) \right) d\bar{V} \quad (2.24)$$

For the rod shown in Figure 2.1a, the non-conservative work is given by:

$$W_{nc} = P_1(t) u(0, t) + P_2(t) u(h, t) - Q(t) \phi(h, t) \quad (2.25)$$

where $Q(t)$ is the total electric charge flowing into or from the transducer's domain. Substituting Equation (2.22) - Equation (2.24) back into Equation (2.12), taking the variation of the integral with respect to $u(z, t)$ and $\phi(z, t)$ and performing integration by parts yields the electromechanical governing equations:

$$\rho u^{(0,2)}(z, t) - \bar{C} u^{(2,0)}(z, t) + \bar{e} \phi^{(2,0)}(z, t) = 0 \quad (2.26)$$

$$\bar{e} u^{(2,0)}(z, t) - \bar{\epsilon} \phi^{(2,0)}(z, t) = 0 \quad (2.27)$$

and the boundary conditions:

$$-A_p (\bar{C} u^{(1,0)}(z, t) + \bar{e} \phi^{(1,0)}(z, t)) + P_{1,2}(t) = 0 \Big|_{z=0,h} \quad (2.28)$$

$$\delta u(z, t) = 0 \Big|_{z=0,h} \quad (2.29)$$

$$A_p (\bar{e} u^{(1,0)}(z, t) - \bar{\epsilon} \phi^{(1,0)}(z, t)) - Q(t) = 0 \Big|_{z=0,h} \quad (2.30)$$

$$\delta \phi(z, t) = 0 \Big|_{z=0,h} \quad (2.31)$$

where

$$\begin{aligned}\bar{C} &= C_{33} - \frac{2C_{13}^2}{C_{11} + C_{12}}, \quad \bar{e} = e_{33} - \frac{2C_{13}e_{31}}{C_{11} + C_{12}}, \\ \bar{\epsilon} &= \epsilon_{33} + \frac{2e_{31}^2}{C_{11} + C_{12}}\end{aligned}\tag{2.32}$$

and A_p is the cross-sectional area of the transducer. Equation (2.28) and Equation (2.29) are the mechanical natural and essential boundary conditions, while Equation (2.30) and Equation (2.31) are the electrical natural and essential boundary conditions, respectively. The solution of Equation (2.27) is obtained by integration:

$$\phi(z, t) = \frac{\bar{e}}{\bar{\epsilon}}u(z, t) + c_1z + c_2\tag{2.33}$$

The value of c_1 could be found by substituting Equation (2.33) in the electrical natural boundary condition Equation (2.30)

$$c_1 = \frac{Q(t)}{A_p \bar{\epsilon}}\tag{2.34}$$

The value of c_2 is arbitrary since it represents the absolute electric potential. The potential difference between the electrodes is given by:

$$\begin{aligned}V(t) &= \phi(h, t) - \phi(0, t) \\ &= \frac{h}{A_p \bar{\epsilon}}Q(t) + \frac{\bar{e}}{\bar{\epsilon}}(u(h, t) - u(0, t))\end{aligned}\tag{2.35}$$

Substituting Equation (2.27) in the first equation of motion, Equation (2.26), yields the mechanical wave equation:

$$\rho u^{(0,2)}(z, t) - \bar{C}^D u^{(2,0)}(z, t) = 0\tag{2.36}$$

where $\bar{C}^D = \bar{C} + \bar{e}^2/\bar{\epsilon}$ is the reduced stiffness of the bar at constant charge (open-circuit conditions). Assuming harmonic plane-wave solution of the form

$$u(z, t) = A_u e^{j(\omega t - kz)} + B_u e^{j(\omega t + kz)} \quad (2.37)$$

where $k = \omega/c$ is the wavenumber, ω is the angular frequency of the wave, $c = (\bar{C}^D/\rho)^{1/2}$ is the speed of sound in the transducer, and A_u, B_u are the complex amplitudes of the forward and backward traveling displacement waves. The value of A_u and B_u can be evaluated from the mechanical boundary conditions given by Equation (2.28) or Equation (2.29).

A more general approach for the estimation of the response of the transducer is to consider it as a 3-port element and focus on relating the inputs and outputs of these elements in a generic sense. In this approach, the interface matching conditions given by Equation (2.28), Equation (2.29) and the electrical boundary conditions Equation (2.35) can be used to express a scattering matrix which relates incident and reflected waves at each port (both electrical and mechanical waves). The transducer scattering matrix \mathbf{S} is given by:

$$\begin{bmatrix} B_1 \\ B_2 \\ B_v \end{bmatrix} = \mathbf{S} \begin{bmatrix} A_1 \\ A_2 \\ A_v \end{bmatrix} = \begin{bmatrix} S_{11} & S_{12} & S_{13} \\ S_{21} & S_{22} & S_{23} \\ S_{31} & S_{32} & S_{33} \end{bmatrix} \begin{bmatrix} A_1 \\ A_2 \\ A_v \end{bmatrix} \quad (2.38)$$

where A_1, B_1, A_2, B_2 are the incident and reflected pressure waves on faces 1 and 2, while A_v, B_v are the incident and reflected voltage waves on the electrodes as shown in Figure 2.1c.

To evaluate the scattering matrix, the total pressure on both faces $P_1(t)$ and $P_2(t)$ as well as the voltage across the electrodes $V(t)$ are written in the form of incident and reflected

waves, as shown in Figure 2.1c, in the form:

$$P_1(z_1, t) = A_1 e^{i(\omega t - k_m z_1)} + B_1 e^{i(\omega t + k_m z_1)} \quad (2.39)$$

$$P_2(z_2, t) = A_2 e^{i(\omega t - k_m z_2)} + B_2 e^{i(\omega t + k_m z_2)} \quad (2.40)$$

$$V(t) = (A_v + B_v) e^{i\omega t} \quad (2.41)$$

and the acoustic velocities ($v_n(z_n, t)$), and electric current flowing into the transducer are then given by:

$$v_1(z_1, t) = \frac{1}{Z_m} (A_1 e^{j(\omega t - k_m z_1)} - B_1 e^{j(\omega t + k_m z_1)}) \quad (2.42)$$

$$v_2(z_2, t) = \frac{1}{Z_m} (A_2 e^{j(\omega t - k_m z_2)} - B_2 e^{j(\omega t + k_m z_2)}) \quad (2.43)$$

$$I(t) = \frac{A_v - B_v}{Z_e} e^{j\omega t} \quad (2.44)$$

where $k_m = \omega/c_m$ is the wavenumber of the external medium, $Z_m = \rho_m c_m$ is the acoustic impedance of the external medium, ρ_m and c_m are the mass density and speed of sound in the surrounding medium (surrounding fluid) and Z_e is an the reference electric impedance usually chosen to be 50Ω .

Applying continuity conditions to both the mechanical and electrical interfaces:

$$u^{(0,1)}(0, t) = v_1(0, t), \quad u^{(0,1)}(h, t) = -v_2(0, t) \quad (2.45)$$

$$I(t) = \frac{dQ}{dt} \quad (2.46)$$

and substituting Equation (2.39) - Equation (2.41) in Equation (2.28), Equation (2.35), and Equation (2.45) yields:

$$\begin{aligned} A_p Z_e \bar{e} \omega (A_2 + B_2) e^{j h k} + j (A_v - B_v) e^{j h k} \bar{e} \\ + j A_p Z_e k \omega (A_u - B_u e^{2 j h k}) (\bar{e}^2 + \bar{C}^D \bar{e}) = 0 \quad (2.47) \end{aligned}$$

$$(A_v - B_v) \bar{e} + -j A_p Z_e \omega \bar{e} (A_1 + B_1) + A_p Z_e k \omega (A_u - B_u) (\bar{e}^2 + \bar{C}^D \bar{e}) = 0 \quad (2.48)$$

$$\bar{\epsilon} (A_v + B_v) = (A (-1 + e^{-j h k}) + B (-1 + e^{j h k})) \bar{e} - \frac{j (A_v - B_v) h}{A_p Z_e \omega} \quad (2.49)$$

$$j \omega A_p Z_m (A_u + B_u) = A_1 - B_1 \quad (2.50)$$

$$j \omega A_p Z_m e^{-j h k} (A_u + B_u e^{2 j h k}) = -A_2 + B_2 \quad (2.51)$$

Equation (2.47) - Equation (2.51) can be arranged into matrix form:

$$\mathbf{M}_1 \begin{bmatrix} B_1 & B_2 & B_v & A_u & B_u \end{bmatrix}^T = \mathbf{M}_2 \begin{bmatrix} A_1 & A_2 & A_v \end{bmatrix}^T \quad (2.52)$$

where \mathbf{M}_1 and \mathbf{M}_2 are (5x5) and (5x3) system matrices. The scattering matrix is then given by:

$$\mathbf{S} = \mathbf{M}_3 \mathbf{M}_1^{-1} \mathbf{M}_2 \quad (2.53)$$

where

$$\mathbf{M}_3 = \begin{bmatrix} 1 & 0 & 0 & 0 & 0 \\ 0 & 1 & 0 & 0 & 0 \\ 0 & 0 & 1 & 0 & 0 \end{bmatrix} \quad (2.54)$$

2.1.2 Rayleigh Model

The thin rod assumption neglects the lateral inertia of the rod which limits its applicability to rods with very large β values (i.e. very slender rods). The Rayleigh rod theory includes the effect of lateral inertia by assuming the displacement fields for an axisymmetric thin rod to have the form [165]:

$$u_z = u(z, t), \quad u_r = -\nu r u^{(1,0)}(z, t), \quad u_\theta = 0 \quad (2.55)$$

where $\nu = C_{13}/(C_{11} + C_{12})$ is Poisson's ratio. This model can be used for transducers with lower aspect ratios up to the limit where radial and shear deformations start affecting the response of the transducer.

As for the thin-rod case, the electric potential is assumed to have the form $\phi(z, t)$. Equation (2.55) can then be used alongside Equation (2.33) to express the strain fields inside the rod by substituting them in Equation (2.11), which in turn can be used to express the stresses and electric displacements through Equation (2.4) - Equation (2.10). Substituting everything into the energy equations Equation (2.13) - Equation (2.16), neglecting the shear stresses (T_4 and T_5), taking the variation of the integral with respect to $u(z, t)$ and $\phi(z, t)$, then performing integration by parts yields the electromechanical governing equations:

$$A_p \rho u^{(0,2)}(z, t) = A_p \bar{C} u^{(2,0)}(z, t) + A_p \bar{e} \phi^{(2,0)}(z, t) + I_p \nu^2 \rho u^{(2,2)}(z, t) \quad (2.56)$$

$$\bar{e} u^{(2,0)}(z, t) - \epsilon_{33} \phi^{(2,0)}(z, t) = 0 \quad (2.57)$$

and the boundary conditions:

$$-A_p \bar{C} u^{(1,0)}(z, t) - A_p \bar{e} \phi^{(1,0)}(z, t) - I_p \nu^2 \rho u^{(1,2)}(z, t) + P_{1,2}(t) = 0|_{z=0,h} \quad (2.58)$$

$$\delta u(z, t) = 0|_{z=0,h} \quad (2.59)$$

$$A_p (\bar{\epsilon} u^{(1,0)}(z, t) - \epsilon_{33} \phi^{(1,0)}(z, t)) - Q(t) = 0|_{z=0,h} \quad (2.60)$$

$$\delta \phi(z, t) = 0|_{z=0,h} \quad (2.61)$$

where I_p is the polar moment of inertia of the rod. The electrical equation of motion Equation (2.57) has the same form as the thin-rod case Equation (2.27), and thus its solution is also given by Equation (2.35) except for replacing the modified electric permittivity ($\bar{\epsilon}$) with (ϵ_{33}). Substituting back in Equation (2.56) yields:

$$A_p \rho u^{(0,2)}(z, t) = A_p \bar{C}^D u^{(2,0)}(z, t) + I_p \nu^2 \rho u^{(2,2)}(z, t) \quad (2.62)$$

The solution of Equation (2.62) can be written in the form:

$$u(z, t) = (A_u e^{-jkz} + B_u e^{jkz}) e^{j\omega t} \quad (2.63)$$

where k is given by:

$$k = \omega \sqrt{\frac{A_p \rho}{A_p \bar{C}^D - I_p \nu^2 \rho \omega^2}} \quad (2.64)$$

As with the thin rod case, the electrical and mechanical continuity conditions can be used to construct the scattering matrix using Equation (2.53).

2.1.3 Bishop Model

The Bishop rod theory accounts for the coupling between longitudinal and radial displacements inside the rod through the shear elastic modulus C_{44} . Following the same energy approach yields slightly more involved governing equations

$$\begin{aligned} A_p \rho u^{(0,2)}(z, t) + C_{44} I_p \gamma^2 u^{(4,0)}(z, t) = \\ A_p \bar{C} u^{(2,0)}(z, t) + A_p \bar{\epsilon} \phi^{(2,0)}(z, t) + I_p \nu^2 \rho u^{(2,2)}(z, t) \end{aligned} \quad (2.65)$$

$$\bar{e}u^{(2,0)}(z, t) - \epsilon_{33}\phi^{(2,0)}(z, t) = 0 \quad (2.66)$$

and boundary conditions:

$$-A_p\bar{C}u^{(1,0)}(z, t) - A_p\bar{e}\phi^{(1,0)}(z, t) + I_p\nu^2(C_{44}u^{(3,0)}(z, t) - \rho u^{(1,2)}(z, t)) + P_{1,2}(t) = 0 \Big|_{z=0,h} \quad (2.67)$$

$$u^{(2,0)}(z, t) = 0 \Big|_{z=0,h}, \quad \delta u(z, t) = 0 \Big|_{z=0,h} \quad (2.68)$$

$$\delta u^{(1,0)}(z, t) = 0 \Big|_{z=0,h} \quad (2.69)$$

$$A_p(\bar{e}u^{(1,0)}(z, t) - \epsilon_{33}\phi^{(1,0)}(z, t)) - Q(t) = 0 \Big|_{z=0,h} \quad (2.70)$$

$$\delta\phi(z, t) = 0 \Big|_{z=0,h} \quad (2.71)$$

Again, the electrical governing equations are the same as those obtained from the Rayleigh assumption, yielding a simplified mechanical governing equation in the form:

$$A_p\rho u^{(0,2)}(z, t) + C_{44}I_p\nu^2u^{(4,0)}(z, t) = A_p\bar{C}^D u^{(2,0)}(z, t) + I_p\nu^2\rho u^{(2,2)}(z, t) \quad (2.72)$$

The solution of Equation (2.72) can be written in the form:

$$u(z, t) = (A_{u1}e^{-jk_1z} + B_{u1}e^{jk_1z} + A_{u2}e^{-jk_2z} + B_{u2}e^{jk_2z}) e^{j\omega t} \quad (2.73)$$

where

$$k_{1,2}^2 = \frac{\rho I_p \nu^2 \omega^2 - A_p \bar{C}^D - A_p \bar{e}^2}{2C_{44}I_p \nu^2} \pm \frac{\sqrt{4A_p C_{44} I_p \nu^2 \rho \omega^2 + \left(A_p \bar{C}^D + \frac{A_p \bar{e}^2}{\bar{\epsilon}} - I_p \nu^2 \rho \omega^2\right)^2}}{2C_{44}I_p \nu^2} \quad (2.74)$$

As with the Rayleigh case, the electrical and mechanical interface matching conditions can be used to construct the scattering matrix. The main difference is the additional two mechanical boundary equations introduced in Equation (2.67) - Equation (2.69).

The interface matching equations could then be arranged in matrix form:

$$\mathbf{M}_1 \begin{bmatrix} B_1 & B_2 & B_v & A_{u1} & B_{u1} & A_{u2} & B_{u2} \end{bmatrix}^T = \mathbf{M}_2 \begin{bmatrix} A_1 & A_2 & A_v \end{bmatrix}^T \quad (2.75)$$

where, in this case, \mathbf{M}_1 and \mathbf{M}_2 are (7x7) and (7x3) system matrices. The scattering matrix is then given by:

$$\mathbf{S} = \mathbf{M}_3 \mathbf{M}_1^{-1} \mathbf{M}_2 \quad (2.76)$$

and

$$M_3 = \begin{bmatrix} 1 & 0 & 0 & 0 & 0 & 0 & 0 \\ 0 & 1 & 0 & 0 & 0 & 0 & 0 \\ 0 & 0 & 1 & 0 & 0 & 0 & 0 \end{bmatrix} \quad (2.77)$$

2.1.4 Infinite Plate Model

When the lateral dimensions of the transducer are much larger than its thickness (very low aspect ratio β), the lateral strains are neglected compared to the strain in the thickness direction, and only the thickness vibrations of the transducer are taken into consideration. i.e.:

$$u_z = u(z, t)$$

Following a similar procedure as the thin rod case and substituting $S_3 = \frac{du_z}{dz} = u^{(1,0)}(z, t)$ into Equation (2.6) and Equation (2.10) yields:

$$T_3 = C_{33}u^{(1,0)}(z, t) + e_{33}\phi^{(1,0)}(z, t) \quad (2.78)$$

$$D_3 = e_{33}u^{(1,0)}(z, t) - \epsilon_{33}\phi^{(1,0)}(z, t) \quad (2.79)$$

Substituting Equation (2.78) and Equation (2.79) in the energy Equations [Equation (2.13) - Equation (2.16)] and then into Hamilton's principle Equation (2.12) then taking the variation of the integral with respect to $u(z, t)$ and $\phi(z, t)$ and performing integration by parts yields the electromechanical governing equations:

$$\rho u^{(0,2)}(z, t) - Cu^{(2,0)}(z, t) + e_{33}\phi^{(2,0)}(z, t) = 0 \quad (2.80)$$

$$e_{33}u^{(2,0)}(z, t) - \epsilon_{33}\phi^{(2,0)}(z, t) = 0 \quad (2.81)$$

and boundary conditions:

$$-A_p(C_{33}u^{(1,0)}(z, t) + e_{33}\phi^{(1,0)}(z, t)) + P_{1,2}(t) = 0 \Big|_{z=0,h} \quad (2.82)$$

$$\delta u(z, t) = 0 \Big|_{z=0,h} \quad (2.83)$$

$$A_p(e_{33}u^{(1,0)}(z, t) - \epsilon_{33}\phi^{(1,0)}(z, t)) - Q(t) = 0 \Big|_{z=0,h} \quad (2.84)$$

$$\delta\phi(h, t) = 0 \Big|_{z=0,h} \quad (2.85)$$

which are very similar to Equation (2.26) - Equation (2.31) in the thin rod case with the only difference being that the system constants (C_{33} , e_{33} , ϵ_{33}) are used instead of the reduced constants (\bar{C} , \bar{e} , $\bar{\epsilon}$). Since the governing equations have the same form as the thin rod case, the same solution approach could be used to reach the simplified mechanical governing equation in the form:

$$\rho u^{(0,2)}(z, t) - C^D u^{(2,0)}(z, t) = 0 \quad (2.86)$$

where $C^D = C_{33} + \frac{e_{33}}{\epsilon_{33}}$ is the stiffness of the plate at constant electric displacement (open-circuit conditions).

Equation (2.86) has a harmonic plane-wave solution in the form:

$$u(z, t) = A_u e^{j(\omega t - kz)} + B_u e^{j(\omega t + kz)} \quad (2.87)$$

$$k = \frac{\omega}{c_1}$$

where $c_1 = (C^D / \rho)^{1/2}$ is the bulk speed of sound in the plate and A_u, B_u are the complex amplitudes of the forward and backward traveling displacement waves.

As with the thin rod case, the electrical and mechanical interface matching conditions can be used to construct the scattering matrix using Equation (2.53). It should be noted that the scattering matrix obtained in this case would be identical to that expressed by considering both KLM and Mason's thickness expander-plate equivalent circuits since they are derived from the same assumptions. These assumptions constrain the applicability of these models to certain aspect ratios for the transducer, which is investigated in Section 2.2.

2.2 Resulting Dynamics and Comparison of the Analytical Models

The accuracy of the analytical models' predictions is investigated next through comparisons to FEM simulations and experimental measurements of the impedance of PZT transducers with various aspect ratios under different loading conditions.

2.2.1 Numerical Model

COMSOL Multiphysics® [168] was used to construct a 2D-axisymmetric model for a cylindrical piezoelectric transducer. A coupled multi-physics model was constructed to model the behavior of the transducer both in vacuo (air)¹ and submerged in a fluid (water/oil). Piezoelectric elements which include direct structural-electrostatic coupling were used to discretize the transducer, and acoustic elements were used for the medium surrounding the

¹Note that for these stiff piezoelectric transducers, air (in the experiments) is a good approximation of in vacuo condition.

transducer. Both domains were discretized using a free triangular mesh with 10 elements per wavelength of the generated acoustic waves inside the fluid medium. This ensures accurate sampling of the waves in all domains, since the wavelength inside PZT for both shear and longitudinal waves is larger than the acoustic wavelength in air, water and oil.

The boundaries of the piezoelectric and acoustic domains were coupled to model the acoustic-structure interaction. Furthermore, radiation boundary conditions on the external boundaries of the medium were enforced to minimize reflection from the boundaries and simulate an infinite medium. The voltage of the nodes on each face of the transducer were coupled together and connected to lumped electrical circuit elements to model the electrical connections to the transducer (i.e. a voltage supply when the transducer is used as a TX and a load resistance when used as an RX).

2.2.2 Experimental Validation

The electrical impedance of two cylindrical piezoelectric transducers, supplied by Steiner & Martins inc., were measured both in air and in oil using a Solartron SI 1260 impedance analyzer. Since the impedance of air is much smaller than that of piezoelectric ceramics, measurement in air represents free boundary conditions on the transducer. Oil, being an electrically non-conductive fluid, was selected to avoid adding insulating layers to the transducer which might have affected its performance. The dimensions of the first transducer were 10 mm in diameter and 25 mm in height ($\beta = 5$) to represent a moderately thick rod, while the second one had a 14 mm in diameter and 12 mm in height ($\beta = 1.7$) representing a cylinder of moderate diameter to height. Both transducers were made of a modified PZT-5 with a thin layer of silver electrodes on each circular face. Thin wires were soldered to the edge of each electrode to connect the transducers to the signal analyzer. The same wires were used to suspend the transducers both in air and in oil.

The impedance was recorded at each frequency and averaged over an integration time of 0.2 s with a linear frequency spacing of 500 Hz. The mass density and dielectric permit-

tivity of the transducers were measured experimentally, and the piezoelectric and elastic constants of the transducers material were identified using a least-squares regression algorithm to fit the FEM to experimental impedance measured for the $\beta = 1.7$ transducer in air. The measured/identified material properties are summarized in Table 2.1.

Table 2.1: Measured/Identified material properties of modified PZT-5

Property	ρ	C_{11}	C_{12}	C_{33}	C_{44}	e_{31}	e_{33}	ϵ_{11}/ϵ_o	ϵ_{33}/ϵ_o	Q_m
Unit	kg/m ³	GPa	GPa	GPa	GPa	C/m ²	C/m ²			
Value	7560	139	92	107	22	-7.2	19	1460	1064	156

2.2.3 Electrical Impedance in Air

Figure 2.2 shows the magnitude plot of the electrical impedance in air for both transducers. The results obtained experimentally are compared to those obtained using the numerical and the different analytical models. The boundary conditions for the transducer in air resembles a free-free boundary in the analytical and FEM models. To obtain the impedance of the transducer using FEM, a voltage source was connected between the two electrodes of the transducer, and natural free boundary conditions were applied to all surfaces of the transducer.

The results of the analytical model were generated using Qucs open source circuit simulation package [169]. A voltage source was connected to the electric port (port 3) of the scattering matrix (evaluated from Equation (2.53) and Equation (2.76) and short circuit (zero impedance) was connected to the acoustic ports (ports 1 and 2). To find the impedance for both cases, the applied voltage was divided by the electric current flowing to the transducer.

For the $\beta = 5$ transducer (Figure 2.2a), an excellent agreement is observed between the experimental results and FEM, Rayleigh and Bishop models. The thin rod model for

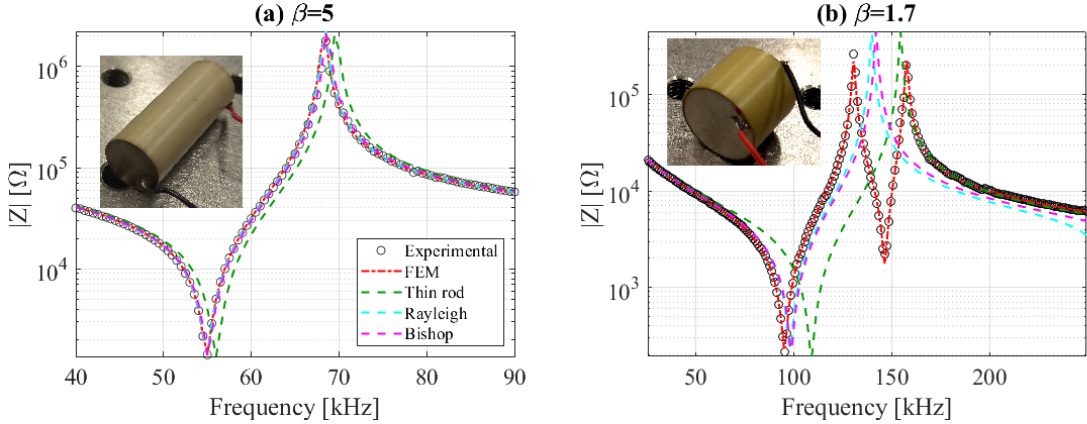


Figure 2.2: Comparison of the electrical impedance in air for two cylindrical transducers with aspect ratios (a) $\beta = 5$ and (b) $\beta = 1.7$. Experimental results are compared with those estimated numerically using FEM and analytically using thin rod, Rayleigh and Bishop rod theories.

this aspect ratio predicts 2% higher resonance and anti-resonance frequencies. This indicates that the effects of lateral inertia cannot be neglected for this aspect ratio or lower. The predictions of both Rayleigh and Bishop models are quite similar, with the relatively simplified Rayleigh model producing slightly more accurate results. This behavior is expected for relatively thin rods, since the Rayleigh model tends to better approximate the FEM prediction of a continuous cylinder at low frequencies (around the first mode of the transducer) while it deviates more quickly for higher frequencies [165].

For the $\beta = 1.7$ transducer (Figure 2.2b), only the FEM model completely captures the experimental impedance, while all the analytical models predict higher values for the first thickness resonance (95 kHz) of the transducer. While the thin rod approximation is clearly not appropriate for this aspect ratio, predictions of the Rayleigh and Bishop only deviate 3% higher than the FEM value. The analytical models fail to capture the first radial resonance appearing around (146 kHz). This is because all the investigated theories are pure longitudinal theories (with one kinematic variable). Even though the effects of lateral inertia are accounted for in Rayleigh and Bishop models, lateral modes are still not considered in the kinematics of the problem. For this aspect ratio, the lateral and longitudinal modes

appear at the same frequency neighborhood, and coupled longitudinal/radial modes start to appear.

The accuracy of the analytical predictions when changing β is investigated in Figure 2.3. The resonance frequency of the first thickness mode is plotted against β while keeping the transducer height $h_p = 12$ mm constant. As β approaches one, the effects of lateral inertia become more prominent as evident from the frequency shift in the FEM results. Since the Rayleigh and Bishop theories include these effects, they follow the same trend predicted by the FEM up to $\beta < 2$, where the effects of lateral resonance cause a dramatic increase in the error of both models compared to FEM.

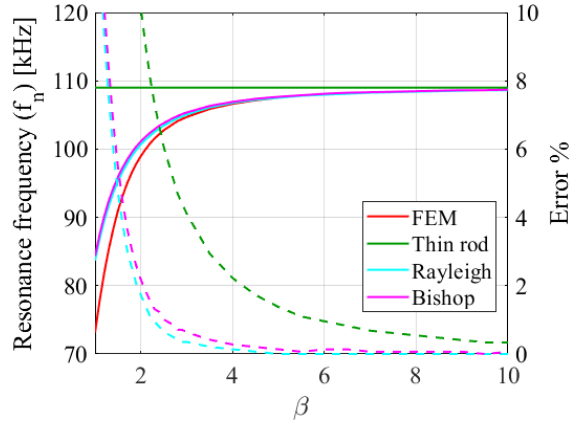


Figure 2.3: In-air resonance frequency of the first thickness mode of a PZT transducer ($h_p = 12$ mm) versus the aspect ratio β . Frequency values are shown in solid lines, and percentage errors relative to FEM are shown in dashed lines of the same color.

2.2.4 Electrical Impedance in Oil

For most practical applications, thickness mode transducers are rarely used in air due to the large impedance mismatch between PZT and air. In many applications, either one face of the transducer or the entire transducer is embedded in a solid or liquid domain which would change its dynamic response. To investigate the validity of the analytical models in such conditions, the impedance of the investigated transducers was measured while the transducers were submerged in soybean oil ($c = 1465$ m/s and $\rho = 917$ kg/m³)

[170]. To capture the effect of fluid loading, the fluid domain around the transducer was included in the simulation and coupled acoustic structure boundaries were applied between the structural and acoustic domains.

The presence of the transducer in a fluid domain is accounted for using the unbaffled acoustic radiation impedance Z_{rad} present on the two acoustic ports of the analytical models. The value of this impedance represents the effect of the fluid on the two circular faces of the transducer. This is compared to the simpler baffled radiation impedance case, where the circular face of the transducer is surrounded by a hard baffle, i.e the transducer is radiating into a half-space.

The radiation impedance of a circular radiator depends mainly on the relation between the wavenumber in the fluid (k_m) and the radius of the radiator (a). Simple approximate formulas for the unbaffled radiation impedance only exist for the cases where $k_m a \ll 1$ and $k_m a \gg 1$. For the investigated aspect ratios $k_m a$ is 1.14 and 2.9 for $\beta = 5$ and $\beta = 1.7$ respectively, which does not allow using such approximations. In this case, the radiation impedance becomes too complicated to be expressed analytically, since the pressure field generated by the transducer is not only dependent on the radiating face, but also the back and lateral sides of the transducer. Neglecting the interactions between the back and lateral sides of the transducer, the radiation impedance can be estimated from Ref. [171]. The resulting formula is complex enough that normalized plots [172] are often used directly instead of the formula itself.

Effect of fluid loading on the electrical impedance of both transducers is shown in Figure 2.4. A very good agreement is observed between the experimental and FEM results for both transducers. Since lateral fluid loading is neglected, the analytical models predict higher/sharper resonance values when the value of β is small enough for lateral stresses to be substantial, but not too small that the lateral surface area becomes negligible. Generally, for $\beta > 10$ or $\beta < 0.1$, the effect of lateral fluid loading is very small and could be safely ignored.

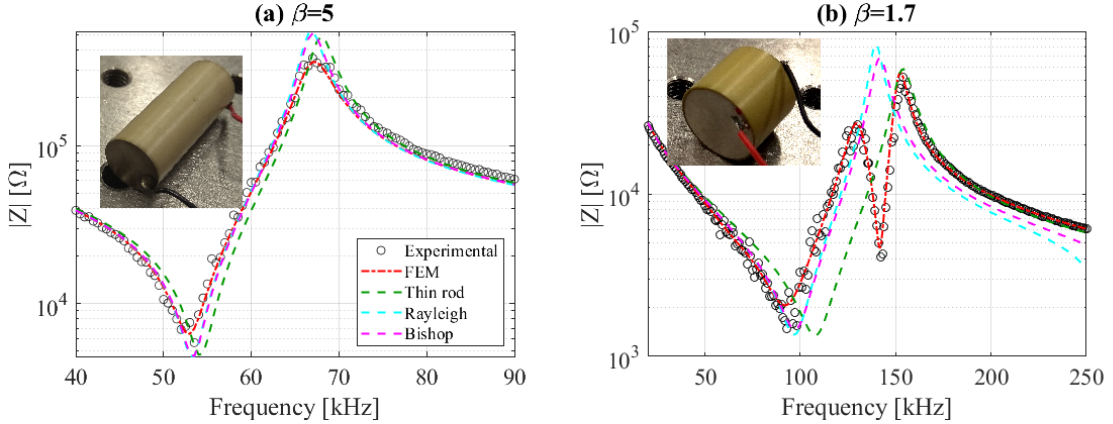


Figure 2.4: Comparison of electrical impedance in oil for two cylindrical transducers with aspect ratios (a) $\beta=5$ and (b) $\beta=1.7$. Experimental results are compared with those estimated numerically and analytically.

2.3 Effect of Aspect Ratio on the Performance of a Thickness-Mode Transmitter

When the transducer is operating as a TX, the main design objective is to provide directional focused ultrasonic waves at the maximum allowed level towards RX. Usually the size of TX is less constrained than the size of RX (within practical limitations). Also, the boundary conditions of TX (side loading/backing) are often easier to control than those of RX. For resonant operating transducers, surrounding the back and sides of the transducer with air seems to be the best approach to maximize the energy generated at the front face of TX [68, 173]. For many energy transfer applications like biomedical implementations and those involving solid (e.g. metal) walls, this represents the easiest approach as TX is usually naturally surrounded by air. Consequently, TX is connected to the medium through one face only, which makes it easy to create a hard baffle around this face to maximize the energy transferred towards RX, and improve the directionality of the generated acoustic beam. This also facilitates the analytical modeling of TX since free boundary conditions could be assumed on the back and sides of the transducer.

The coupled performance of the transducer is then easily analyzed analytically by connecting a voltage source to the electrical port (port 3), assuming one of the acoustic ports (port 1) to be free (short circuit/zero impedance), and applying the baffled piston radiation

impedance to the other acoustic port (port 2). The radiation impedance of a baffled piston (Z_{rad}) is readily available in literature in the form [64]:

$$Z_{rad} = Z_m \left(1 - \frac{J_1(2k_ma)}{k_ma} + j \frac{H_1(2k_ma)}{k_ma} \right) \quad (2.88)$$

where J_1 and H_1 are the first order Bessel and Struve functions. The surface velocity of port 2 represented by the current flowing through Z_{rad} could then be used to estimate the pressure field outside the transducer by solving the Rayleigh integral [64]:

$$P(r, z) = \frac{i\omega\rho_m U_o}{2\pi} \int_{dS} \frac{e^{-jk_m R}}{R} dS \quad (2.89)$$

The effect of aspect ratio on the performance of the transducer could be evaluated using two approaches: (1) the height of the transducer could be fixed, and hence its resonance frequency, while its radius is varied to change the aspect ratio. This means that the volume of the transducer would change as its aspect ratio changes. (2) The volume of the transducer could be kept fixed while varying the aspect ratio (i.e. changing the relative values of both its radius and its thickness). Since the efficiency of receivers and energy harvesters is usually characterized by the output power per unit volume of the material, the second approach will be followed.

A cylindrical transducer with constant volume of 1 cm^3 made of modified PZT-5 is considered. The aspect ratio is varied between $\beta = 10$ (thin rod case), $\beta = 5$ (thick rod), $\beta = 1$ (comparable height to radius cylinder), and $\beta = 0.1$ (thick plate).

All the analytical models considered in this work assume that the velocity across the face of the transducer is constant. This is an approximation as the longitudinal velocity of the surface varies with the radius of the transducer. This behavior is difficult to capture analytically but could be captured in the FEM simulation. In order to compare the analytical predictions with the FEM ones, the average surface velocity of the transducer U_o is compared in both cases.

Figure 2.5 shows the effect of aspect ratio of the transducer at constant volume on the average surface velocity of its face when generating ultrasonic waves in water. For all transducers, the electric field applied to the transducer is kept constant at 1 kV/m (as a convenience) which corresponds to an applied voltage $v \approx 32, 20, 7, 2$ V for aspect ratios $\beta = 10, 5, 1, 0.1$ respectively.

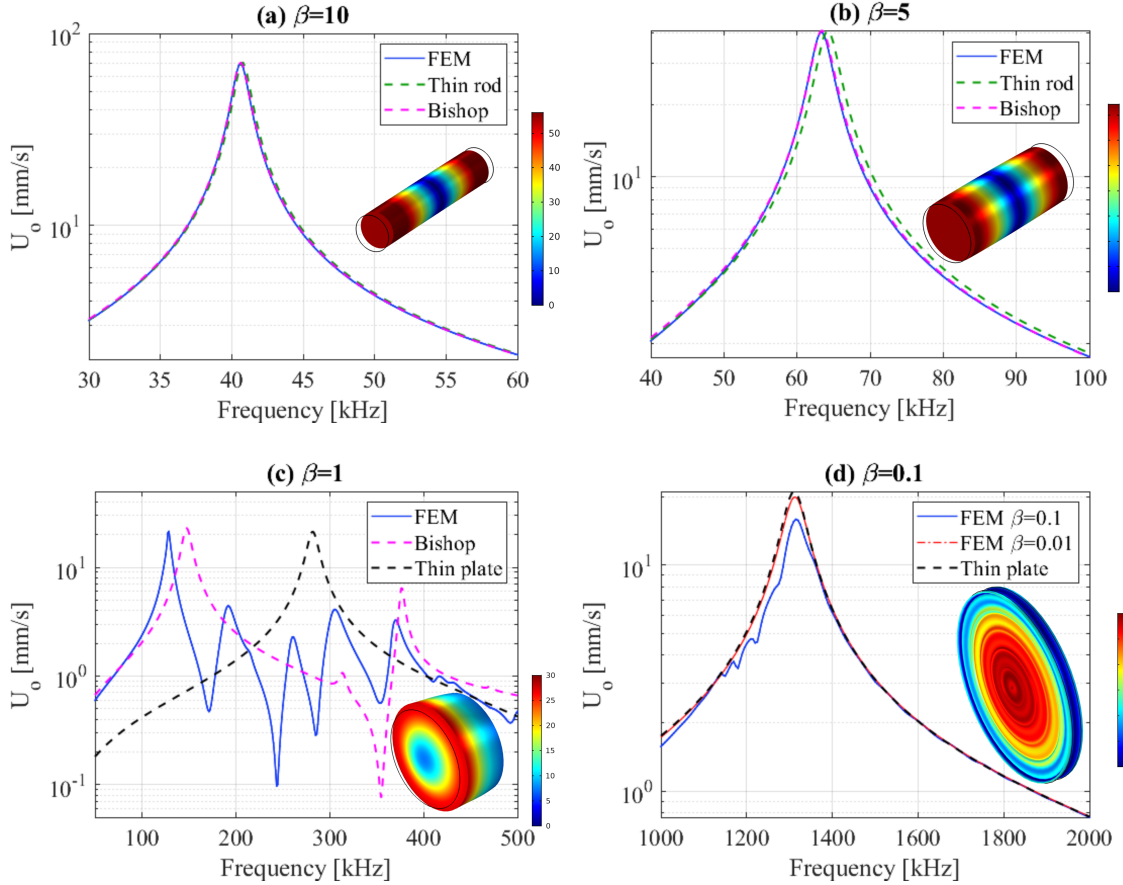


Figure 2.5: Effect of aspect ratio on the average normal surface velocity of the transducers. The aspect ratio is varied between (a) $\beta = 10$, (b) $\beta = 5$, (c) $\beta = 1$, and (d) $\beta = 0.1$. The insets show surface plots of the distribution of the surface velocity in the axis direction of the transducer (z-direction). In all cases, the applied electric field is the same (1 kV/m).

As shown in Figure 2.5a and Figure 2.5b, the analytical models capture the effect well for thin and moderately thick rods ($\beta = 10, 5$), since the fluid loading of the domain is only applied to the front face of the transducer.

For moderately thick plates ($\beta = 0.1$), the infinite plate approximation captures the resonance of the plate; however, it tends to overestimate the average surface velocity of

the transducer as shown in Figure 2.5d. The higher order radial modes of thick plates affect the first thickness mode, yielding a non-uniform normal velocity on the surface of the transducer as shown in the inset of Figure 2.5d which causes the discrepancy between FEM and analytical predictions. Keeping the same thickness and decreasing the aspect ratio further to $\beta = 0.01$ (also Figure 2.5d) causes the FEM response to converge towards the thin plate (infinite plate) approximation. However, this aspect ratio ($\beta = 0.01$) might not be practical especially for air backed transducers due to structural strength considerations.

For $\beta = 1$ (Figure 2.5c) both lateral and longitudinal modes are highly coupled yielding inaccurate estimations of the normal surface velocity for both the thin plate and Bishop approximations. The longitudinal mode is still dominant in this aspect ratio, as shown in the inset of Figure 2.5c; however, the radial and longitudinal mode coupling results in lower overall surface velocity for all the coupled modes.

The FEM nearfield pressure plots of the considered transducers are summarized in Figure 2.6. The directivity of the transducer improves with reducing β since the pressure directivity is only controlled by the relationship between the wavelength inside the medium and the radius of the radiator $k_m a$. For the considered aspect ratios, $k_m a$ at resonance varies between $k_m a = 0.6, 1, 3.6$, and 95.5 respectively. This shows that, although the average surface velocity for the thin rod case is relatively higher compared to the other cases, the generated pressure field is almost spherical, and the generated pressure diverges in an open medium making it less suitable for operating as TX, and perhaps more suitable for RX applications since it will be less sensitive to the angle of incidence.

2.4 Effect of Aspect Ratio on the Performance of a Thickness-Mode Receiver

We consider the case in which RX is completely submerged in an unbounded medium and subject to an acoustic plane wave with an amplitude of $P_i = 1 \text{ kPa}$ incident normal to its front circular face. Similar to the TX case, a constant volume of 1 cm^3 of modified PZT-5 and the same aspect ratios are considered. The load resistance connected across the

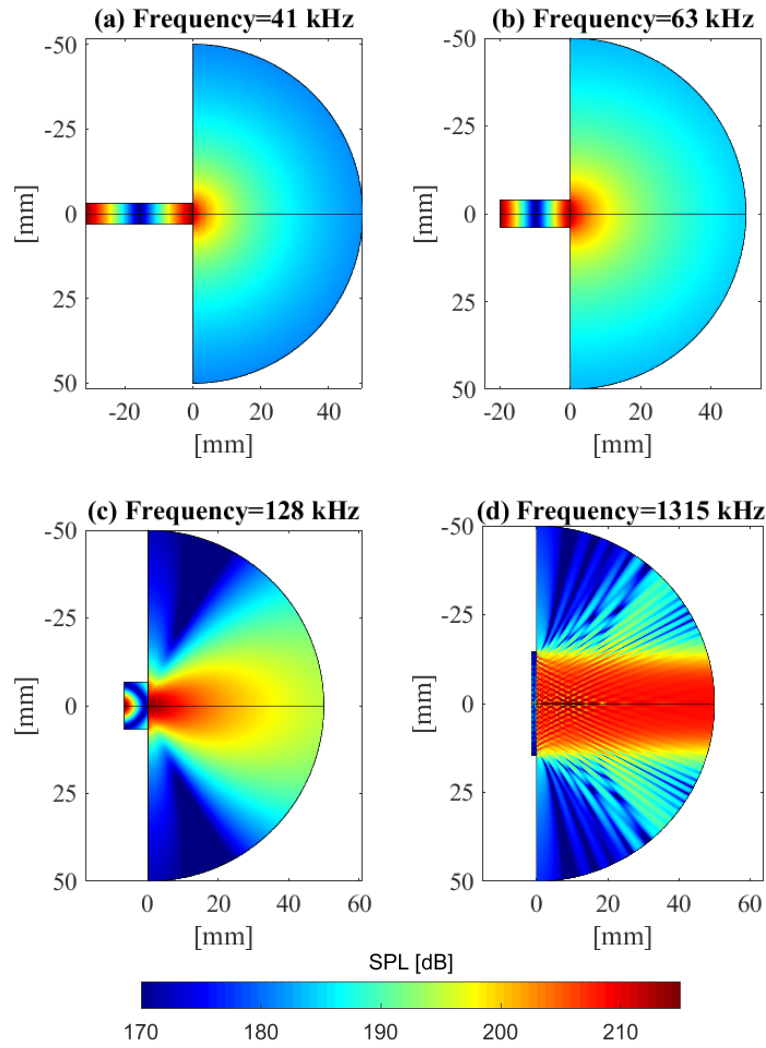


Figure 2.6: Effect of aspect ratio on the near field sound pressure level (SPL) generated by the baffled TX estimated using FEM for (a) $\beta = 10$, (b) $\beta = 5$, (c) $\beta = 1$, and (d) $\beta = 0.1$. The color contour inside the transducer represents the normalized velocity in the axial direction.

electrodes of the transducer is varied across a wide range of resistance values to capture optimum load resistance for maximum power output. The frequency of excitation for each aspect ratio is varied around the expected first longitudinal mode of TX.

The RX case presents a challenge for the analytical models considered here for all aspect ratios. For thin and thick rods, fluid loading and pressure incident from the side face cannot be neglected, and for plates, higher order radial modes appear alongside the thickness mode which are not accounted for in the analytical models. For the cases where $\beta \approx 1$, it is even more involved since the pressure field around the transducer becomes too complicated for any analytical approach to the problem. Exceptions to these limitations are the extreme cases where the transducer is a very thin long rod ($\beta \gg 1$) or a very large thin plate ($\beta \ll 1$); however, these cases are of limited practical importance for a single thickness mode RX.

A numerical approach is then the most applicable approach to tackle the RX problem. The FEM model results for the output power for different aspect ratios are shown in Figure 2.7. For each aspect ratio, the load resistance was varied to ensure that the peak power output of RX is captured. It is observed that as β decreases, the optimum load resistance decreases. This is because the capacitance and resonance frequency of the transducer increases with reduced values of β which decreases the effective electrical impedance of the transducer. It should be noted that for $\beta = 1$ case, a different trend for the power output is observed when the resistance is higher than the optimum value of $1\text{ k}\Omega$. Multiple thickness and radial modes are coupled for this aspect ratio, and they are affected by the electromechanical coupling differently. Modes which are better coupled to the electrical domain tend to shift to higher frequencies as the connected resistance increases causing increased bandwidth, but lower amplitude.

The maximum absolute power output among all the considered cases was that of the lowest value for β (Figure 2.7d), since the normal area to the incident acoustic intensity is the largest for this case. Another factor to be considered is the ratio of the output electric

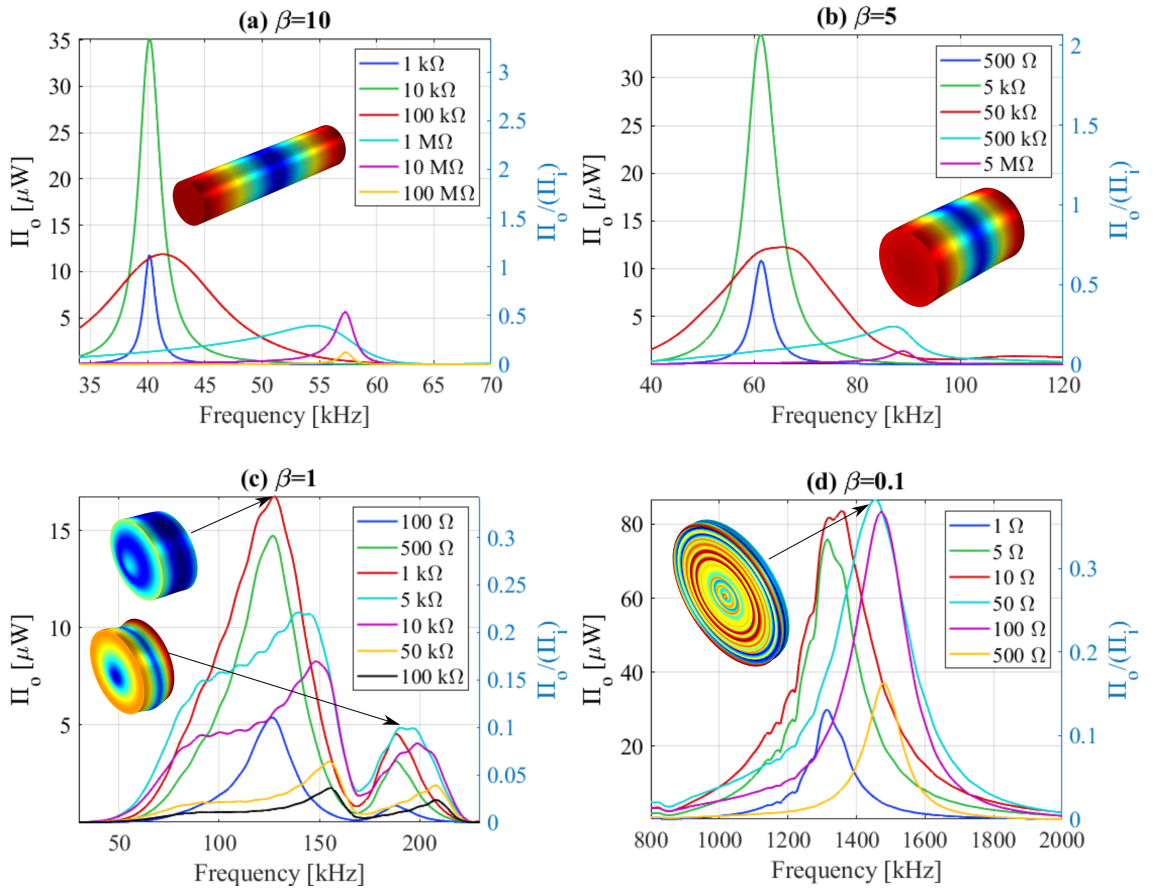


Figure 2.7: Effect of the aspect ratio on the power output of RX. The transducers are submerged in water and subjected to incident plane harmonic waves of amplitude (1 kPa) and the power output under different values for the load resistance is estimated using the FEM for (a) $\beta = 10$, (b) $\beta = 5$, (c) $\beta = 1$, and (d) $\beta = 0.1$. The normalized displacement amplitude of the transducers are shown in the insets.

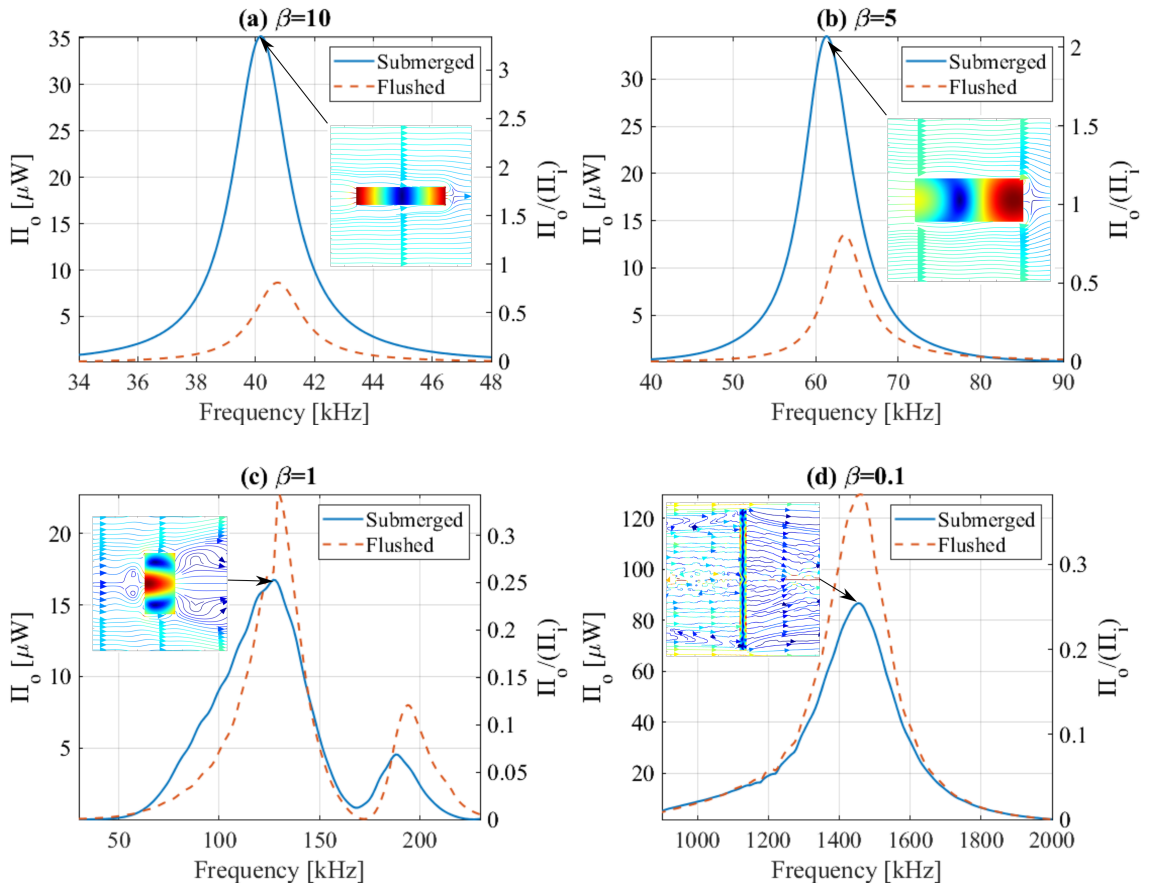


Figure 2.8: Output power of RX at the optimal load when completely submerged inside the fluid medium versus the flushed case where only the front face of the transducer is coupled to the fluid and the other faces are free. The aspect ratio is varied between (a) $\beta = 10$, (b) $\beta = 5$, (c) $\beta = 1$, and (d) $\beta = 0.1$. The insets show the acoustic intensity stream lines for the submerged case. The normalized displacement amplitude of the transducers are also shown.

power (Π_o) to the acoustic power incident normal to the transducer face (Π_i):

$$\Pi_i = \frac{P_i^2 A_p}{2\rho_m c_m} \quad (2.90)$$

where P_i is the pressure amplitude of the incident acoustic wave. In this case, the performance of the rod transducer (Figure 2.7a,b) is found to be better than that of the low β case (Figure 2.7d). The output power for higher values of β is in fact higher than the incidence acoustic power on the front face of the transducer.

This discrepancy can be explained by considering Figure 2.8, where the power output of the submerged transducer is compared to a flushed transducer where the medium is coupled to the transducer from the front face only. For the $\beta = 10$ case, the output power is much higher in the submerged case, when it is compared to the flushed case. This indicates that the acoustic power is not captured by the front face only, but also the lateral and rear faces of the transducer.

Additionally, the intensity streamlines (shown in the insets of Figure 2.8a) indicate that the area of the effective acoustic power captured by this aspect ratio ($\beta = 10$) is larger than just the normal face area of the transducer. This can be explained by comparing the lateral dimensions of the transducer to the incident wavelength. Since $k_m a < 1$ for this case, the transducer is effectively a point receiver, and its directivity is almost spherical as shown in the TX case (Figure 2.6a). In contrast, for the $\beta = 0.1$ case (Figure 2.8d), the acoustic power from the submerged transducer is less than the flushed one. This stems from the fact that for the submerged case, a portion of the acoustic power received by the front face of the transducer is radiated from the back face as expected when $k_m a \gg 1$.

Another aspect to consider is the strength of the longitudinal mode, and how well it is excited by the incident acoustic waves. When considering the maximum absolute power output for the $\beta = 5$ case, we find that it is smaller than the $\beta = 10$ case even though it has higher normal area intercepting the incident acoustic waves. This is because the

longitudinal mode for higher β values is less coupled to the lateral motion and thus the incident acoustic waves are converted more efficiently into longitudinal motion, and hence generates more electric power. It also explains the degraded peak power output of the $\beta = 1$ case where the longitudinal and lateral motions are strongly coupled, and no dominant mode is observed. As a result, peak power output is smaller compared to all the other cases.

2.5 Conclusions

Several continuum analytical models for estimating the thickness-mode dynamics of a piezoelectric transducer with a cylindrical shape have been investigated with a focus on the effect of aspect ratio. When the radius of the transducer is very small (i.e. $\beta > 10$), the thin rod analytical model can be used to predict the surface velocity of the transducer around its resonance frequency. The Rayleigh and Bishop rod models can be used to predict the surface velocity of rod transducers with ($\beta > 3$) around their resonance frequency given that the lateral sides of the transducer are not fluid loaded. When the diameter of the transducer is comparable to its length ($\beta \approx 2$), the longitudinal and lateral motion (hence modes) are strongly coupled, and they become difficult to model analytically. Only when the radius of the transducer is very large compared to its thickness ($\beta < 0.1$), the thin plate thickness vibration continuum model can be used to describe behavior of the transducer.

All the considered analytical models could not predict the effect of fluid loading on the lateral sides of the transducer, which becomes significant when the diameter of the transducer is comparable to its length. The analytical models are also not accurate for modeling the fluid loaded transducer except for cases with extreme aspect ratios ($\beta \gg 1$ or $\beta \ll 1$).

For receiver applications of the transducers, the electric power generated by a rod-like receiver ($\beta = 10$) was higher than acoustic power incident on its front face. The effective receiving area of the transducer was higher than the normal area to the incident acoustic

wave. This indicates that arrays of rod like transducers might be more efficient than a plate like receiver of the same size. Also, since the directivity of the rod like receiver is almost spherical, it would be less sensitive to variations in the angle of incidence of the acoustic beam (e.g. due to misalignment of the transmitted beam with respect to the receiver axis), making it a more effective omnidirectional receiver.

Such broad range of aspect ratios are relevant to power transfer problems. For instance Chapter 3 and Chapter 5 use transducers with $\beta = 0.14$ which could be approximated by thin plate models with some limitations discussed in Chapter 3. Chapter 4, on the other hand, uses transducers with $\beta = 1.7$ for low frequency underwater power transfer, and thus a finite element model will be used to simulate it without considering analytical models.

It should be noted that for applications in which the acoustic power needs to be sent for a short distance with a high power density such as in power transfer through metals applications, it makes sense to use directional transmitters and receivers with low β values to reduce the power dissipated in the medium and maximize the efficiency. A thin plate transducer model will be discussed in the context of a complete ultrasonic power transfer system for sending power through metallic barriers in the next chapter.

CHAPTER 3

SYSTEM-LEVEL ANALYSIS WITH A FOCUS ON POWER TRANSFER THROUGH METALLIC BARRIERS

In this chapter, the elements needed for a through-metal UPT system are analytically modeled, and the key factors for assessing the system performance such as the efficiency and voltage transfer function are analyzed. A base through-metal UPT system with bonded transducers is studied to highlight the effect of different mechanical components on the performance of the system and to point out bottlenecks that hinder efficient system operation. The design and selection of interfacing circuits such as power amplifiers and bridge rectifiers are discussed while highlighting designs that are more suited for UPT systems.

A dry-coupled through-metal UPT system is then developed for practical detachable and portable operation. A setup that relies on attracting magnets is designed to provide good contact between the transmitter and the metallic barrier. Elastomers with different thickness and elasticity values are investigated to determine the most suitable material for dry coupling. The detachable system is experimentally tested with the best elastomer to estimate its total efficiency, and the maximum power that it could deliver to a DC load.

3.1 Analytical Modeling

A simple representation for a through-metal power transfer system is shown in Figure 3.1. It consists of a transmitting and receiving piezoelectric disc transducers with the metallic wall in the middle. The transducers can be mounted on the metallic wall using a glue (epoxy, polyurethane, cyanoacrylate, etc.) or a coupling gel (glycerin, honey, ultrasound gel, etc.). The accurate modeling of the coupling (bonding) layer is important since it has a strong influence on power transmission, especially at higher frequencies. The transmitter is connected to a power source with a certain impedance Z_{sc} capable of applying a voltage V_i ,

while the receiver is connected to a resistive load R_L . For high-frequency systems similar to the one considered in Figure 3.1, the lateral dimensions of the transducer are usually much larger than its thickness which allows for assuming 1D propagation of ultrasonic waves from the transmitter to the receiver and neglecting lateral propagating waves. The validity of this approximation for the base model will be assessed in Section 3.2.3.

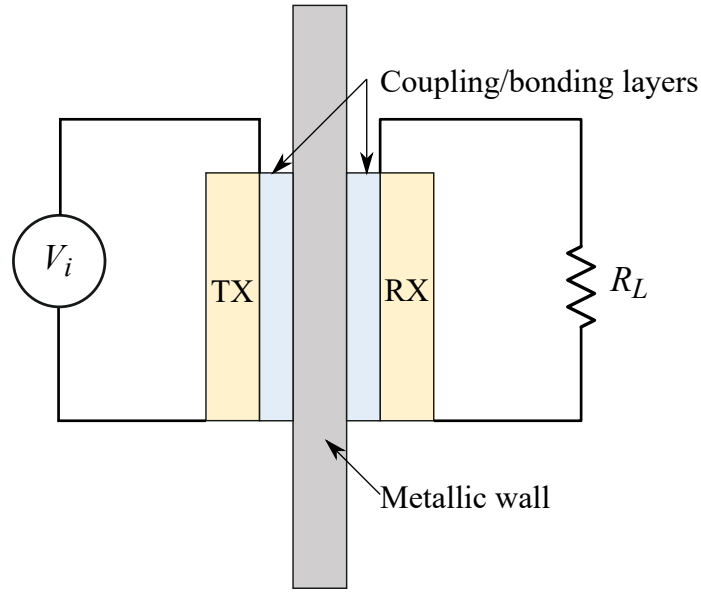


Figure 3.1: Basic configuration of a through-metal UPT system for AC input and AC output.

Transmission line models (1D waveguide models) are commonly used for predicting the behavior of 1D ultrasonic systems [84, 92, 174]. These models are typically valid for frequencies above 100 kHz where the wavelength of the propagating waves is smaller than the thickness of the metallic wall. For low-frequency systems operating below 100 kHz, lumped parameter models and lumped circuit elements become more appropriate [18, 175], since the wavelength becomes much longer than the thickness of the system.

A 1D ultrasonic system can be modeled as a series of cascaded elastic/acoustic layers representing different components of the system. Each elastic layer could be modeled as a two-port element with a 2×2 matrix relating the acoustic pressure and velocity at each port. Among the different representations that could be used for modeling 2-port elements (S-

parameters, Z-parameters, Y-parameters,...etc), the transfer matrix (also known as ABCD parameters in radiofrequency (RF) literature) simplifies the algebraic manipulations needed to solve the system. The transfer matrix relates the force and velocity at the input of a layer F_1, v_1 to the output F_2, v_2 by:

$$\begin{bmatrix} F_1 \\ v_1 \end{bmatrix} = \mathbf{T} \begin{bmatrix} F_2 \\ v_2 \end{bmatrix}, \quad \mathbf{T} = \begin{bmatrix} T_{11} & T_{12} \\ T_{21} & T_{22} \end{bmatrix} \quad (3.1)$$

where velocity directions are shown in Figure 3.2a. The elastic transfer matrix is analogous to the electric transfer matrix (Figure 3.2b) with forces replaced by applied voltages and velocities by electric currents.

For an ultrasonic system consisting of n cascaded layers, the transfer matrix of the overall system can be represented by a single transfer matrix T_{sys} calculated by multiplying layer matrices:

$$\mathbf{T}_{sys} = \mathbf{T}_1 \mathbf{T}_2 \dots \mathbf{T}_n \quad (3.2)$$

The transfer matrix of a passive elastic layer with acoustic impedance Z_n and thickness h_n can be calculated from the relation:

$$\mathbf{T}_n = \begin{bmatrix} \cos(k_n h_n) & jZ_n A_n \sin(k_n h_n) \\ j\frac{\sin(k_n h_n)}{Z_n A_n} & \cos(k_n h_n) \end{bmatrix} \quad (3.3)$$

where $k_n = \omega/c_n$ is the wavenumber of the ultrasonic wave in layer n , c_n is the speed of sound in the layer, and A_n is the surface area of the layer. Equation (3.3) could be used to calculate the transfer matrices for the metallic and bonding layers shown in Figure 3.1.

The piezoelectric layers, on the other hand, cannot be represented directly as a 2-port transfer matrix since they possess a third electrical port in addition to the two mechanical ports, and are thus represented as a 3-port element. For a thin plate transducer model, the electrical and mechanical equations of motion can be organized instead into the impedance

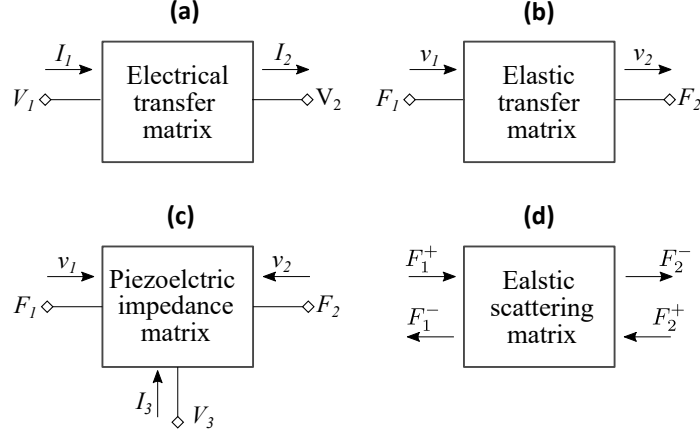


Figure 3.2: Transfer matrix parameters for (a) an elastic layer and (b) an electrical circuit. (c) The impedance matrix representation for a piezoelectric transducer. (d) The scattering matrix representation for an elastic layer.

matrix (Z-parameters) form as [176]:

$$\begin{bmatrix} F_1 \\ F_2 \\ V_3 \end{bmatrix} = \mathbf{Z}_p \begin{bmatrix} v_1 \\ v_2 \\ I_3 \end{bmatrix}, \quad \mathbf{Z}_p = -j \begin{bmatrix} Z_p \cot(k_p h_p) & Z_p \csc(k_p h_p) & \frac{\bar{h}_{33}}{\omega} \\ Z_p \csc(k_p h_p) & Z_p \cot(k_p h_p) & \frac{\bar{h}_{33}}{\omega} \\ \frac{\bar{h}_{33}}{\omega} & \frac{\bar{h}_{33}}{\omega} & \frac{1}{\omega C_p} \end{bmatrix} \quad (3.4)$$

where $Z_p = \rho_p c_p A_p$ is the mechanical impedance of the piezoelectric layer, $\bar{h}_{33} = e_{33}/\epsilon_{33}^s$ is known as the transmitting coefficient, e_{33} is the piezoelectric voltage constant, ϵ_{33}^s is the permittivity at constant strain, $k_p = \omega/c_p$ is the wavenumber in the piezoelectric layer, and $C_p = \epsilon_{33}^s A_p/h_p$ is the piezoelectric layer capacitance at constant strain (i.e. when mechanically clamped). The directions for the velocities and current used to deduce the impedance matrix in Equation (3.4) are defined as shown in Figure 3.2c.

Assuming that the acoustic impedance Z_b at the backside of the transducer is known, Equation (3.4) could be reduced to the transfer matrix form by substituting the relation:

$$F_2 = -Z_b A_p v_2 \quad (3.5)$$

This yields the transfer matrix for a piezoelectric layer operating as a receiver:

$$\mathbf{T}_r = \begin{bmatrix} C/A & D - BC/A \\ 1/A & -B/A \end{bmatrix} \quad (3.6)$$

where

$$A = Z_{31} - \frac{Z_{32}Z_{21}}{Z_b + Z_{22}} \quad (3.7)$$

$$B = \frac{Z_{32}Z_{23}}{Z_b + Z_{22}} - Z_{33} \quad (3.8)$$

$$C = Z_{11} - \frac{Z_{12}Z_{21}}{Z_b + Z_{22}} \quad (3.9)$$

$$D = \frac{Z_{12}Z_{23}}{Z_b + Z_{22}} - Z_{13} \quad (3.10)$$

and Z_{ij} are elements of the piezoelectric impedance matrix given in Equation (3.4).

The transfer matrix for a layer operating as a transmitter is given by:

$$\mathbf{T}_t = \begin{bmatrix} B/D & BC/D - A \\ -1/D & -C/D \end{bmatrix} \quad (3.11)$$

Please note that Equation (3.11) is not simply the matrix inverse of the transmitter as the order of the ports is different.

For power transfer applications, the backside of the piezoelectric layer is typically left exposed to air ($Z_b \approx 0$) since its impedance is much lower than piezoelectric materials, and thus virtually no power is lost through the backside of the transducer.

The equivalent transfer matrix for the system shown in Figure 3.1 can be calculated by multiplying transfer matrices of the cascaded layers:

$$\mathbf{T}_{sys} = \mathbf{T}_t \mathbf{T}_b \mathbf{T}_w \mathbf{T}_b \mathbf{T}_r \quad (3.12)$$

where \mathbf{T}_b , \mathbf{T}_w are the transfer matrices for the bonding layers and the metallic wall respectively.

3.1.1 Modeling Attenuation

Accurately modeling wave attenuation is crucial for estimating the efficiency of UPT systems; however, attenuation is a complex phenomenon with several factors contributing to the total attenuation even in a homogeneous medium. Attenuation is also frequency-dependent in most materials which further complicates its characterization and reporting in literature. A phenomenological approach for defining attenuation involves defining a complex wavenumber:

$$k = \omega/c - j\alpha \quad (3.13)$$

where α is a frequency dependent attenuation coefficient. α defines an exponential decay for a propagating wave given by:

$$\begin{aligned} A(x, t) &= A_o e^{j(\omega t - kx)} \\ &= A_o e^{-\alpha x} e^{-j\frac{\omega}{c}x} e^{j\omega t} \end{aligned} \quad (3.14)$$

where A_o is the initial amplitude of the wave, and $A_o e^{-\alpha x}$ is the attenuated amplitude after traveling a distance x . The attenuation coefficient α has the units of Np/m; however, it is commonly reported with the units dB/mm in the ultrasonics literature where:

$$\begin{aligned} \alpha[\text{Np/m}] &= \frac{20 \log_{10}(e)}{1000} \alpha[\text{dB/mm}] \\ &= \frac{8.686}{1000} \alpha[\text{dB/mm}] \end{aligned} \quad (3.15)$$

The use of the unit [dB/mm] stems from the typical approach for estimating α experimentally by calculating the decay in wave amplitude in decibels:

$$\alpha[\text{dB/mm}] = \frac{20 \log_{10} \left(\frac{A(x)}{A_o} \right)}{x[\text{mm}]} \quad (3.16)$$

α can also be related to the material loss factor (η) commonly used for representing damping of low frequency vibrating systems. The loss factor η is defined by considering a complex elasticity matrix to represent hysteretic damping in a material¹:

$$\bar{\mathbf{C}} = \mathbf{C}(1 + j\eta) \quad (3.17)$$

The quality factor $Q = 1/\eta$ is also used in place of η in some conventions. While η is constant for most metals at frequencies below 5 MHz, η (or more generally α) is frequency-dependent in polymers and composite materials [63].

The relation between η and α could be derived from the relation between the wavenumber and the elasticity of the material. The complex wavenumber is given by:

$$\begin{aligned} k &= \omega/c - j\alpha \\ &= \omega/\bar{c} \end{aligned} \quad (3.18)$$

where \bar{c} is the complex wave speed which is defined for longitudinal waves as:

$$\bar{c} = \sqrt{\frac{C_{33}(1 + j\eta)}{\rho}} \quad (3.19)$$

Using Equation (3.18) and Equation (3.19) the relationship between α and η could be deduced as:

$$\alpha = -\text{Im} \left\{ \frac{\omega}{c\sqrt{1 + j\eta}} \right\} \quad (3.20)$$

¹Note that η is sometimes referred to as the mechanical loss tangent ($\tan \delta$) of the material.

For small values of η , the binomial approximation $\frac{1}{\sqrt{1+j\eta}} \approx 1 - j\frac{\eta}{2}$ could be used to further simplify the relation to:

$$\alpha = \frac{\omega\eta}{2c} = \frac{\pi\eta f}{c} \quad (3.21)$$

While Equation (3.21) represents a good approximation for attenuation in many solids, a more generalized form is necessary to describe complex damping behavior. This form is usually a polynomial in frequency defined as:

$$\alpha = \sum C_n f^n \quad (3.22)$$

where C_n are the attenuation coefficients commonly given in the units [dB/m/MHz ^{n}] and n are integer or rational exponents used to fit attenuation measured experimentally.

A common model for attenuation in homogeneous metals is given by Mason and McSkimin [177]:

$$\alpha = C_d f + C_R f^4 \quad (3.23)$$

where $C_d = \pi\eta/c$ is the viscous damping coefficient, and C_R is the Rayleigh scattering coefficient. The term C_R is attributed to the scattering of the waves from the grain boundaries of the metal which becomes important at higher frequencies (i.e. above 5 MHz for most metals). For more information about damping mechanisms for ultrasonic waves and the values of the attenuation coefficients for various solids, please refer to Ref. [63] for an excellent discussion.

In a 1D model, other forms of power losses could be modeled in the form of a frequency-dependent attenuation as well. This includes the power lost to exciting shear waves and other lateral modes in the structure, as well as other forms of power losses due to the lateral and angular misalignment between the transducer and the receiver, among others. While some of these forms of attenuation could be accounted for in the 1D model by fitting attenuation coefficients to experimental results, other forms are more complex and require higher fidelity models (such as a FEM) to capture the 2D and 3D effects. The need for such

models will depend on the aspect ratio of the transducer and its directionality as previously discussed in Chapter 2.

3.1.2 Performance Metrics

Several key metrics could be used to assess the performance of through-metal UPT systems. The metrics include the voltage transfer function, the input and output impedance, but perhaps the most important metric is the power transfer efficiency which relates the useful output power of the system to the total input power. We will focus first on quantifying the operating efficiency of the ultrasonic system (η_{US}) when it is connected to a standard 50Ω load. Here, η_{US} is defined as the ratio of the electrical power consumed by the electric load to the electric power input to the ultrasonic system². It does not account for the electrical power reflected to the power source by the ultrasonic system due to impedance mismatch. The total efficiency of the UPT system includes η_{US} as well as that of the other UPT system components such as the power amplifier and AC-to-DC conversion. The performance of the ultrasonic system can be assessed by only knowing its equivalent transfer matrix elements and the load impedance.

The elements of the system transfer matrix (calculated from Equation (3.12)) relate the input and output voltages and currents to the ultrasonic system by the relation:

$$\begin{bmatrix} V_{in} \\ I_{in} \end{bmatrix} = \begin{bmatrix} T_{11} & T_{12} \\ T_{21} & T_{22} \end{bmatrix} \begin{bmatrix} V_{out} \\ I_{out} \end{bmatrix} \quad (3.24)$$

²The terms "ultrasonic system" and "mechanical system" will be used interchangeably throughout this chapter.

By substituting the load impedance relation $V_{out} = Z_L I_{out}$ into Equation (3.24), and assuming a known voltage V_{in} is applied to the system we arrive to:

$$V_{out} = \frac{V_{in}Z_L}{T_{11}Z_L + T_{12}} \quad (3.25)$$

$$I_{out} = \frac{V_{in}}{T_{11}Z_L + T_{12}} \quad (3.26)$$

$$I_{in} = \frac{T_{21}Z_L + T_{22}}{T_{11}Z_L + T_{12}} V_{in} \quad (3.27)$$

The voltage Frequency Response Function (FRF), also known as voltage transfer function or voltage gain of the ultrasonic system, is given by:

$$\frac{V_{out}}{V_{in}} [dB] = 20 \log_{10} \left(\frac{Z_L}{T_{11}Z_L + T_{12}} \right) \quad (3.28)$$

The real input and output power to the system could be defined as:

$$P_{in} = \frac{1}{2} \operatorname{re} (V_{in} I_{in}^*) \quad (3.29)$$

$$P_{out} = \frac{1}{2} \operatorname{re} (V_{out} I_{out}^*) \quad (3.30)$$

where the exponent * indicates the complex conjugate. The operating ultrasonic efficiency is then given by:

$$\eta_{US} = \frac{P_{out}}{P_{in}} \times 100\% \quad (3.31)$$

The ultrasonic efficiency depends on the properties of the layers of the system, and on how well the system is matched to the electrical load. The main factor limiting the operating efficiency of the 1D ultrasonic system model is the attenuation present in the system. For a completely lossless system, the operating efficiency is 100% regardless of reflections, and hence it is critical to accurately model the attenuation to reliably predict the efficiency.

Given the presence of inevitable attenuation in the system, internal reflections contribute to the degradation of the system efficiency. When the impedance of all the UPT domains are well-matched, the ultrasonic waves travel once through the domain without reflection experiencing minimum attenuation. The presence of impedance mismatches causes multiple internal reflections in each layer, and thus the traveling wave experiences additional attenuation each time it is reflected back and forth in the system which reduces the efficiency.

The amount of reflection at an interface between two domains can be better visualized using the scattering matrix which relates incident waves (voltage or force) to the reflected and transmitted waves. For a two-port domain, the scattering matrix is defined as:

$$\begin{bmatrix} F_1^- \\ F_2^- \end{bmatrix} = \begin{bmatrix} S_{11} & S_{12} \\ S_{21} & S_{22} \end{bmatrix} \begin{bmatrix} F_1^+ \\ F_2^+ \end{bmatrix} \quad (3.32)$$

where F_1^+ & F_2^+ are the complex incident force (pressure) on ports 1& 2 of the system, and F_1^- & F_2^- are the pressure coming out of the system as shown in Figure 3.2d. For example, if F_1^+ is the pressure incident to the system F_1^- is the reflected pressure, and F_2^+ is the transmitted pressure. The scattering matrix can also be defined for voltage signals (V^+, V^-) depending on whether the domain port is electrical or mechanical.

The scattering matrix elements can only be defined with respect to a particular impedance at each port of the system. This impedance represents the domain from which the waves are incident on the port. In radiofrequency (RF) circuits, it is customary to select this impedance as 50Ω which is a standard reference impedance to which standard electrical devices are matched such as coaxial cables used to connect the components, the output impedance of signal generators, and the input and output impedance of commercial RF power amplifiers to name a few. For the mechanical ports, however, the choice of the reference impedance does not need to follow RF standards, and thus it could be selected as the mechanical impedance of a common medium of operation such as water for example. Please note that the mechanical impedance is defined as $Z_m A_m$ where Z_m is the charac-

teristic acoustic impedance of the medium in Rayleighs and A_m is the effective area of the medium or the area of the transducer for piezoelectric domains.

The elements of the scattering matrix could be calculated from the transfer matrix using the relations [178]³:

$$S_{11} = \frac{T_{11}Z_2 + T_{12} - T_{21}Z_1^*Z_2 - T_{22}Z_1^*}{T_{11}Z_2 + T_{12} + T_{21}Z_1Z_2 + T_{22}Z_1} \quad (3.33)$$

$$S_{12} = \frac{2Z_2(T_{11}T_{22} - T_{12}T_{21})}{T_{11}Z_2 + T_{12} + T_{21}Z_1Z_2 + T_{22}Z_1} \quad (3.34)$$

$$S_{21} = \frac{2Z_1}{T_{11}Z_2 + T_{12} + T_{21}Z_1Z_2 + T_{22}Z_1} \quad (3.35)$$

$$S_{22} = \frac{T_{22}Z_1 - T_{21}Z_1Z_2^* - T_{11}Z_2^* + T_{12}}{T_{11}Z_2 + T_{12} + T_{21}Z_1Z_2 + T_{22}Z_1} \quad (3.36)$$

where Z_1 and Z_2 are the reference impedance for ports 1 and 2 respectively. S_{11} and S_{22} represent the complex reflection coefficients with respect to ports 1 and 2 respectively while S_{12} and S_{21} are the complex transmission coefficients. The elements of the scattering matrix could be evaluated experimentally using a vector network analyzer (VNA) or by simultaneously measuring the input voltage and current to one port of the UPT system and the output voltage on a reference load (50Ω) connected to the other port. The relations between the input impedance, voltage transfer function, and the S-parameters are given by [180]:

$$S_{11} = \frac{Z_{in}/Z_1 - 1}{Z_{in}/Z_1 + 1} \quad (3.37)$$

$$S_{21} = \frac{V_{out}}{V_{in}} (1 + S_{11}) \quad (3.38)$$

³Please note that in RF literature, the scattering matrix is usually defined in terms of power waves $a = V/\sqrt{Z}$ which changes the definition of S_{21} and S_{12} by the ratio of the port impedance. Please see Refs. [162, 178, 179] for more details on power waves.

Note that since most through-metal UPT systems operate in the long-wavelength region of RF waves (below 10 MHz) the actual electric impedance of the coaxial cables used have a negligible effect on the performance of the system unless they are tens of meters long.

3.2 Benchmark System Performance

In this section, the practical implementation of the through-metal UPT (shown in Figure 3.1) will be discussed first to establish the practical model geometry and physical parameters. The performance of the system will then be characterized analytically, numerically using the FEM, and experimentally. The performance of the 1D analytical model will then be compared to 2D FEM model predictions and experimental results to assess the validity of the 1D approximations for the considered system.

3.2.1 Experimental Validation

A piezoelectric transducer with a radius 15 mm and a thickness of 2.1 mm, supplied by Steiner & Martins inc., was selected as a compromise between 1) maximizing the directivity of the transducer to minimize energy lost to lateral propagation, 2) minimizing the attenuation by keeping the frequency as low as practically possible, 3) keeping the impedance of the transducer close to 50Ω to ensure compatibility with commercial RF equipment, and 4) keeping the dimensions of the transducer reasonably small. The transducer material was selected to be a hard PZT ceramic (PZT-4/SM111) which has a high-quality factor compared to other piezoelectric ceramics thus minimizing the power dissipated in the transducer. The material properties of the transducer are summarized in Table 3.1, and the reduced properties for the 1D piezoelectric transducer are summarized in Table 3.2.

An anodized aluminum wall was used in the experiment (Figure 3.3) to limit electrical cross-talk between the piezoelectric tiles that might interfere with the measurement. A thin layer of gold was then deposited on each side of the wall to facilitate the electrical connection to the electrode in contact with the wall. The transducer was then bonded to

Table 3.1: Material properties of Steminc SM111 (modified PZT4)

Property	ρ	C_{11}	C_{12}	C_{33}	C_{44}	e_{31}	e_{33}	ϵ_{11}/ϵ_o	ϵ_{33}/ϵ_o	Q_m	$\tan \delta$
Unit	kg/m ³	GPa	GPa	GPa	GPa	C/m ²	C/m ²				%
Value	7900	140	84	138	27	-8.97	14.36	1450	1400	500	0.4

Table 3.2: Material properties used in the transducer 1D model

Property	ρ_p	c_p	\bar{h}_{33}	C_{33}^D	C_p	Q_m	$\tan \delta$
Unit	kg/m ³	m/s	kV/mm	GPa	nF		%
Value	7900	4706	2594	175	1.9	500	0.4

Table 3.3: Dimensions and material properties of elastic layers in the base model

Property	ρ	E	ν	c	Z	α	Thickness
Unit	kg/m ³	GPa		m/s	MRayl	dB/mm/MHz	mm
Aluminum	2700	69	0.33	6153	16.6	0.004	3.1
3M DP460 epoxy	1100	4	0.35	2416	2.66	0.5	0.005

the aluminum wall using epoxy in a vacuum bonding procedure to ensure minimum epoxy thickness and avoid any trapped air bubbles. A thin bonding layer of thickness 10 μm was achieved using 3M DP-460 high shear strength epoxy. The exact material properties of DP-460 epoxy were not readily available in the literature, so an average value for epoxy resins was used instead. The material properties of the different passive solid layers are summarized in Table 3.3.

The experimental setup shown in Figure 3.3 was used to characterize the performance of the UPT system. The system was excited with a frequency sweep from 100 KHz to 10 MHz generated by an Agilent 33250A 80 MHz arbitrary waveform generator. The actual voltage applied to the input piezoelectric tile was measured as close to the tile as possible

using a 10x oscilloscope probe connected to a Tektronix TDS5034B digital oscilloscope. The current supplied to the tile was measured simultaneously using a Tektronix P6022 AC current probe. A 50Ω 1% precision resistor was connected to the output tile, and a CalTest CT4068 differential oscilloscope probe was used to measure the output voltage. The differential probe was used to ensure that the output tile was floating, and that it was not coupled to the input signal via the oscilloscope mains earth connection.

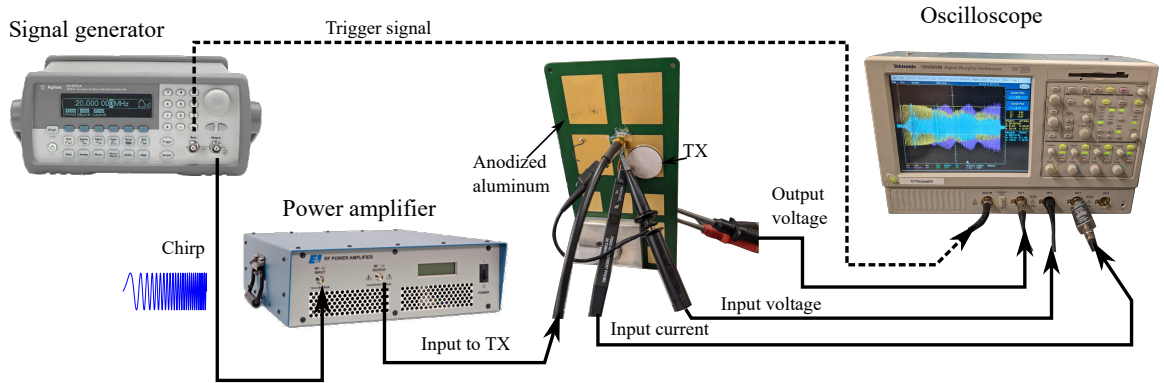


Figure 3.3: Experimental setup for characterizing the performance of the developed through-metal UPT.

3.2.2 Numerical Model

A high-fidelity FEM was used to evaluate the validity of the approximations made by the 1D analytical model, and the influence of lateral modes on system performance. An axisymmetric piezoelectric-structural-circuit model was constructed using the material properties, and dimensions summarized in Table 3.3. The element size was chosen so that at least 5 elements are used per wavelength at the highest studied frequency. Isotropic structural damping was used to model the attenuation in the different elastic layers as well as the piezoelectric layers. Dielectric losses in the piezoelectric layer were also included in the analysis. The aluminum wall was modeled with an extended radius of 25 mm and with non-reflecting boundary conditions at the lateral edge. Extending the wall further did not show a significant change in the calculated performance of the system, given that the ma-

jority of the elastic waves were localized between the piezoelectric transducers as shown in Figure 3.4.

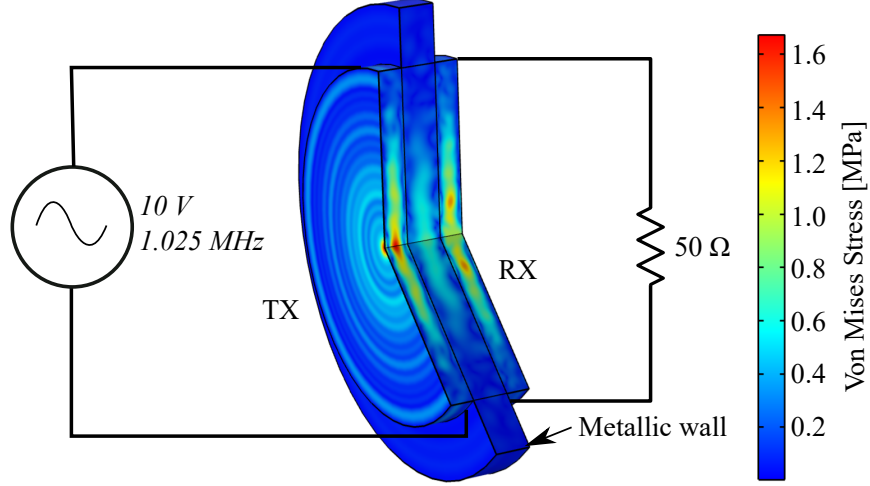


Figure 3.4: A cross-section in the base UPT FEM model showing Von Mises stress magnitude distribution calculated numerically when the system is excited with a steady-state 10 V sinusoidal voltage at 1.025 MHz.

3.2.3 Benchmark Results and Discussion

The voltage FRF and efficiency of the UPT system are summarized in Figure 3.5. The 1D analytical predictions are compared to the 2D axisymmetric numerical results, and to the experimental measurements of the system. A very good agreement is observed between the voltage and efficiency predictions of the numerical model and the experimental results. The influence of lateral and radial modes of the system is visible in the form of a “noisy” response for both the voltage FRF and efficiency in the experimental and numerical results. These fluctuations are not captured by the 1D analytical model; however, it still accurately approximates the profile of the voltage FRF as shown in Figure 3.5a. As shown in Figure 3.5b, the analytical model over-predicts the efficiency of the system for most of the considered frequencies as it does not include the power lost to exciting the lateral modes. The analytical predictions, thus, represents an envelope for the maximum theoretical effi-

ciency for a given configuration, and the actual efficiency achieved is usually lower. The peak experimental operating efficiency for the base system was 83% at 1.025 MHz.

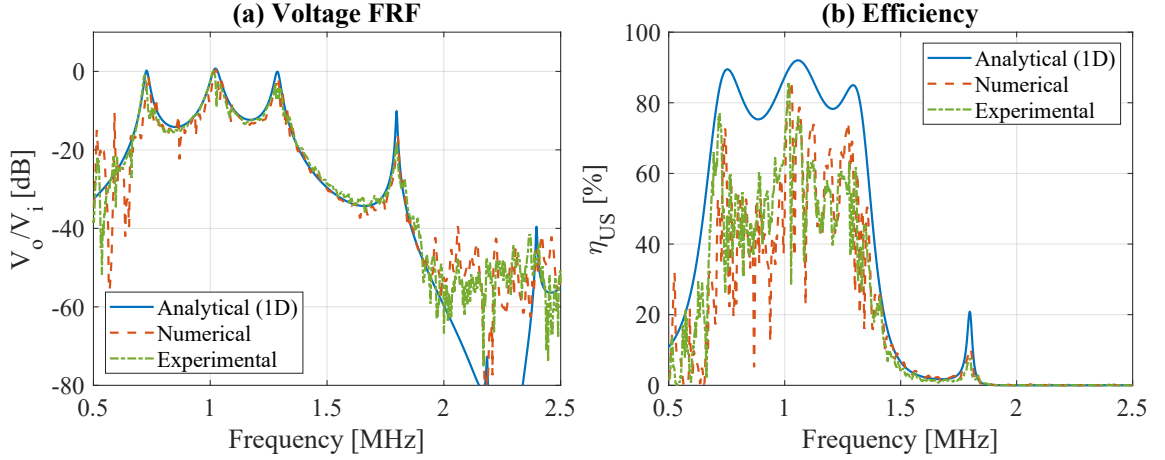


Figure 3.5: (a) Voltage FRF between the input and output piezoelectric transducer. (b) Operating (ultrasonic) efficiency of the system. The experimental results are compared to 1D analytical model and numerical model predictions.

The performance of the system is further analyzed by considering a larger frequency range for the voltage FRF and efficiency as shown in Figure 3.6. Three classes of overlapping peaks at different frequency intervals are observed in the response due to the resonance of the different components of the system. As shown in Figure 3.6a, the piezoelectric transducer resonance dominates the overall response of the system with global peaks at odd multiples of the thickness resonance of the transducer seen around 1.1, 3.3, 5.5, and 7.7 MHz. The voltage FRF is minimum around even multiples of the transducer resonance around 2.2, 4.4, 6.6, and 8.8 MHz, since the electrical and mechanical domains do not couple at the even modes of piezoelectric transducers [176, 181]. Using a thinner transducer would shift these global peaks to higher frequencies and increase the interval between them.

The second class of resonances originates from the standing waves in the aluminum wall (frequencies at which the thickness of the wall is an integer multiple of the pressure waves traveling through it). The sharpness of these resonance peaks depends on the impedance mismatch between the metal and the piezoelectric domain. The frequency in-

terval of these peaks depends mainly on the thickness of the aluminum wall with thicker walls resulting in smaller intervals.

The third class of resonances is related to higher-order radial modes in the transducers, and they appear as a noisy response around the fundamental frequency of the transducer. The strength of these modes depends on the aspect ratio of the transducer, and their effect diminishes for higher odd multiples of the transducer resonance.

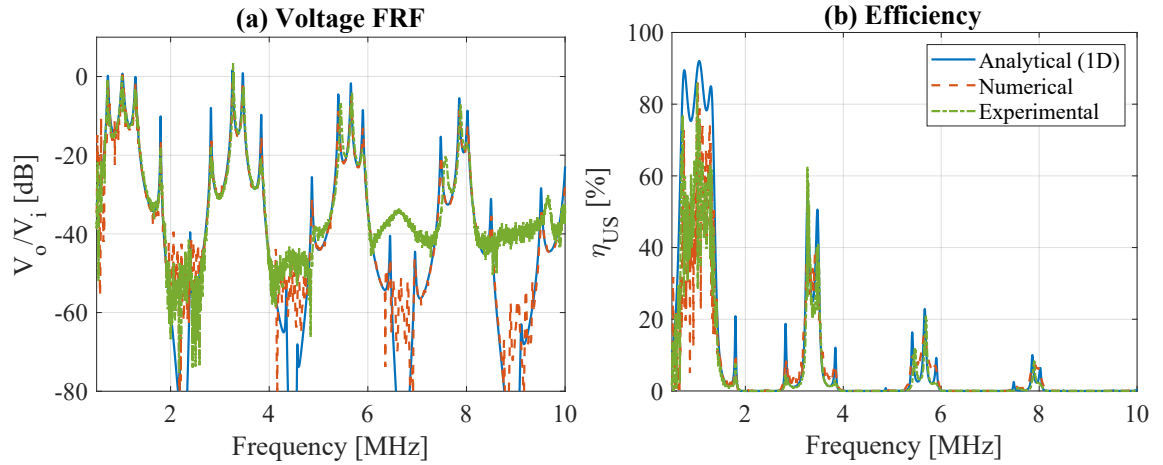


Figure 3.6: (a) Voltage FRF between the input and output piezoelectric transducer. (b) Operating (ultrasonic) efficiency of the system. The experimental results are compared to the 1D analytical model and numerical model predictions over frequencies ranging from 0.5 MHz to 10 MHz.

3.2.4 Maximum Achievable Efficiency

As discussed in Section 3.1.2, the UPT system efficiency is limited by two mechanisms: 1) the attenuation of the different elements as the waves propagate from the source to the load, and 2) wave reflection between the different components of the system. While attenuation is an inherent property of the materials used, and can only be enhanced by using lower loss materials, losses due to reflection can be reduced by matching the input and output impedance of the system to the source and load impedance values. It can also be reduced by matching the impedance between the different elastic layers. The use of acoustic matching

layers, however, might introduce additional attenuation to the system which might be larger than the reduction of reflection losses.

For the mechanical system, the maximum achievable efficiency occurs when the reflections at the input and the output of the system are minimized. This maximum efficiency can be calculated by determining the impedance that is required at the input and output of the system to minimize the reflections (simultaneous conjugate matching). This efficiency only depends on the system parameters and could be calculated using the relation [180]:

$$\eta_{max} = \frac{1}{1 - |\Gamma_S|^2} |S_{21}|^2 \frac{1 - |\Gamma_L|^2}{|1 - S_{22}\Gamma_L|} \times 100\% \quad (3.39)$$

where the matched source and load reflection coefficients (Γ_S, Γ_L) are given by:

$$\Gamma_S = \frac{B_1 \pm \sqrt{B_1^2 - 4|C_1|^2}}{2C_1} \quad (3.40)$$

$$\Gamma_L = \frac{B_2 \pm \sqrt{B_2^2 - 4|C_2|^2}}{2C_2} \quad (3.41)$$

where:

$$B_1 = 1 + |S_{11}|^2 - |S_{22}|^2 - |\Delta|^2 \quad (3.42)$$

$$B_2 = 1 + |S_{22}|^2 - |S_{11}|^2 - |\Delta|^2 \quad (3.43)$$

$$C_1 = S_{11} - \Delta S_{22}^* \quad (3.44)$$

$$C_2 = S_{22} - \Delta S_{11}^* \quad (3.45)$$

$$\Delta = S_{11}S_{22} - S_{12}S_{21} \quad (3.46)$$

Figure 3.7 shows the maximum achievable efficiency for the benchmark system compared to the operational efficiency obtained when the receiver is terminated with a 50Ω resistor. The results show that the peak operational efficiency of the system (at 1.025 MHz) is very close to the maximum achievable efficiency which means that the system is closely

matched to 50Ω at this frequency. The peak of the maximum achievable efficiency is inversely proportional to the frequency which is expected since it is only limited by the attenuation present in the system. At higher frequencies, however, the difference between the maximum efficiency and the operational efficiency is large which indicates that the impedance mismatch is large. Electrical impedance matching can thus be used to enhance the operating efficiency around the higher transducer resonance frequencies (i.e 3.3, 5.5, 7.7 MHz, etc).

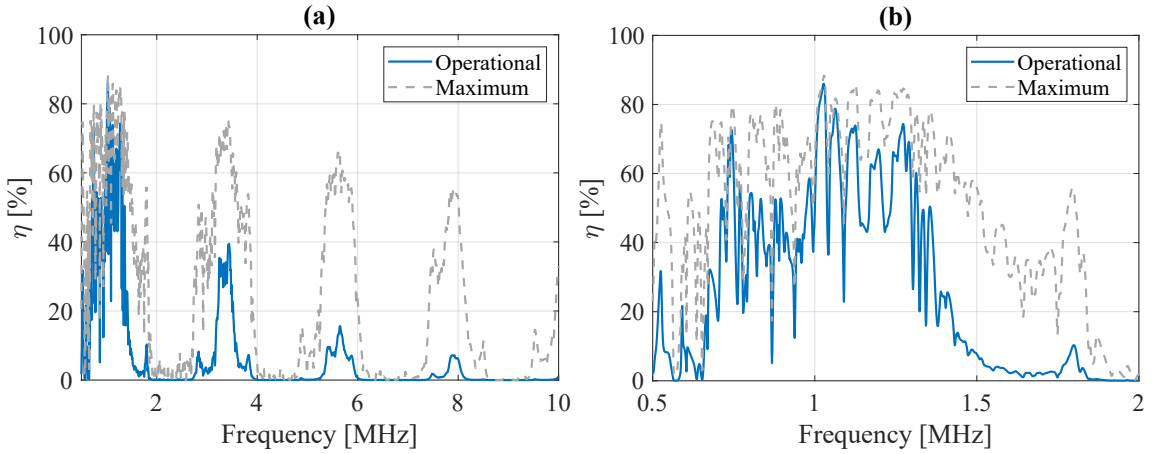


Figure 3.7: (a) Operating (ultrasonic) efficiency of the base system obtained numerically compared to the maximum achievable efficiency calculated using Equation (3.39). The frequency range from 0.5 MHz to 2 MHz is shown in (b).

3.3 Transducers with Wrap-around Electrodes

Transducers with wrap-around electrodes, as shown in Figure 3.8, allow for easy electrical access to the bonded side of the transducer without the need for using the metallic wall as a common electrical connection or gold plating electrodes on top of the anodized metallic wall as discussed in Section 3.2.1. The wrap-around electrode portion of the transducer, however, does not contribute to the active area of the transducer, and introduces asymmetries in the active transducer geometry which might excite additional lateral modes limiting the efficiency of the structure.

In this section, four transducers with wrap-around electrodes but different shapes, thickness, and area are investigated. Their performance will be compared to the base model which uses transducers with full coverage electrodes. Additionally, the sensitivity of the UPT system performance to transducer size and shape variation will also be discussed.

An anodized aluminum plate with a thickness of thickness 1/4" (6.35 mm) was considered, and a pair of transducers were bonded at the center of the plate as shown in Figure 3.8. Three circular SM111 (ct. Table 3.1) transducers with dimensions of 30 mm x 2.1 mm (the same as the base model), 15 mm x 1 mm, and 10 mm x 0.5 mm were considered as well as a rectangular transducer with dimensions of 20 mm x 15 mm x 2.1 mm.

The voltage FRF and operating efficiency for the considered transducers are shown in Figure 3.9. Since the plate used for this set of experiments is twice the thickness of that used in the base model, the wall resonances visible in Figure 3.9a are closer in frequency compared to Figure 3.6a. For the 30x2.1 (1MHz) transducer, the peak operating efficiency (80% as shown in Figure 3.9) is only slightly lower than that observed in the base model (83%) using the same transducer dimensions (Figure 3.9b). The transducer used in the base model had full coverage electrodes which suggests that the presence of wrap-around electrodes has a limited effect on the operating efficiency when the transducers are aligned properly. On the other hand, the rectangular transducers had the wrap-around part of the electrode at the corner as shown in Figure 3.8d which made it impossible to align the wrap-around part of the transmitting and receiving transducer. This contributed to the reduction in the peak efficiency (50% for the rectangular tile vs 80% for the circular tile). The difficulty of aligning the rectangular transducers as well as other corner effects may have also contributed to the loss of efficiency. The efficiency of the rectangular tiles is, however, expected to improve if transducers with opposite wrap-around corners are used.

The results for the higher frequency tiles show the expected trend of reduction in efficiency as the frequency of operation increases. The smaller transducers are also more sensitive to alignment issues which most likely contributed to the reduced operating ef-

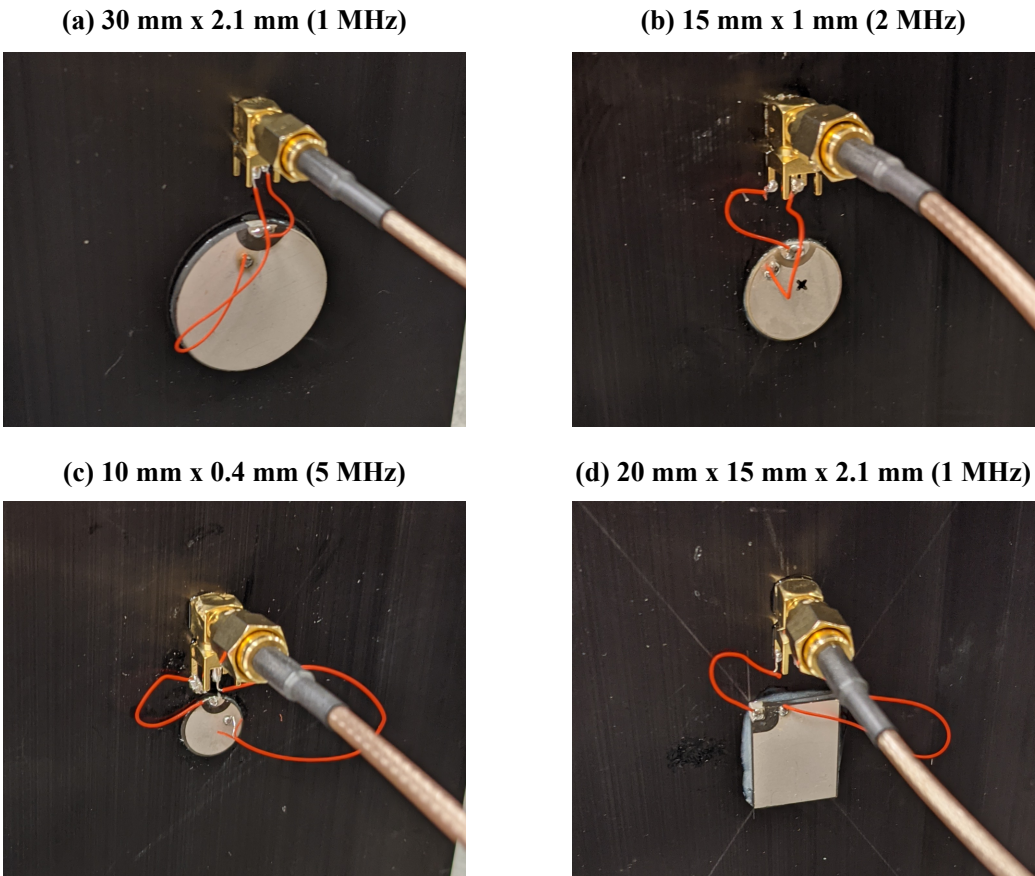


Figure 3.8: Experimental setup for through-metal UPT systems using circular transducers with dimensions (a) 30 x 2.1 mm, (b) 15 x 1 mm (c) 10 x 0.5 mm, and (d) a rectangular transducer with dimensions 20 x 15 x 2.1 mm.

ficiency. As shown in Figure 3.9b, the 15x1 (2 MHz) and 10x0.5 (5 MHz) transducers showed a peak efficiency of 67% and 61% respectively. The peak efficiency obtained by a thin transducer around its resonance (10 x 0.5 transducer for example) was larger than that obtained by using the higher-order modes of a thicker transducer (third mode of the 30 x 2.1 transducer).

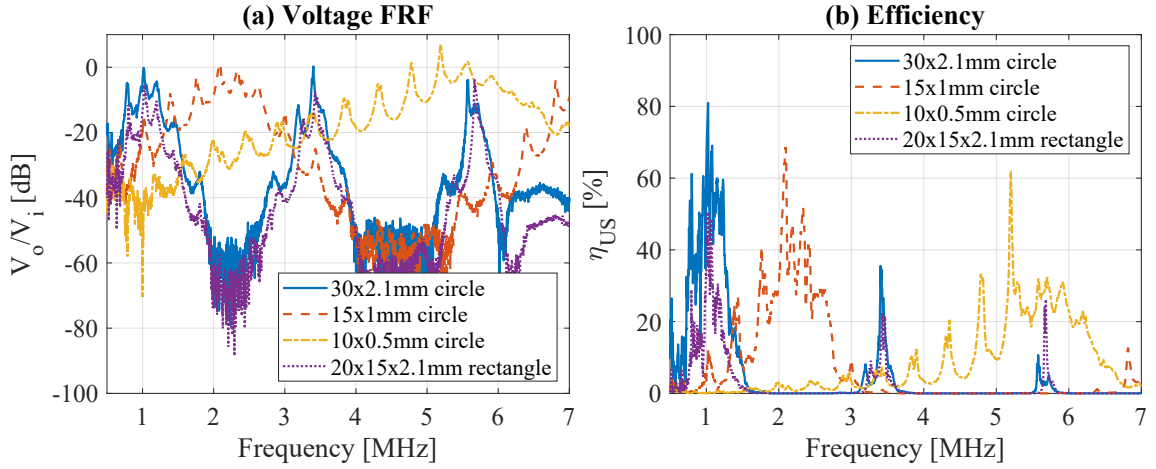


Figure 3.9: Experimental (a) voltage FRF and (b) operating efficiency for UPT systems for the transducers shown in Figure 3.8.

3.4 Interfacing Circuits

For a working implementation of a UPT system, it is necessary to consider the interfacing electronics in addition to the ultrasonic system itself. The essential components for a minimal functional UPT system are shown in Figure 3.10. Electric power is commonly available in DC form either directly from a battery or through rectified AC mains. In order to excite the ultrasonic system, the available DC power needs to be converted to an AC signal at the peak efficiency/power transfer frequency of the system. The AC signal is supplied from a signal generation circuit connected to drive a power amplifier circuit designed to operate efficiently at the system frequency.

A rectified DC output is also required for most modern electric devices. Since few electrical loads can directly operate using the raw high-frequency AC power at the output

of the ultrasonic system, an AC-to-DC rectifier circuit is usually needed at the output of the ultrasonic system. The rectified DC power could then be used to charge a battery (or a supercapacitor) or it could be directly used to drive an electrical load.

Common driving and rectifying circuits include active nonlinear components such as transistors and diodes. Therefore, a nonlinear circuit solver is needed for characterizing the overall performance of the system. Since UPT systems are modeled and characterized in the frequency domain, a nonlinear harmonic balance (HB) solver is better suited for simulating the system compared to more commonly used time-domain-based software such as SPICE or SIMULINK. The harmonic balance method directly solves for the steady-state system response at the fundamental frequency of excitation and its harmonics which is usually faster than simulating many time steps before the time-domain solver reaches steady-state operation [182].

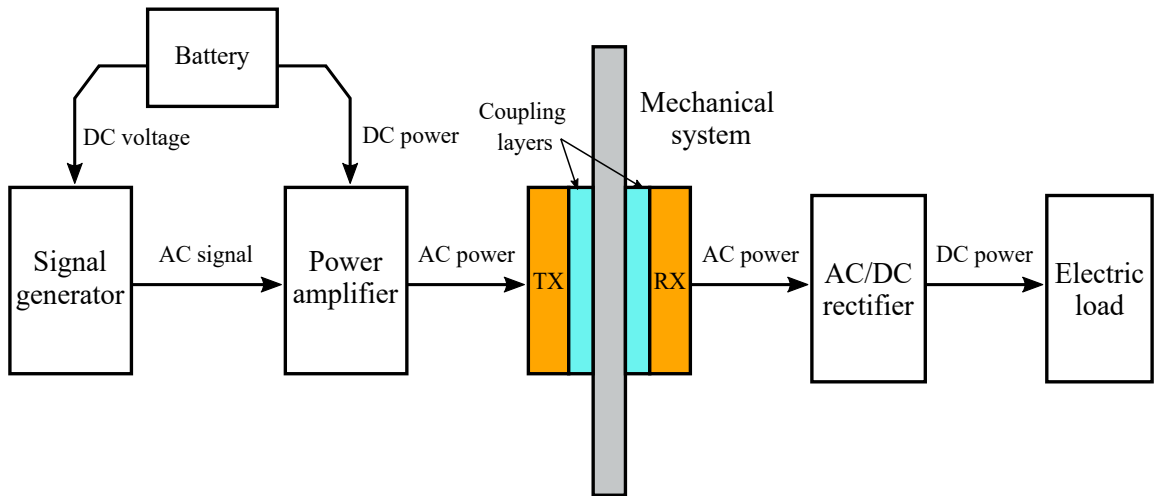


Figure 3.10: A block diagram showing the essential components for a through-metal UPT system and the flow of power between them.

3.4.1 AC-to-DC Conversion

Several rectification circuit configurations could be used with UPT systems. When the output voltage is much higher than the forward bias voltage of two diodes (typically around 1 V per diode), a full bridge configuration such as that shown in Figure 3.11a could be used

for achieving the conversion efficiently. For lower voltages, a voltage doubler circuit such as that shown in Figure 3.11b could be used instead. The voltage doubler circuit both rectifies the AC input signal and doubles the output DC voltage compared to a full-bridge configuration. Since the voltage is doubled, the output impedance of the system is also doubled, which limits the amount of current the system can supply. The diodes in the circuits shown in Figure 3.11 could also be replaced with active elements (transistors), to eliminate the diode voltage drop and improve the efficiency in low power applications [183, 184].

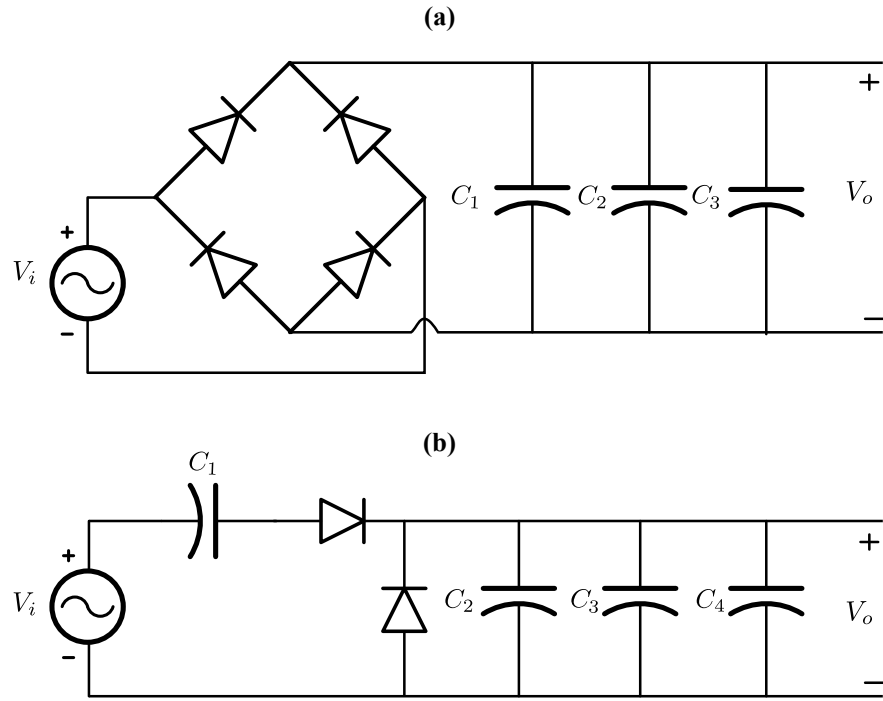


Figure 3.11: (a) Full bridge AC-to-DC rectifier circuit (b) Half-wave voltage doubler circuit.

For UPT systems operating in the low MHz frequency range, it is beneficial to select Schottky diodes with fast recovery time to minimize the power loss while switching. It is also important to carefully select the smoothing capacitors. Low equivalent circuit inductance (ESL) capacitors are necessary to ensure proper smoothing of the output voltage. Usually the larger the capacitor value, the larger its parasitic inductance (ESL) which limits its bandwidth and frequency of operation. Even the leads of the capacitor introduce enough

parasitic inductance to limit its bandwidth and thus surface mount components with very short leads are preferred to larger through-hole components.

To ensure a smooth DC output from the rectifier with minimum ripple, multiple capacitors with an order of magnitude difference in capacitance can be used in parallel. The larger capacitors provide enough current for a smooth DC operation, and the smaller capacitors filter out the high-frequency signal components. The exact value of the capacitors used is dependent on the circuit configuration, but values ranging between 0.01, 0.1, 1, and $10\ \mu\text{F}$ are a good ballpark for low MHz UPT systems.

3.4.2 Power Amplifiers

Common power amplifier circuits consist of one or more power transistors, with impedance matching and filtering circuits designed to optimize their performance for specific bandwidth, and power requirements. Metal oxide semiconductor field-effect transistors (MOSFETs) are ideally situated to operate with the maximum efficiency at low MHz frequency range. Compared to other common types of transistors such as bipolar junction transistors (BJTs), isolated gate bipolar transistors (IBJTs), and other types of FETs, they offer faster switching times with high power handling capabilities and low drain to source resistance R_{DS} (low ON resistance).

Depending on how the transistor is biased and operated, several classes of power amplifier designs can be used to drive the UPT system. In linear power amplifier classes (class A, class B, and class AB) shown in Figure 3.12a-c, the transistor operates in its active region (i.e. the resistance of the transistor varies proportionally with the input signal to generate the output power signal). In class A designs, the transistor is biased at the center of its active region, and thus the transistor is always on, and it dissipates power even when no signal is present at its input (the gate for MOSFETs). The result is a linear output with low harmonic distortion, but at the expense of a maximum theoretical efficiency of 50% [185]. In Class B, the transistor is biased to work for only half a sinusoidal cycle, and is thus turned

off when no signal is present. This improves the efficiency of the device up to a maximum of 76.8% [185], but introduces higher-order harmonics due to the clipping of the output signal. Class AB operates the transistor at a conduction angle between (180° and 360°), thus providing a trade-off between the linearity of class A and the improved efficiency of class B. All power amplifier classes could be operated in a push-pull configuration where two transistors are used simultaneously with each transistor handling half of the sinusoidal cycle. This has the advantage of allowing for more power to be delivered and reduces the nonlinearities present in class B and class AB designs.

For efficiency-centric applications such as UPT, switching mode power amplifier designs (such as class D and class E) offer improved efficiency over linear designs. In switching mode power amplifiers, the transistor operates as a switch, i.e. either fully ON or fully OFF. Since the transistor has the lowest resistance when it is fully ON, it dissipates much lower power compared to operating in the active region.

In class E designs (Figure 3.12d), the transistor is used to drive a resonating circuit near its resonance. The transistor in class E amplifiers ideally only switch when the output voltage is zero (ZVS), and thus the power dissipated during switching is minimized. For these reasons, the efficiency of class E amplifier designs can theoretically reach 100% [186] with practical implementations reaching a total efficiency higher than 90% [187]. These advantages come at the expense of a narrower operating bandwidth, and limited flexibility in controlling the output power of the amplifier which stems from the need for accurately tuning the operating point of the amplifier to achieve ZVS operation. Optimum class E operation can be achieved by tuning its frequency of operation, the inductor value, and the duty cycle of the driving square wave signal. The characteristics of class E power amplifiers are nevertheless well suited for power transfer applications which have motivated recent efforts aiming at tuning class E amplifier designs to be used for inductive power transfer applications [187–192] as well as UPT [193].

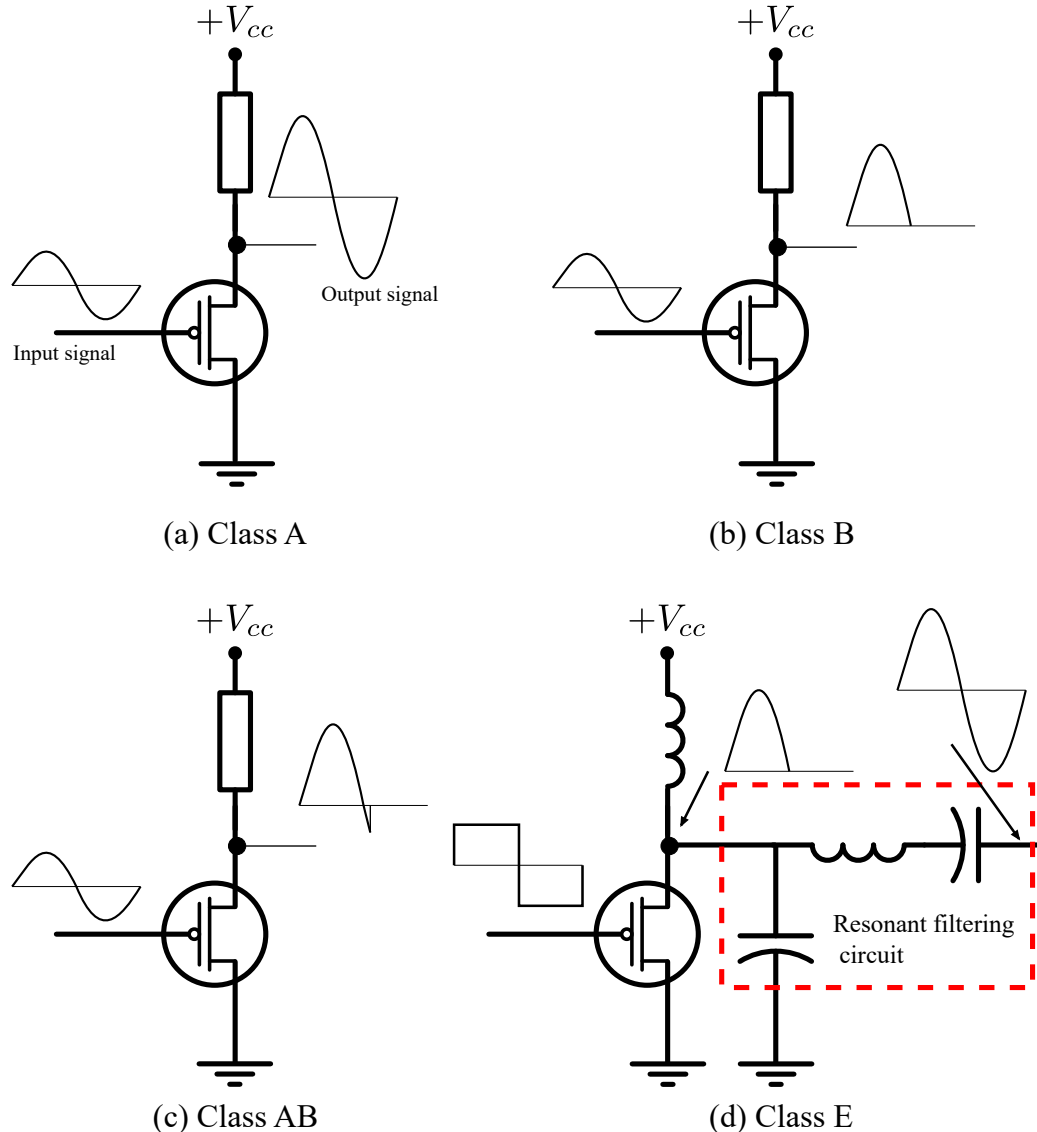


Figure 3.12: Power amplifier design classes depending on how the power transistor is biased and the nature of the excitation signal (sinusoidal vs. square wave).

3.4.3 Class E Amplifier Design for UPT

In this section, we investigate the design of class E power amplifiers for operation with piezoelectric UPT systems. We suggest a design that relies on the resonant mechanical system to double as the filtering circuit of the amplifier. This reduces the required electrical power components to a single feed inductor connected to the DC power supply.

Class E power amplifiers traditionally rely on the resonant circuit shown in Figure 3.12d to provide the transient response required for the amplifier operation and to filter the square wave driving signal to generate an output sinusoidal signal. Since piezoelectric UPT systems are resonant and capacitive in nature, the system itself could provide the transient response required for the operation of the amplifier, and the harmonics generated are filtered mechanically providing a clean sinusoidal output at the piezoelectric receiver. This tight integration, however, requires a coupled electromechanical model for optimizing the operation of the amplifier.

A coupled electromechanical harmonic balance circuit simulation was constructed to design the proposed amplifier using Keysight Advanced Design System (ADS) software as shown in Figure 3.13. The dynamics of the mechanical system is exported from the FEM model as a touchstone file (S-parameters representation) and then imported into ADS as indicated in Figure 3.13. A FQP30N06 power MOSFET (manufactured by ON Semiconductors inc.) was selected for the design because of its low ON resistance ($R_{DS} = 40 \text{ m}\Omega$) and fast switching time ($t_{on}^{(max)} = 210 \text{ ns}$). The feed inductor was tuned to provide ZVS conditions at the peak efficiency frequency of the mechanical system (1.025 MHz). The parasitic inductance from the TO-220 package of the MOSFET as well as the wires connected to the mechanical system are included in the model.

A Raspberry Pi Pico microcontroller was used to provide a programmable square wave signal to the power amplifier circuit as shown in Figure 3.14. The microcontroller was connected to a UCC27423P high-speed MOSFET gate driver Integrated Circuit (IC). The gate driver was used to supply the large instantaneous current required to drive the power

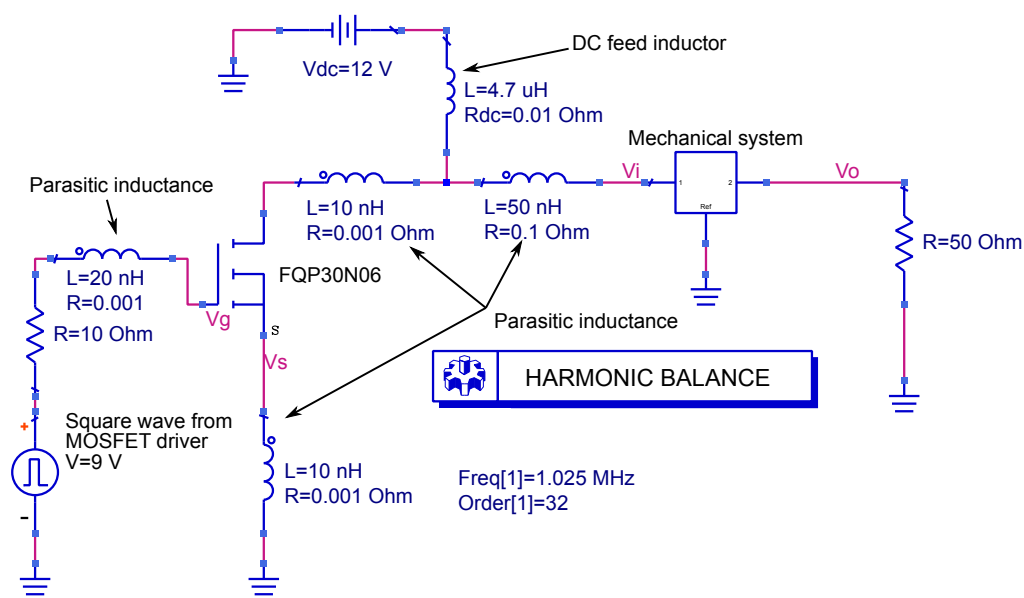


Figure 3.13: A circuit simulation using the harmonic balance method for a class E amplifier connected to the base model shown in Figure 3.1.

transistor. The Raspberry Pi Pico was programmed to supply a square wave signal with adjustable frequency to the MOSFET driver IC. The frequency and the duty cycle of the signal were controlled using two trimming potentiometers connected to the analog inputs of the microcontroller as shown in Figure 3.14. The circuit was designed to operate with 5-15 V DC supply levels allowing for direct operation from a single 9 V alkaline battery or a 7.2 V lithium-ion battery pack.

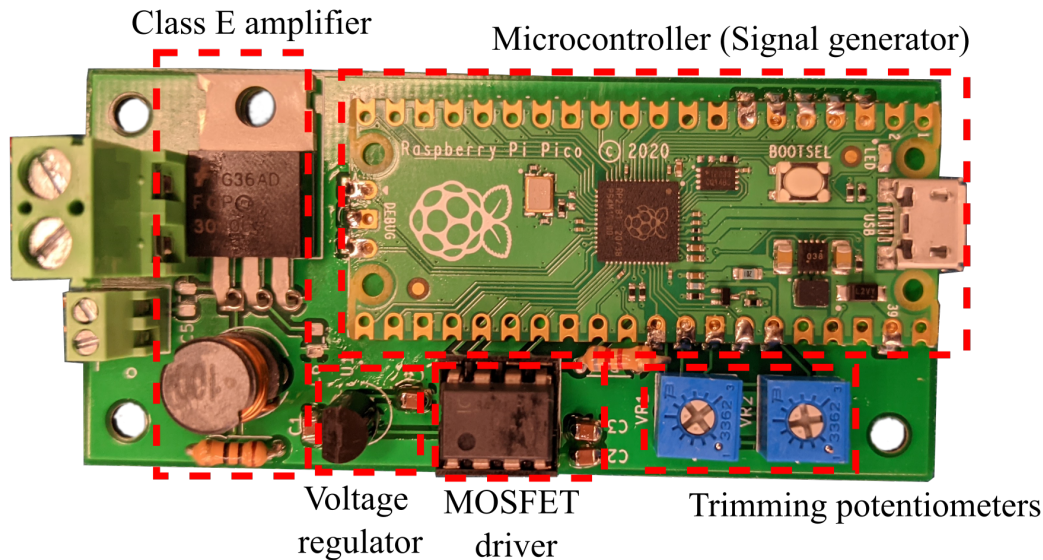


Figure 3.14: The printed circuit board of the designed class E power amplifier with a microcontroller used as a variable square wave generator and the MOSFET driving circuitry. The different components of the circuit are highlighted.

3.5 UPT with an Integrated Power Amplifier (DC-to-AC Operation)

The performance of the UPT system with an integrated class E amplifier is evaluated in this section. The simulated and experimental results for the input and output voltage waveforms to and from the system are shown in Figure 3.15 when a 12 V power supply is used to drive the circuit. An excellent match is observed between the experimental measurements and the simulated waveforms. In Figure 3.15a, the input voltage to the ultrasonic system is zero when the MOSFET is turned ON in the time interval between 0 and 0.5 μ s, and it swings sinusoidally depending on the system dynamics when the MOSFET is switched OFF as

shown in the interval between 0.5 and 1 μ s. The output of the system is a mechanically filtered sinusoidal signal, nevertheless, as shown in Figure 3.15b.

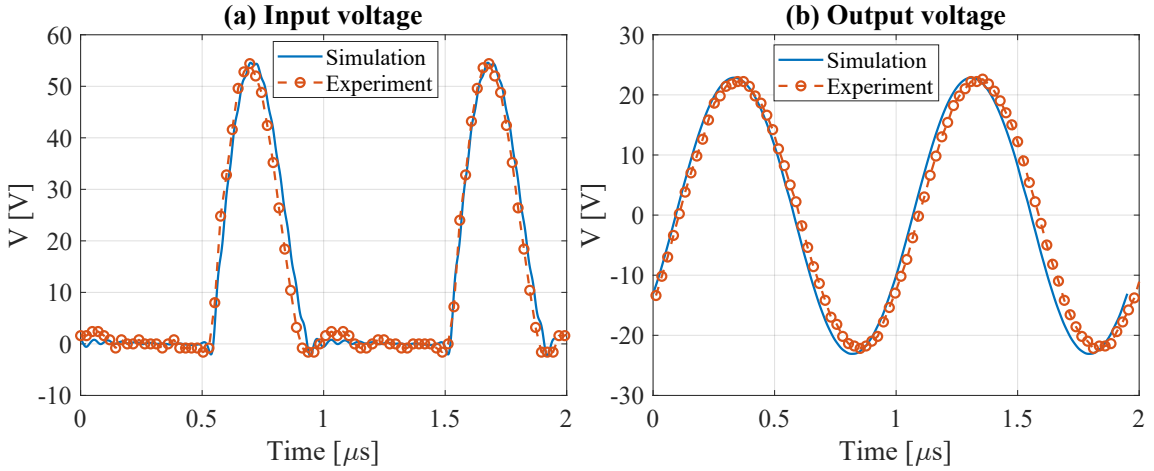


Figure 3.15: Simulated and experimental (a) input and (b) output voltage waveforms to and from the ultrasonic system as supplied from the designed power amplifier. The simulation results are obtained from the circuit shown in Figure 3.13.

For an efficient operation of class E power amplifiers, a ZVS condition must be achieved which depends on the mechanical system properties, operating frequency, driving circuit duty cycle, and the feed inductance value. Since the operating frequency and the mechanical system properties are fixed, the amplifier is tuned by adjusting the duty cycle and the feed inductor value. Figure 3.16 shows the voltage waveform at the MOSFET drain (input to the ultrasonic system) for a tuned operation when ZVS is achieved vs detuned operation. In the detuned operation, the transistor switches off when the drain voltage is not zero causing high-frequency oscillations due to the parasitic components in the circuit.

The total DC power supplied to drive the amplifier circuit (including the driving circuitry) was measured by using an Agilent E3641A DC power supply with a current readout. In order to quantify the total DC-to-AC efficiency of the UPT system with the integrated amplifier, the input DC voltage to the amplifier was varied from 5-16 V and both the input power to the ultrasonic system, and the output power was recorded. The operating

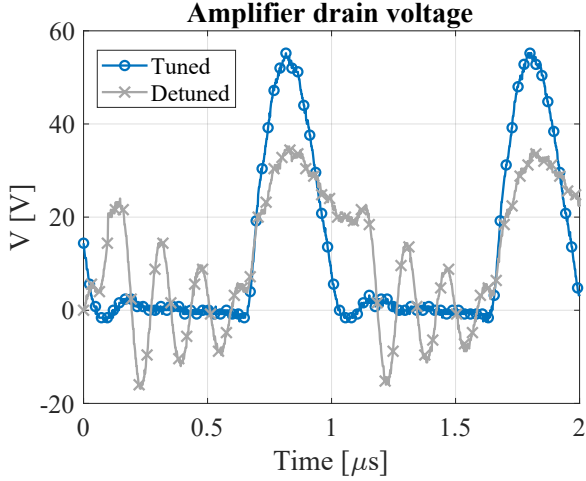


Figure 3.16: Experimental MOSFET drain voltage when the amplifier operation is tuned by selecting a proper feed inductor ($4.7 \mu\text{H}$) versus the detuned operation when a different inductor is used ($10 \mu\text{H}$ in the case shown).

efficiency from a DC supply was calculated from:

$$\eta_{DC-AC} = \frac{P_o}{P_{DC}} \times 100\% \quad (3.47)$$

where P_o is the output AC power supplied to a 50Ω resistive load and P_{DC} is the total DC power supplied to the system including the power needed to drive the microcontroller and the gate driving circuit (a constant current of 90 mA).

The total DC-to-AC efficiency is shown in Figure 3.17a vs the DC supply voltage. The detuned efficiency is also shown in the same figure to highlight the importance of tuning the amplifier. The efficiency of the detuned system drops sharply at 12 V which is most likely caused by overheating of the transistor due to inefficient operation. The system shows a peak DC-to-AC efficiency of 77% for tuned operation. The efficiency drops to 60% for lower power transfer because of the overhead of powering the microcontroller and driving circuit. The efficiency of the ultrasonic system was measured to be 89% at peak DC-to-AC efficiency, and thus the efficiency achieved by the class E amplifier was 86.5% including the power needed to drive the amplifier driving circuit. As shown in Figure 3.17, the system was able to deliver 9 W of power to a 50Ω load with a 16 V input. The system output power

was only limited by the breakdown voltage of the MOSFET used and could thus deliver larger output power with a higher rated transistor as discussed in the following section.

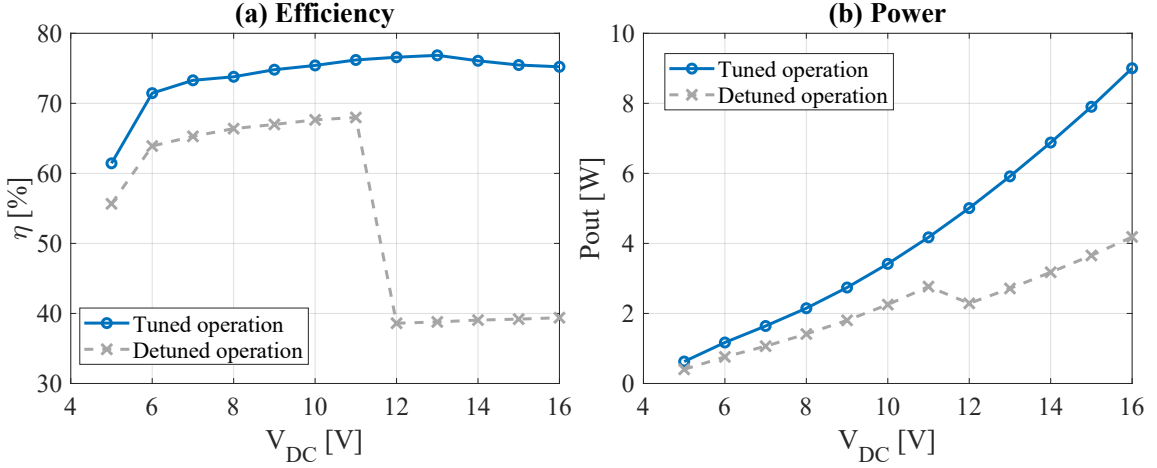


Figure 3.17: (a) DC-to-AC experimental system efficiency vs DC input voltage. The efficiency is calculated by dividing AC output power supplied to a $50\ \Omega$ load by the total input DC power. (b) The output power vs the input DC voltage supplied.

3.6 Overall System Performance (DC-to-DC Operation)

The full DC-to-DC operation for the UPT system was then studied by adding a full bridge rectifier as discussed in Section 3.4.1. The circuit shown in Figure 3.18 is used to simulate a complete through-metal UPT system that transfers power supplied from a DC source to DC power consumed by a load. A CDBHM260L-HF full-bridge Schottky rectifier is used at the output of the UPT to convert the ultrasonic system's AC output power into DC power. The power transistor used in Section 3.5 was upgraded to an IRFBV4019PBF power MOSFET capable of handling 150 V to allow for using a larger DC voltage supply. The circuit was implemented experimentally and the steady-state results are compared to the simulation predictions in Figure 3.19. An excellent agreement between the simulations and experimental measurement is observed for both the input and output voltage waveforms. The experimental results, however, show larger oscillations compared to simulations when the MOSFET is turned ON (i.e. when the input voltage is close to zero) which is caused by other electrical parasitics not captured by the model. The experimental DC output shows

slight ripples compared to the simulations which is caused by the ESL of the smoothing capacitors used as discussed in Section 3.4.1.

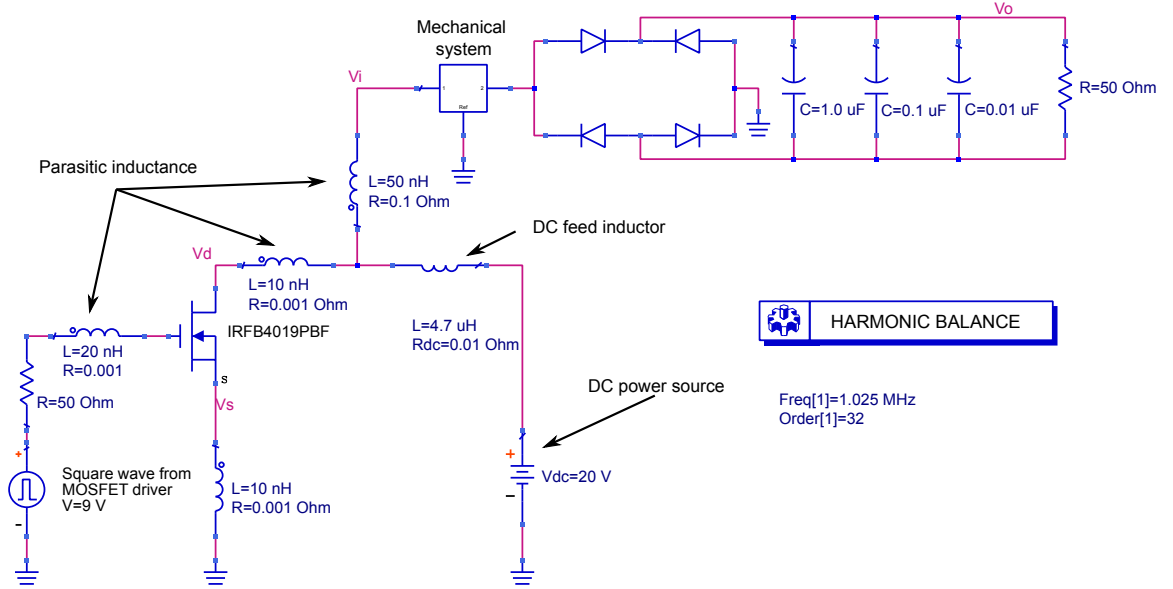


Figure 3.18: Harmonic balance simulation of a complete through-metal DC-to-DC UPT system.

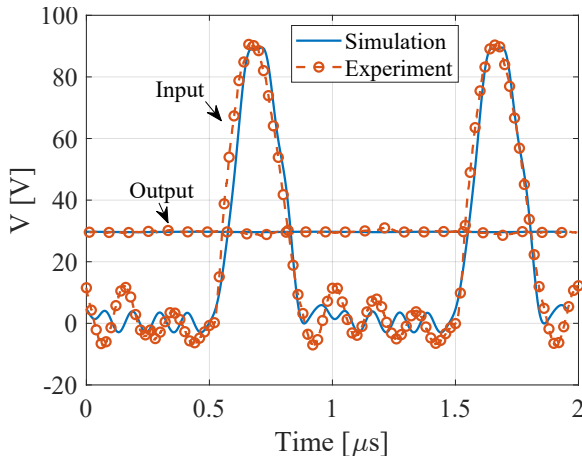


Figure 3.19: Input voltage (V_i) and output voltage (V_o) waveforms (see Figure 3.18) of the complete DC-to-DC UPT system operated from a 20V power supply. The simulated waveforms obtained using the circuit shown in Figure 3.18 are compared to experimental measurements.

The DC supply voltage to the system was then varied from 5-20 V to study its effect on the system efficiency and output power. The total input power from the DC power supply

and the output DC power delivered to a 50Ω as well as a 100Ω load were recorded, and then used to calculate the total system efficiency (DC-to-DC) efficiency:

$$\eta_{tot} = \frac{P_{DCo}}{P_{DCi}} \times 100\% \quad (3.48)$$

$$= \eta_{amp}\eta_{US}\eta_{rec} \quad (3.49)$$

As shown in Figure 3.20, the DC-to-DC efficiency to a 50Ω load remained constant around 68% for V_{DC} above 8 V. For lower V_{DC} values the efficiency of the system drops quickly due to inefficient amplifier operation. This is likely caused by insufficient MOSFET gate drive voltage and the reduced bridge rectifier efficiency. The efficiency of the system drops to 66% when driving a 100Ω load which is expected due to the power reflection caused by the impedance mismatch between the UPT system and the load. The system was capable of delivering 17.5 W of useful DC power which was limited by reaching the current limit of the DC power supply employed.

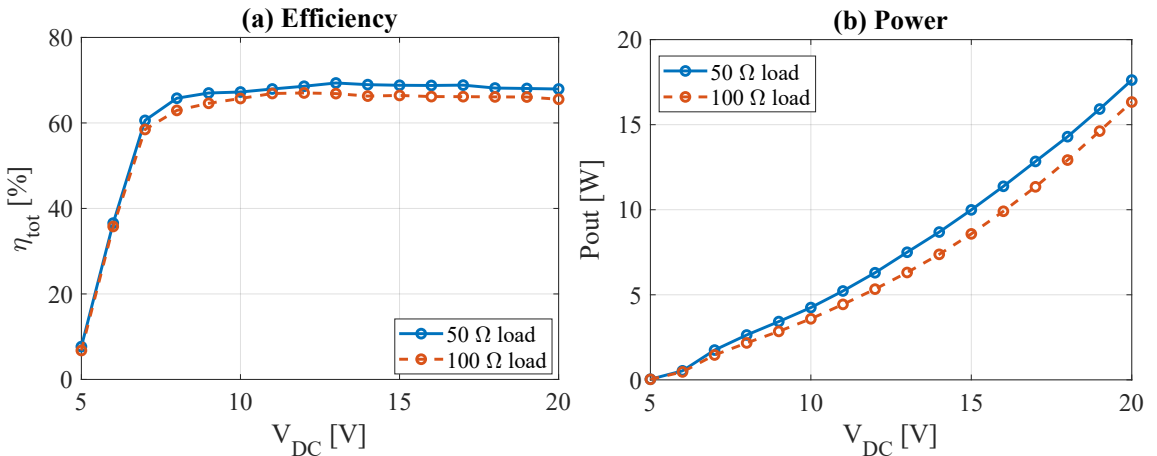


Figure 3.20: (a) Total experimental system efficiency vs DC input voltage. The efficiency is calculated by dividing output power supplied to a 50Ω load by the total input DC power. (b) The DC output power vs the input DC voltage supplied.

The recorded input amplifier drain voltage and DC output voltage waveforms are shown in Figure 3.21 for the tested DC supply voltage range. As shown in Figure 3.21, the amplitude of the voltage ripple due to transistor parasitics seems to increase when the supply

voltage is increased. The ripples are caused by a slightly detuned operation of the amplifier which can be adjusted by actively adjusting the duty cycle of the driving signal and using a different DC feed inductor value more suited for the full DC-to-DC operation of the system. The ripple of the output DC voltage (Figure 3.21b&c) seems to also increase with the amplitude of the output voltage which is expected since the amplitude of the ripple is directly proportional to the supplied DC voltage. Also, note that the ripple observed for the 50Ω load is larger than that for the 100Ω load which is expected since the current demand is larger. The UPT system used was capable of supplying 17.5 W (30 V & 0.59 A) to a 50Ω load, and 16 W (40 V & 0.4 A) to a 100Ω load using a 20 V power supply.

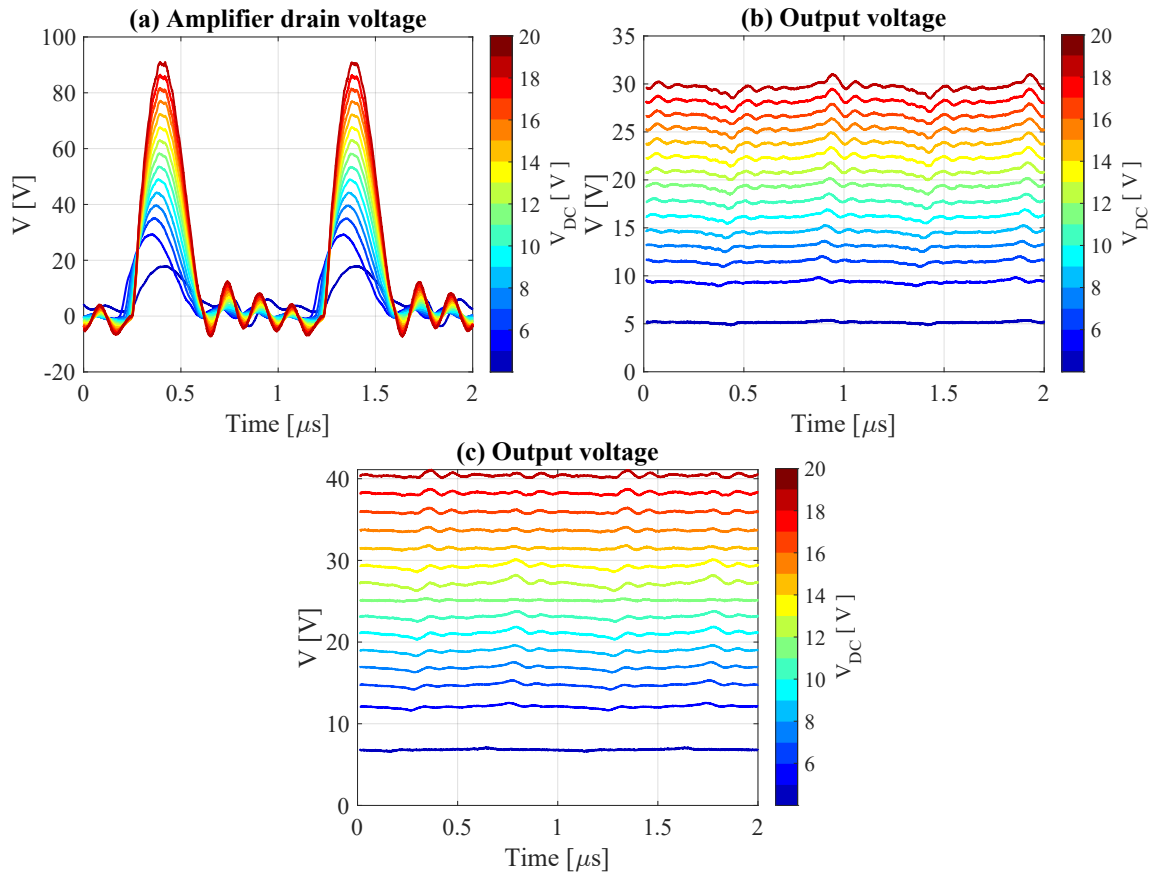


Figure 3.21: Experimental (a) amplifier drain voltage and (b&c) DC output voltage waveforms when (b) a 50Ω load and (c) a 100Ω loads were used. The waveforms are measured at the DC supply voltage levels shown in the color bar.

3.7 Dry-coupled Detachable Power Transfer System

It is useful to have a detachable charger (transmitter) for many portable devices, while the receiver remains bonded inside the device. Efficient detachable UPT operation requires good mechanical contact between the transducer and the metallic enclosure, which is typically achieved either through permanent bonding as discussed in the previous section or by using a liquid or gel couplant. A detachable system for power transfer through a metallic wall was first proposed by Moss *et al.*. They used two 4.2 MHz piezoelectric discs bonded to neodymium rare earth magnets to transfer power through an aluminum wall. The magnets were used to align the two transducers, and to provide the force necessary to hold the transducers against the wall. Up to 34% efficient power transfer was achieved using a high impedance ultrasonic gel couplant to provide the contact between the transducers and the wall. The use of ultrasonic gel couplants is however inconvenient in many situations since they either dry out during operation, require frequent reapplication, or leave traces that are difficult to remove and might accelerate corrosion.

Dry coupling of piezoelectric transducers has been investigated in the non-destructive testing (NDT) industry since the 1960s [194]. Dry ultrasonic pulse echo measurements at elevated temperatures were achieved by momentary coupling through impact using a steel hammer [195–197], and through rolling contact using a steel roller under pressure [198]. More recently, Bhadwal *et al.* [199] suggested using annealed silver as a soft layer to couple a 3 MHz lithium niobate piezoelectric transducer to a low carbon steel block. They needed to apply pressure of 12.7 MPa to achieve a similar performance to that obtained with ultrasonic gel.

Rubbers and elastomers have also been proposed for dry contact NDT [194]. Compared to other solids, they require the least force to deform, and thus could be forced to fill the microscale voids between two hard surfaces (i.e. between the transducer and the metallic surface as shown in Figure 3.22). Drinkwater *et al.* [200, 201] designed an ultrasonic

wheel probe made of a low loss rubber material to achieve dry coupling. The developed probes operated reliably at frequencies below 500 kHz, but their performance was sensitive to orientation when a 10 MHz transducer was used.

Ultrasonic transmission through a dry solid-solid interface is a complex problem to address especially when one of the solids is an elastomer. Many parameters can affect the ultrasonic transmission at the interface including the material properties of both solids, the surface roughness of both materials, the applied pressure, the presence of contaminants such as dust at the interface, and other surface properties. Most of the experimental studies in literature focused on solid-solid interfaces for the same material [202–207], while very little experimental data is available for ultrasonic transmission through dissimilar solid-solid interfaces (especially solid-elastomer interfaces). Drinkwater *et al.* [208, 209] studied the effect of the applied pressure, solid surface roughness, and the presence of dust on the reflection from a dry rubber-perspex interface. They used a 2 mm low attenuation rubber sheet wrapped around a solid cylinder and pressed against a flat perspex plate to evaluate the ultrasonic reflection coefficient. They showed that increased surface roughness and the presence of dust increased the contact pressure required to minimize ultrasonic reflection. They also showed that a 0.5 MPa contact pressure was enough to minimize the reflection at the interface. They did not provide details, however, about the modulus of elasticity or the hardness of the rubber used which might have a strong influence on the required contact pressure. The influence of elastomer thickness, and elastomer material properties such as hardness on the contact pressure required for good ultrasonic transmission is still not clear in the literature.

In this section, we develop a through-metal UPT system with a bonded receiving transducer and an external detachable transmitting transducer that does not require a gel couplant. The mechanical contact is achieved through a soft elastic layer with low ultrasonic attenuation placed between the metallic wall and the detachable transducer. The contact pressure is applied using the magnetic force between two arrays of neodymium magnets

(one array attached to the transducer and the other to the metallic enclosure). The practical efficiency and power delivery of the system are characterized, and the effects of key parameters are experimentally investigated, including the operating frequency, transducer geometry, and the elastic layer thickness and material properties.

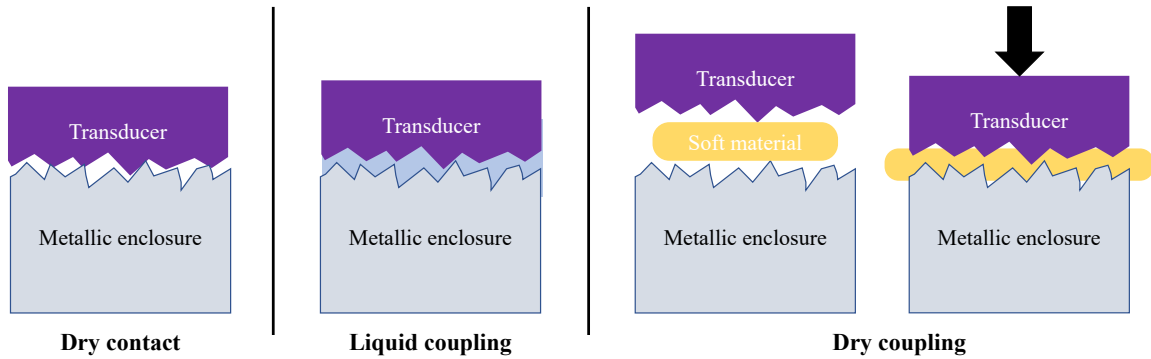


Figure 3.22: Different approaches to achieve ultrasonic coupling at the interface between two rigid solids. The surface roughness of the transducer and metallic enclosure is exaggerated to highlight the contact problem.

3.7.1 Experimental Setup

The detachable power transfer setup shown in Figure 3.23 was designed to test power transfer efficiency using dry contact. The setup relies on attractive magnetic forces to compress a soft elastomer between a piezoelectric transducer and an aluminum plate. The role of the soft layer is to minimize the contact pressure required for achieving good ultrasonic transfer through the dry interface. For the receiving side of the setup, a Steminc SMD30T21F1000S 1 MHz piezoelectric disc transducer (2.1 mm thickness and 30 mm diameter) was bonded to an anodized 3 mm aluminum plate with gold plated electrodes. The plate was anodized to prevent having any common electrical reference between the transmitter and the receiver. Thin gold electrodes were deposited on the plate to provide easy access for the bonded side of the receiving transducer. A vacuum bonding process was used to ensure a minimum thickness (10 μm) for the DP460 epoxy glue used.

A similar Steminc SMD30T21F1000R piezoelectric disc transducer with wraparound electrodes was used in the transmitter assembly. The wraparound electrode allowed for a flat contact surface without any solder bumps. The transmitter assembly consisted of a 3D-printed holder with a circular pattern for mounting 16 1/4" x 1/4" cylindrical neodymium-iron-boron NdFeB Grade N42 rare earth magnets supplied by K&J Magnetics, Inc. Another 3D-printed magnet assembly with the same pattern was glued to the aluminum plate. The magnets' polarity was switched between each two adjacent magnets to facilitate their assembly, and provide an easy approach to remove the transmitter by applying a twisting motion. Multiple detachable 3D-printed holders for the transducer were designed with a height increment of 0.5 mm to allow for adjusting the magnetic gap shown in Figure 3.23. The magnetic contact force is sensitive to the gap between the magnets as shown in Figure 3.24. The transducer holder height was selected such that a gap of at least 0.5 mm exists between the magnets. This would ensure that the maximum contact force allowed by this setup is applied at the dry interface. The total force applied by the magnets at 1 mm separation is approximately 147 N which results in a minimum of 0.2 MPa of contact pressure applied at the interface.

Three low-loss soft elastomer materials were initially tested to determine the best performing elastomer for this setup. The material properties of the elastomers supplied by Innovation Polymers, Inc. are summarized in Table 3.4. Each elastomer was tested at a thickness of 0.5 mm, and 1 mm to estimate its influence on the performance of the material. A single piezoelectric transducer was used for this set of measurements to reduce any variability related to transducer properties. In order to have a single dry interface (between the soft material and the aluminum plate), a liquid couplant was used between the transducer and the elastomer. The couplant was used instead of glue to avoid variations related to the quality of the bond from one material to the other. Aquasilox for example is based on silicone which requires a special type of glue to be bonded to the transducer. A liquid

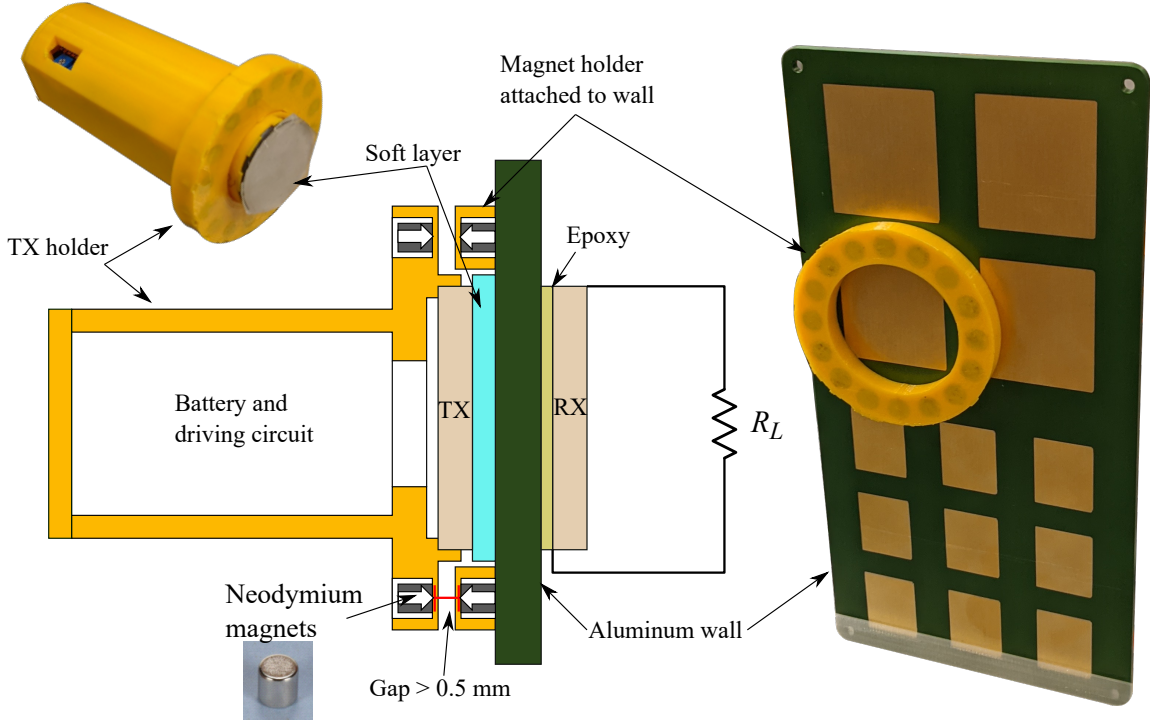


Figure 3.23: Schematic of the proposed dry-coupled detachable through-metal UPT system.

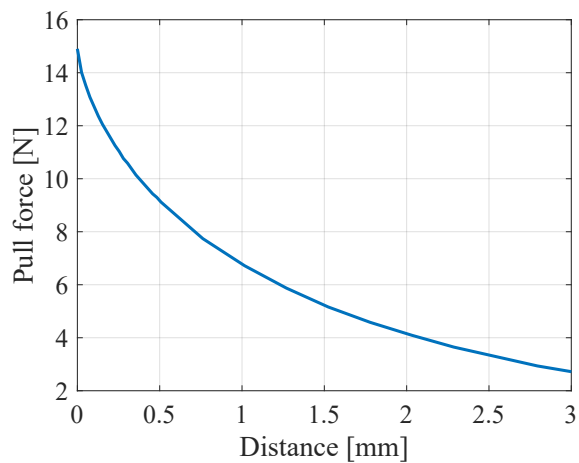


Figure 3.24: Pulling force between two 1/4" x 1/4" NdFeB Grade N42 magnets vs separating distance.

couplant was then used to avoid using a different type of glue for each material. The effect of using glue with the best performing elastomer is discussed in Section 3.7.3.

Table 3.4: Material properties of elastomer layers used in the study

Property	ρ	c	Z	α	Shore A hardness
Unit	kg/m ³	m/s	MRayl	dB/mm/MHz	-
ACE100	920	1541	1.4	0.2	42
Aquasilox100	1020	1004	1.02	0.18	23
Aqualink100	970	1476	1.4	0.088	5

3.7.2 Experimental Results

The measurement setup shown in Figure 3.25 was used to estimate the efficiency and voltage frequency response function FRF for the different elastomers considered. The setup is identical to the one used to evaluate the performance of the base model discussed in Section 3.2.1.

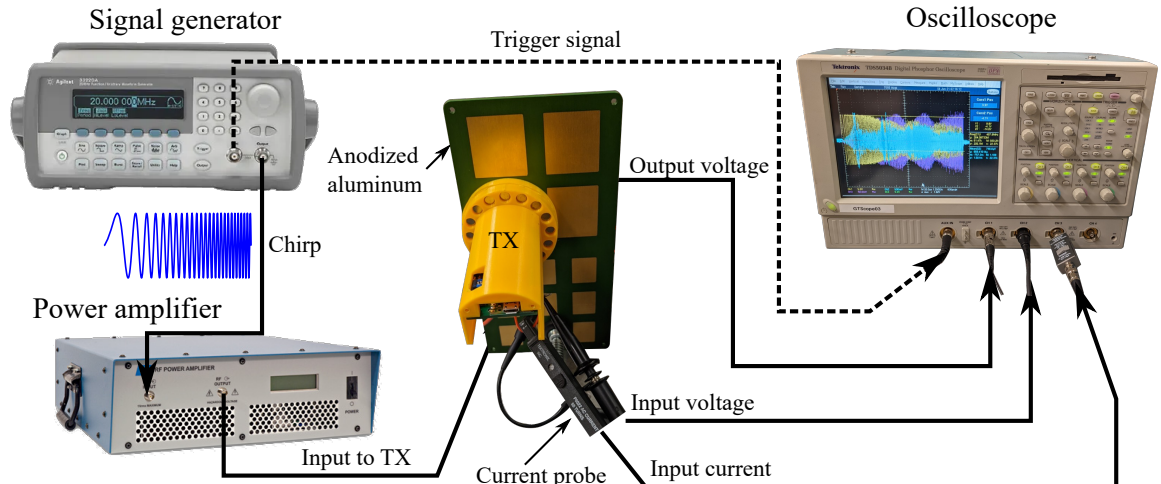


Figure 3.25: Experimental setup for evaluating the electromechanical performance of the developed detachable through-metal UPT system.

To establish a baseline for the performance of the detachable system, the magnetic assembly was tested with a dry interface between the transmitter and the aluminum wall without an elastomer or couplant. Then the test was repeated using an ultrasonic couplant (Olympus D12) between the transmitter and the wall. The results for the direct contact are shown in Figure 3.26. As expected, the detachable system does not operate properly without the presence of the couplant, and almost no power is transferred in the dry contact case. When the couplant is used, the system operates with a peak operating efficiency of 60% and a peak FRF close to 0 dB. The operating efficiency with couplant is, however, lower than the bonded system discussed in Section 3.2 (83% see Figure 3.5).

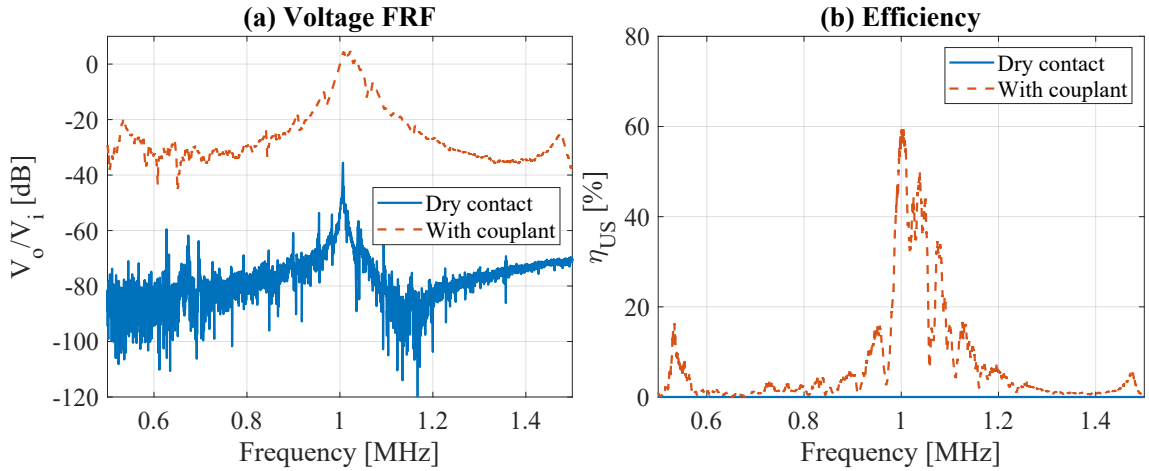


Figure 3.26: (a) Experimental voltage FRF and (b) operating efficiency for the detachable setup with direct contact between the transmitter and the aluminum wall with and without the use of a liquid ultrasonic couplant.

Figure 3.27 shows the efficiency and voltage FRF for the three considered soft layers when a thickness of 0.5 mm was tested. The same measurements are shown for a 1 mm thick layer in Figure 3.28. The soft materials considered had similar peak efficiencies for the 0.5 mm samples. The exact frequency at which the peak efficiency varied slightly from one measurement to the other using the same material. This variation was true for all of the considered thickness and material values. The value of the peak efficiency however was consistent for the same material and thickness value. The 1 mm samples had better peak efficiency compared to the 0.5 mm samples for all the considered materials despite

the added attenuation associated with the thicker materials. The thicker samples are more compressible than the thinner ones, allowing for better contact.

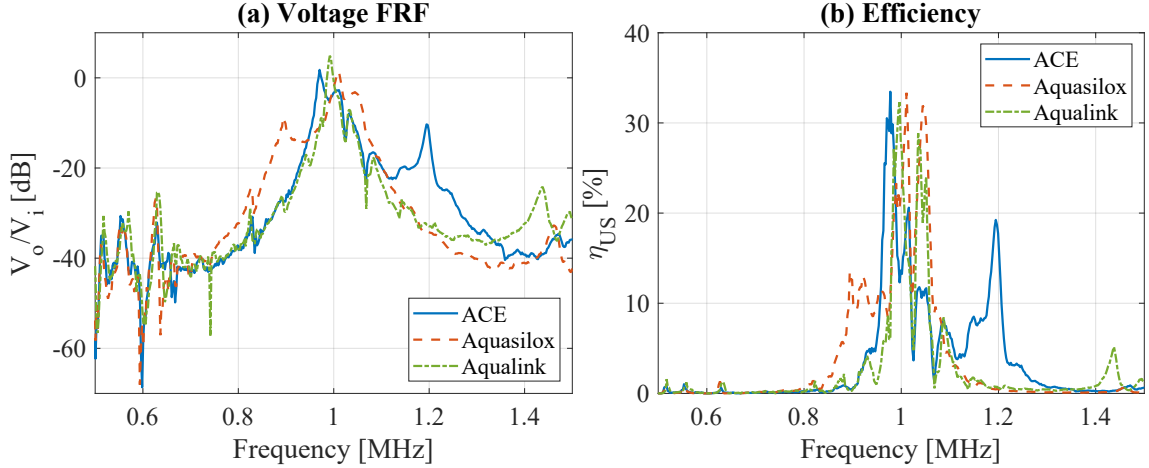


Figure 3.27: (a) Experimental voltage FRF for the detachable setup with a soft layer of thickness 0.5 mm for the soft materials tested. (b) The operating efficiency of the system.

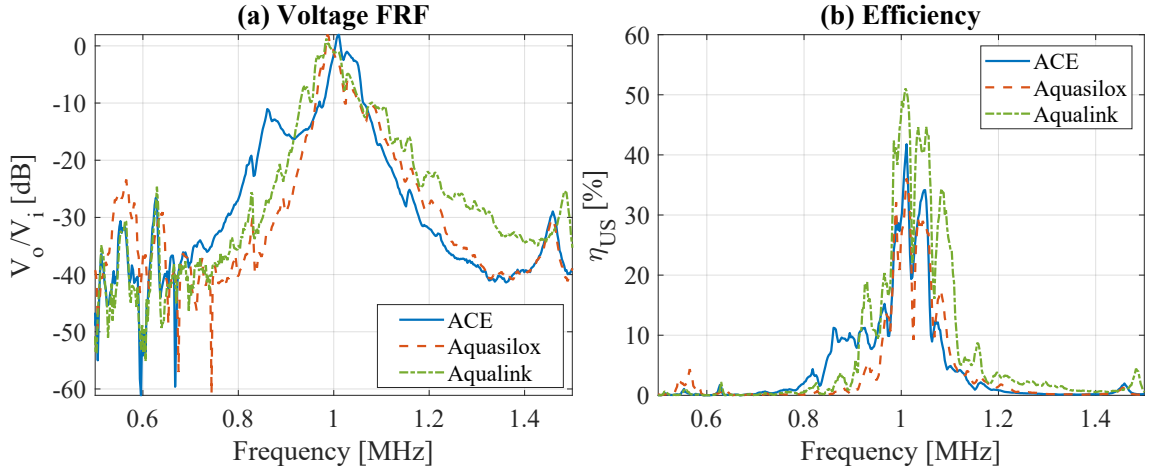


Figure 3.28: (a) Experimental voltage FRF for the detachable setup with a soft layer of thickness 1 mm for the soft materials tested. (b) The operating efficiency of the system.

Aqualink, which is the softest material considered, showed significant improvement with increased thickness. To confirm this, additional samples of 2 mm and 3 mm thickness were considered, and the results for the performance of Aqualink for all the considered thickness values were summarized in Figure 3.29. The 3 mm sample proved too unstable to get a repeatable measurement. The added thickness caused the system to be too flexible with an added rotation degree of freedom. The 2 mm sample showed the best performance

among all the tested samples with a peak efficiency of 66% at 1.04 MHz. It was also the most sensitive sample to alignment issues during the setup of the experiment. The added degree of freedom due to the compliance of the thick elastomer lead to a large variation of the peak efficiency depending on how the transducer was mounted. This form of instability was reported previously by Drinkwater *et al.* [208] where a thick rubber layer might be compressed from one side and lacks proper contact on the other. A compromise in system efficiency might be necessary by selecting a thin soft layer to ensure reliable and consistent operation of the dry-contact system.

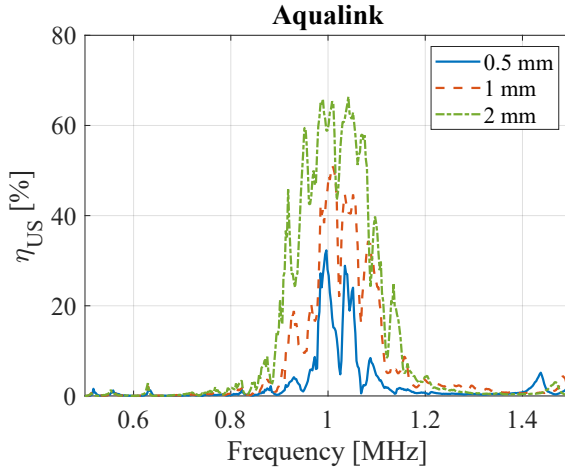


Figure 3.29: The operating efficiency of the system when a soft layer made of Aqualink100 was used. Results for a 0.5, 1, 2 mm thick layer are shown.

3.7.3 Effect of Gluing the Soft Layer to the Transmitter

The soft layer needs to be glued to the transmitting transducer for a practical detachable UPT system. Figure 3.30 compares the efficiency of the detachable system when the soft layer is glued to the transmitter versus when they are only coupled acoustically through an ultrasonic couplant. For all cases, a dry interface existed between the soft layer and the aluminum wall. A cyanoacrylate adhesive (Loctite 402) was used to bond the Aqualink and ACE samples to the piezoelectric transducer. A special silicone adhesive (Sil-poxy by Smooth-On Inc.) was used for successfully gluing Aquasilox. The system with glued

Aquasilox configuration, however, had a much lower efficiency compared to when a liquid couplant was used (Figure 3.30a).

The efficiency of the system was sensitive to the quality of the glue layer. Special care during the gluing process was needed to avoid introducing air bubbles between the soft layer and the transducer which negatively impacted the performance of the system. Even with special care, most of the glued samples had lower peak efficiency compared to when a liquid couplant was used (Figure 3.30b). A few well-glued samples such as that shown in Figure 3.30c achieved operating efficiencies higher than that achieved with a couplant suggesting that refining the gluing process will have a positive impact on the system efficiency.

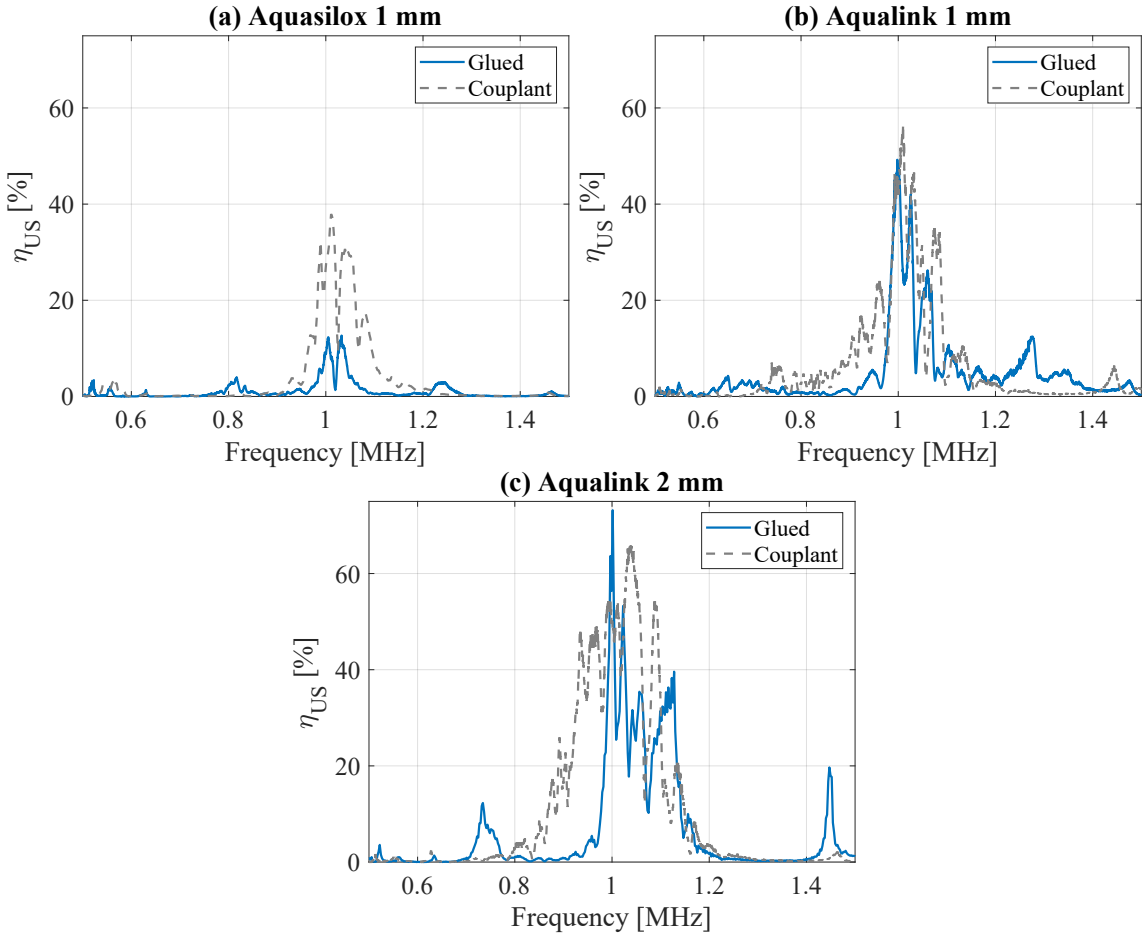


Figure 3.30: Comparing the performance of the dry-coupled system when the soft layer is glued to the transmitter vs when a liquid couplant is used. The results are shown for (a) Aquasilox 1 mm, (b) Aqualink 1 mm, and (c) Aqualink 2 mm soft layers.

3.7.4 Overall System Performance

The performance of a portable system consisting of the driving circuit, discussed in Section 3.4, and the detachable transmitter, shown in Figure 3.23, was then experimentally tested to determine the overall operating efficiency of the system when supplying power to a resistive load. The system was designed to operate with a DC input voltage between 5 and 25 V. Practical battery-operated designs can make use of a single 9 V alkaline battery or a lithium-ion battery pack capable of generating 7.2 V or higher. Alternative designs might incorporate a single lithium-ion battery with an adjustable boost converter for controlling the power sent through the device.

The system was first tested using the experimental setup shown in Figure 3.31. A controllable DC power supply (Agilent E3646A) was used to sweep the supply voltage through the allowable voltage range for the device to study its performance when a 50Ω power resistor was connected at the output. A transmitter with a glued 2 mm Aqualink soft layer was set to transmit power at 1 MHz. The input and output voltage and current waveforms were then recorded to calculate the power flowing through the system. The power delivered by the power supply was then used to calculate the overall efficiency of the system. The results of the voltage sweep are summarized in Figure 3.32 and Figure 3.33.

The operation of the system was tested when its output was connected directly to a 50Ω load (AC output) and with an AC-to-DC bridge rectifier to characterize the overall DC-to-DC operation. The voltage waveforms at the drain of the amplifier (input to the ultrasonic system) are shown in Figure 3.32a. The waveforms show a slightly detuned operation of the amplifier with ripples caused by the parasitics of the amplifier. A slightly more efficient operation for the amplifier is expected with careful tuning of the DC feed inductor value to achieve ZVS. The introduction of the bridge rectifier had a negligible effect on the input voltage waveform (Figure 3.21a). Clean sinusoidal and DC output waveforms were measured with minimal ripple or distortion. A peak output DC voltage of 13.5 V was measured for an input of 11 V.

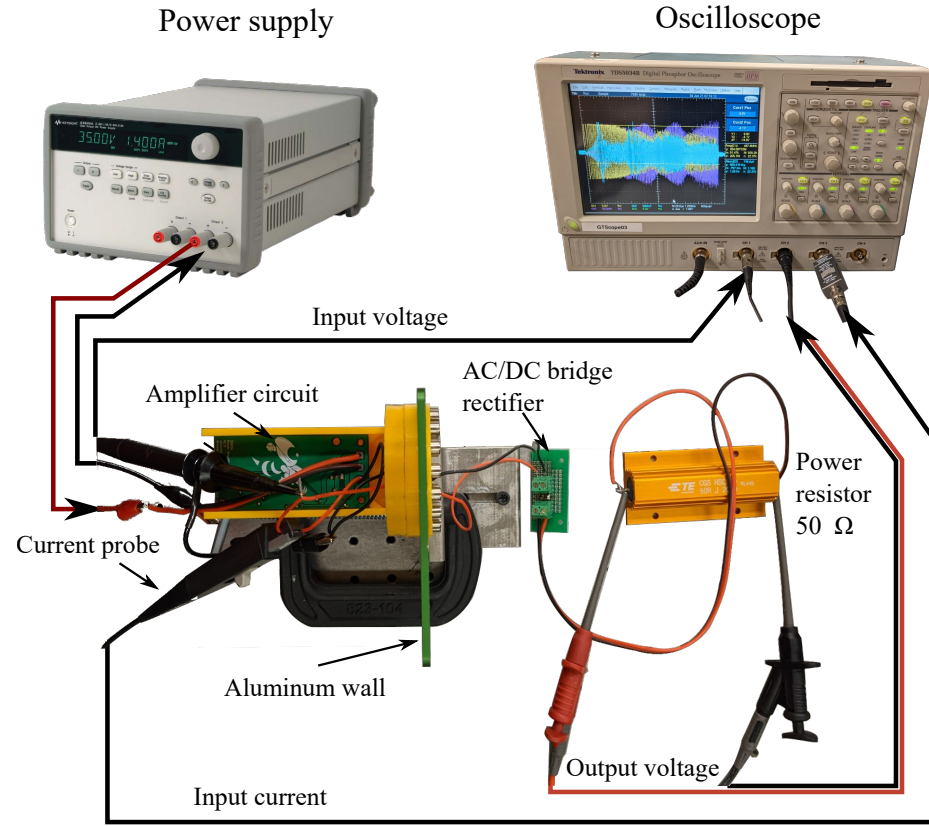


Figure 3.31: Experimental setup for evaluating the overall performance (DC-to-DC operation) of the developed detachable through-metal UPT system.

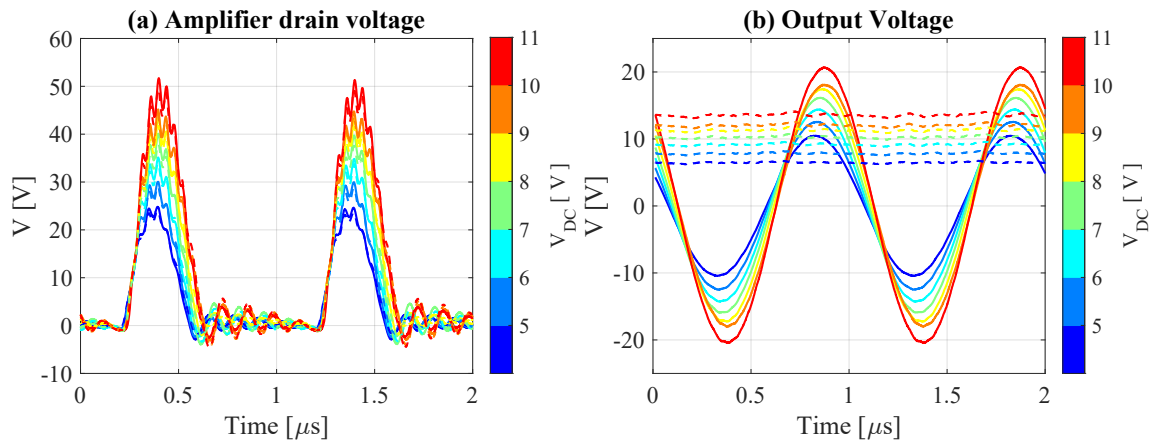


Figure 3.32: Experimental (a) amplifier drain voltage and (b) output voltage waveforms for AC and DC output operation of the dry-coupled system at the DC supply voltage levels shown in the color bar. The operation of the system with the AC-to-DC bridge rectifier is shown using dashed lines and without it using solid lines

The total system efficiency and the ultrasonic system efficiency are shown in Figure 3.33a. The ultrasonic efficiency decreases at voltages higher than 6 V indicating that the heat generated during the operation is affecting the UPT system performance. This leads to an overall system efficiency peak at 50% when the supply voltage is 9 V. The peak resulted from an improved amplifier and AC-to-DC bridge efficiency with increased input voltage counteracted by the reduction in ultrasonic system efficiency. The measured efficiency for voltages below 11 V was stable over time indicating that the system could operate reliably at this voltage range. For voltages higher than 11 V, the efficiency dropped quickly with time which prevented a stable measurement. The measurement was repeated after the system cooled down and the efficiency climbed back to 50% before dropping with time verifying that the heat generated is the problem. The breakdown temperature of Aqualink is low (around 60 °C) which justifies the drop in efficiency at higher power levels. The developed system could thus be used to deliver up to 3 W of power at 50% total efficiency. For higher power levels, a heat-resistant material with similar Shore hardness and ultrasonic attenuation properties to Aqualink is needed to maintain efficient operation.

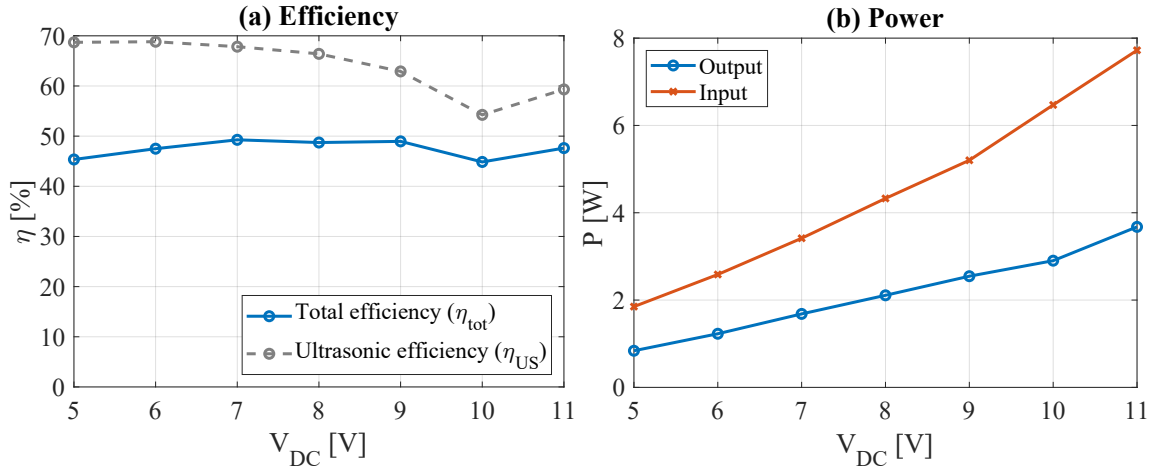


Figure 3.33: (a) Experimental total system efficiency and ultrasonic efficiency vs DC input voltage for the dry-coupled system. (b) The total input and output DC power vs the input DC voltage supplied to the system.

3.8 Conclusions

Two configurations for through-metal ultrasonic power transfer were developed and experimentally tested. The first setup included a bonded transmitter and receiver sending ultrasonic power through an anodized aluminum wall. An efficient class E power amplifier was designed to be tightly integrated into the ultrasonic system with minimal electronic components. The developed amplifier relied on the ultrasonic system for filtering its output signal. A complete power transfer system that includes the amplifier, the ultrasonic setup, and a full bridge rectifier was simulated and then experimentally verified. The system was able to deliver 17.5 W of DC power to a 50Ω resistive load at a total DC-to-DC efficiency of 66%.

A dry-coupled detachable through-metal power transfer system was also designed to provide efficient ultrasonic power transfer without the need for a liquid ultrasonic couplant. The system consisted of a battery-operated detachable charger that could be attached to an aluminum wall through a magnetic setup. Three soft elastomers were tested to select the material suitable for achieving the best power efficiency. Samples with different thicknesses were also tested. The results showed that soft layers with 1-2 mm thickness made of the softest tested material (Aqualink with 5 Shore 00 hardness) achieved the best ultrasonic coupling possible. The developed charger could deliver up to 3 W of DC power through a 3 mm aluminum wall with 50% efficiency when operating on a 9 V alkaline battery.

CHAPTER 4

PERFORMANCE ENHANCEMENT BY LEVERAGING PHONONIC CRYSTALS AND WAVE FOCUSING

Wireless sensor nodes deployed in the ocean could be meters to even kilometers away from the power source. This limits the operating frequency of the underwater UPT system to tens of kHz, and allow for the waves to travel between TX and RX with minimum attenuation. The efficiency of the system becomes limited by power spreading in the medium unlike through-metal UPT systems in which the spreading losses were minimal.

In this chapter, we introduce two 3D-printed gradient-index phononic crystal (GRIN-PC) lens designs intended for focusing and collimating acoustic waves underwater and in air. The lenses are introduced to improve the efficiency of acoustic power transfer systems by focusing incident acoustic waves at the receiver. A finite-element model is developed to design the unit cell dispersion properties and to construct the 3D lenses for wave field simulations. Numerical simulations are presented to confirm the focusing of incident plane waves and to study the sensitivity of the refractive index profile to the direction of wave propagation.

The two lenses are then fabricated, and their theoretical focusing characteristics are validated experimentally using a scanning hydrophone setup for measuring the underwater pressure field and a scanning microphone setup under speaker excitation to measure pressure field in air. The underwater lens is used to enhance the performance of an underwater power transfer system with low directivity transducers. Similarly, the in-air lens is used to enhance the performance of a piezoelectric unimorph transducer placed at its focal point. For each of the tested systems, introducing the GRIN-PC lenses dramatically enhances the power delivered by the system.

4.1 GRIND-PCs for Underwater Focusing

We introduce a simple structure and design approach for GRIN-PCs that allow for the manipulation of underwater acoustic waves. The unit cell of the PC consists of trapped air inclusions in a 3D-printed Polylactic Acid (PLA) elastic matrix as shown in the inset of Figure 4.1a. The PLA polymer acts as the background medium allowing for a close impedance matching to water while air acts as an impedance contrasting inclusion. This allows for the construction of a simple lightweight PC compared to other common PCs with dense metallic inclusions. The shape of the inclusion is chosen to facilitate its 3D printing via the commonly employed Fusion Deposition Modeling (FDM) process without difficulty [210].

4.1.1 Underwater Unit Cell Analysis and Refractive Index Tailoring

Using an elastic material as the lens background material introduces additional complexity as compared to the fluid background of in-air PC lens realizations [131]. First, as shown in Figure 4.1a, two modes of propagation exist in the elastic domain (pressure and shear waves), and thus both modes should be considered when analyzing wave propagation in the PC domain. To simplify the analysis, shear waves (S-waves) in the PC were neglected assuming incident acoustic waves in water were mainly coupled to pressure waves (P-waves) in the PC domain for the configurations explored in this study. Secondly, the lattice periodicity of the PC, as well as the inclusion size and shape, introduces anisotropy (hence directional dependence) in the effective properties of the PC. The resulting anisotropy is more significant in an elastic background compared to a fluid background which is isotropic by nature and less sensitive to inclusion shape and periodicity. In the following analysis, we only consider waves propagating in the ΓX direction to characterize the effective properties of the crystal, in an effort to demonstrate the focusing of plane waves propagating in a

known direction (omnidirectional implementation would require a more complex unit cell geometry and fabrication challenge).

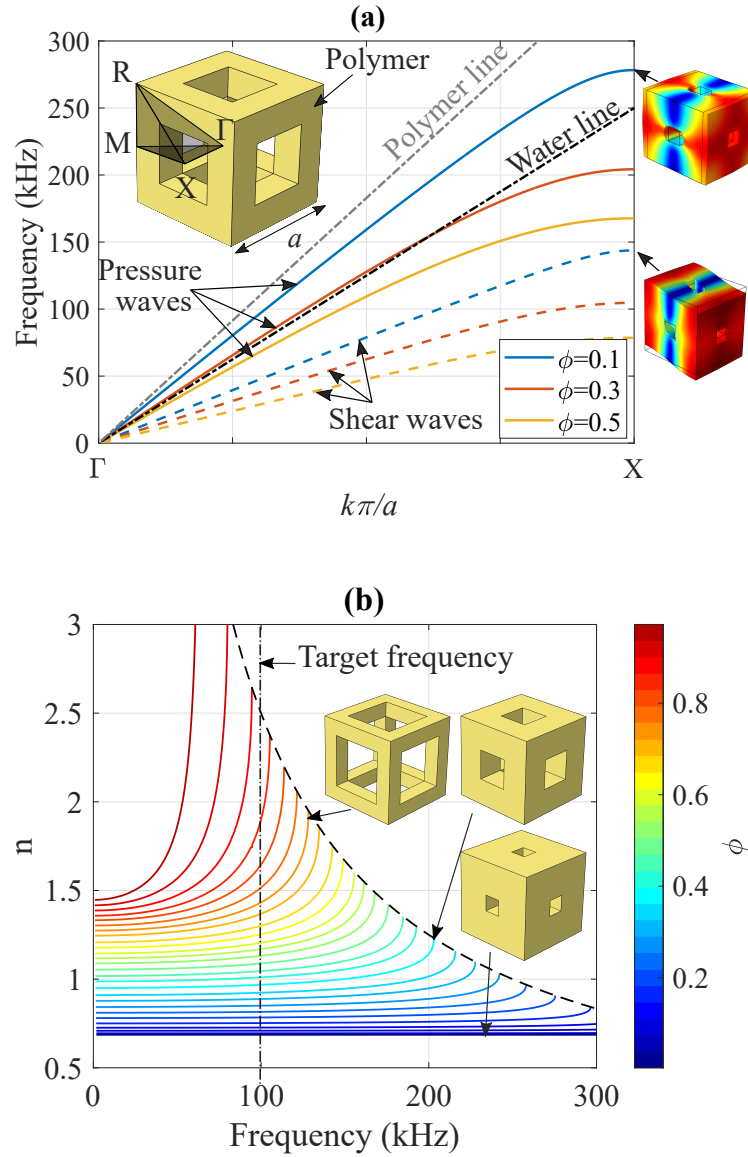


Figure 4.1: (a) Band structure of the proposed PC for different filling fractions (ϕ) of air volume per unit cell volume (propagation modes of different branches are shown as insets). (b) Frequency dependence of the PC refractive index for different filling fractions.

An elastic Finite Element Model (FEM) of the PC unit cell with periodic boundary conditions was used to obtain the band structure shown in Figure 4.1a. The material properties of the 3D-printed PLA used in the FEM were obtained experimentally since they usually differ from standard PLA properties depending on the 3D printing process parameters. In

order to identify the actual material properties of the printed structure, homogeneous slender bar samples were printed using the same 3D printing process parameters as the PC. The first few axial vibration modes of those samples were employed to estimate the elastic modulus and loss by using the approach detailed in Ref. [211]. The identified properties of the 3D-printed PLA were: Young's modulus $E = 3200$ MPa, density $\rho = 1250$ kg/m³, Poisson's ratio $\nu = 0.36$, P-wave speed $c_p = 2194$ m/s, S-wave speed $c_s = 1026$ m/s, and structural loss factor $\eta = 0.02$. Furthermore, due to the large impedance mismatch between PLA and air, the inclusions were modeled as free boundary conditions to the elastic domain. While acoustic propagation modes exist in the air inclusions, these modes are weakly coupled to the elastic domain (and to water outside the PC), due to the large impedance mismatch, and do not contribute to the pressure wave propagation in the PC. As shown in Figure 4.2, including the air as a fluid in the unit cell simulation introduces localized acoustic modes in air. These modes, however, have a negligible effect on the elastic modes that dominate the response of the lens underwater.

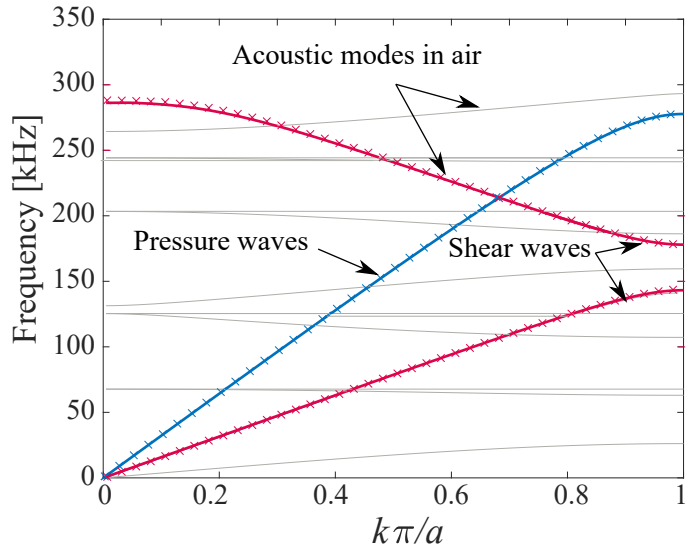


Figure 4.2: The effect of including air as an acoustic material on the bandstructure of the proposed unit cell. The bandstructure of the cell with air modeled as an acoustic domain is shown as solid lines while the model assuming air as a free boundary condition is shown as markers.

Figure 4.1a is obtained for a unit cell with periodicity $a = 3$ mm for different filling fractions ϕ defined as the volume of air inclusion to the total volume of the cell. The effective phase velocity of P-waves \tilde{c}_p and S-waves \tilde{c}_s are given by the relation $\tilde{c}_{p,s} = (2\pi f)/k_{p,s}$, where f is the frequency in Hz and $k_{p,s}$ is the wave number corresponding to the propagation mode. The refractive index of the PC with respect to water is defined as $n = c_w/\tilde{c}_p$, where c_w is the speed of sound in water. When the filling fraction of the air inclusions in the PC is increased, the effective P-wave velocity \tilde{c}_p decreases, i.e. the refractive index of the PC increases. The dependence of the PC refractive index on the frequency is shown in Figure 4.1b for different filling fractions. The refractive index profile is relatively flat at lower frequencies and increases rapidly as the frequency approaches the Bragg bandgap of the PC marked by the dashed line. As the filling fraction increases, the bandgap shifts to lower frequencies. As a result, the refractive index profile becomes steeper and hence less broadband. A target frequency of $f = 100$ kHz is selected so that a range of ϕ can be used to set the refractive index of the PC from $n = 0.7$ (for $\phi = 0$) to $n = 1.9$ (for $\phi = 0.9$) as shown in Figure 4.3a.

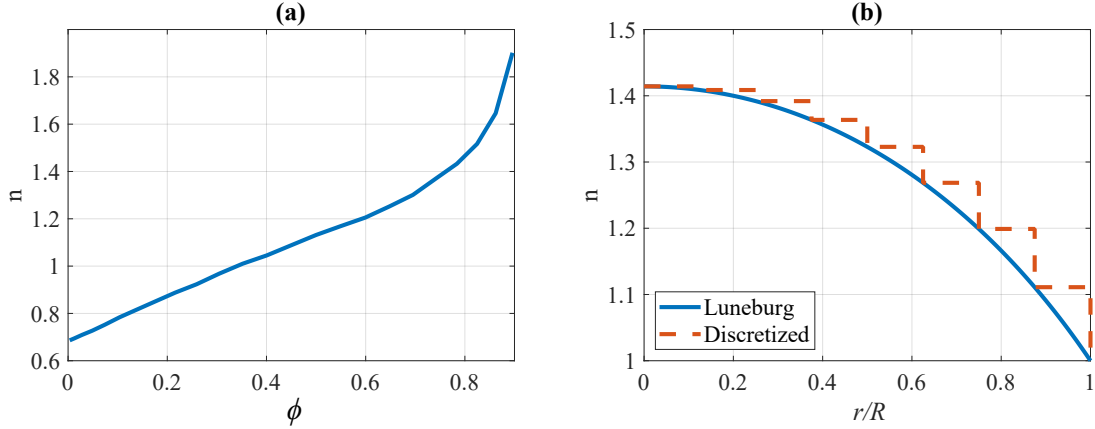


Figure 4.3: (a) PC refractive index versus the filling fraction at the target design frequency of 100 kHz. (b) Refractive index profile for a continuous Luneburg lens and the discretized GRIN-PC implementation. Simulations are for waves propagating in the ΓX direction.

4.1.2 Underwater Phononic Crystal Lens Design

The proposed PC was used to design and fabricate a 3D GRIN-PC lens based on the Luneburg lens profile (Figure 4.3b): $n = \sqrt{2 - r^2/R^2}$, where r is the distance from the center of the lens, and $R = 24$ mm is the radius of the lens which consists of 8 unit cells in the radial direction (Luneburg profile is normally omnidirectional, although this work explores the focusing of waves propagating in a single known direction as mentioned previously). In order to reduce the effects of discretization, the air inclusions were tapered to introduce a gradient in the filling fraction between neighboring cells. The performance of the lens was simulated using a coupled elastic-acoustic FEM implemented using Comsol Multiphysics. The lens was placed in water that was modeled as an acoustic domain with $\rho_w = 1000$ kg/m³ and $c_w = 1500$ m/s. Radiation boundary conditions were applied to the external boundary of the acoustic domain, and both elastic and acoustic domains were discretized so that there were at least 7 elements per wavelength at the highest excitation frequency. An acoustic plane wave in the form of a Gaussian pulse with a center frequency of 100 kHz and bandwidth of 30 kHz was provided as the excitation through one of the acoustic domain boundaries and the time-domain response of the lens was computed.

An ideal 3D implementation of the Luneburg lens would be of spherical shape; however, since the lens background is an elastic domain, the shape of the interface between the lens and water will affect its performance due to mode conversion between pressure and shear waves. The interface domain will also have a strong effect on how well incident acoustic waves in water couple to P-waves inside the lens. In addition to the common spherical shape for the Luneburg lens, a cube-shaped lens was constructed by setting \tilde{c}_p of the unit cells outside the spherical profile to match c_w . The cube shape provides a flat interface with incident plane waves and thus would provide better coupling to P-waves inside the lens domain.

The effect of mode conversion on the performance of the lens is analyzed in Figure 4.4 and Figure 4.5 by comparing the focusing power of cube and sphere-shaped lenses made

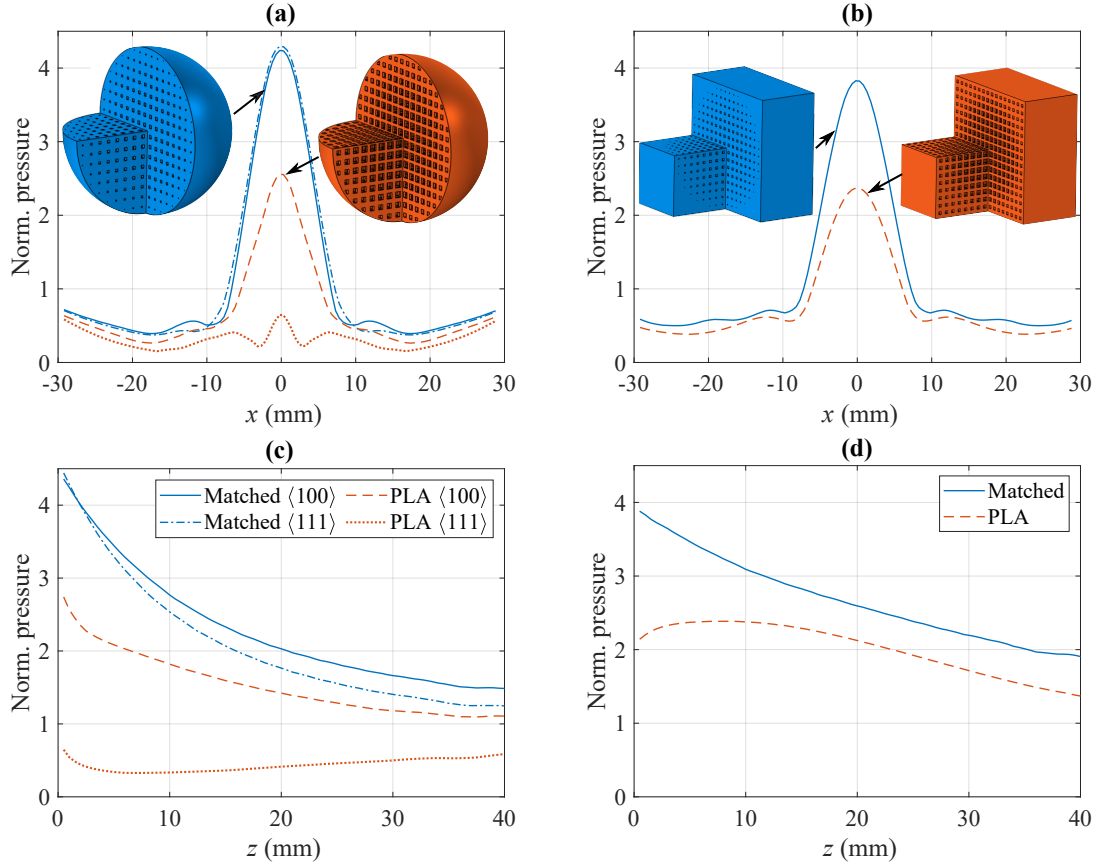


Figure 4.4: Normalized pressure field in the focus region of a sphere-shaped lens design (left column) and a cube-shaped lens design (right column). The pressure is shown in (a&b) the propagation (z) direction and (c&d) the focal plane (x -direction). Two different materials for the lens are considered: an elastic material matched to water ($c_p = 1500$ m/s, $c_s = 700$ m/s) shown in solid blue and PLA shown in dashed red. For the sphere lens, the pressure field for waves incident in the TX $\langle 100 \rangle$ direction are compared to TX $\langle 111 \rangle$ incidence. The internal structures of the lens designs are shown in the insets of (a) and (b).

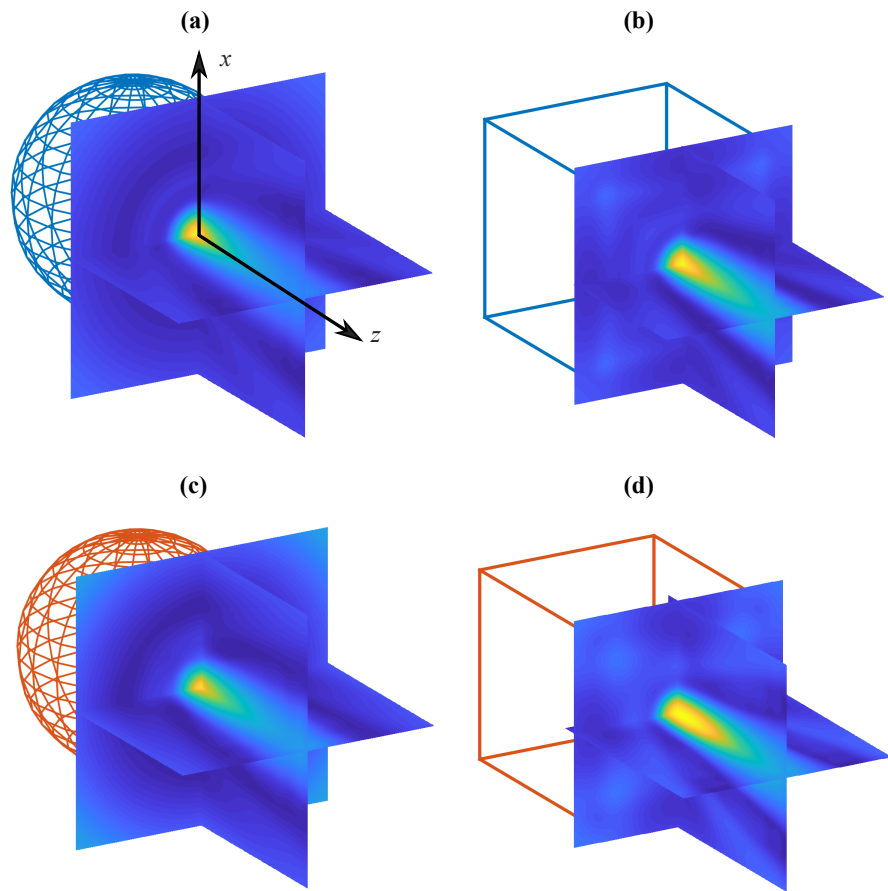


Figure 4.5: Cross-sections of the peak pressure field distributions behind the cube and sphere lenses (i.e. in the focus region) are shown for the (a&b) matched material and (c&d) PLA.

of PLA to lenses made of a material with P-wave speed matched to water ($c_p = c_w$) and much lower S-wave speed ($c_s = 700 \text{ m/s}$) i.e. softer material. Overall a soft lens with P-wave speed matched to water outperforms a lens made of PLA; yet, PLA and similar stiff polymer materials are more practically used as filaments in FDM 3D printers. For the matched material, the shape of the lens had a limited effect on its performance as shown by comparing the solid blue curves in Figure 4.4a&b, as well as Figure 4.5a&c. However, when PLA is considered, the shape of the lens has a strong effect on the focal spot size as shown by comparing Figure 4.5b&d. The focal spot size (i.e. neck of the focus) is much larger for the cube-shaped lens even though the pressure amplitude is comparable in both cases. This indicates that a spatially wider high-pressure region is enabled by the cube PLA lens compared to its spherical counterpart.

The effect of varying the direction of incident plane waves was also considered in Figure 4.4a&c. Plane waves propagating in the $\Gamma\text{X} \langle 100 \rangle$ direction of the lattice are compared to waves propagating in the $\Gamma\text{R} \langle 111 \rangle$ direction. For the matched lens, the direction had a limited effect on the lens performance, i.e. the lens retains the omnidirectional characteristics of the Luneburg lens. For PLA on the other hand, the performance of the lens deteriorates in the $\langle 111 \rangle$ direction. Since PLA has c_p greater than water, larger filling fractions are required to realize the Luneburg profile, as shown in the insets of Figure 4.4a. The larger filling fraction introduces larger anisotropy in c_p , which causes the Lens profile to change depending on the direction of incidence. This anisotropy, however, could be reduced by considering a more complex lattice structure [212] ideally, which would bring fabrication challenges as a compromise.

4.1.3 Experimental Validation

A proof of concept cube-shaped PLA lens was fabricated using a desktop 3D printer (Ultimaker 3), with standard printing parameters, and a printing layer height of 0.2 mm. The lens consists of 16x16x16 (4096) unit cells with a lattice parameter of 3 mm, yielding the

overall dimensions of 48.8 mm x 48.8 mm x 48.8 mm. It was designed to achieve focusing around a target frequency of 100 kHz. The external surface of the lens was sealed with a subwavelength 0.4 mm wall of 3D-printed PLA to avoid any leakage.

The internal structure of the fabricated lens was scanned using a Scanco uCT50 micro-computed tomography (micro-CT) X-ray imaging system. Figure 4.6c&d show the internal structure of the lens with the gradient variation of the air inclusions size. The corners of the cubic structure were rounded to a radius of approximately 0.5 mm, which was expected since sharp corners are hard to realize using common 3D printing techniques. Some small voids were also observed in the PLA domain, which is another limitation of the FDM printing technique used. Nevertheless, since the unit cell is much smaller than the incident wavelength ($a = 0.2\lambda$ where $\lambda = 15$ mm is the wavelength in water at 100 kHz), minor defects are expected to have a limited effect on the overall performance of the device.

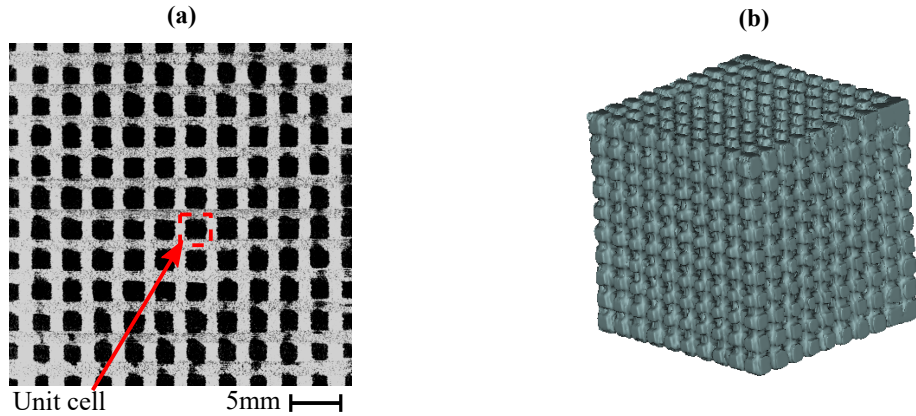


Figure 4.6: (a) X-ray scan of the internal structure at the midsection of the 3D-printed lens. (b) 3D reconstruction of an X-ray scan of the inner 10 cells of the lens.

The pressure field in the focus region behind the lens was mapped experimentally by mounting the lens inside a water tank with a scanning hydrophone setup as shown in Figure 4.7a&b. A hydrophone (B&K 8103) was used as a spherical point source transmitter to enable plane waves in its far-field. The distance between the transmitter and the center of the lens was set to 280 mm (18.6λ) to ensure sufficient distance for plane wave formation. Another receiver hydrophone (RESON TC 4013) was mounted on a precision stage for

accurate 3D positioning. The acoustic center of the hydrophone is located 10 mm from its tip, which limits the minimum distance for measuring the pressure field from the surface of the lens to this distance. The transmitter hydrophone was excited with a 30 kHz bandwidth Gaussian pulse centered at 100 kHz using an arbitrary signal generator (HP 33120A) and a piezoelectric amplifier (Khron-Hite 7500). The receiving hydrophone was used to scan the pressure field behind the lens by connecting it through a pre-amplifier (Stanford Research Systems SR560) to a digital oscilloscope (HandyScope HS3). The control of the stage, excitation signal, and the data acquisition were integrated into a single LABVIEW program on a laptop which was connected to both the oscilloscope and the signal generator.

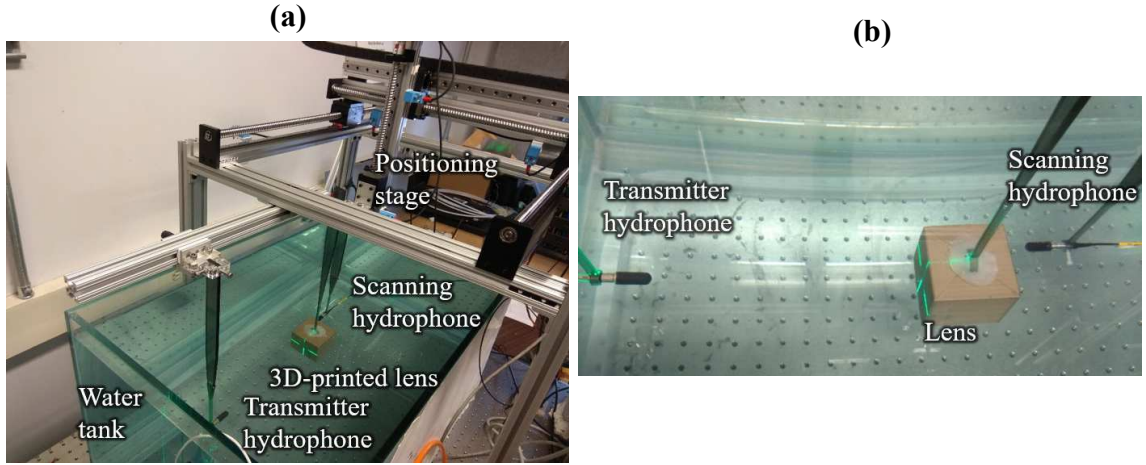


Figure 4.7: (a) Overview and (b) close-up view of the experimental setup for plane wave generation and for scanning the pressure field behind the 3D-printed PC lens.

The lens was excited with a plane wave traveling in the positive z -direction, and the peak of the pressure field behind the lens was plotted in Figure 4.8 for three perpendicular measurement planes. The pressure field obtained experimentally (shown in Figure 4.8a) is in excellent agreement with that obtained numerically (shown in Figure 4.8b). A clear 3D wave focusing is observed by comparing the experimental and numerical results to the baseline experimental pressure field without the presence of the lens (shown in Figure 4.8c).

The pressure fields at the focal plane along the x -direction as well as along the propagation direction (z -direction) are shown in Figure 4.9. The experimental and numerical

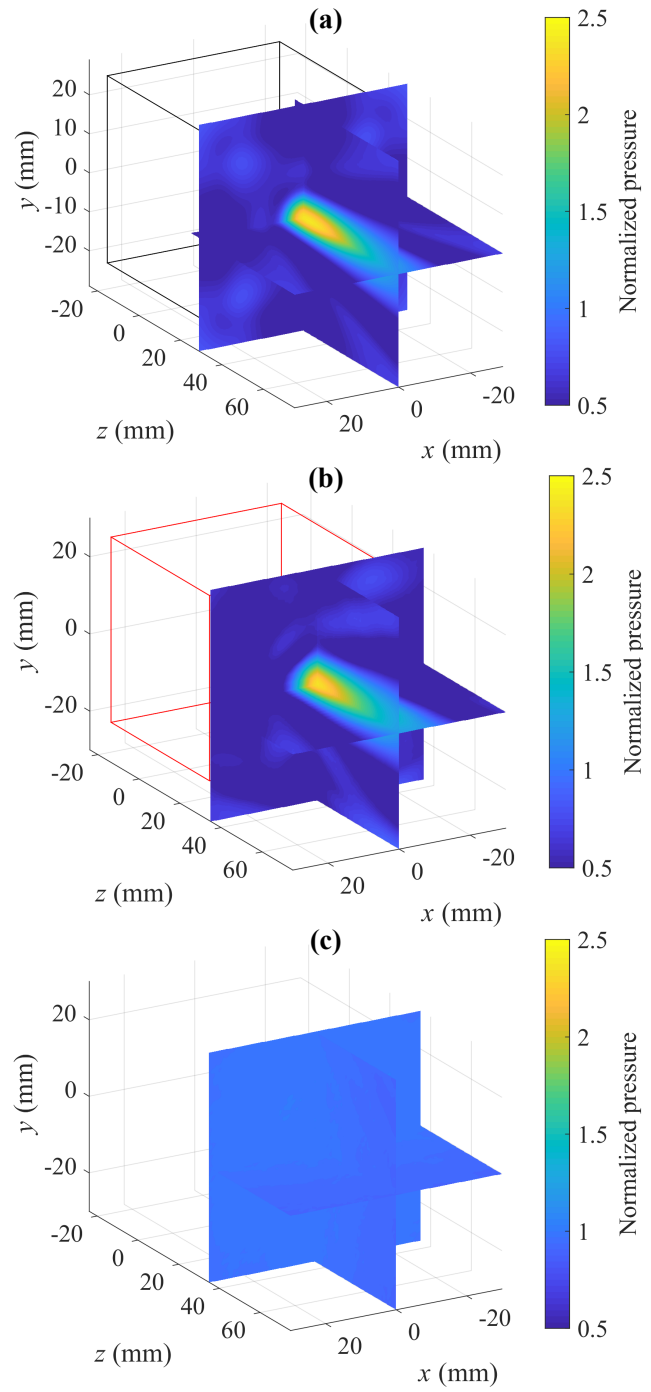


Figure 4.8: Peak pressure field behind the lens (focus region) revealing a substantial enhancement of the pressure intensity via focusing: (a) Numerical (FEM) simulation, (b) experimental data (via scanning using the hydrophone), and (c) baseline case without the lens (obtained from experiments).

results are in excellent agreement, especially near the focal point. The inhomogeneities observed in the microstructure of the printed lens (Figure 4.6a) had little effect on the performance of the lens which was expected since their dimensions are much smaller than the wavelength at the target frequency. It should be noted that accurate identification of material properties of the printed material is important for designing the structure of the lens as well as getting good agreement between experimental results and numerical predictions.

A peak amplification factor of 2.38 is observed experimentally which corresponds to a power gain of 5.7 and a 7.5 dB gain compared to the field without the presence of the lens. Higher amplitude gains were shown numerically (up to a factor of 4.25 as shown in Figure 4.4a); however, further tuning of the filaments/3D printing processes might be needed to achieve this performance.

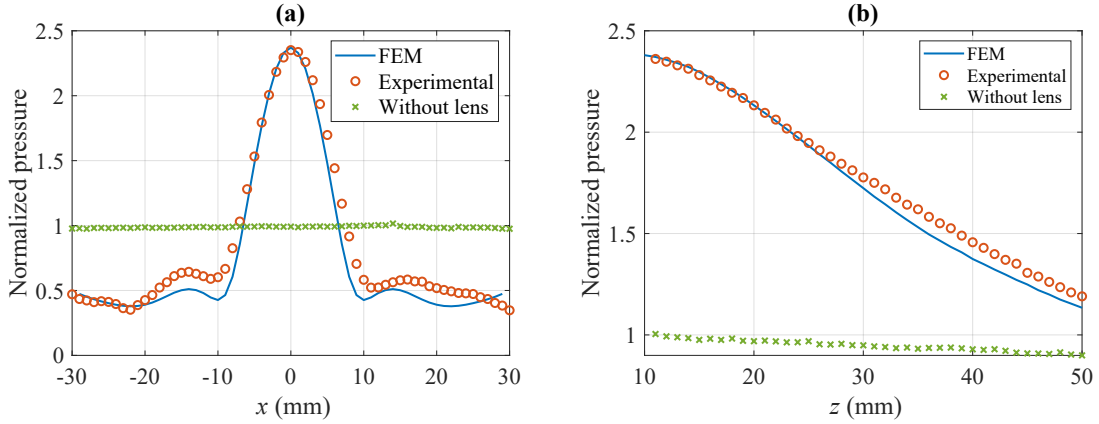


Figure 4.9: Comparison of the experimental and numerical pressure distributions along the (a) x -axis of the focal plane normal to the propagation direction, and along (b) the z -axis (in the propagation direction). The baseline case without the lens is also shown for reference.

4.2 Underwater Power Transfer Enhancement Using GRIN-PCs

The developed lens could be used to enhance the power transferred by a UPT system. In addition to focusing incident acoustic waves on the receiver, the lens enhances the directivity of a point source transmitter placed at its focal point. The GRIN-PC, in this case, collimates the radiated waves from the transmitter and improves its directivity as shown in

Figure 4.10a. An ideal Luneburg lens with a large aperture compared to the wavelength converts a point source placed at its focal point to plane waves at the opposing side (conversely to focusing incident plane waves with ray tracing arguments). When the aperture of the lens is comparable to the wavelength, as in the current implementation of the lens ($\lambda = 15$ mm while $R = 24$ mm), the finite aperture acts as a piston radiator instead of generating pure plane waves as shown in Figure 4.10.

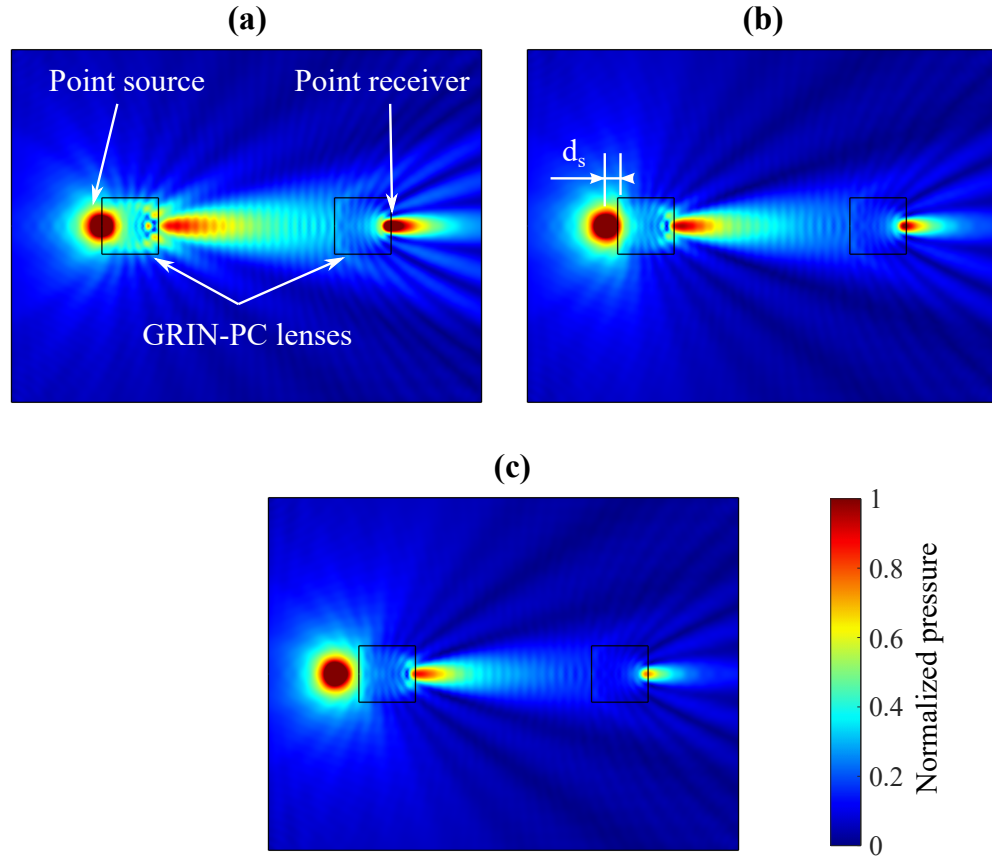


Figure 4.10: Normalized pressure field at 100 kHz for two GRIN-PC lenses used for enhancing the acoustic power delivered from a point source to a point receiver. The field is obtained numerically using a 2D acoustic FEM. The distance between the point source and the lens is varied between (a) $d_s = 0$, (b) $d_s = 10$ mm, and (c) $d_s = 20$ mm.

The directivity of the new aperture depends on its size, the frequency of operation, as well as the distance between the point source and the lens as shown in Figure 4.10a-c. The further the point source is from the lens, the closer the natural focus of the aperture gets to the opposing side of the lens. This could be leveraged to tune the directivity of a hybrid

transmitter consisting of a point source and a GRIN-PC lens. The receiver lens, on the other hand, is far enough from the transmitter that the focal point remains at the natural location regardless of the transmitter's directivity.

The two-lens acoustic power transfer system was experimentally tested using the setup shown in Figure 4.11. The power transferred between two RESON TC 4013 hydrophones was enhanced using two GRIN-PC lenses identical in geometry to the lens discussed in Section 4.1.2. The new lenses were printed with further optimized 3D-printing process parameters and a finer layer printing height (0.1 mm). By design, the hydrophones are omnidirectional around 100 kHz, so they approximate an acoustic point source at this frequency. The source hydrophone was excited with a wideband Gaussian pulse centered at 90 kHz with 70% bandwidth. A frequency of 90 kHz was chosen to excite the hydrophone in its flat band, since its frequency response has a cut-off frequency near 120 kHz. The voltage signal from the receiver hydrophone was recorded with a Tektronix TDS5034B oscilloscope with an input impedance of $1 \text{ M}\Omega$. The distance between the hydrophones and the lenses was kept to a minimum; however, the acoustic center of the hydrophone (the piezoelectric element) was 10 mm from its tip which makes it the minimum distance that could be practically achieved.

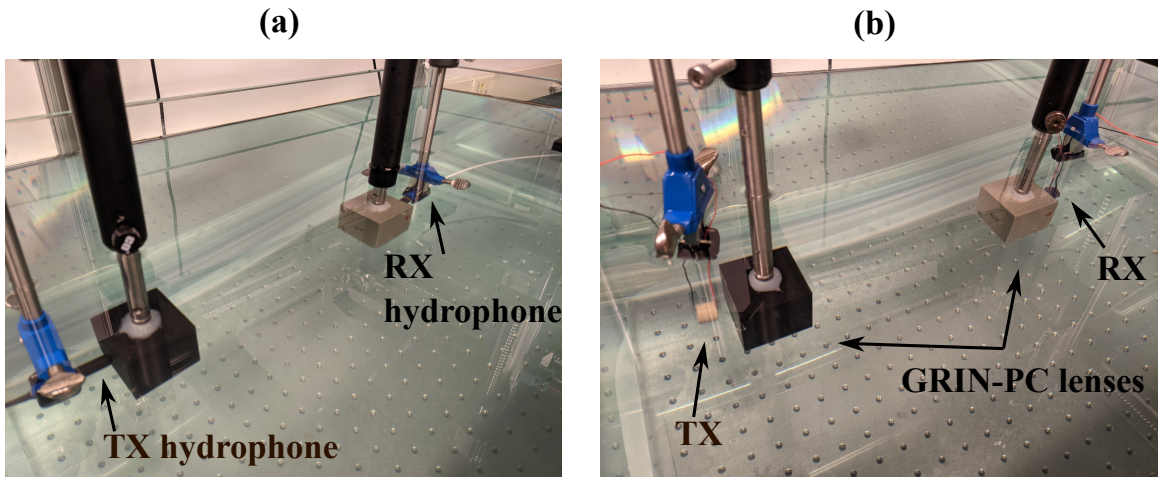


Figure 4.11: Experimental setup for measuring the received power enhancement of a two-lens GRIN-PC power transfer system. (a) Hydrophones are used as a point TX and point RX. (b) Piezoelectric transducers are used as TX and RX.

The hydrophones were separated by 250 mm which is the maximum distance achievable before reflections from the water surface of the tank started interfering with the direct pulse from the TX. The received electric power was recorded first without the presence of the lenses, then with one lens at the transmitter, with one lens at the receiver, and finally with two lenses simultaneously. The normalized power spectrum of the received signal for each case is shown in Figure 4.12a. An order of magnitude increase in the received power is observed when each lens was introduced to the system. The introduced lenses significantly improved the directivity of the source and focused the power at the receiver boosting the power at the receiver across a wide range of frequencies.

The power gain, shown in Figure 4.12b, shows that the lens at TX introduced a larger power gain for frequencies between 70 kHz and 90 kHz. The lens at RX had more gain at higher frequencies between 90 kHz and 120 kHz. The overall power gain of the system peaked between 90 kHz and 100 kHz which is the frequency range targeted by the lens design. A filtered time signal around 90 kHz with 10% bandwidth is shown in Figure 4.12c. Compared to the baseline case without the lenses, the signal shows a significant improvement in the delivered power when the GRIN-PC lenses are introduced.

The TX and RX hydrophones were then replaced with waterproofed piezoelectric transducers to increase the amount of power that can be transmitted through the system as shown in Figure 4.11b. The used piezoelectric transducers (Steminc SMC14H12111) had a diameter of 14 mm and a thickness of 12 mm. The impedance of the transducers was measured previously as discussed in Section 2.2.4 of Chapter 2, and it exhibits a resonance frequency around 95 kHz as shown in Figure 2.4. The transducers have a moderate aspect ratio, and thus the pressure field generated by them has low directivity as shown in Figure 4.13a. The GRIN-PC lenses could then be used to improve the directivity of TX and focus acoustic power on RX enhancing the power delivered by a system consisting of the two transducers as shown in Figure 4.13b.

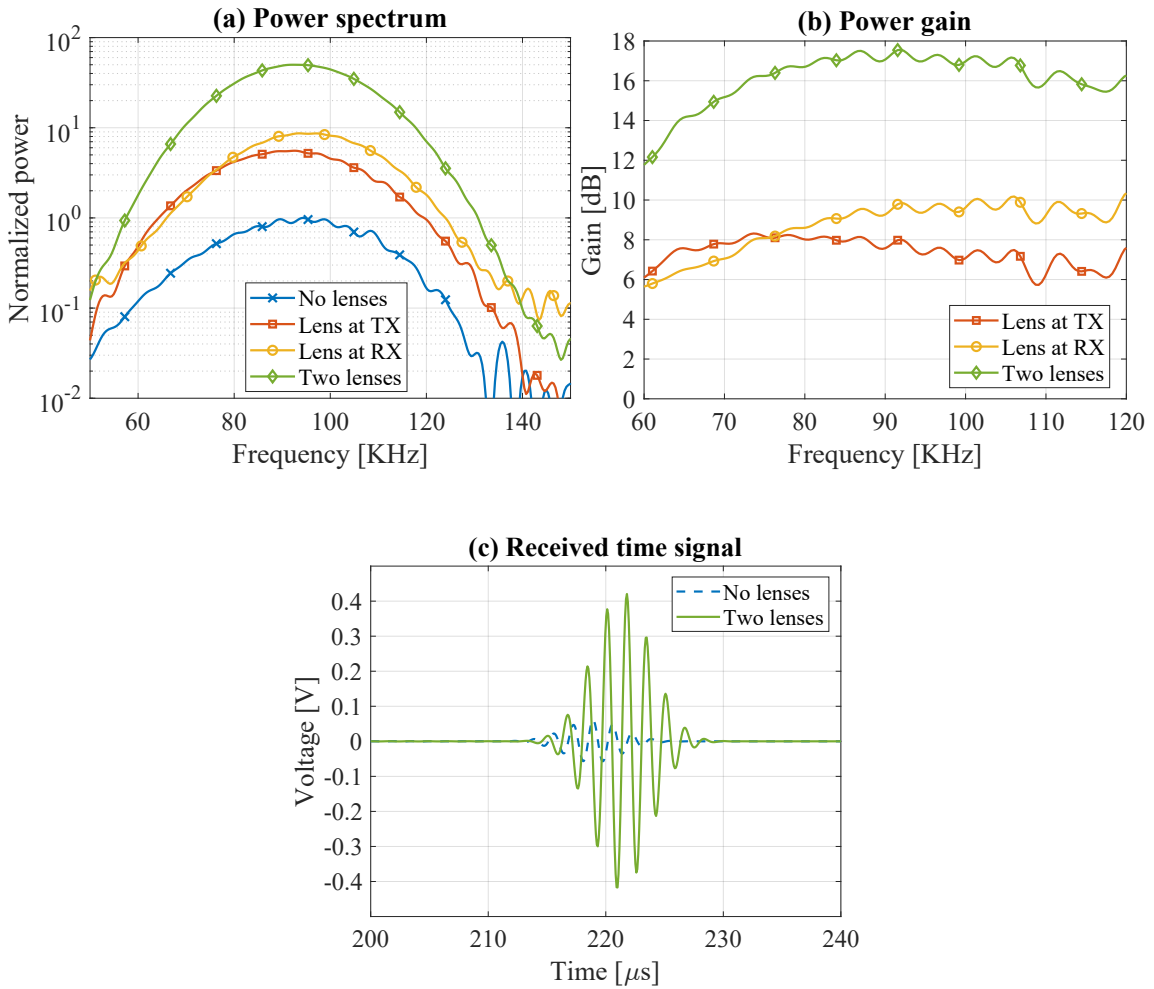


Figure 4.12: (a) Power spectrum (power spectral density) of the voltage signal generated by the RX hydrophone when the TX hydrophone was excited by a 10 V voltage Gaussian pulse centered around 90 kHz. (b) The power gain due to the introduction of the lenses with respect to the received power without the lenses. (c) Filtered received voltage pulse showing the gain in amplitude when the lenses were introduced. The received signal was filtered from 85 kHz to 95 kHz to obtain this pulse response.

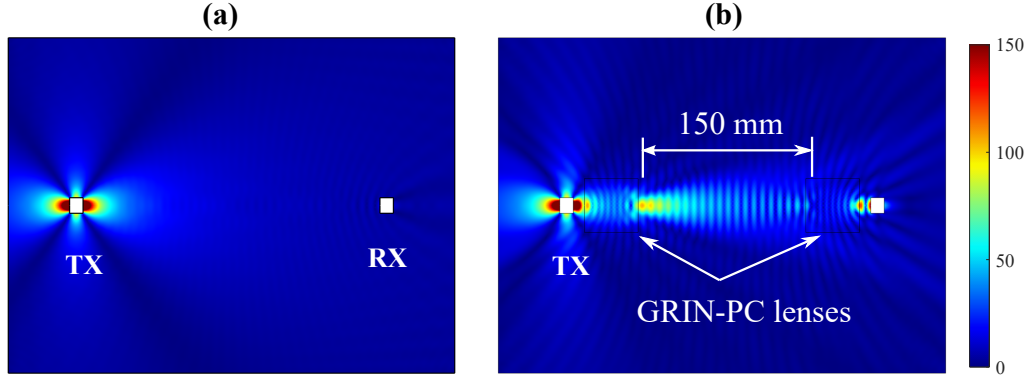


Figure 4.13: Normalized pressure field at 100 kHz for (a) the selected piezoelectric transducers without the lens. (b) The effect of introducing the GRIN-PC lenses on the pressure field of the transducers. The field is obtained numerically using a 2D acoustic FEM.

The TX transducer was excited with a 200 V Gaussian pulse through the piezoelectric amplifier connected to the signal generator. The pulse was centered around 90 kHz with a bandwidth of 70%, however, the actual bandwidth measured at RX was much lower due to the limited bandwidth of the transducers as shown in Figure 4.14a. The RX transducer was connected to a $2800\ \Omega$ resistor selected to match the electrical impedance of the transducer at resonance as previously shown in Figure 2.4.

Since the piezoelectric transducers' directivity is better than a point source (the hydrophones), the received power of without the lenses is larger. Nevertheless, introducing the lenses to the system increases the received power by an order of magnitude. The size of the transducer is also larger than the focal spot of the lens, and hence the power gain is lower when comparing Figure 4.14b to Figure 4.12b.

The voltage output by the system for a 10% wide Gaussian pulse centered about 90 kHz is shown in Figure 4.14c. The peak output voltage increases from 1.25 V without the lens to 4.5 V improving the output power of the system nearly 15 fold from $250\ \mu\text{W}$ up to $3.6\ \text{mW}$. It is worth mentioning that the design of the piezoelectric transducers used was not optimized. The output power could be improved further through proper backing, as well as electrical and acoustical impedance matching of the transducers.

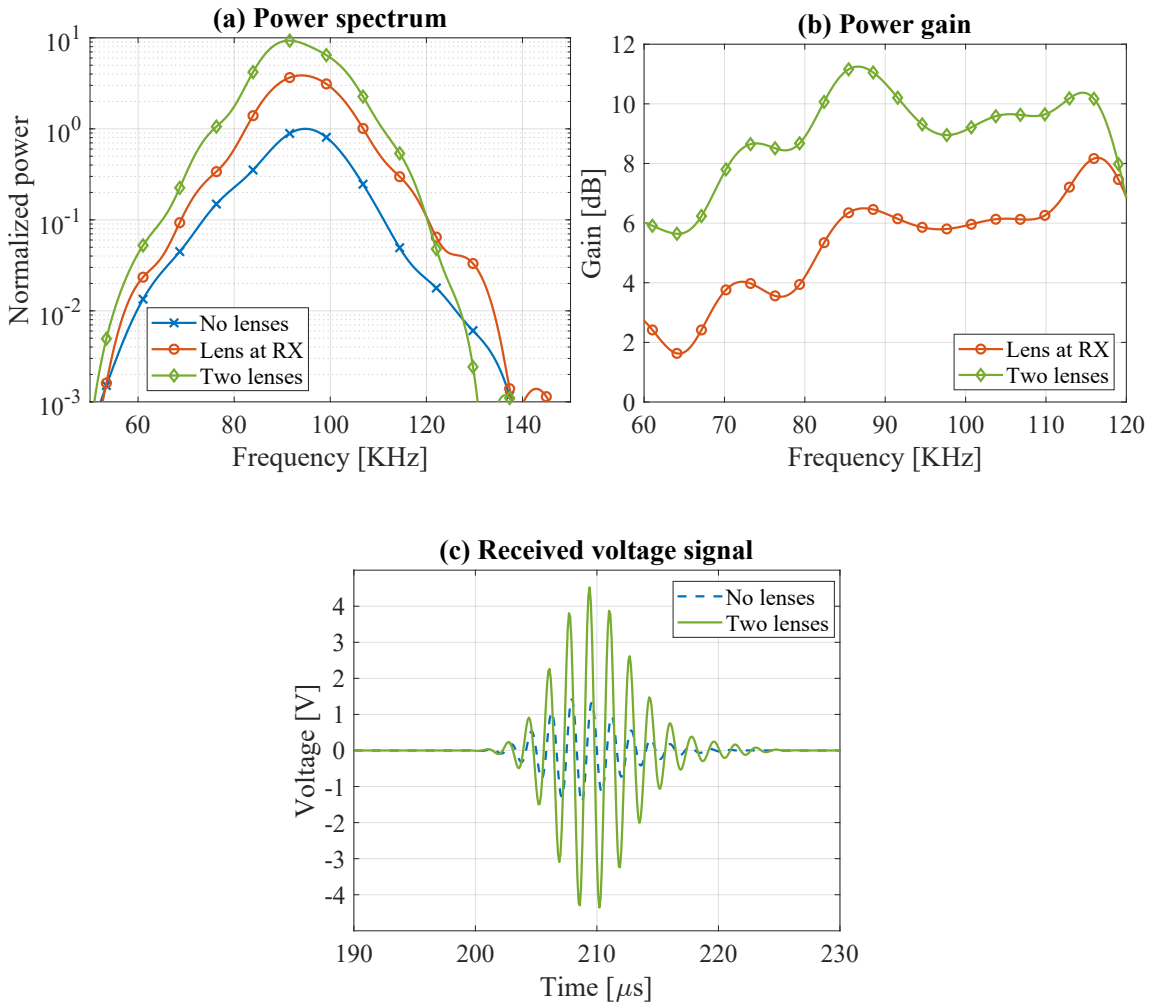


Figure 4.14: (a) Experimental power spectrum (power spectral density) of the voltage signal generated by the RX piezoelectric transducer when TX was excited by a 200 V voltage Gaussian pulse centered around 90 kHz. (b) The power gain due to the introduction of the lenses. (c) Received voltage signal when TX was excited with a 10% bandwidth Gaussian pulse centered around 90 kHz.

4.3 GRIN-PCs for Focusing in Air

In this section, we design, analyze, and fabricate a GRIN-PC 3D lens to focus airborne audio-frequency acoustic waves at a piezoelectric transducer in order to enhance the electrical power delivered to a resistive load. In the following, first, the PC unit cell structure and characteristics are discussed in detail highlighting the sources of anisotropy that arise from the geometry of the PC. A 3D GRIN-PC lens is then designed, simulated, 3D-printed, and experimentally validated. The factors affecting the lens performance are discussed with the aim of maximizing the amplitude of the acoustic pressure intensity at the focal spot.

4.3.1 In-Air Unit Cell Analysis and Refractive Index Tailoring

A simple cubic unit cell consisting of a 3D-printed cross-shaped polymer structure in air is considered (inset of Figure 4.15a) with a lattice size of $a = 3\text{ mm}$. The unit cell is based on the structure proposed by Xie et al. [131], but with tapered links to avoid sudden changes in the link cross-section between two neighboring cells. Comsol Multiphysics [168] was used to construct an acoustic finite element model (FEM) for a single PC unit cell in order to obtain the dispersion curves as shown in Figure 4.15a. Air was modeled as a periodic acoustic domain with a speed of sound $c_{air} = 343\text{ m/s}$ and mass density $\rho_{air} = 1.14\text{ kg/m}^3$. Since the level of impedance mismatch between the polymer and air is several orders of magnitude, the polymer domain was assumed to be rigid and was modeled as internal hard acoustic boundaries. The volume filling fraction of the unit cell is defined as $\phi = (3ah^2 - 2h^3)/a^3$, representing the volume of the polymer to the total volume of the cubic cell. The effective speed of sound $c_{eff} = 2\pi f/k$ can be controlled by changing the value of ϕ which changes the slope of the dispersion relation as shown in Figure 4.15a, where f is the frequency in Hertz and k is the wavenumber. The effective refractive index of the unit cell in air, defined as $n = c_{air}/c_{eff}$, is shown in Figure 4.15b. For a constant filling fraction, the effective refractive index of the material becomes more frequency-dependent,

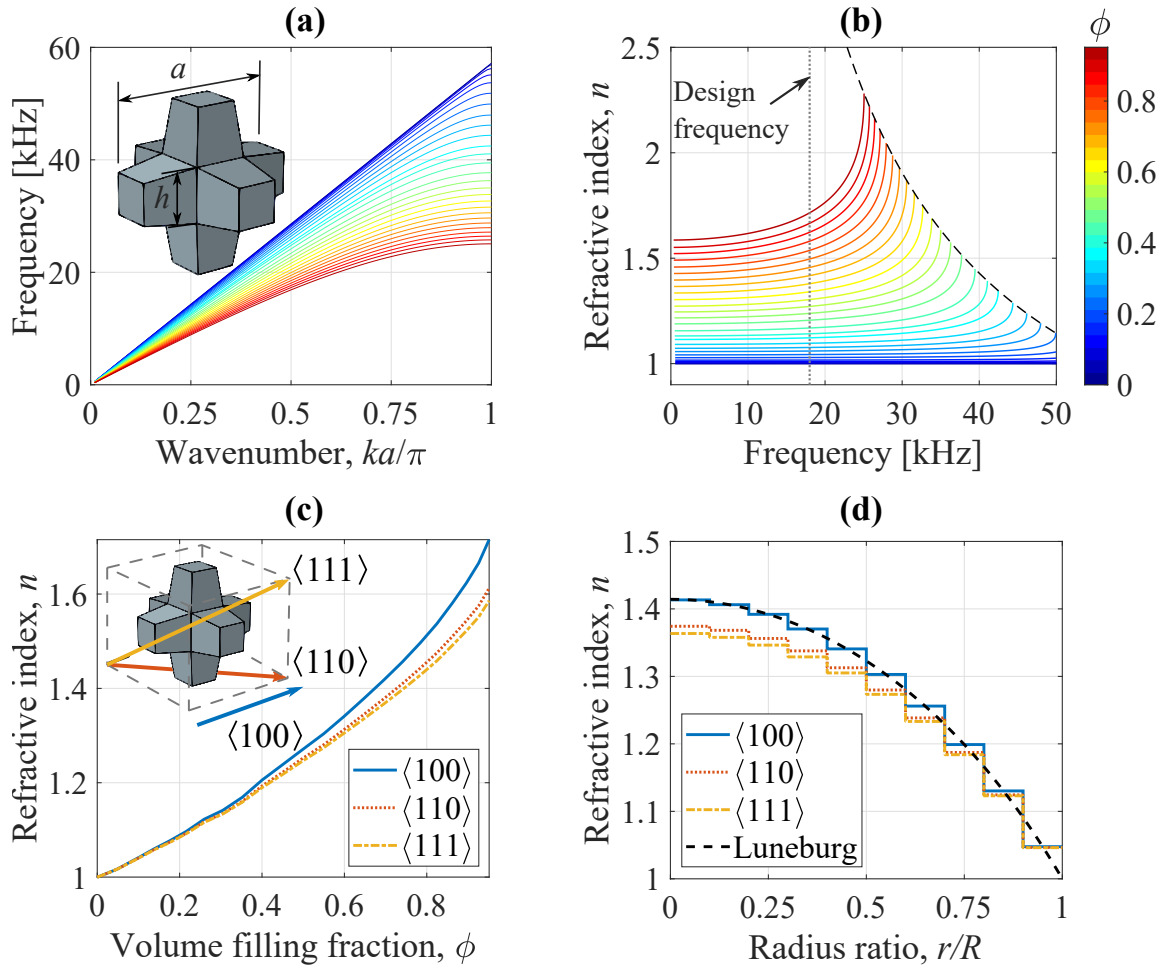


Figure 4.15: (a) Dispersion plots of a unit cell in the main direction of wave propagation for different volume filling fraction values (ϕ), i.e. different polymer to cubic unit cell volume ratios. (b) The effective refractive index of the PC versus frequency for different ϕ values. (c) Effective refractive index at the design frequency (18 kHz) versus ϕ for different directions. (d) Analytical refractive index profile of an ideal Luneburg lens versus the discretized profile used in the implementation of the GRIN-PC lens for different directions. The effective refractive index in the diagonal $\langle 110 \rangle$ and $\langle 111 \rangle$ directions are also shown.

i.e. less broadband, as the frequency increases (approaches the Bragg bandgap). The refractive index also becomes more frequency-dependent as the filling fraction increases. A frequency of 18 kHz was selected as a design frequency for the GRIN-PC lens, and the effective refractive index was plotted against the filling fraction in Figure 4.15c. Note that, Figure 4.15c is only valid at 18 kHz, but since the refractive index curve below this frequency is relatively flat for filling fractions of interest (below 0.7), it could be used to design broadband devices up to the design frequency. Figure 4.15c could be used to construct a desired GRIN-PC refractive index profile by choosing the filling fraction corresponding to the desired refractive index value. To study the directional dependence of the PC, its effective refractive index was calculated in directions $\langle 100 \rangle$, $\langle 110 \rangle$, and $\langle 111 \rangle$ as shown in Figure 4.15c. The specified directions were chosen since they represent extreme values with respect to the cubic symmetry of the lattice. As shown in Figure 4.15c, the refractive index of the PC is anisotropic (at the design frequency), and the degree of anisotropy is proportional to the filling fraction. The anisotropy arises from the simple cubic periodicity of the unit cell, as well as its geometry. As the polymer volume in the unit cell increases, the geometry becomes comparable to the effective wavelength of the propagating acoustic waves, giving rise to increased anisotropy as shown in Figure 4.15c.

The refractive index profile in direction $\langle 100 \rangle$ was used to construct a GRIN-PC lens with the Luneburg profile given by $n(r) = \sqrt{2 - (r/R)^2}$. The continuous analytical Luneburg profile, as well as the discretized refractive index in the main lattice directions, are shown in Figure 4.15d. The refractive index slightly deviates from the analytical profile for the $\langle 110 \rangle$ and $\langle 111 \rangle$ directions which reduces the performance of the lens in these directions. The GRIN-PC lens is thus expected to be omnidirectional, however with a slight variation in its performance depending on the direction. Moreover, this anisotropy could be further reduced by operating at lower frequencies or by using smaller unit cells.

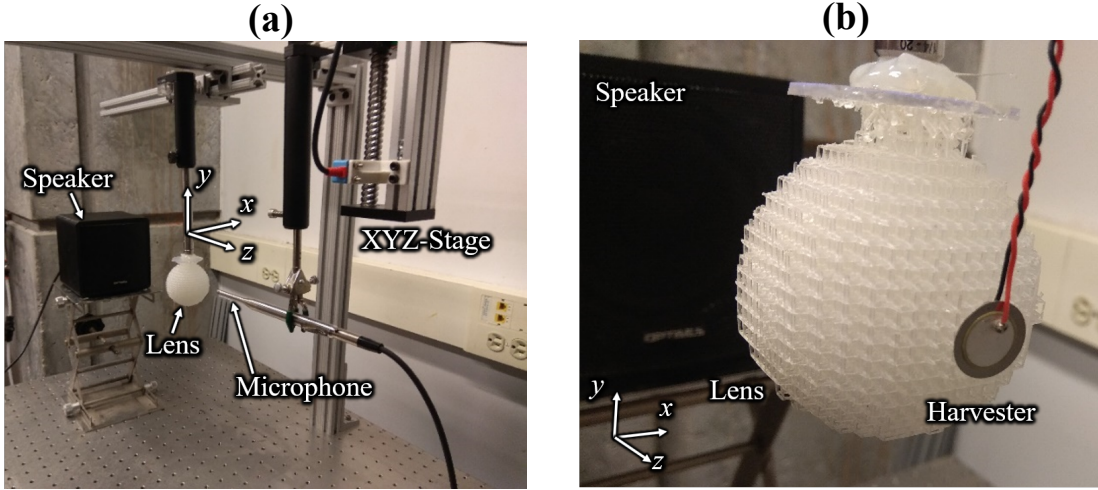


Figure 4.16: Experimental setup (a) for measuring the acoustic pressure field of the 3D-printed GRIN-PC lens (microphone mounted on an XYZ stage scans the pressure field) and (b) for measuring the electrical power enhancement of a piezoelectric receiver placed at the focal spot of the GRIN-PC lens.

4.3.2 In-Air Phononic Crystal Lens Design

The analytical profile was discretized for a unit cell of size $a = 3$ mm to construct a lens of radius $R = 30$ mm with 10 unit cells along the radius as shown in Figure 4.16. The lens was constructed by using Figure 4.15c to select the required filling fraction at each unit cell, and the cross-sections of the links between every two neighboring cells were tapered to reduce the effect of discretization between the neighboring unit cells.

On the wave propagation simulation side, a time-domain acoustic FEM was constructed to simulate incident plane waves on the lens. The lens was modeled as a hard boundary to an acoustic domain discretized with 7 elements per wavelength. The lens was ensonified with a plane Gaussian pulse centered at 18 kHz with 6 kHz bandwidth (BW), and the acoustic domain was surrounded with radiation boundaries to minimize wave reflections. A Courant-Friedrichs-Lowy (CFL) condition of 0.2 was used to select the proper time step for the simulation.

The designed lens was 3D printed using a Formlabs Form 2 stereolithography (SLA) 3D printer with a layer height of 100 μm and clear Formlabs resin. The scanning microphone

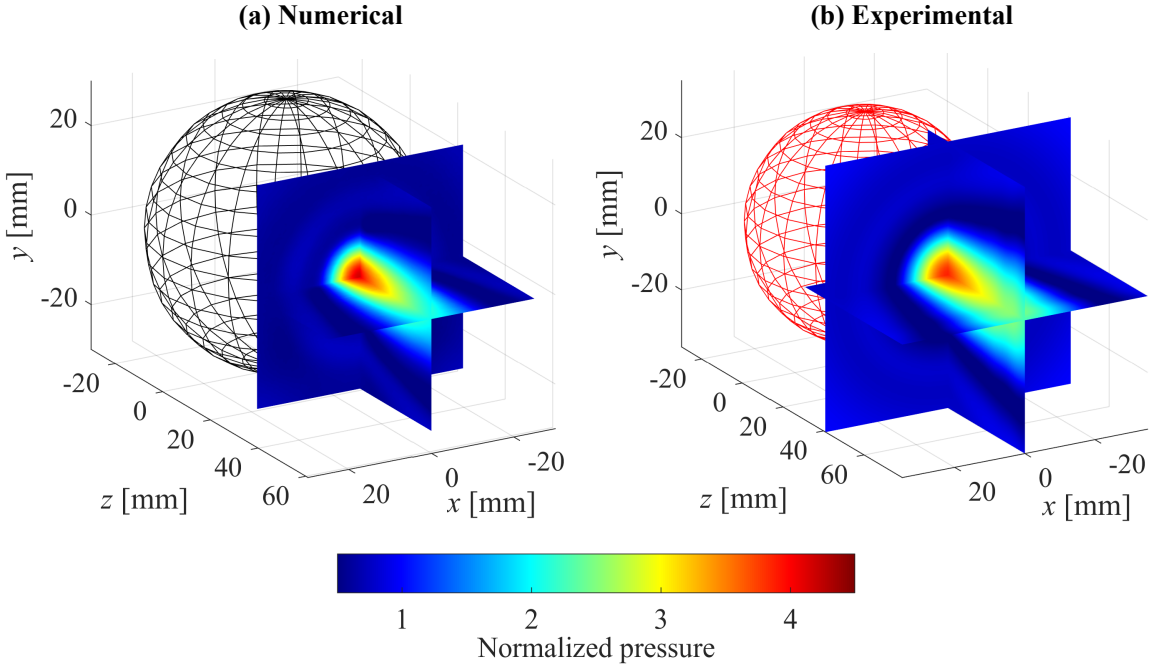


Figure 4.17: Normalized peak pressure field behind the lens obtained (a) numerically and (b) experimentally.

setup, shown in Figure 4.16a, was used to measure the pressure field behind the lens due to an incident plane wave. A speaker with a frequency range of 1 - 22 kHz was excited with the same Gaussian pulse as in the numerical simulations. A 1/4" free field Larson Davis 2520 microphone was mounted on an automated XYZ stage to scan the pressure field at three perpendicular planes behind the lens. The grid cover of the microphone was removed to ensure that the pressure field could be measured as close as possible to the back surface of the lens. The microphone signal was digitized with a Handyscope HS3 oscilloscope, and a LABVIEW program was used to synchronize the excitation of the speaker with data acquisition. The received signal was time-gated to avoid including any wall or other hard surfaces reflections in the measurement. The pressure field was measured once with the lens present, then with the lens removed to obtain the normalized pressure gain due to the presence of the lens. Subsequently, the lens was rotated to simulate plane waves incident from a different angle and the measurement was repeated.

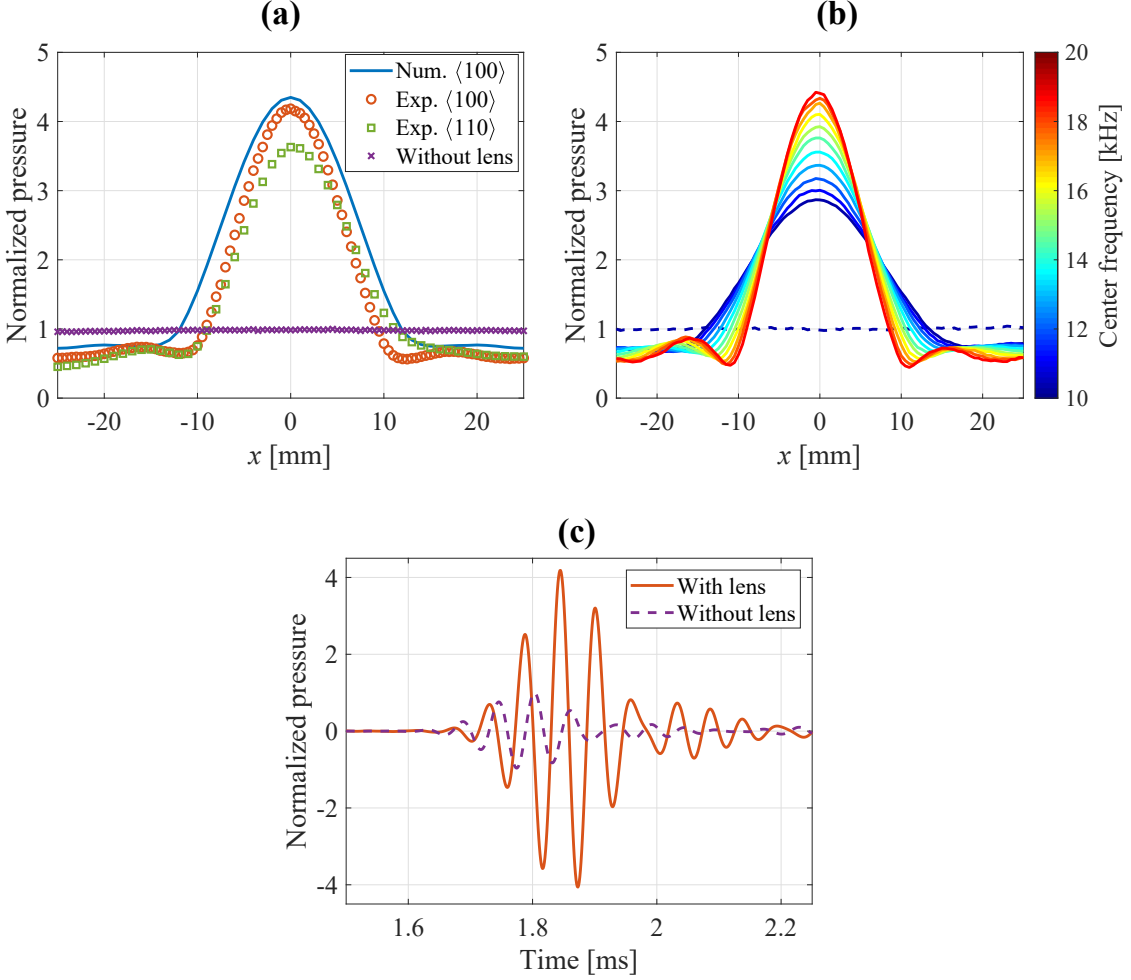


Figure 4.18: (a) Normalized pressure at the focal plane obtained numerically and experimentally. The experimental pressure fields are shown for waves propagating in the directions $\langle 110 \rangle$ and $\langle 100 \rangle$ with respect to the PC lattice. (b) Normalized peak pressure obtained experimentally for different Gaussian pulse center frequencies. The bandwidth was kept constant at 6 kHz. (c) Time series for the pressure at the focal position of the lens compared to its absence. The case shown is for a pulse with 18 kHz center frequency.

4.3.3 Experimental Results

The peak pressure field of the lens is shown in Figure 4.17 at the focal spot of the lens with incident acoustic waves traveling in the positive z -direction (shown in Figure 4.16a). A clear focal spot is observed behind the lens, and the experimentally measured focal spot size and shape are in good agreement with the numerical predictions. The pressure field at the center of the focal plane is shown in Figure 4.18a. The experimental results show a narrower and lower amplitude at the focal spot than that predicted by the finite element simulations. The achieved gain is 6% lower than the predicted gain of 4.5 which is attributed to manufacturing tolerances of the 3D printing process as well as the directional pattern of the speaker. The results for $\langle 110 \rangle$ wave incidence show a reduction of 15% in the peak pressure amplitude compared to $\langle 100 \rangle$. This reduction is attributed to the inherent anisotropy in the PC which caused a deviation from the exact Luneburg profile in this direction as shown in Figure 4.15d.

The effect of changing the center frequency of the excitation was studied experimentally as shown in Figure 4.18b. The figure shows that the lens can be used to focus incident waves from frequencies lower than 10 kHz to frequencies higher than 20 kHz. However, more focusing is observed at higher frequencies, since the lens is diffraction limited. Figure 4.18c shows the experimental pressure time series at the focal position of the lens compared to the baseline case (in the absence of the lens). At the target design frequency (18 kHz), a pressure gain of 4.2 was observed in both the peak and RMS pressures at the focal positions. This corresponds to an increase in acoustic intensity (power) at the focal spot by a factor of 17.6. The pressure gain of the lens could be further improved by increasing the lens aperture (size) allowing for more energy to be directed toward the focal spot. However, this is typically bounded by the size limitations of the 3D printing process as well as the space available for the lens (to keep it compact in a given application).

4.4 Sound Power Enhancement using GRIN-PCs

To demonstrate the ability of the 3D GRIN-PC lens for sound power enhancement, a piezoelectric transducer was placed at the focal spot of the lens as shown in Figure 4.16b. The transducer was selected to operate near the center of the lens design frequency bandwidth around 15 kHz. It is a circular unimorph with an outer diameter of 13.5 mm with a substrate layer of thickness 0.2 mm made of stainless steel and a piezoelectric layer of thickness 0.15 mm and diameter 10 mm made of PZT-4. The mechanical quality factor of the receiver is $Q_m = 50$.

A frequency-domain piezoelectric FEM was constructed to predict the performance of the piezoelectric transducer. An axisymmetric FEM of the receiver was subjected to a uniform harmonic pressure of 30 Pa (≈ 120 dB, reference pressure: 20 μ Pa) and the output electrical power across different load resistance values was obtained in Figure 4.19. Two power peaks at 14.5 kHz and 15.5 kHz are observed representing the short and open-circuit resonance frequencies of the transducer. The output power is larger for resistance values closer to the open-circuit resonance (around $30\text{ k}\Omega$); however, the frequency bandwidth is narrower compared to the bandwidth of resistor values between $1\text{ k}\Omega$ and $10\text{ k}\Omega$.

The experimental setup shown in Figure 4.16b was used to measure the output power enhancement by the lens. The lens-receiver system was excited with a modulated Gaussian pulse generated through a loudspeaker. Three different pulses were used: the first pulse was centered around 15 kHz and had a bandwidth of 4 kHz which is much larger than the bandwidth of the transducer (around 500 Hz as shown in Figure 4.19). Additionally, two narrowband pulses (500 Hz bandwidth) centered around 14.5 kHz and 15 kHz were chosen to target the bandwidth of the receiver. The amplitude of the incident acoustic wave was kept constant for all pulses and was set to 30 Pa (≈ 120 dB) measured at the receiver location in the absence of the lens. A variable load resistor was connected to the receiver via two thin wires which were also used to suspend the transducer to emulate free

boundary conditions. The voltage generated across the load resistor was measured and used to calculate the output power from the receiver at different resistance values. The lens was then removed and the output power was measured again as a baseline to determine the power enhancement due to the presence of the lens.

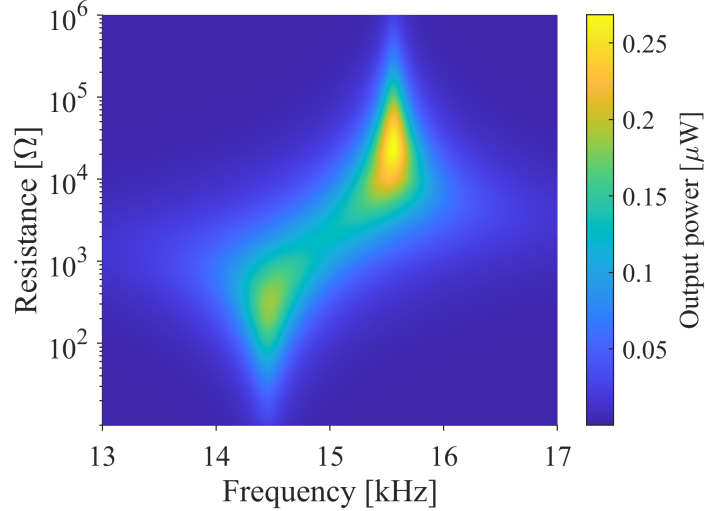


Figure 4.19: Simulated output power of the receiver when subjected to a uniform harmonic pressure of 30 Pa (≈ 120 dB). The power is plotted vs excitation frequency and load resistance.

The peak power generated for different resistor values and pulses of different center frequencies and bandwidth is summarized in Figure 4.20a. Clearly, the presence of the lens increases the electrical power delivered to the load by an order of magnitude as compared to the respective baseline case without the lens. The electrical power gain is slightly lower than the acoustic power gain [cf. Figure 4.18b squared] since the dimensions of the receiver are larger than the focal spot of the lens at these frequencies (i.e. the transducer was not optimized). For all resistance values, the electrical power output for the wideband pulse was lower than the narrowband pulses, which is expected, since the bandwidth of the transducer is limited to a narrow band of approximately 500 Hz as shown in Figure 4.19. A narrowband pulse centered at 14.5 kHz (close to the short-circuit resonance frequency) generated more electrical power at lower resistor values (closer to optimal short-circuit resonance load as expected [9]) compared to the 15 kHz pulse. A maximum power output of $1.2 \mu\text{W}$

was observed for the 15 kHz pulse at a load resistance of $6\text{ k}\Omega$ which is close to the optimal resistance value for the transducer employed. The voltage time series for this case is shown in Figure 4.20b.

It should be noted that the bandwidth of the lens-receiver system is mainly limited by that of the receiving transducer in this case, which can be further improved by using a transducer with larger bandwidth, such as those exploiting designed nonlinearities [213]. Moreover, the lens was designed for a peak performance near 18 kHz, while the receiver was chosen to operate around 15 kHz. It is possible to achieve a slightly better performance if the lens was designed at the same center frequency as the transducer (i.e. 15 kHz), however at the expense of reduced performance at higher frequencies.

4.5 Conclusions

Gradient index phononic crystals (GRIN-PCs) constructed from an air/3D printed polymer matrix were shown to focus energy efficiently in acoustic power transfer systems. This would allow for transmitting energy at lower frequencies thus experiencing lower attenuation. Two GRIN-PC lens designs were introduced for focusing and collimating acoustic waves in air and under water. The lenses improved the power output from piezoelectric receivers by at least an order of magnitude compared to the baseline cases.

The proposed underwater GRIN-PC lens does not require bulky or heavy inclusions to enable the required refractive index profile compared to the state-of-the-art designs that incorporate metals. Two GRIN-PC lenses designed for operation around 100 kHz were used to improve the power transmitted between two hydrophones by two orders of magnitude. A lens was used at the transmitting hydrophone significantly to significantly enhance its directivity and a second one at the receiver to focus energy at its location. The introduction of the lenses to a second underwater power transfer system consisting of two piezoelectric transducers enhanced the power output from the system 15 times from $250\text{ }\mu\text{W}$ up to 3.6 mW . The overall concept, beyond the specific lens design, may pave the way for

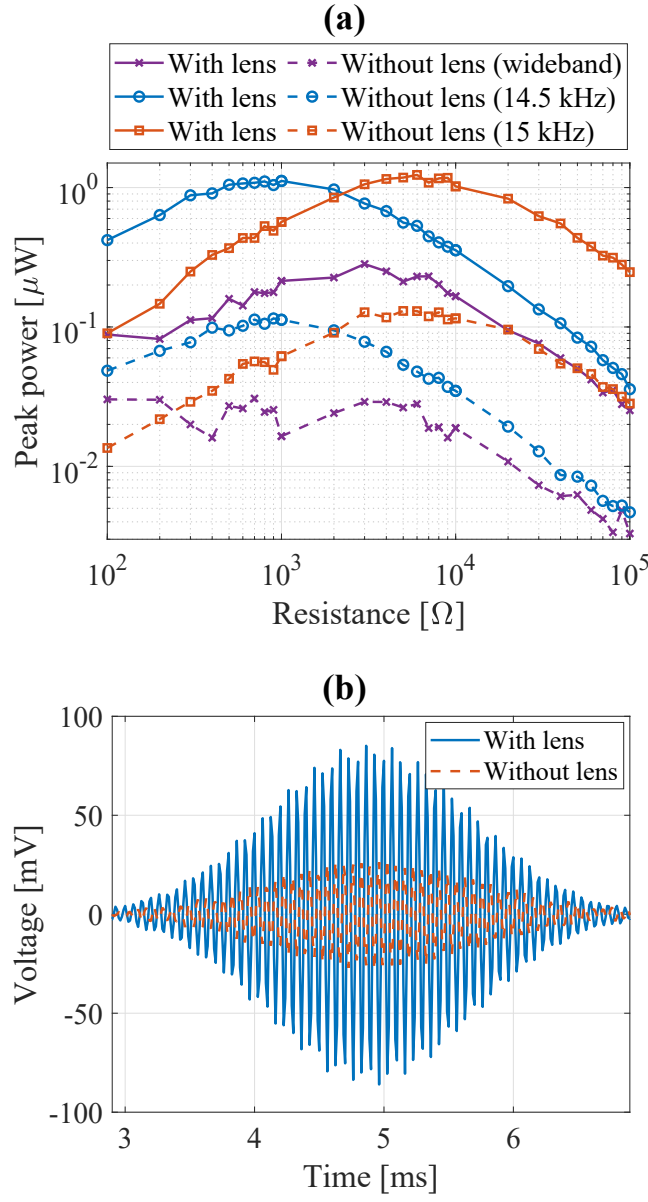


Figure 4.20: (a) Experimental peak received electrical power versus load resistance for an incident acoustic plane wave with a peak pressure of 30 Pa (≈ 120 dB) on the lens-receiver system. The output power from a pulse with center frequency $f_c = 15$ kHz and bandwidth $\text{BW}=4$ kHz (wideband) is compared to pulses with narrower bandwidth ($\text{BW}=500$ Hz) and centered around $f_c = 14.5$ kHz and $f_c = 15$ kHz. The baseline case without the lens is also shown for all the pulse shapes considered. (b) The voltage time series obtained experimentally for the maximum power output obtained with a pulse centered at $f_c = 15$ kHz with $\text{BW}=500$ Hz and a load resistance of $R_l = 6\text{ k}\Omega$ connected to the transducer.

leveraging 3D-printed GRIN-PC structures to achieve power or signal enhancement in applications spanning from underwater acoustic sensing to biomedical imaging.

A GRIN-PC lens was also designed for audio frequency acoustic waves and employed to enhance the electrical power of a piezoelectric transducer placed at its focal position. Pressure field measurements of the designed lens revealed its ability to focus acoustic power over a broad frequency range between 10-20 kHz, with acoustic power gain levels as high as 17.6 fold. As a result, the use of the lens enhanced the power delivered to a piezoelectric transducer by more than an order of magnitude as compared to the baseline case (without the lens). The system was able to generate $1.2 \mu\text{W}$ of electric power from 120 dB airborne sound, which is well above most sound energy harvester designs with similar scale that produce nano-Watt level power.

It should be noted that all the receivers discussed in this chapter were not acoustically, or electrically matched to water which limited their bandwidth, and the useful power that could be harvested from them. In the next chapter, the acoustical and electrical impedance matching for piezoelectric transducers are analyzed with the aim of minimizing the power reflection and increasing the bandwidth of the transducer.

CHAPTER 5

ACOUSTIC AND ELECTRICAL IMPEDANCE MATCHING FOR SIMULTANEOUS POWER AND DATA TRANSFER

Simultaneous communication and power transfer can be realized by varying the electrical impedance connected to a piezoelectric RX to switch between absorbing and reflecting incident ultrasonic waves. In a simultaneous power and data UPT system, the receiver is usually connected to an energy harvesting circuit used to power the digital electronics responsible for communication, sensing, and actuation, or to store the energy (either in a battery or a capacitor). The communication electronics then switches a transistor which is connected in parallel or series to the transducer. As shown in Figure 5.1, when the transistor is off no power flows to the electrical domain and most of the incident acoustic power is reflected. When the transistor is on, power flows to the energy harvesting circuit (rectification and voltage regulation), and thus a smaller portion of the incident power is reflected. The amount of power absorbed by the energy harvesting circuit, as well as the contrast between the reflecting and absorbing states (receiver sensitivity), depend on how well the electrical and acoustic domains are coupled (electrical and acoustic matching). However, little analytical work has been done to highlight the factors affecting this sensitivity.

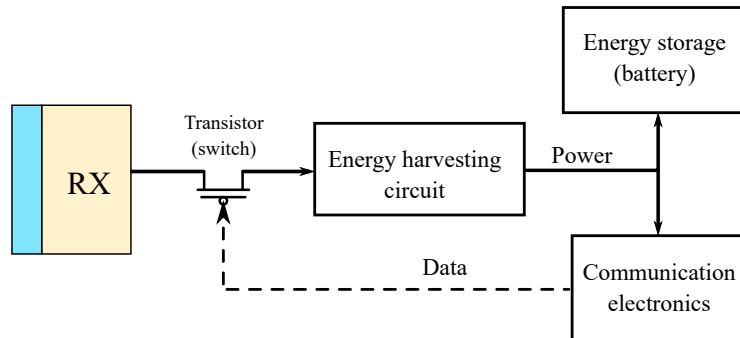


Figure 5.1: Basic implementation of a simultaneous power and data transfer UPT system.

Simultaneous power and data transfer impose new requirements on ultrasonic transducer design which are seldom discussed in the literature. In this chapter, these requirements and the design trade-offs associated with them are discussed. The factors affecting the transducer bandwidth (data transfer rate) and sensitivity such as electrical and acoustic impedance matching are analyzed analytically. Designs for optimizing power transfer and data transfer are developed analytically then tested experimentally. A new transducer design to achieve uninterrupted power harvesting with backscatter communication is introduced and experimentally verified. The design is based on dedicating frequency channels for power and data where the switching of the data channels has no effect on the power flow.

5.1 Modeling Reflection from a Piezoelectric Layer

Consider a transducer consisting of a thin piezoelectric disc poled in the thickness direction with thin electrodes plated on each face. The transducer is connected to an electric load with equivalent complex impedance Z_e as shown in Figure 5.2. The front face of the transducer is submerged under water and the back is in contact with a material with mechanical impedance Z_b . As discussed in Chapter 3, the impedance matrix (\mathbf{Z}) of the transducer relates the input forces (F_1, F_2) and voltage (V_3) to the velocities (v_1, v_2) and current (I_3), and is given by [176]:

$$\begin{bmatrix} F_1 \\ F_2 \\ V_3 \end{bmatrix} = -j \underbrace{\begin{bmatrix} Z_p \cot(k_p h_p) & Z_p \csc(k_p h_p) & \frac{\bar{h}_{33}}{\omega} \\ Z_p \csc(k_p h_p) & Z_p \cot(k_p h_p) & \frac{\bar{h}_{33}}{\omega} \\ \frac{\bar{h}_{33}}{\omega} & \frac{\bar{h}_{33}}{\omega} & \frac{1}{\omega C_p} \end{bmatrix}}_{\mathbf{Z}} \begin{bmatrix} v_1 \\ v_2 \\ I_3 \end{bmatrix}, \quad (5.1)$$

For brevity, the piezoelectric impedance matrix could be written as:

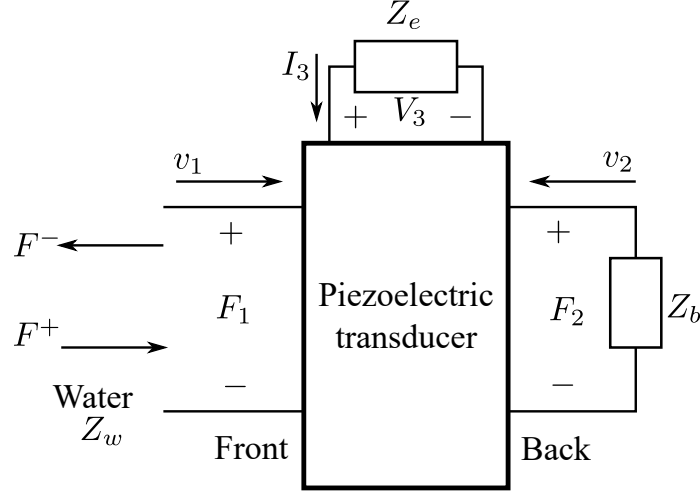


Figure 5.2: A schematic of a piezoelectric disc transducer represented as a 3-port element connected to arbitrary electrical impedance Z_e and an arbitrary backing layer with mechanical impedance Z_b .

$$\mathbf{Z} = \begin{bmatrix} Z_{11} & Z_{12} & Z_{13} \\ Z_{12} & Z_{11} & Z_{13} \\ Z_{13} & Z_{13} & Z_{33} \end{bmatrix} \quad (5.2)$$

The electrical and backing impedance yield the equations:

$$F_2 = -v_2 Z_b \quad (5.3)$$

$$V_3 = -I_3 Z_e \quad (5.4)$$

which could be substituted in Equation (5.2) to find the relation between the force and acoustic velocity at the front face of the transducer:

$$F_1 = \underbrace{\left(Z_{11} - \frac{Z_{12}^2 - \frac{Z_{12} Z_{13}^2}{Z_e + Z_{33}}}{Z_b + Z_{11} - \frac{Z_{13}^2}{Z_e + Z_{33}}} - \frac{Z_{13}^2 - \frac{Z_{12} Z_{13}^2}{Z_b + Z_{11}}}{Z_e + Z_{33} - \frac{Z_{13}^2}{Z_b + Z_{11}}} \right)}_{Z_{in}} v_1 \quad (5.5)$$

where Z_{in} is the input mechanical impedance of the transducer, and its value determines the amount of reflection from the transducer. Equation (5.5) shows that Z_{in} is a function

of the transducer geometry and material, the backing layer impedance, as well as the electrical impedance. By changing the electrical impedance connected to the transducer, its mechanical impedance changes which enables backscatter communication.

The amount of reflection could be determined by calculating the complex reflection coefficient of the piezoelectric transducer (S_{11}) by assuming incident and reflected mechanical waves F^+, F^- on the front face of the transducer as shown in Figure 5.2. The incident and reflected waves are related to the total force and velocity at the face by:

$$\begin{aligned} F_1 &= F^+ + F^- \\ v_1 &= \frac{F^+ - F^-}{Z_w} \end{aligned} \quad (5.6)$$

where $Z_w = \bar{Z}_w A_p$ and \bar{Z}_w is the characteristic acoustic impedance of water in Rayleighs.

The complex reflection coefficient is:

$$S_{11} = \frac{F^-}{F^+} \quad (5.7)$$

By solving Equation (5.5) and Equation (5.6) together, the complex reflection coefficient of the transducer with respect to water is given by:

$$S_{11} = \frac{Z_w - Z_{in}}{Z_w + Z_{in}} \quad (5.8)$$

5.2 Acoustic Reflection from a Piezoelectric Transducer

A basic piezoelectric transducer is first considered in order to visualize its reflection coefficient and analyze how it is affected by varying the electrical impedance. A piezoelectric disc transducer of thickness 2.1 mm and diameter 30 mm is chosen to target the 1 MHz frequency neighborhood. A hard PZT material is chosen for the transducer (PZT-4), since it is characterized by a high piezoelectric coefficient, and low damping to minimize the

Table 5.1: Material properties of PZT-4 used in the transducer 1D model

Property	ρ_p	c_p	\bar{h}_{33}	C_{33}^D	C_p	Q_m	$\tan \delta$
Unit	kg/m ³	m/s	kV/mm	GPa	nF	-	%
Value	7500	4706	2727	166	1.98	500	0.4

power dissipated in the transducer. The material properties of the piezoelectric layer are summarized in Table 5.1.

Air is chosen as the backing layer since it has a large impedance mismatch with water and PZT-4 so virtually no acoustic power is lost to the backside of the transducer¹. This helps improve the efficiency and the sensitivity of the transducer at the expense of limiting its bandwidth. However, the transducer bandwidth could be enhanced through simultaneous electrical and acoustic impedance matching which will be discussed in the following sections.

The amplitude of the acoustic reflection coefficient of the transducer in water for different resistive loads is shown in Figure 5.3a. The response of the transducer is narrowband, and it is sensitive to the resistive load connected to it which is a common characteristic of unmatched piezoelectric transducers. The resistive sweep shows that the transducer absorbs most of the incident acoustic waves at a narrowband near 1 MHz when a resistance of 10Ω is connected across its terminals. A similar response is observed at 1.2 MHz with a 500Ω load. These two frequencies are commonly referred to as the short circuit (SC) and open circuit (OC) resonance frequencies of the transducers which can be deduced if we consider the electrical input impedance of the transducer shown in Figure 5.3b. The resonance frequencies occur when the electrical input impedance of the transducer is real

¹The backing layer of commercial transducers designed for imaging applications is usually made from a lossy material with impedance close to PZT. The material is chosen to increase the bandwidth of the transducer at the expense of lower sensitivity. Nearly half the input power to the transducer is lost to the backing layer in this configuration.

(i.e. phase is zero). The resistance at these frequencies corresponds to the resistive load which is needed to match the acoustic domain to the electrical domain.

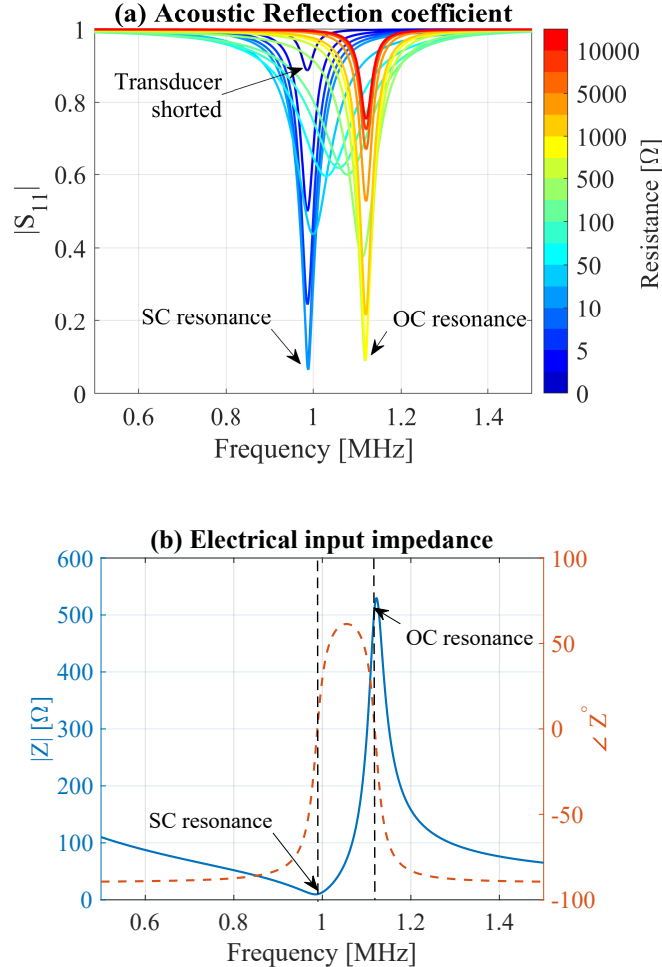


Figure 5.3: (a) Analytical acoustic reflection coefficient of an air-backed 1 MHz piezoelectric transducer submerged in water and connected to a resistive load ranging from 0-10 k Ω . (b) Electrical input impedance of the transducer with the front face submerged in water.

It worth noting that the reflection coefficient is not one for all frequencies when the transducer is shorted as shown in Figure 5.3a. Even though a shorted transducer does not convert power to the electrical domain, it still absorbs some of the power near its resonance due to the presence of mechanical and dielectric losses.

Figure 5.4a shows the reflected signal from the transducer when a broadband acoustic pulse (bandwidth $BW = 50\%$) centered around the SC resonance ($f_c = 988$ kHz) is incident on it. The reflected signal is shown for a 9 Ω resistor (SC resonance resistance

) and a very large resistance ($1 \text{ M}\Omega$) which are connected to the transducer to switch between absorbing incident power and reflecting it. Since the response of the transducer is narrowband as shown in Figure 5.4b, most of the power is reflected and only a small portion corresponding to the transducer bandwidth is absorbed. This causes the reflected time signals to have elongated oscillations, and the difference in the reflected pulse between the two states to be minimal.

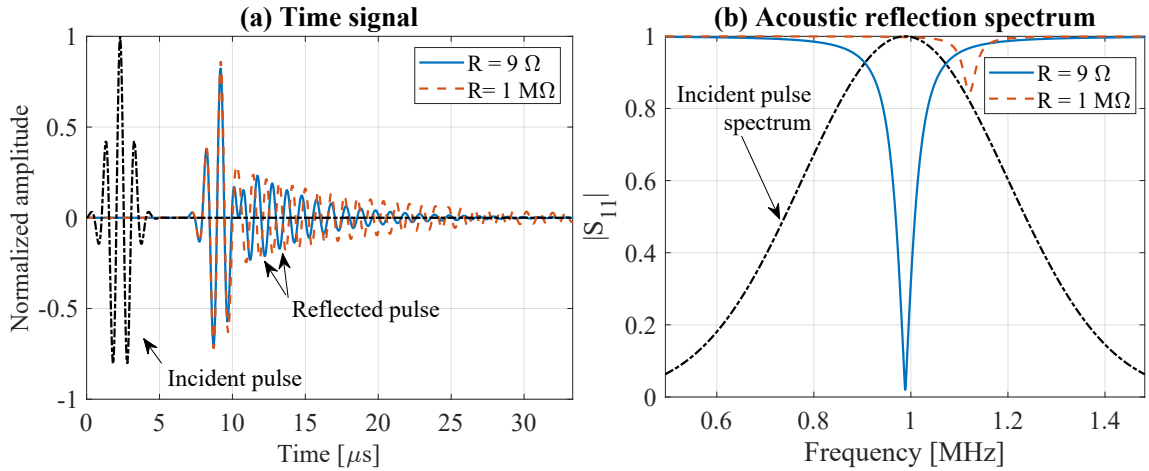


Figure 5.4: (a) Time history of a normalized broadband ultrasonic Gaussian pulse ($f_c = 998 \text{ kHz}$, $BW = 50\%$) incident on the front face of an air-backed transducer. The reflected pulse when the transducer is connected to the SC resonance resistance (9Ω) is compared to that when a $1 \text{ M}\Omega$ is connected. (b) The acoustic reflection coefficient of the transducer with respect to water when the different electric loads are used. The normalized frequency spectrum of the incident pulse is also shown.

When a narrowband pulse (bandwidth 5%) is incident on the transducer as shown in Figure 5.5, the difference between the 9Ω (matched resistance) and the $1 \text{ M}\Omega$ reflections is more pronounced. The contrast improves using a narrower bandwidth signal; however, this comes at the expense of longer time between pulses, and hence a lower data rate.

The considerations for power transfer are different than data, since power is commonly sent as a continuous wave (CW) excitation (i.e. at a single frequency). Assuming the load circuit has an impedance close to the SC resonance resistance of the transducer, almost none of the incident acoustic power is reflected and most of the power is delivered to the electric load. This is confirmed by plotting the acoustic to electrical transmission efficiency

η_{Tr} as shown in Figure 5.6. The transducer power conversion efficiency is given by:

$$\eta_{Tr} = |S_{21}|^2 \frac{Z_1}{Z_2} \quad (5.9)$$

where Z_1 is the mechanical impedance of water, Z_2 is the connected electrical impedance, and S_{21} is the complex transmission coefficient discussed in Section 3.1. From Figure 5.6, the air-backed transducer has a power conversion efficiency $\eta_{Tr} = 94\%$ at 988 MHz when delivering power to the optimized load of 9Ω .

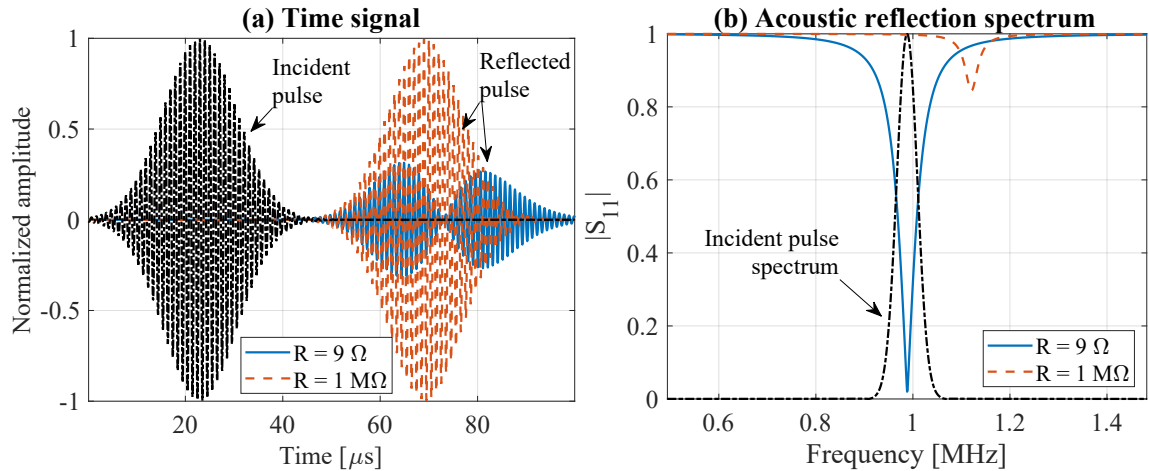


Figure 5.5: (a) Time history of a normalized narrowband ultrasonic Gaussian pulse ($f_c = 998\text{ kHz}$, $BW = 5\%$) incident on the front face of an air-backed transducer. The reflected pulse when the transducer is connected to the SC resistance (9Ω) is compared to that when a $1\text{ M}\Omega$ is connected. (b) The acoustic reflection coefficient of the transducer with respect to water when the different electric loads are used. The normalized frequency spectrum of the incident pulse is also shown.

5.3 The Smith Chart

The Smith chart is a useful tool for visualizing how well a port of a system is matched to a particular reference impedance. It helps visualize and facilitate the impedance matching process whether a broadband match is needed or the matching is intended for a single frequency. Although the Smith chart is common in elementary RF textbooks [162, 179], the chart is rarely seen in the acoustics literature perhaps due to the limited options available

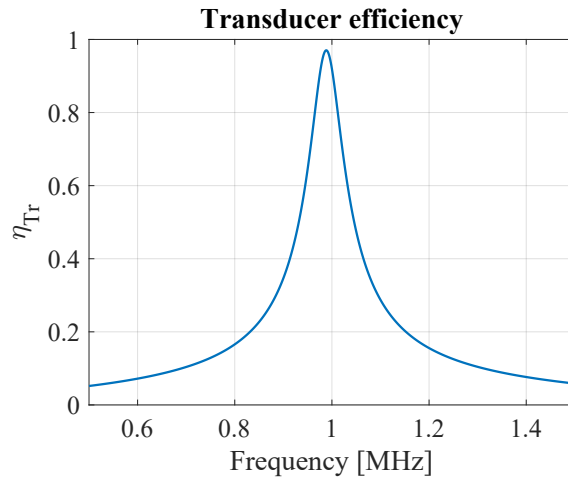


Figure 5.6: Acoustic to electric transmission efficiency for an air-backed transducer placed in water and connected to a 9Ω resistive load.

for acoustic impedance matching (mostly limited to quarter-wavelength matching layers). However, in electromechanical systems such as those involving piezoelectric transducers, it has been used to match transducers to electrical and acoustic domains since elements from both domains could be used simultaneously to impedance match a transducer [214].

The Smith chart (Figure 5.7) is an XY-plot of the real and imaginary components of the complex reflection coefficient of a port (S_{nn}). Since the magnitude of the reflection coefficient cannot be greater than one, all the possible values that it could take are inside the unit circle, and thus the shape of the chart is circular. A reflection coefficient value close to the origin of the chart represents low reflection, and thus a better match to the reference impedance. This reference impedance is commonly chosen to be 50Ω in RF circuits; however, it could be set to the resistance of any electric load that needs to be powered. For acoustic ports, the reference impedance could be chosen as the mechanical impedance of the medium in which the transducer will operate such as water, tissue, or metal for example.

The goal of any impedance matching effort is to minimize the value of the reflection coefficient by adding electrical or mechanical elements that would shift the impedance of the system towards the center of the plot. The horizontal line in the middle of the chart

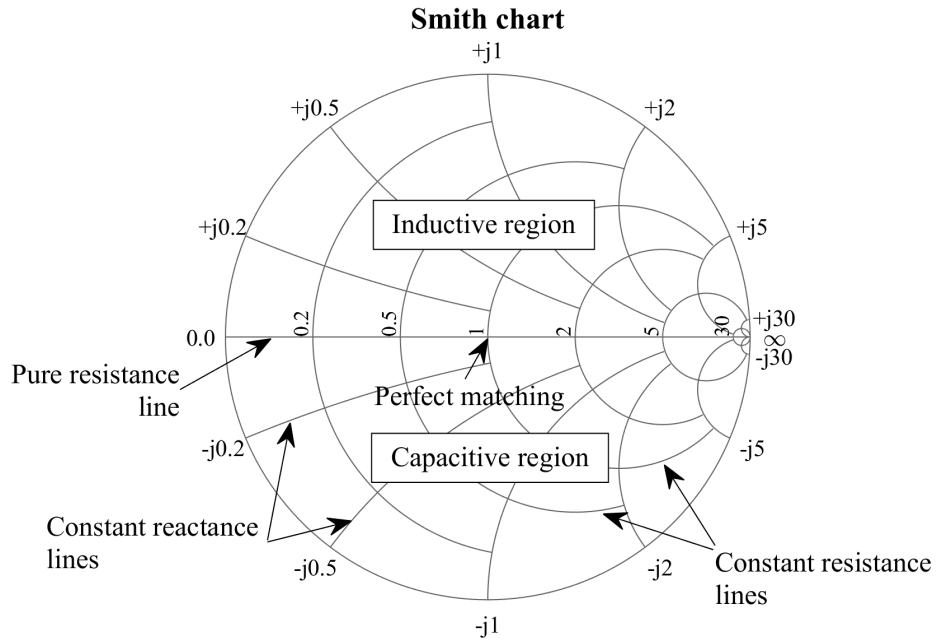


Figure 5.7: Fundamentals of the Smith chart.

represents a purely resistive impedance, while the top and bottom halves represent inductive and capacitive impedance values respectively. Lines of constant resistance, reactance, conductance, and susceptance can be shown on the chart to guide the impedance matching efforts. All the values displayed on the chart are normalized with respect to the chosen reference impedance. For more information on the Smith chart, please refer to Ref. [215] for a comprehensive discussion.

5.4 Simultaneous Acoustic and Electrical Impedance Matching

The air-backed transducer discussed in Section 5.2 is revisited in this section from a Smith chart perspective. The goal is to identify the issues limiting broadband operation then modify the design to achieve better performance.

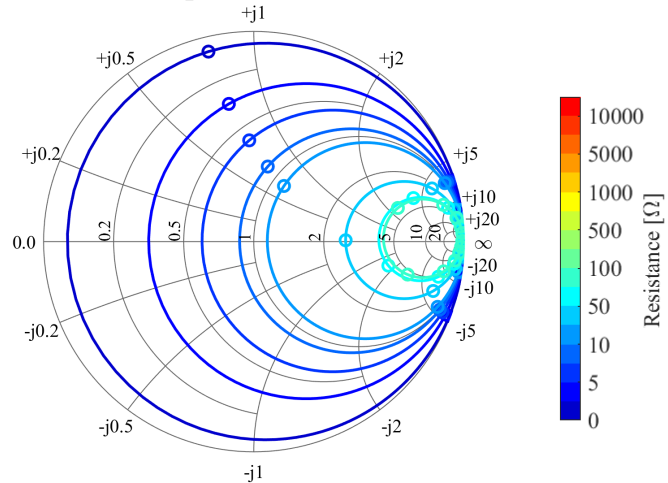
The Smith chart for the reflection from the acoustic port of the transducer is shown in Figure 5.8 for a range of resistive loads connected to the electrical port. The charts in

Figure 5.8 are normalized with respect to the impedance of water which means that the center of the plot represents an impedance matched to water (i.e. zero reflection). The resistive load connected to the electrical port was swept between 0 and 10 k Ω to show its effect on the acoustic reflection. The chart was split into two subfigures (Figure 5.8a&b) for easier visualization as the trends for the reflection coefficient for near SC resistance values (0-75 Ω) shown in Figure 5.8a are reversed compared to near OC resistance values (100-10 k Ω) shown in Figure 5.8b. The resistive sweep shows that there is an optimum resistance between 75 Ω and 100 Ω at which the variation (spread) of the input acoustic impedance of the transducer is minimum. However, this optimum resistance value would match the transducer to a piezoelectric medium which is why a circle surrounding the normalized impedance of 20 (close to 35 MRayl) is formed. The curves close to the SC and OC resistance (close to 10 Ω and 500 Ω) cross the resistance axis near the origin of the plot, and therefore, the transducer is matched to water at these particular resistance/frequency combinations. The matching is, however, very narrowband and a slight variation in operating conditions might shift it to other frequency/resistance combinations.

A similar observation can be reached if we examine the reflection from the electrical port of the transducer on the Smith chart as shown in Figure 5.9 when the acoustic port is connected to water. The electrical port shows a large circle in the Smith chart indicating a resonant behavior in the system. The curve intersects the resistance axis at two points corresponding to the SC and OC resonances.

The large size of the S_{22} circle complicates any electrical matching efforts in this configuration since inductive as well as capacitive impedance values need to be matched at different frequency values. In order to reduce the variation of the electrical impedance, the acoustic port needs to be better matched to water. This can be realized using one or more quarter wavelength matching layers as commonly done in literature [214].

(a) Acoustic port S₁₁ (low elec. res.)



(b) Acoustic port S₁₁ (high elec. res.)

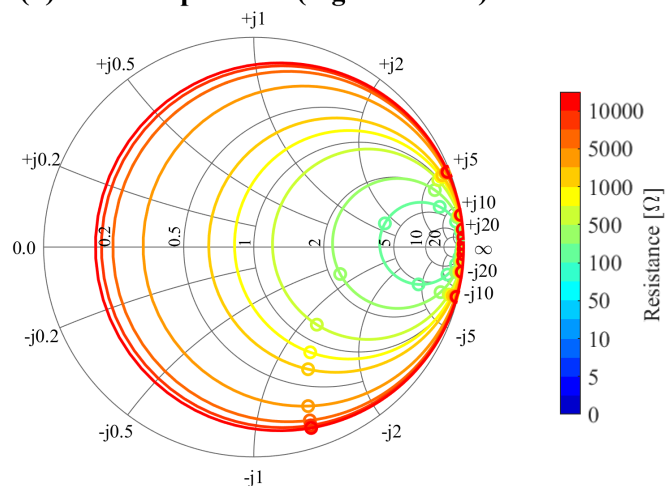


Figure 5.8: Smith chart of the air-backed transducer acoustic reflection coefficient S_{11} with respect to water when the electric resistance connected to the transducer varies (a) from 0-75 Ω and (b) from 100-10 000 Ω

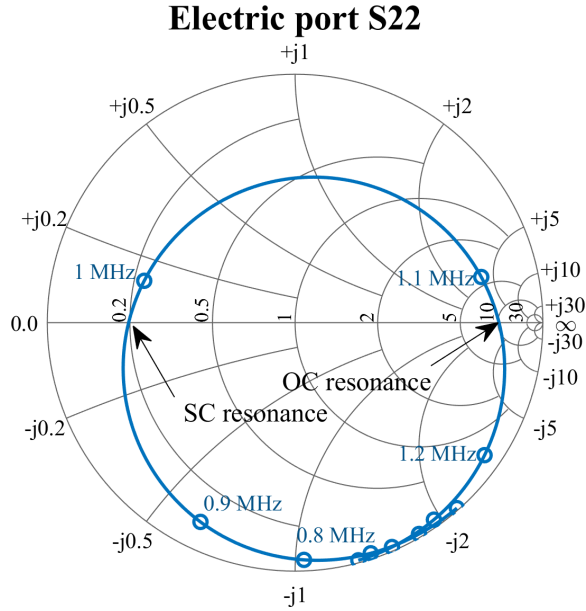


Figure 5.9: Smith chart of the air-backed transducer electric reflection coefficient (S_{22}) with respect to 50Ω when the acoustic port is in water.

5.4.1 Single Matching Layer

A single quarter wavelength matching layer is commonly used to match piezoelectric transducers to water in ultrasonic transducers literature. The material for a quarter wavelength matching layer needs to have an acoustic impedance at the geometric mean of the two media that need to be matched, i.e. for matching a piezoelectric transducer to water:

$$Z_m = \sqrt{Z_p Z_w} \quad (5.10)$$

where Z_m is the acoustic impedance of the single matching layer. Equation (5.10) is derived by maximizing the acoustic transmission between two passive layers while the piezoelectric layer involves electrical coupling. Thus, Equation (5.10) should be only used as a guideline for matching piezoelectric transducers, and several publications offer modified formulas for matching a piezoelectric transducer [214].

A quarter wavelength matching layer is designed based on perfect transmission at a specific frequency where the thickness of the layer (h_m) is a quarter wavelength, i.e.:

$$\begin{aligned} h_m &= \frac{\lambda}{4} \\ &= \frac{c_m}{4f_o} \end{aligned} \quad (5.11)$$

where c_m is the speed of sound in the matching layer, and f_o is the target frequency of operation. For frequencies in the neighborhood of f_o , the matching layer will still improve the acoustic match; however, its effectiveness will decrease as the frequency deviates further from f_o . On the other hand, for piezoelectric layers, the matching layer response will interact with the frequency response of the transducer resulting in a modified response.

The influence of a matching layer targeting 1 MHz on the electrical and acoustic reflection coefficients of the piezoelectric transducer is shown in Figure 5.10. As the acoustic matching layer thickness increases, each point of S_{11} (Figure 5.10a) is rotated counter-clockwise in the Smith chart about a fixed point on the resistance axis determined by the impedance of the matching layer. The angle of rotation of each point on the curve depends on the thickness of the matching layer, i.e. the phase change introduced by the layer. A quarter wavelength layer corresponds to a 180° rotation at the target frequency.

Since the matching layer shifts S_{11} closer to the origin of the Smith chart, the matching between the electrical and acoustic domain improves as indicated by the reduction in the radius of the electrical impedance circle S_{22} shown in Figure 5.10b. The result of this interaction is a double-humped reflection coefficient (Figure 5.10c) which is commonly reported in the literature for air-backed transducers with geometric mean matching layer [181].

The effect of changing the acoustic impedance of the matching layer while keeping its thickness constant to $\lambda/4$ at 1 MHz is shown in Figure 5.11. Decreasing the acoustic impedance of the layer shifts S_{11} (Figure 5.11a) to lower resistance (acoustic impedance) value. Matching layers with acoustic impedance between 5-7 MRayl generates the smallest

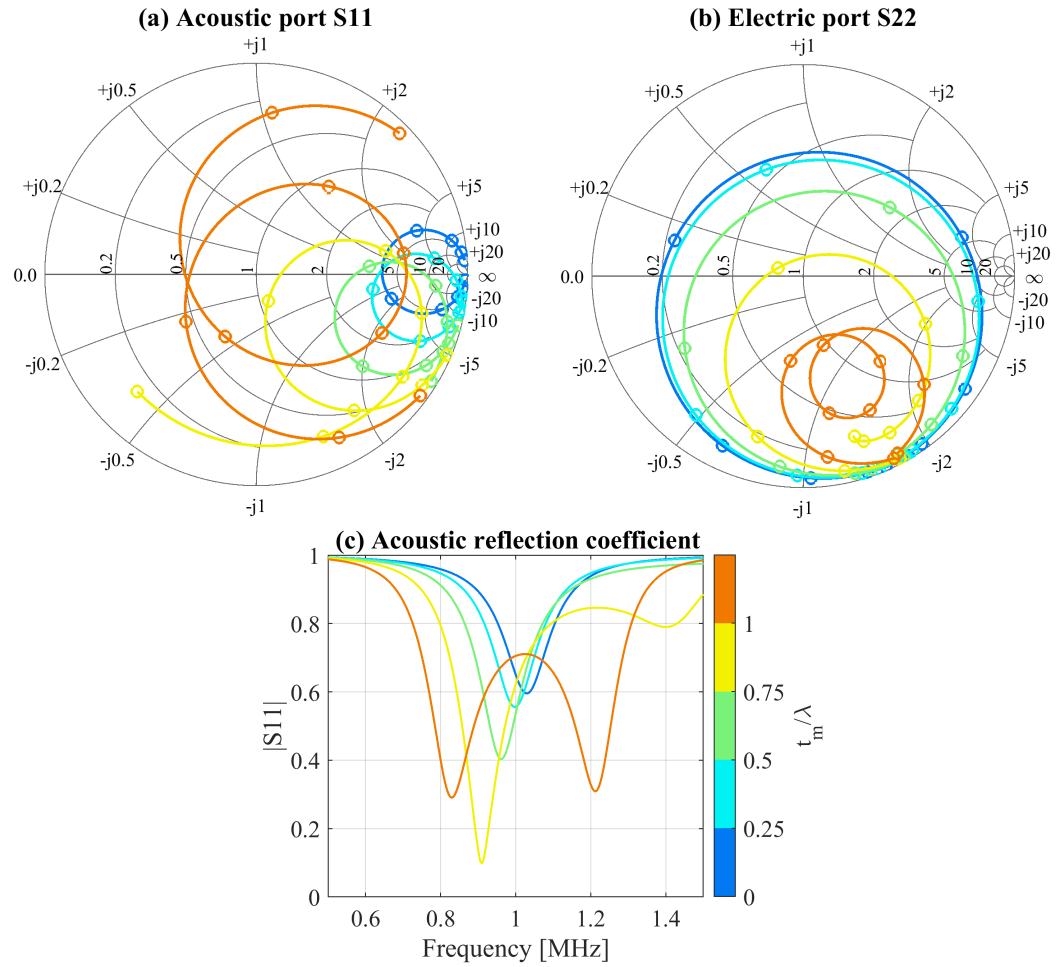


Figure 5.10: Smith chart of the (a) acoustic and (b) electric reflection coefficients of an air-backed piezoelectric transducer with a single matching layer of impedance $Z_m = (Z_p Z_w)^{1/2}$ with different thickness. The amplitude of the acoustic reflection coefficient is shown in (c).

variation in S_{22} (the electric impedance) on the Smith chart shown in Figure 5.11b, and thus a value of 6 MRayl was investigated further for electrical matching. There are, however, a few low loss natural materials with an acoustic impedance between 5 and 7 MRayl which is one of the reasons a single matching layer might not be suitable for high sensitivity/low loss applications such as simultaneous power and data transfer.

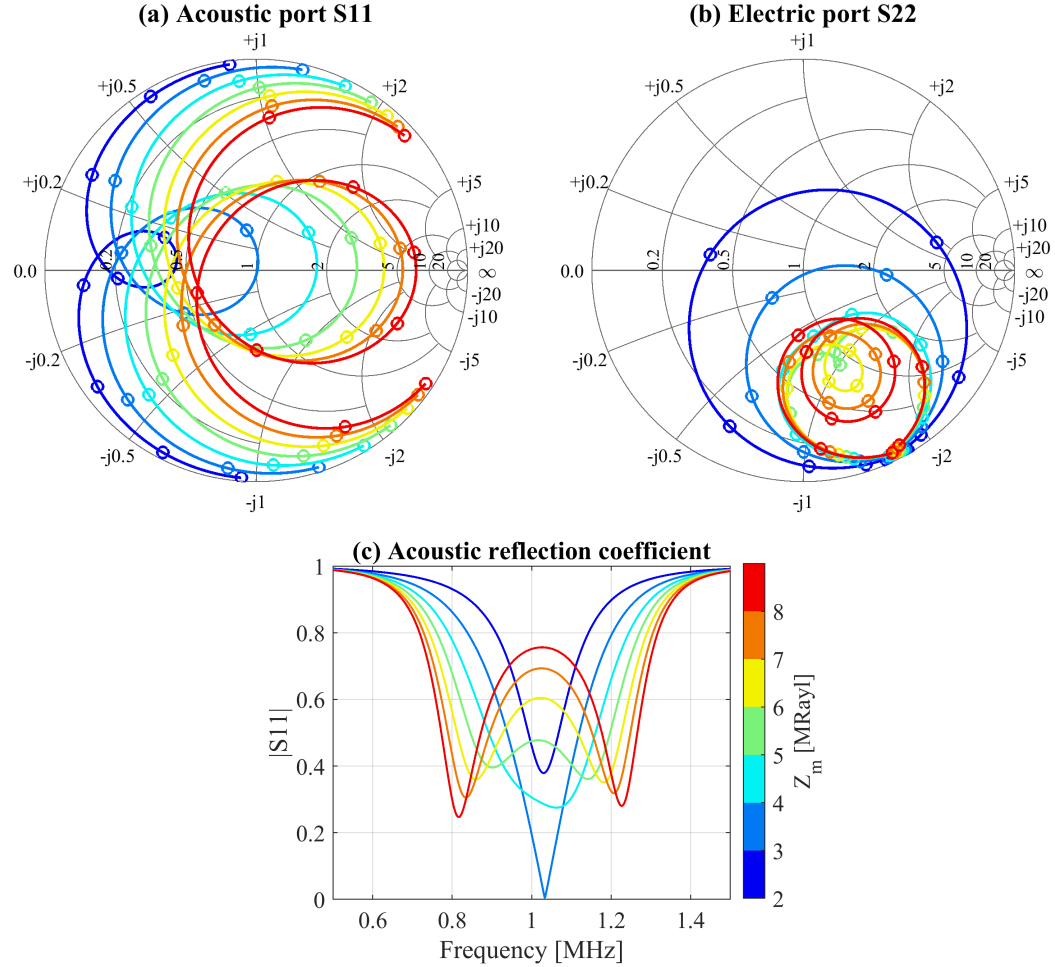


Figure 5.11: Smith chart of the (a) acoustic and (b) electric reflection coefficients of an air-backed piezoelectric transducer acoustically matched with a single quarter wavelength matching layer with varying acoustic impedance. The amplitude of the acoustic reflection coefficient is shown in (c).

Figure 5.12 shows the effect of adding a series inductor for electrical impedance matching. As shown in Figure 5.12, the inductor shifts S_{22} upwards on the Smith chart closer to the origin, and thus improves the overall impedance match as indicated by the reduction

of S_{11} circle shown in Figure 5.12a. Adding a series inductor causes all the points on the chart to follow constant resistance lines towards the origin of the plot. The match could be further improved by using a parallel inductor to shift more points towards the center thus improving the system bandwidth. However, an inductor of 7-9 μH was sufficient to achieve a high sensitivity bandwidth of 50% (Figure 5.12c) which is a significant improvement compared to the unmatched transducer shown in Figure 5.3. The bandwidth of the system will be further enhanced by considering a two-layer acoustic matching in the following subsection.

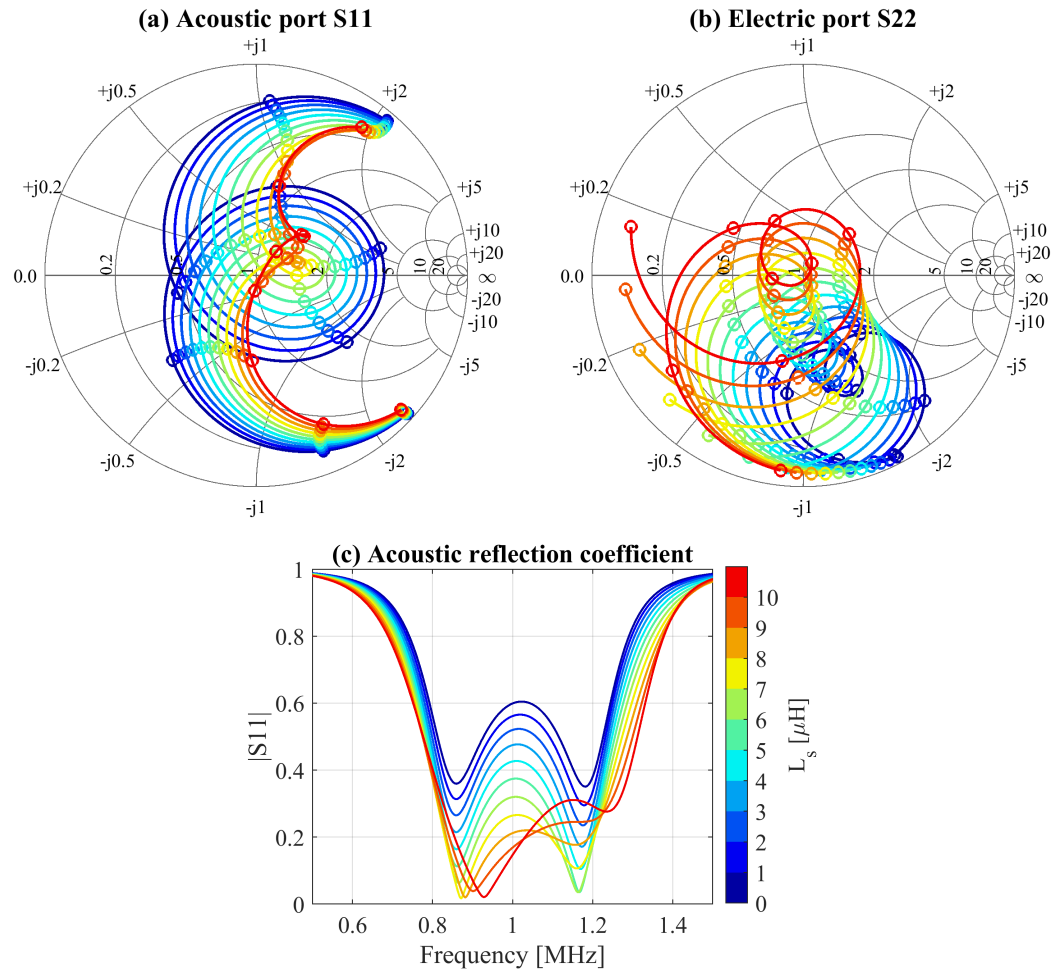


Figure 5.12: Effect of using a series inductor on the Smith chart of the (a) acoustic and (b) electric reflection coefficients of an air-backed piezoelectric transducer with a single quarter wavelength matching layer of acoustic impedance 6 MRayl. The amplitude of the acoustic reflection coefficient is shown in (c).

5.4.2 Two-layer Acoustic Impedance Matching

Two quarter wavelength layers can be used for enhancing the bandwidth of the piezoelectric transducer [216]. For passive layers, the impedance of each matching layer could be deduced from [217]:

$$\begin{aligned} Z_{m1} &= Z_p^{2/3} Z_w^{1/3} \\ Z_{m2} &= Z_p^{1/3} Z_w^{2/3} \end{aligned} \quad (5.12)$$

where Z_{m1} is the matching layer adjacent to the transducer, and Z_{m2} is the one adjacent to water. The acoustic impedance of quartz glass is around 12.1 MRayl which is very close to the value calculated for Z_{m1} from Equation (5.12). The value calculated for Z_{m2} is 4.3 which lies in the neighborhood of metal-filled epoxies such as silver epoxy or tungsten-filled epoxy for example. These materials, however, have very high acoustic attenuation, and are not suitable for our target application. Pure epoxy (3 MRayl) has lower attenuation and is easy to cast and polish to exact thickness for fine-tuning the matching process, so it was used instead. Epotek-301 is a clear epoxy commonly used in the ultrasound literature because of its low viscosity which allows it to be easily cast without trapping air bubbles in the process.

The acoustic and electrical reflection coefficients for a two-layer matched transducer with air backing are shown in Figure 5.13. The size of S_{22} circle (Figure 5.13b) without electrical matching is smaller than that obtained for a single acoustic matching layer (Figure 5.12b) indicating a more broadband response for the transducer. The electrical impedance is shifted to the center of the Smith chart for electrical matching using a $6\text{ }\mu\text{H}$ series inductor then a $15\text{ }\mu\text{H}$ inductor parallel to the 50Ω load as shown in (Figure 5.13b). Figure 5.13c shows that the matched transducer achieves a large flat bandwidth close to 80% with a large sensitivity. The sensitivity is evident in the large difference between

the reflection from the transducer when connected to a large resistance (OC) versus when electrically matched as shown in Figure 5.13d.

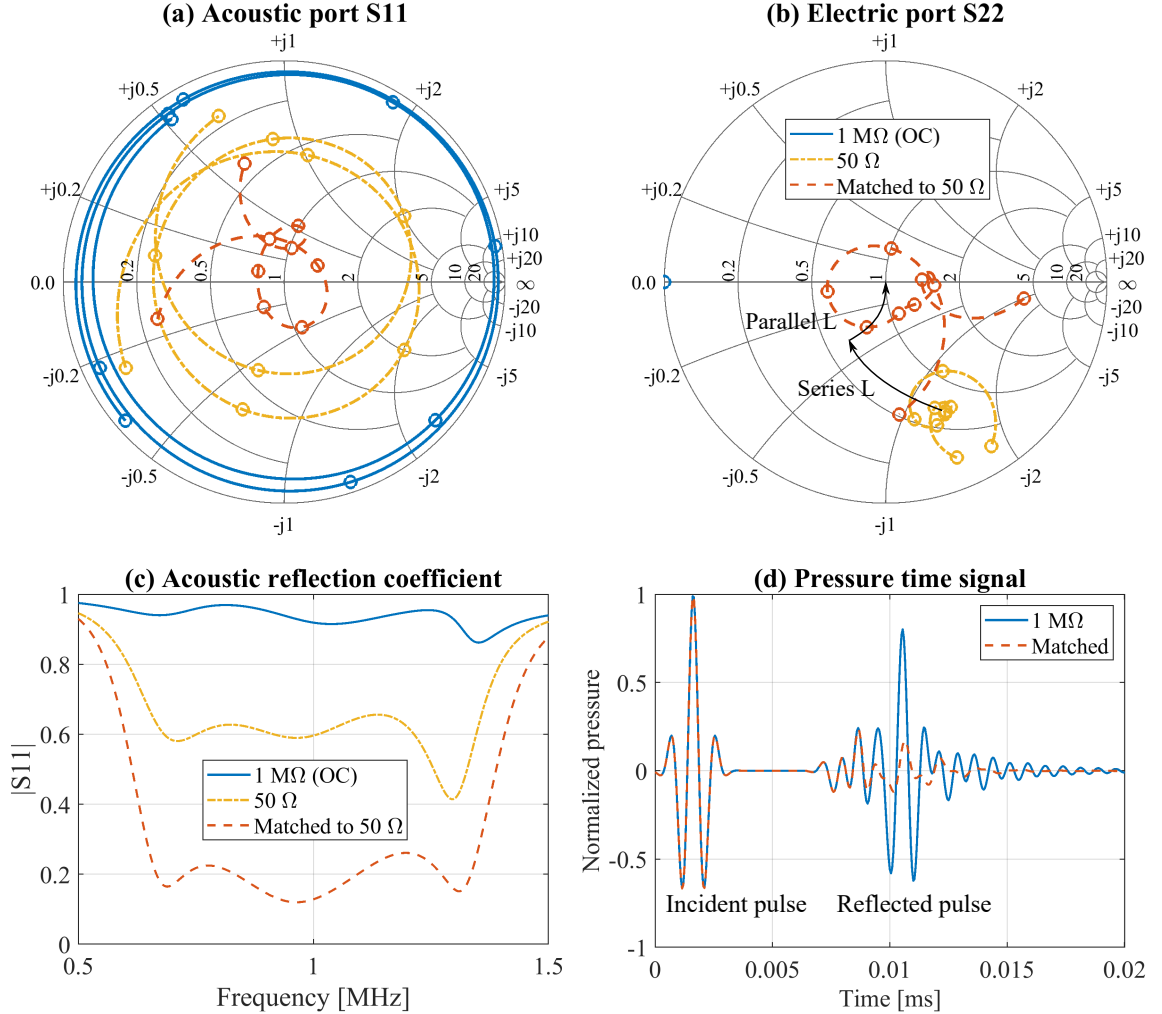


Figure 5.13: Electrical impedance matching of a transducer with two quarter-wavelength matching layers (quartz glass and epoxy). The effect of using a parallel then series inductor is shown on the Smith chart of the (a) acoustic reflection coefficient and (b) electric reflection coefficient. The electric load connected to the transducer in each case is shown in the legend. (c) The amplitude of the acoustic reflection for the different electric loads. (d) A reflected acoustic pulse from the transducer when using the matching circuit compared to the case when a $1 \text{ M}\Omega$ load (OC) is used.

Table 5.2: Dimensions of the fabricated transducers

Layer	Unit	U1	U2	M1	M2	M3
PZT	mm	2.1	2.1	2.1	2.1	2.1
Epoxy	μm	-	-	10	10	10
Quartz glass	mm	-	-	1.6	1.6	1.56
Epotek 301	mm	-	-	0.4	0.5	0.6

5.5 Experimental Verification

Two sets of transducers were fabricated for testing ultrasonic power and data transfer. The first set was not acoustically matched, and was used as a baseline to verify the developed analytical models (U1&U2). The second set had the two-layer acoustic matching design discussed in Section 5.4.2. The thickness of the epoxy layer was varied between 0.65-0.75 mm to obtain a transducer with the best possible match between the electrical and the acoustic domains. The dimensions of the fabricated transducers are summarized in Table 5.2.

5.5.1 Transducer fabrication

The transducer casings were 3D printed using an Ultimaker 3 printer. The casings shown in Figure 5.14 were designed so that they could provide air backing to the transducers by only supporting the piezoelectric layers from the edge. To fabricate the unmatched transducers, a coaxial cable was first soldered to the back of a piezoelectric disc (Steminc SMD30T21F1000R). The transducer was mounted in the casing so that it sits flush with the front edge as shown in Figure 5.14a, and the edges, as well as the wire opening, were sealed using 3M DP100 epoxy. The epoxy was used to coat the casing except for the transducer area to provide water tightness and seal the air backing since 3D printed PLA is water permeable.

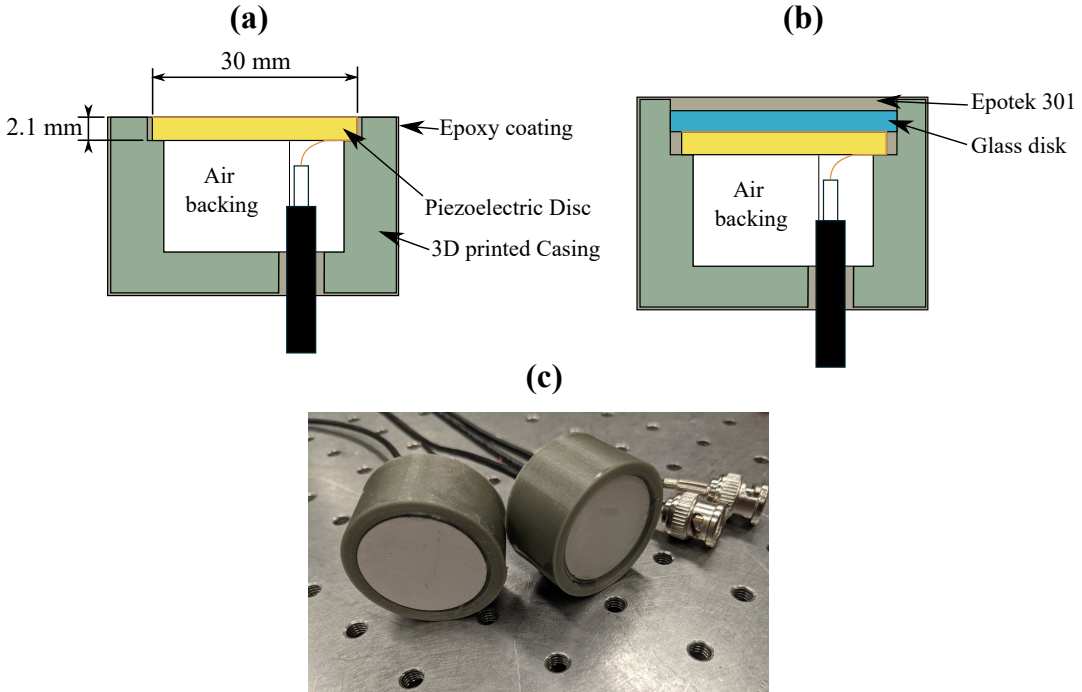


Figure 5.14: (a) Schematic of an air-backed transducer without acoustic matching layers. (b) Construction of the two-layer acoustically matched transducer. (c) Fabricated transducers U1 and M1 before polishing.

The matched transducers (Figure 5.14b) were fabricated by first bonding a 1 1/4" x 1/16" fused quartz glass disc supplied by TGP Inc. ($\rho_1 = 2200 \text{ kg/m}^3$, $c_1 = 5500 \text{ m/s}$, $Z_1 = 12.1 \text{ MRayl}$, $\alpha_1 = 5 \text{ dB/m/MHz}$) [218] to the front face of the piezoelectric layer through a vacuum bonding process. The minimum thickness commercially available for the quartz glass was 1/16" (1.56 mm) which is slightly larger than the quarter wavelength thickness at 1.43 mm. A coaxial cable was then soldered to the piezoelectric disc and the piezo/glass assembly was then mounted inside the casing. The casing for the matching transducer was designed so that the remaining height would match that intended for the epoxy matching layer. The transducer was sealed and coated using Epotek 301 epoxy ($\rho_2 = 1090 \text{ kg/m}^3$, $c_2 = 2640 \text{ m/s}$, $Z_2 = 2.85 \text{ MRayl}$, $\alpha_2 = 250 \text{ dB/m/MHz}$) [218], and a heat gun was used to ensure that no air bubbles remained trapped in the epoxy layer before leaving it to cure for 24 hours. The cured layer was then sanded down till it was

Table 5.3: Experimentally identified modified PZT-4 material properties from electrical impedance data in air

Property	ρ_p	c_p	\bar{h}_{33}	C_{33}^D	C_p	Q_m	$\tan \delta$
Unit	kg/m ³	m/s	kV/mm	GPa	nF	-	%
Value	7900	4714	2313	175	2.4	500	0.4

flush with the front of the casing using 200 grit sandpaper followed by 400 grit then 600 grit. The fabricated transducers are shown in Figure 5.14c.

5.5.2 Measuring the Electrical Impedance of the Transducers

An Agilent 33250A signal generator and a Tektronix TDS5034B oscilloscope were used to experimentally measure the electrical impedance of the fabricated transducers. The signal generator was connected to the tested transducer and then programmed to apply a voltage chirp signal that swept from 100 kHz up to 2 MHz. The applied voltage and the current flowing to the transducer were simultaneously measured using a 10x 150 MHz voltage probe and a current probe (Tektronix P6022). The voltage and current signals were then converted to the frequency domain and used to calculate the input electrical impedance of the transducer.

For each transducer, the electrical impedance was measured twice. Once in air then a second time while it was mounted inside a 30"x20"x15" water tank to compare its results to the analytical models. The electrical impedance of an unmatched transducer in air was first used to estimate the exact piezoelectric material properties using the procedure described in Ref. [181]. The experimentally measured piezoelectric properties are summarized in Table 5.3.

The experimental electric impedance of the different transducers is compared to the analytical predictions in Figure 5.15. The experimental results agree well with the numerical predictions with limited deviation caused by the uncertainties in the material properties and

geometry of the different layers. The matching of the transducer was very sensitive to the exact thickness of the glass and epoxy layers as shown by the difference in circle size on the Smith chart between transducers M1 to M3. A better acoustic match could be achieved by fine-tuning the glass and epoxy layers geometry as shown in Figure 5.12. Transducer M3 showed the best electrical matching (smallest variation on the Smith chart), so it will be investigated further for electrical impedance matching.

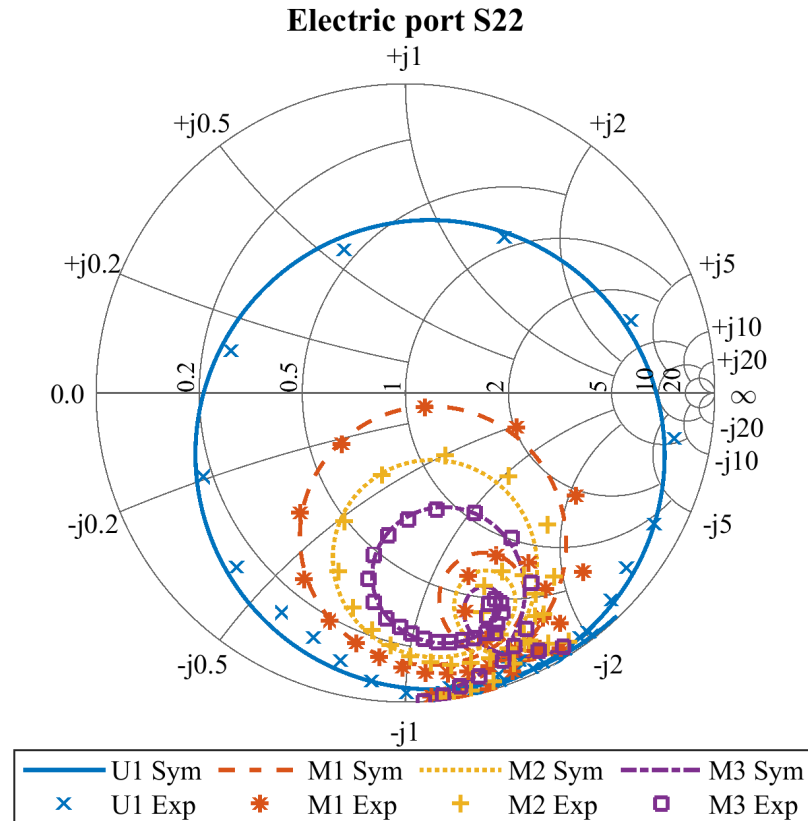


Figure 5.15: Analytical (lines) and experimental (markers) electric impedance underwater for three matched transducers (M1-M3) with different epoxy layer thickness as summarized in Table 5.2. The impedance of a transducer without acoustic matching (U1) is also shown for comparison.

5.5.3 Setup for Measuring the Acoustic Reflection Coefficient

The acoustic reflection coefficient of the fabricated transducers was measured using the setup shown in Figure 5.16. A Panametrics 5800 pulser/receiver was used to excite a broadband Olympus V394 transducer. The filtered and amplified reflected signal was connected

to an oscilloscope for display and recording. The pulser was set to excite the transducer with a $12.5 \mu\text{J}$ pulse with a repetition rate of 500 Hz. The echo signal was filtered with a 100 kHz-10 MHz bandpass filter to reduce the noise then amplified with a 20 dB gain.

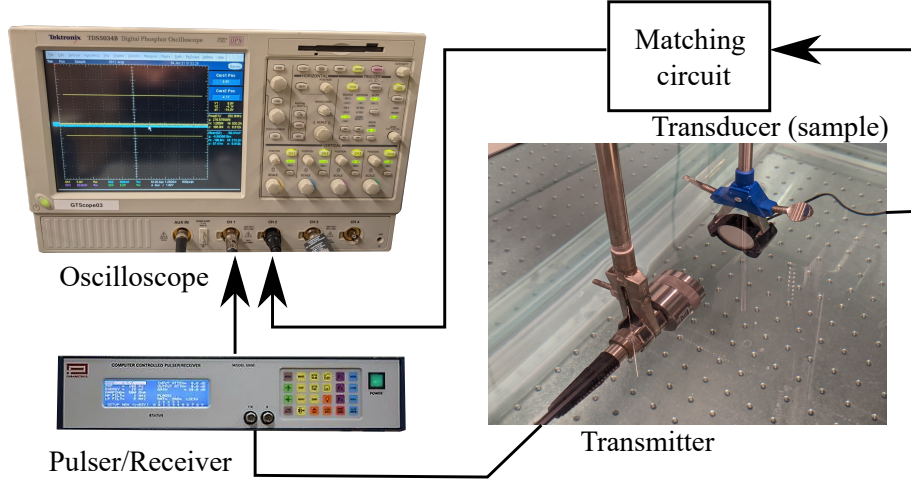


Figure 5.16: Experimental setup for measuring the acoustic reflection coefficient of the fabricated transducers.

The acoustic reflection coefficient of the samples was calibrated using the echo from normal incidence on a stainless-steel 304 cylinder of 26.4 mm thickness and 101 mm diameter. Normal incidence was verified by rotating the calibration cylinder until the maximum echo amplitude was achieved. The first echo from the sample and the calibration cylinder were windowed and then converted to the frequency domain. The acoustic reflection coefficient from the sample was then calculated using the relation:

$$S_{11} = R_{st} \frac{A_{sample}}{A_{calib}} \quad (5.13)$$

where A_{sample} is the reflected signal from the sample, A_{calib} is the reflected signal from the stainless-steel cylinder, and R_{st} is the reflection coefficient of a water-steel interface calculated from:

$$R_{st} = \frac{Z_{st} - Z_w}{Z_{st} + Z_w} \quad (5.14)$$

where $Z_{st} = 46.57 \text{ MRayl}$ is the acoustic impedance of stainless steel.

The experimental acoustic reflection coefficients for the unmatched and matched transducers (U1 and M3) are compared to the analytical models as shown in Figure 5.17. The reflection coefficient is measured and simulated with respect to a 50Ω output for both samples, i.e. no electrical matching was done for this measurement. For both samples, the amplitude of the experimental reflection coefficient is lower than that in the simulations for all frequencies. This discrepancy is caused by slight misalignment between the source transducer and the sample, as well as the directivity of the source transducer. Nevertheless, the frequency response predicted from the analytical models of both transducers agrees well with the experimental measurements within a scaling factor caused by losses due to diffraction and misalignment between the transducers.

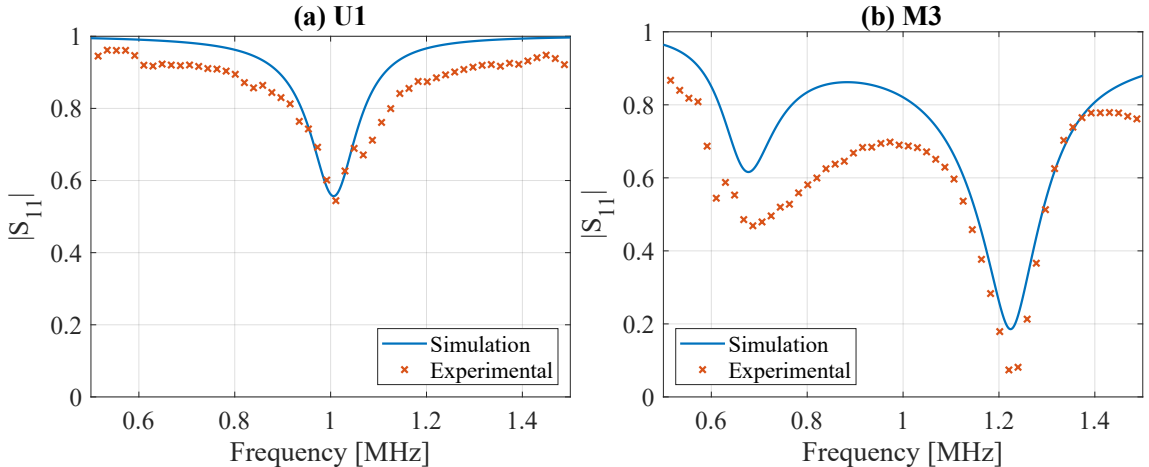


Figure 5.17: Experimental versus analytical acoustic reflection coefficient for (a) the transducer without acoustic matching (U1), and (b) the two-layer acoustically matched transducer (M3).

5.6 Impedance Matching for Data Transfer

The two-layer acoustically matched transducer M3 was electrically matched to achieve maximum bandwidth while connected to a 50Ω electric load. The four-element electrical matching network shown in Figure 5.18 was designed and optimized using the impedance matching tool in Keysight ADS software. The random optimization algorithm built into the software was used to minimize S_{22} for the frequency bandwidth between 0.5 MHz and

1.5 MHz. Even though a single inductor is sufficient to achieve broadband operation for the acoustically matched transducer as discussed in Section 5.4.2, the electrical network was developed, optimized, and implemented on a breadboard to further increase the bandwidth.

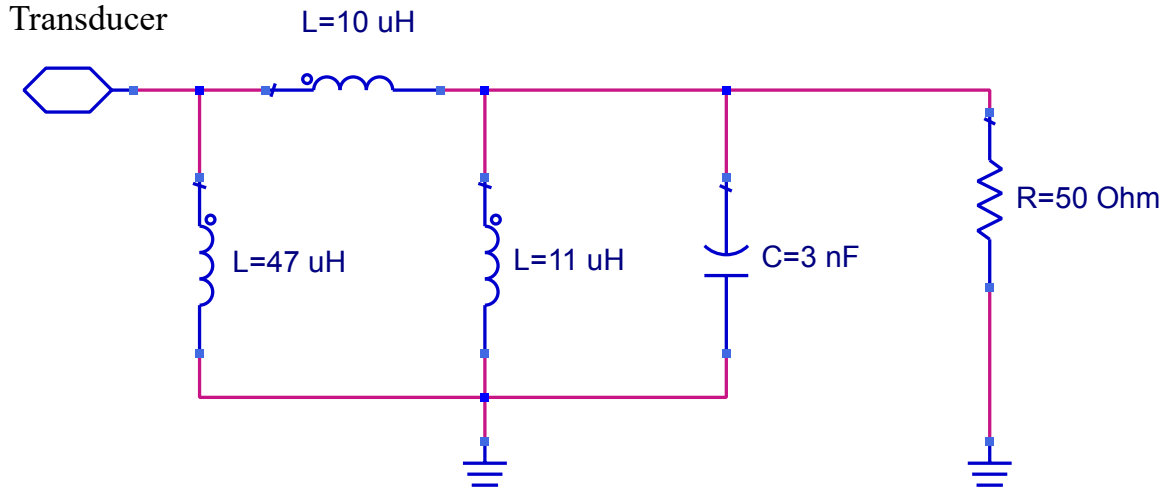


Figure 5.18: Electrical circuit used to achieve a broadband electrical match with the two-layer acoustically matched transducer (M3).

The experimental acoustic reflection from the transducer with the matching circuit is compared to open circuit termination in Figure 5.19. The matched transducer achieved up to 70% bandwidth centered around 900 kHz with a factor of 3 change in amplitude between the open circuit and matched states as shown in Figure 5.19a. Considering the modulation of the echo signal shown in Figure 5.19b, a data rate of at least 200 kbps could be transmitted using this setup with simple amplitude shift keying (ASK) modulation. Much higher data rates could be achieved with advanced modulation techniques such as OFDM. It should be noted that the echo signal in Figure 5.19b is different than that estimated analytically in Figure 5.13 for two reasons. First, the signal plotted in Figure 5.19b is that for the echo signal as generated by the transmitter not the actual reflected pressure signal, i.e., the signal is multiplied by the two way transfer function of the transducer. Second, the impedance matching achieved shown in Figure 5.13 is different from that obtain experimentally due to the use of a thicker glass matching layer, and a different electrical matching circuit.

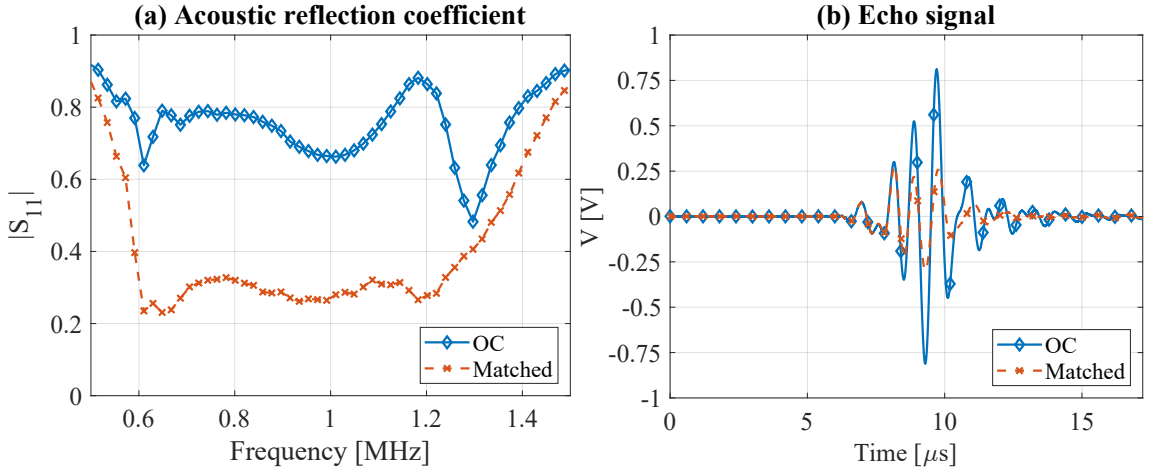


Figure 5.19: (a) Experimental acoustic reflection coefficient for an electrically and acoustically matched transducer. Broadband electrical matching is shown using the circuit in Figure 5.18 versus when the transducer was open circuit. (b) Time waveform showing the modulation of the reflected pulse by varying electrical circuit connected to the transducer.

5.7 Impedance Matching for Power Transfer

Power is commonly transmitted at a constant frequency, hence the bandwidth of the transducer is only important to account for tolerances in the transducer material properties and geometry. Otherwise, it is only necessary to match the transducer at a single frequency of operation to achieve the maximum sensitivity possible and minimize power reflections. A power transfer system with low loss transducers without acoustic matching layers could thus be used to transfer power with an efficiency higher than that using acoustically matched transducers with lossy matching layers. The relative performance between these two systems will only depend on the amount of attenuation present in the matching layers and in the transducer material.

An experimental setup similar to that described in Section 3.2.1 was used to measure the ultrasonic efficiency of a system consisting of two unmatched transducers (U1 and U2). The transmitter was connected to a signal generator and the receiver was connected to a 50Ω load. No electrical matching was used for either transducer. The receiver transducer

was mounted to the motorized stage shown in Figure 4.7, and the efficiency was measured while varying the frequency and the separation distance between the two transducers.

The frequency response of the power transfer efficiency of the system is shown in Figure 5.20 for different separating distances (D) between the transmitter and the receiver. The efficiency frequency response shows similar characteristics to that discussed for metal power transfer systems in Chapter 3. A global peak for the efficiency is observed around the resonance frequency of the transducers (1 MHz), as well as multiple local peaks due to the resonance of the water layer between the transducers. As the distance between the transducers increases, the frequency separation between these peaks decreases. The amplitude of these local peaks also decreases with distance as the diffraction losses become more dominant.

The peak efficiency of the system versus distance is shown in Figure 5.21. Two distinct regions are observed: 1) The nearfield response below 80 mm (53λ) and 2) the farfield response above 80 mm. The peak efficiency in the near field had an average value close to 52% for the entire region accompanied by large fluctuations below 25 mm (16λ). The amplitude of the fluctuations significantly dropped for distances above 25 mm. The farfield response was characterized by a uniform drop in efficiency with distance dominated by the spreading losses. It is worth mentioning that the distance observed for the transition between the nearfield and the farfield decay for the efficiency of the system (80 mm) is lower than the shortest estimate for the Rayleigh distance reported in literature ($D_{Rayl} = a^2/\lambda = 150$ mm). This can be partially due to slight misalignment between the TX and RX. Also, estimates of the Rayleigh distance are mostly defined for the on-axis region where the response matches the farfield response. It is common that the transition region starts before the Rayleigh distance [219]

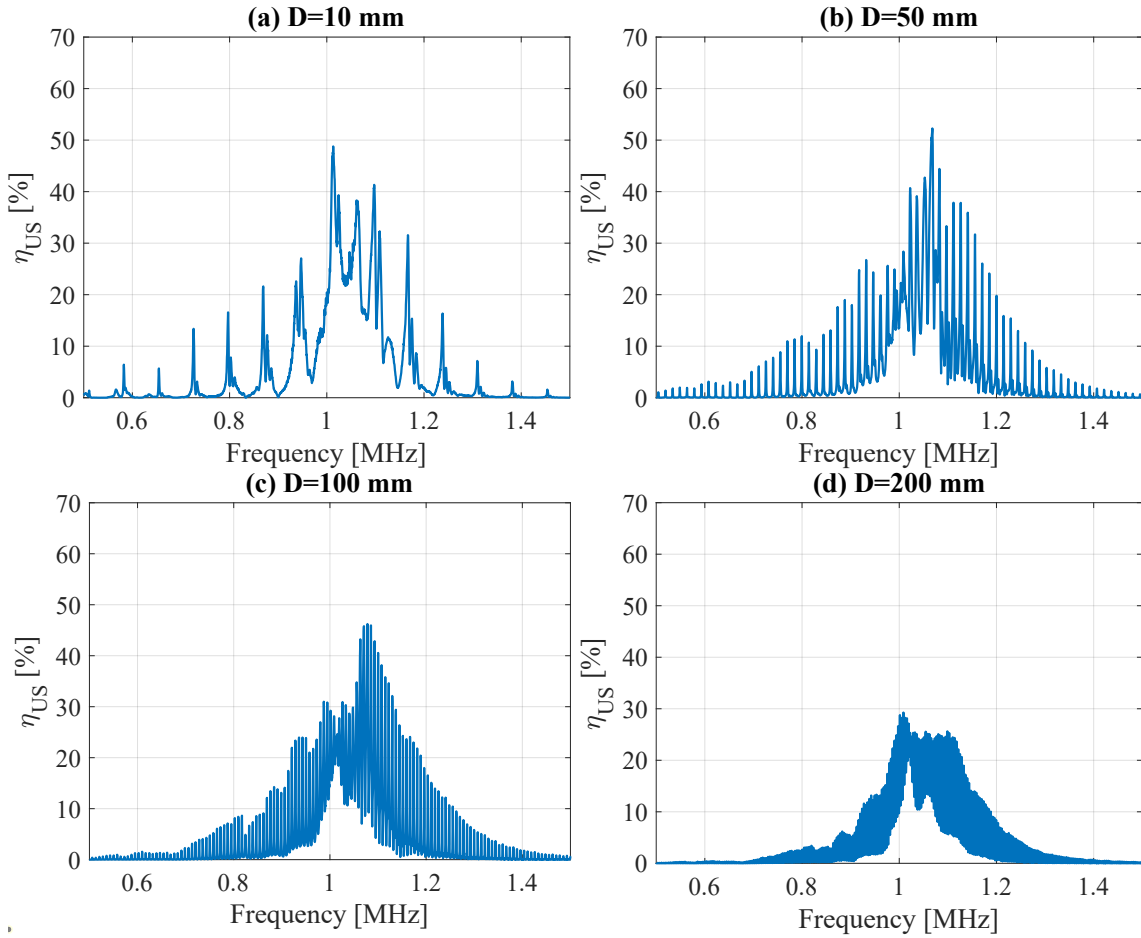


Figure 5.20: Ultrasonic efficiency versus frequency for two air-backed transducers without acoustic impedance matching. The efficiency is shown for a separating distance between the transducers of (a) 10 mm, (b) 50 mm, (c) 100 mm, and (d) 200 mm.

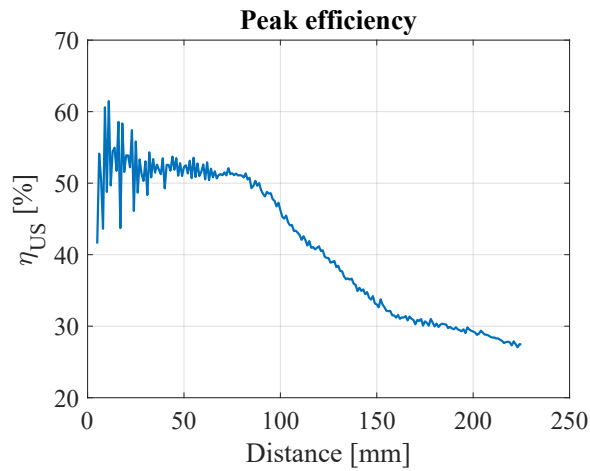


Figure 5.21: Peak efficiency of the ultrasonic power transfer system without acoustic matching versus the separating distance between the transducers.

5.8 Simultaneous Power and Data Transfer

Uninterrupted power transfer could be achieved while transmitting data simultaneously by multiplexing the matched transducer frequency response between a narrowband power channel and a broadband data channel. This multiplexing can be realized using the circuit shown in Figure 5.22. It consists of a power splitter designed to direct incident frequencies between 600 kHz and 900 kHz to a dummy communication load while directing the power signal (sent continuously at 1.3 MHz) to the power harvesting circuit. The splitter is realized using a series LC circuit to act as a narrow bandpass filter for the power signal. A second parallel LC circuit is used as a bandstop filter to pass all frequencies to a communication load except for the power frequency (1.3 MHz). By switching the data branch on and off, incident frequencies other than the power signal are modulated while the power signal is continuously fed to an energy harvesting circuit for powering the wireless device.

The circuit in Figure 5.22b was implemented on a breadboard, and the experimental acoustic reflection coefficient was measured as shown in Figure 5.23a. The communication branch is switched to transmit backscatter communication signal in the frequency range between 600 kHz and 900 kHz. The power branch at 1.3 MHz is not affected by the communication signal and almost all the power incident on the transducer at this frequency is absorbed.

The normalized spectrum of the voltage signals received at the different branches of the system are shown in Figure 5.23b. As intended, the communication branch load absorbs the incident power in its target data channel frequency range (600 kHz-900 kHz) while rejecting the power signal above 1 MHz. The power branch, on the other hand, absorbs power most efficiently around the target frequency of 1.3 MHz. The sensitivity of the power branch is higher than the data branch due to its target narrowband operation. The peak of the received signal of the power branch appears slightly below 1.3 MHz which is only caused by the roll-off of the incident ultrasonic pulse since the transmitting transducer used

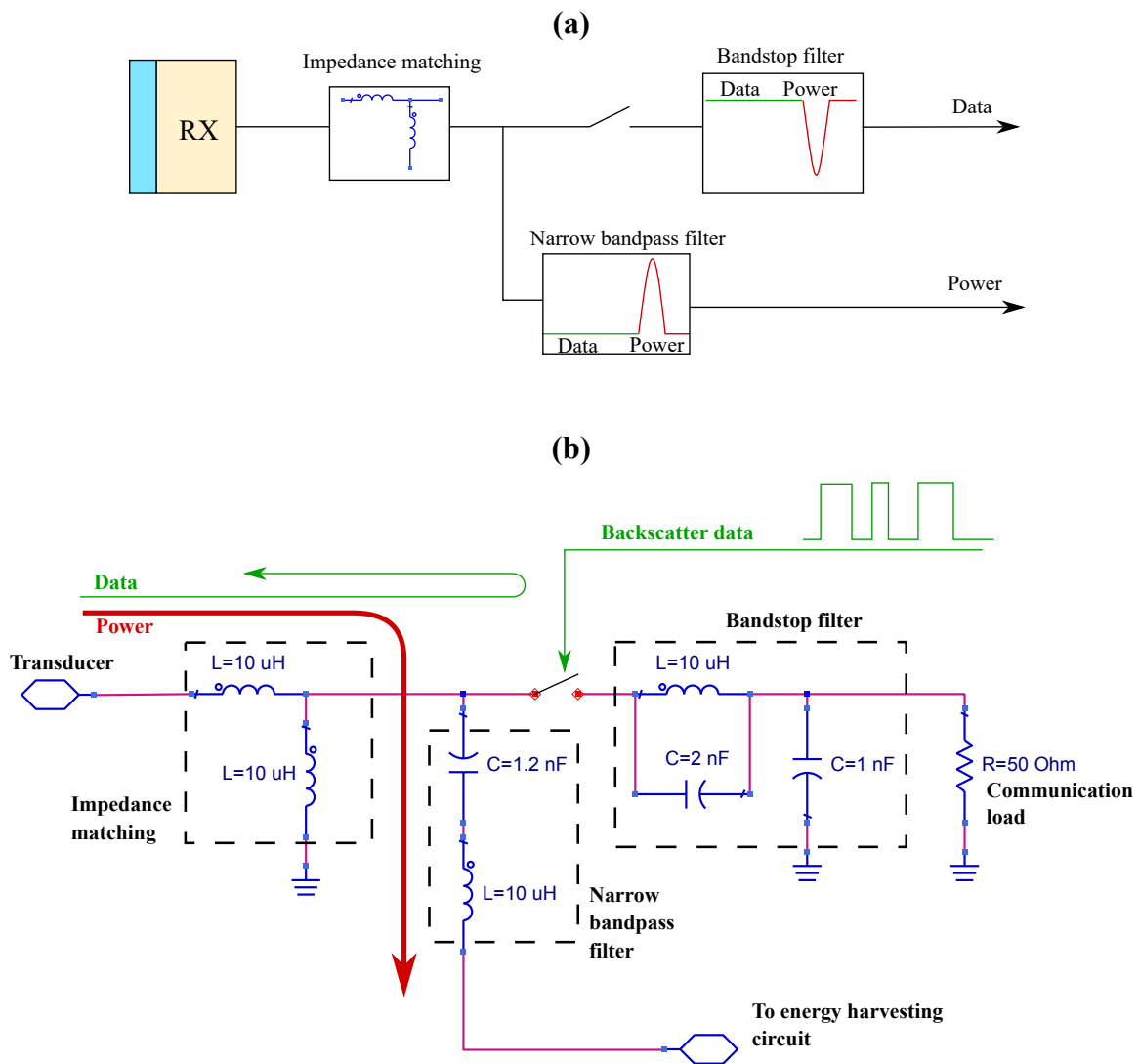


Figure 5.22: (a) Schematic and (b) implementation of an electrical circuit for simultaneous ultrasonic power and data transfer. The circuit routes in incident power and data signals to two separate electrical branches allowing for uninterrupted power flow to an energy harvesting circuit while transmitting backscatter data.

has a bandwidth of 60% centered at 1 MHz. The time signal for the echo received by the transmitter filtered in the data channel bandwidth between 600 kHz and 800 kHz is shown in Figure 5.23c. The difference between the two communication states is more than the double demonstrating high sensitivity.

It should be noted that the data and power frequency channels could be swapped to allow for power transfer at lower frequencies (around 700 kHz) by modifying the filters center frequencies. The power transmission frequency can be chosen to maximize the efficiency depending on the distance between the transmitter, and the receiver, and whether the system is divergence limited or attenuation limited. The power received at the data channel while it is modulated to absorb incident power (transmitting a 0 by not reflecting the incident acoustic power) could also be routed to the energy harvesting circuit to further increase the power available to the system.

5.9 Conclusions

An ultrasonic system for simultaneous underwater power and data transfer using the same transducer was developed and experimentally validated. The system relies on frequency multiplexing power and data signals to ensure an uninterrupted power transmission to an underwater wireless sensor, and thus increasing the continuous power that can be delivered to the device while maintaining backscatter communication with large data bandwidth. A high sensitivity data bandwidth of 300 kHz was obtained while achieving uninterrupted power transfer with minimum reflection.

Simultaneous acoustic and electric impedance matching was shown to be important for achieving the maximum operating bandwidth from the transducer while maintaining a high sensitivity. Using only electric or acoustic matching was sufficient to achieve large sensitivity at a limited bandwidth which might be sufficient for power transfer, but limits the maximum data rate that could be attained by the system.

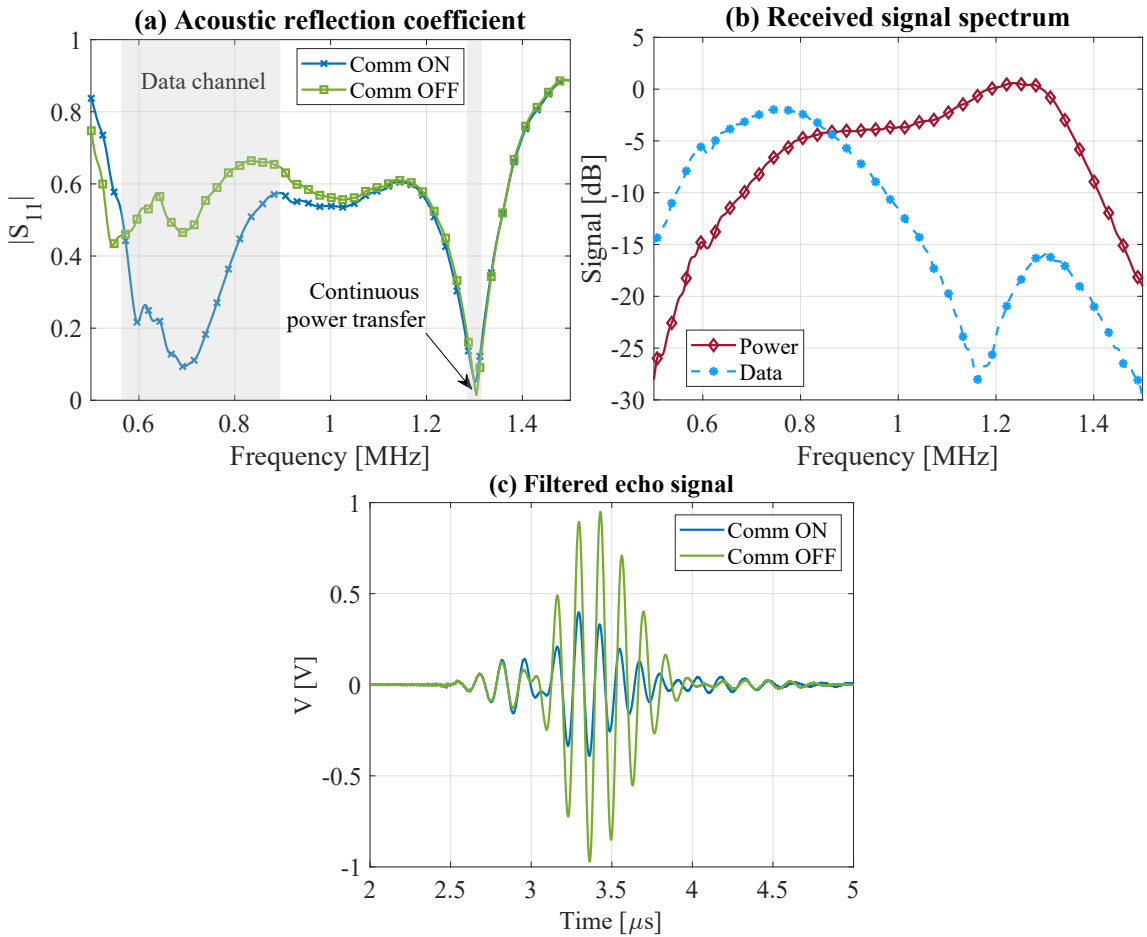


Figure 5.23: (a) Experimental acoustic reflection coefficient for a transducer connected to the simultaneous power and data transfer circuit shown in Figure 5.18. (b) The spectrum of the signal received by the power branch of the circuit versus that received by the data branch for an incident ultrasonic pulse. (c) Filtered echo signal showing the data bandwidth between 600 kHz and 800 kHz.

Electrical and acoustic impedance matching strategies for achieving maximum power transfer, maximum data bandwidth with maximum sensitivity, and simultaneous power and data transfer were discussed. Using a two-layer acoustically matched PZT transducer, the electrical matching circuit was optimized for power transfer yielding a peak ultrasonic efficiency of 52% at a distance of 10 cm and 27% at a distance of 22.5 cm underwater. Optimizing the circuit for data transfer yielded a 600 kHz (70%) bandwidth with a 10 dB difference between connecting the matching circuit and keeping the transducer open allowing for reliable backscatter communication with high data rates.

The developed power and data transfer system could be modified to suit a wide range of applications that require ultrasonic power and data transfer such as biomedical implants, underwater for ocean monitoring and navigation, and through-metal power and data transfer for shielded devices and enclosures.

CHAPTER 6

CONCLUSIONS, CONTRIBUTIONS, AND FUTURE WORK

6.1 Summary and Conclusions

This work covered the modeling, analysis, experimental validation, as well as performance improvement in acoustic power transfer for multiple applications. This approach highlighted the unique challenges faced in each application, as well as the common challenges between the different fields.

6.1.1 Aspect Ratio-Dependent Piezoelectric Transmitter and Receiver Dynamics

In Chapter 2, the analytical models for thickness-mode piezoelectric transducers with different aspect ratios were investigated. Thickness-mode transducers were studied since they are the most common type of transducers used in the literature.

Experimental and numerical results showed that thin-plate and thin-rod analytical approximations commonly used in the literature were only valid for accurately predicting the surface velocity at the face of a transmitter with a very large aspect ratio for either very long slender rods with $\beta > 10$ (defined as height/radius), or very thin wide plates $\beta < 0.1$. New analytical models based on Rayleigh and Bishop rod models were developed to model transducers with thick-rod aspect ratios between $10 < \beta < 3$ and no fluid loading on their sides. None of the analytical models were able to predict the response of transducers with moderate aspect ratios ($\beta \approx 2$) because of the coupling of longitudinal and lateral motion not captured by the models. Also, the analytical models did not account for fluid loading on the lateral sides of transducers with moderate aspect ratios.

The acoustic power received by a submerged piezoelectric receiver was also difficult to quantify analytically, except for thin-plate transducers. The results showed that thin-

rod transducers can capture acoustic power through their lateral sides since they resemble an acoustic point receiver. The effective receiving area of a thin rod was shown to be larger than its actual physical area normal to the incident excitation. The results suggest that a resonant thin-rod piezoelectric receiver might be more efficient at capturing incident acoustic waves compared to a transducer with a moderate aspect ratio of the same volume placed in the same acoustic field.

6.1.2 System-Level Analysis with Focus on Ultrasonic Power Transfer through Metallic Barriers

Chapter 3 focused on quantifying the operating efficiency and voltage characteristics of a through-metal power transfer system. The ultrasonic systems were studied in the context of a full system-level analysis that captures the coupled performance of the mechanical system with the electrical power source, and energy harvesting circuitry.

A bonded as well as a detachable setup for complete DC-to-DC ultrasonic power transfer through-metals were studied. The first tested setup consisted of a transmitter and a receiver bonded to a 3 mm aluminum wall. The ultrasonic efficiency of the system was tested experimentally, and the results were compared to analytical and numerical predictions. The results showed an ultrasonic efficiency of 83% which matches the numerical predictions, but was found to be lower than the analytical ones. The discrepancy was attributed to the lateral modes of the transducer since its aspect ratio was not small enough to neglect their effect.

A class E amplifier was designed to be integrated with the ultrasonic system relying on its dynamic response to maximize the overall power conversion efficiency of the system. The overall system which included the power amplifier, the mechanical system, and a full-bridge rectifier was designed and simulated using a coupled nonlinear harmonic balance analysis. The system was then experimentally tested, and the results showed excellent

agreement with the simulations. The system was able to deliver 17.5 W of DC power to a 50Ω resistive load with a total DC-to-DC efficiency of 66%.

A second mechanical system was designed for portable/detachable operation in which the transmitter is only attached to the metallic enclosure when charging the internal circuit and removed when not used. The charger was designed to allow for efficient operation without the need for an ultrasonic couplant. Several low attenuation soft elastomers were experimentally tested to determine the most suitable material for achieving efficient dry-coupled operation. The results showed that the elastomer with the lowest elasticity (lowest hardness) provided the most efficient operation for the system. A 2 mm layer was sufficient to achieve a peak ultrasonic efficiency of 63% at 1.04 MHz without the need for a liquid couplant. The charger could deliver up to 3 W of DC power with 50% DC-to-DC efficiency when operating on a 9 V alkaline battery. The power supplied by the charger was limited by the temperature stability of the elastomeric layer used, and thus, a larger power could be supplied by considering a heat resistant material with the same hardness and attenuation characteristics of the material used.

6.1.3 Performance Enhancement by Leveraging Phononic Crystals and Wave Focusing

Chapter 4 investigated enhancing the output power of an underwater ultrasonic power transfer (UPT) system by limiting its divergence losses through wave focusing and collimation. Gradient index phononic crystals (GRIN-PCs) lenses constructed from an air/3D printed polymer matrix were investigated to focus and collimate incident acoustic excitation with minimal reflections.

Two GRIN-PC lenses were designed, simulated, fabricated, and experimentally tested for focusing acoustic waves in air and underwater. The GRIN-PC relied on trapping air inside a polymer matrix that acted as a background medium. Since the acoustic impedance of polymers was close to water, it allowed for an efficient coupling for the incident acoustic

waves. The 3D-printed lens is much lighter than the state-of-the-art GRIN-PC lens implementations which required dense metallic inclusions to operate underwater.

The performance of a UPT system consisting of a point source and point source receiver was dramatically enhanced by introducing two lenses (one in front of the transmitter, and the other in front of the receiver). The output power of the system was improved by two orders of magnitude when the lenses were introduced compared to the baseline case. The lenses were additionally tested in a system consisting of weakly directional piezoelectric transducers which enhanced the power output by 15 fold from $250\text{ }\mu\text{W}$ up to 3.6 mW .

A second GRIN-PC lens was also designed, fabricated, and experimentally tested for focusing audio and low-frequency ultrasonic waves just above the audio spectrum to enhance the output power from a receiver placed at its focal point. The lens was excited with a speaker and a scanning microphone setup was used to map the acoustic field around its focal point. The lens showed broadband characteristics with the ability to focus incident acoustic waves between $10\text{-}20\text{ kHz}$. A circular piezoelectric unimorph harvester was then placed at the focal position of the lens, and its performance was characterized with a resistor sweep in the absence and presence of the lens. More than an order of magnitude enhancement in the harvested power was achieved using the lens. The 3D-printed lens substantially enhanced the intensity of sound energy via focusing, yielding $1.2\text{ }\mu\text{W}$ of usable electric power from a 120 dB sound source.

6.1.4 Acoustic and Electrical Impedance Matching for Simultaneous Power and Data Transfer

Chapter 5 investigated acoustic and electrical impedance matching of a thin-plate air-backed piezoelectric transducer for power and data (backscatter) transfer. An analytical model was developed for quantifying the change in the acoustic reflection coefficient of the transducer due to the change in the electrical circuit connected to the transducer. The electrical and acoustic impedance of the transducer were analyzed using the Smith chart to pin-

point areas for improving the impedance matching. Single and double quarter-wavelength acoustic matching layers were studied, and their influence on the transducer bandwidth, sensitivity, and acoustic signature was analyzed. Simultaneous electrical and acoustic matching was incorporated to maximize the bandwidth and sensitivity of the transducer for data transfer applications.

Several acoustically matched and unmatched air-backed transducers were fabricated, and their experimental acoustic reflection coefficient and electrical impedance were characterized. The results show excellent agreement for the electrical impedance of the developed transducers. The experimental acoustic reflection coefficient was lower than the analytical predictions for all frequencies owing to beam divergence losses.

An electrical matching circuit was developed and experimentally tested for maximizing the bandwidth of a two-layer acoustically matched transducer. The matched transducer achieved a 600 kHz (70%) bandwidth around 1 MHz with a 10 dB difference between connecting the matching circuit and keeping the transducer open allowing for reliable communication with high data rates. Optimizing the transducer for power transfer yielded a peak experimental ultrasonic efficiency of 52% at a distance of 10 cm and 27% at a distance of 22.5 cm underwater.

A new approach for achieving backscatter communication while maintaining an uninterrupted power flow to the wireless node was developed. The system relies on multiplexing the power and data signals in the frequency domain, therefore, maximizing the power delivered to the transducer and its range of operation. The signals received by the transducer are split into two paths, one for power and the other for data using bandpass and band-stop filters. A data bandwidth of 300 kHz was obtained experimentally while achieving uninterrupted power transfer with minimum reflection.

6.2 Contributions

The following summarizes the major contributions of this dissertation to the state-of-the-art:

- Derivation of two analytical models that could be integrated into circuit simulation software for a thick rod piezoelectric transducer based on the Rayleigh and Bishop thick rod models (Chapter 2).
- Experimental verification of the analytical models using electrical impedance measurements in air and submerged in oil (Chapter 2).
- Numerical investigation of the effect of a piezoelectric transducer aspect ratio on its performance as a transmitter and a receiver (Chapter 2).
- Analytical, numerical, and experimental validation of the performance of a power transfer system for transferring power through metallic barriers using ultrasonic waves (Chapter 3).
- Development, fabrication, and experimental validation of a new design for an efficient class E electrical power amplifier which relies on the properties of the mechanical system to operate (Chapter 3).
- Experimental investigation of using low loss elastomers for maximizing the power transfer efficiency of a detachable dry-coupled through-metal power transfer system (Chapter 3).
- Development and experimental validation of a portable, detachable charger for transmitting ultrasonic power through metallic barriers (Chapter 3).
- Development, numerical analysis, fabrication, and experimental validation of the first 3D gradient-index phononic-crystal lens for focusing underwater ultrasonic waves (Chapter 4).

- Design, simulation, and experimental testing of an underwater acoustic power transfer system that uses two gradient index phononic crystal lens for improving the directivity of the transmitter and focusing ultrasonic waves on the receiver (Chapter 4).
- Development, numerical analysis, fabrication, and experimental validation of a 3D gradient-index phononic-crystal lens for focusing audio-frequency acoustic waves in air (Chapter 4).
- Experimental and numerical investigation of the enhancement of the output power from placing a piezoelectric energy receiver at the focal point of the lens for harvesting sound power (Chapter 4).
- Analytical investigation, fabrication, and experimental validation of large-bandwidth high-sensitivity piezoelectric transducer for high-speed backscatter communication under water (Chapter 5).
- Development, and experimental validation of a new circuit for achieving uninterrupted ultrasonic power and data transfer using a single piezoelectric transducer (Chapter 5).
- Experimental evaluation of the underwater power transfer efficiency of the developed transducers versus the separation distance between them and the frequency of operation (Chapter 5).

6.3 Future Work

The surveyed analytical models for modeling piezoelectric transducers in Chapter 2 showed the lack of models that could accurately predict the average surface velocity of thick plates. Such models will be particularly useful given the popularity of thick plates in ultrasonic literature. The available options for modeling thick plates are limited to numerical approaches such as FEM models which are not computationally efficient, especially given

the high frequency commonly targeted by these transducers. Reduced-order models for plates and moderate aspect ratio transducers could also simplify UPT system design, and facilitate the integration of the transducer models in circuit simulations software.

Since a large power can be transferred ultrasonically through metals, the amplitude of the excitation could trigger electrical, piezoelectric, as well as ultrasonic nonlinearities not captured by the linear models investigated in this work. Additionally, the heat generated by the different mechanical and electrical components can change their material properties triggering various thermal/material nonlinearities. These types of nonlinearities can be incorporated in the developed models to better capture the behavior of the ultrasonic systems at higher power levels. The nonlinear models can help predict the power limits of the systems as well as bottlenecks limiting the power flow through the system. This is especially important for detachable systems where the nonlinearity is more pronounced due to the presence of dry contact interfaces.

In Chapter 4, a cube-shaped lens was developed to focus incident plane waves. While the cube shape might be easy to fabricate, it restricts the focusing capabilities of the gradient index lens to only three perpendicular directions. We have shown that a material with a sound speed close to water would require lower air inclusions, and achieve a near omnidirectional response. Hydrogels might be a suitable candidate material for achieving this lens design since they mainly consist of water. However, their 3D printing techniques have not matured enough to allow for printing a reliable complex structure similar to what could be achieved with PLA. Other materials with impedance close to water such as nitrile rubber might be good candidates as well, and thus future work can look into the feasibility of 3D-printing them to construct omnidirectional GRIN-PC lenses.

Chapter 4 was also limited to GRIN-PC lens designs based on the Luneburg lens profile. Testing other lens profiles [102] might be useful to achieve focusing and other extreme wave manipulations such as those based on the black hole concepts [220]. Another possible design for GRIN-PC materials is to mimic the gradient index lens in the dolphin

biosonar [221, 222]. By using soft materials to construct the GRIN-PC, its focal length could be actively adjusted by applying pressure to the lens similar to dolphin behavior.

Chapter 5 showed the importance of acoustic matching for having full control on the bandwidth and sensitivity of the designed transducer. It also showed that finding a low-loss natural material that satisfies the required impedance can be challenging, and trade-offs had to be made between using a low-loss material and one that has the correct impedance value. Passive phononic crystals can be used to match the impedance of the medium using two approaches. First, a quarter wavelength matching layer could be engineered by carefully selecting the structure of a uniform phononic crystal. Since the material properties of phononic crystals can be adjusted by considering the geometry of the unit cell, the matching layer could be designed using common low-loss materials. Another approach would be to use a tapered phononic crystal whose internal structure gradually changes from the impedance of the transducer to that of the medium minimizing the impedance mismatch.

We have also shown that GRIN-PCs could be used to focus ultrasonic waves with minimum power reflection due to the gradual change of refractive index inside the developed lens. Since the acoustic impedance also gradually changes with the refractive index, a new class of lenses could be designed while considering both the impedance and the refractive index. This class of lenses would allow for simultaneous focusing of the energy while gradually matching the impedance to that of the receiver. It would also allow for channeling power to the transducer, minimizing any reflection due to impedance mismatch and considerably improving the efficiency of the UPT system.

REFERENCES

- [1] D. Seo, R. M. Neely, K. Shen, U. Singhal, E. Alon, J. M. Rabaey, J. M. Carmena, and M. M. Maharbiz, “Wireless Recording in the Peripheral Nervous System with Ultrasonic Neural Dust,” *Neuron*, vol. 91, no. 3, pp. 529–539, Aug. 2016. DOI: 10.1016/j.neuron.2016.06.034.
- [2] T. J. Lawry, K. R. Wilt, J. D. Ashdown, H. A. Scarton, and G. J. Saulnier, “A high-performance ultrasonic system for the simultaneous transmission of data and power through solid metal barriers,” *IEEE Transactions on Ultrasonics, Ferroelectrics, and Frequency Control*, vol. 60, no. 1, pp. 194–203, Jan. 2013. DOI: 10.1109/TUFFC.2013.2550.
- [3] J. Jang and F. Adib, “Underwater backscatter networking,” ACM, Aug. 2019, pp. 187–199, ISBN: 978-1-4503-5956-6. DOI: 10.1145/3341302.3342091.
- [4] R. Guida, E. Demirors, N. Dave, and T. Melodia, “Underwater Ultrasonic Wireless Power Transfer: A Battery-less Platform for the Internet of Underwater Things,” *IEEE Transactions on Mobile Computing*, pp. 1–1, 2020. DOI: 10.1109/TMC.2020.3029679.
- [5] G. K. Ottman, H. F. Hofmann, A. C. Bhatt, and G. A. Lesieutre, “Adaptive piezoelectric energy harvesting circuit for wireless remote power supply,” *IEEE Transactions on Power Electronics*, vol. 17, no. 5, pp. 669–676, Sep. 2002. DOI: 10.1109/TPEL.2002.802194.
- [6] S. Roundy, P. K. Wright, and J. Rabaey, “A study of low level vibrations as a power source for wireless sensor nodes,” *Computer Communications, Ubiquitous Computing*, vol. 26, no. 11, pp. 1131–1144, Jul. 2003. DOI: 10.1016/S0140-3664(02)00248-7.
- [7] S. P. Beeby, M. J. Tudor, and N. M. White, “Energy harvesting vibration sources for microsystems applications,” *Meas. Sci. Technol.*, vol. 17, no. 12, R175–R195, Oct. 2006. DOI: 10.1088/0957-0233/17/12/R01.
- [8] P. D. Mitcheson, E. M. Yeatman, G. K. Rao, A. S. Holmes, and T. C. Green, “Energy Harvesting From Human and Machine Motion for Wireless Electronic Devices,” *Proceedings of the IEEE*, vol. 96, no. 9, pp. 1457–1486, Sep. 2008. DOI: 10.1109/JPROC.2008.927494.
- [9] A. Erturk and D. J. Inman, *Piezoelectric Energy Harvesting*. Apr. 2011.

- [10] M. Amin Karami and D. J. Inman, “Powering pacemakers from heartbeat vibrations using linear and nonlinear energy harvesters,” *Appl. Phys. Lett.*, vol. 100, no. 4, p. 042 901, Jan. 2012. DOI: 10.1063/1.3679102.
- [11] A. Kurs, A. Karalis, R. Moffatt, J. D. Joannopoulos, P. Fisher, and M. Soljačić, “Wireless Power Transfer via Strongly Coupled Magnetic Resonances,” *Science*, vol. 317, no. 5834, pp. 83–86, Jul. 2007. DOI: 10.1126/science.1143254.
- [12] S. Li and C. C. Mi, “Wireless Power Transfer for Electric Vehicle Applications,” *IEEE Journal of Emerging and Selected Topics in Power Electronics*, vol. 3, no. 1, pp. 4–17, Mar. 2015. DOI: 10.1109/JESTPE.2014.2319453.
- [13] S. Y. R. Hui, W. Zhong, and C. K. Lee, “A Critical Review of Recent Progress in Mid-Range Wireless Power Transfer,” *IEEE Transactions on Power Electronics*, vol. 29, no. 9, pp. 4500–4511, Sep. 2014. DOI: 10.1109/TPEL.2013.2249670.
- [14] A. Christ, M. G. Douglas, J. M. Roman, E. B. Cooper, A. P. Sample, B. H. Waters, J. R. Smith, and N. Kuster, “Evaluation of Wireless Resonant Power Transfer Systems With Human Electromagnetic Exposure Limits,” *IEEE Transactions on Electromagnetic Compatibility*, vol. 55, no. 2, pp. 265–274, Apr. 2013. DOI: 10.1109/TEMC.2012.2219870.
- [15] M. G. L. Roes, J. L. Duarte, M. A. M. Hendrix, and E. A. Lomonova, “Acoustic Energy Transfer: A Review,” *IEEE Transactions on Industrial Electronics*, vol. 60, no. 1, pp. 242–248, Jan. 2013. DOI: 10.1109/TIE.2012.2202362.
- [16] Y. Hu, X. Zhang, J. Yang, and Q. Jiang, “Transmitting electric energy through a metal wall by acoustic waves using piezoelectric transducers,” *IEEE Transactions on Ultrasonics, Ferroelectrics, and Frequency Control*, vol. 50, no. 7, pp. 773–781, Jul. 2003. DOI: 10.1109/TUFFC.2003.1214497.
- [17] C. F. Lü, J. S. Yang, J. Wang, and W. Q. Chen, “Power transmission through a hollow cylinder by acoustic waves and piezoelectric transducers with radial polarization,” *Journal of Sound and Vibration*, vol. 325, no. 4, pp. 989–999, Sep. 2009. DOI: 10.1016/j.jsv.2009.04.002.
- [18] H. F. Leung, B. J. Willis, and A. P. Hu, “Wireless electric power transfer based on Acoustic Energy through conductive media,” in *2014 9th IEEE Conference on Industrial Electronics and Applications*, Jun. 2014, pp. 1555–1560. DOI: 10.1109/ICIEA.2014.6931416.
- [19] M. E. Kiziroglou, D. E. Boyle, S. W. Wright, and E. M. Yeatman, “Acoustic energy transmission in cast iron pipelines,” *J. Phys.: Conf. Ser.*, vol. 660, no. 1, p. 012 095, 2015. DOI: 10.1088/1742-6596/660/1/012095.

- [20] M. E. Kiziroglou, D. E. Boyle, S. W. Wright, and E. M. Yeatman, “Acoustic power delivery to pipeline monitoring wireless sensors,” *Ultrasonics*, vol. 77, pp. 54–60, May 2017. DOI: 10.1016/j.ultras.2017.01.017.
- [21] H. Basaeri, D. B. Christensen, and S. Roundy, “A review of acoustic power transfer for bio-medical implants,” *Smart Materials and Structures*, vol. 25, no. 12, p. 123 001, Dec. 2016. DOI: 10.1088/0964-1726/25/12/123001.
- [22] F. Mazzilli, M. Peisino, R. Mitouassiwou, B. Cotté, P. Thoppay, C. Lafon, P. Favre, E. Meurville, and C. Dehollain, “In-vitro platform to study ultrasound as source for wireless energy transfer and communication for implanted medical devices,” in *2010 Annual International Conference of the IEEE Engineering in Medicine and Biology*, Aug. 2010, pp. 3751–3754. DOI: 10.1109/IEMBS.2010.5627541.
- [23] F. Mazzilli, C. Lafon, and C. Dehollain, “A 10.5 cm Ultrasound Link for Deep Implanted Medical Devices,” *IEEE Transactions on Biomedical Circuits and Systems*, vol. 8, no. 5, pp. 738–750, Oct. 2014. DOI: 10.1109/TBCAS.2013.2295403.
- [24] M. J. Weber, Y. Yoshihara, A. Sawaby, J. Charthad, T. C. Chang, and A. Arbabian, “A Miniaturized Single-Transducer Implantable Pressure Sensor With Time- Multiplexed Ultrasonic Data and Power Links,” *IEEE Journal of Solid-State Circuits*, vol. 53, no. 4, pp. 1089–1101, Apr. 2018. DOI: 10.1109/JSSC.2017.2782086.
- [25] M. Alam, S. Li, R. U. Ahmed, Y. M. Yam, S. Thakur, X.-Y. Wang, D. Tang, S. Ng, and Y.-P. Zheng, “Development of a battery-free ultrasonically powered functional electrical stimulator for movement restoration after paralyzing spinal cord injury,” *Journal of NeuroEngineering and Rehabilitation*, vol. 16, no. 1, p. 36, Mar. 2019. DOI: 10.1186/s12984-019-0501-4.
- [26] C. Shi, V. Andino-Pavlovsky, S. A. Lee, T. Costa, J. Elloian, E. E. Konofagou, and K. L. Shepard, “Application of a sub-0.1-mm³ implantable mote for in vivo real-time wireless temperature sensing,” *Science Advances*, vol. 7, no. 19, eabf6312, May 2021. DOI: 10.1126/sciadv.abf6312.
- [27] B. Gil, S. Anastasova, and G. ..Z. Yang, “Low-powered implantable devices activated by ultrasonic energy transfer for physiological monitoring in soft tissue via functionalized electrochemical electrodes,” *Biosensors and Bioelectronics*, vol. 182, p. 113 175, Jun. 2021. DOI: 10.1016/j.bios.2021.113175.
- [28] T. Maleki, N. Cao, S. H. Song, C. Kao, S.-C. Ko, and B. Ziaie, “An Ultrasonically Powered Implantable Micro-Oxygen Generator (IMOGEN),” *IEEE Transactions on Biomedical Engineering*, vol. 58, no. 11, pp. 3104–3111, Nov. 2011. DOI: 10.1109/TBME.2011.2163634.

- [29] A. Kim, J. Zhou, S. Samaddar, S. H. Song, B. D. Elzey, D. H. Thompson, and B. Ziaie, “An Implantable Ultrasonically-Powered Micro-Light-Source (μ Light) for Photodynamic Therapy,” *Sci Rep*, vol. 9, no. 1, p. 1395, Feb. 2019. DOI: 10.1038/s41598-019-38554-2.
- [30] D. K. Piech, J. E. Kay, B. E. Boser, and M. M. Maharbiz, “Rodent wearable ultrasound system for wireless neural recording,” in *2017 39th Annual International Conference of the IEEE Engineering in Medicine and Biology Society (EMBC)*, Jul. 2017, pp. 221–225. DOI: 10.1109/EMBC.2017.8036802.
- [31] J.-Y. Tsai, K.-H. Huang, J.-R. Wang, S.-I. Liu, and P.-C. Li, “Ultrasonic wireless power and data communication for neural stimulation,” in *2011 IEEE International Ultrasonics Symposium*, Oct. 2011, pp. 1052–1055. DOI: 10.1109/ULTSYM.2011.0258.
- [32] Y.-S. Luo, J.-R. Wang, W.-J. Huang, J.-Y. Tsai, Y.-F. Liao, W.-T. Tseng, C.-T. Yen, P.-C. Li, and S.-I. Liu, “Ultrasonic Power/Data Telemetry and Neural Stimulator With OOK-PM Signaling,” *IEEE Transactions on Circuits and Systems II: Express Briefs*, vol. 60, no. 12, pp. 827–831, Dec. 2013. DOI: 10.1109/TCSII.2013.2286000.
- [33] J. Charthad, M. J. Weber, T. C. Chang, and A. Arbabian, “A mm-Sized Implantable Medical Device (IMD) With Ultrasonic Power Transfer and a Hybrid Bi-Directional Data Link,” *IEEE Journal of Solid-State Circuits*, vol. 50, no. 8, pp. 1741–1753, Aug. 2015. DOI: 10.1109/JSSC.2015.2427336.
- [34] J. Charthad, T. C. Chang, Z. Liu, A. Sawaby, M. J. Weber, S. Baker, F. Gore, S. A. Felt, and A. Arbabian, “A mm-Sized Wireless Implantable Device for Electrical Stimulation of Peripheral Nerves,” *IEEE Transactions on Biomedical Circuits and Systems*, vol. 12, no. 2, pp. 257–270, Apr. 2018. DOI: 10.1109/TBCAS.2018.2799623.
- [35] B. Lee, M. K. Koripalli, Y. Jia, J. Acosta, M. S. E. Sendi, Y. Choi, and M. Gho-vanloo, “An Implantable Peripheral Nerve Recording and Stimulation System for Experiments on Freely Moving Animal Subjects,” *Sci Rep*, vol. 8, no. 1, p. 6115, Apr. 2018. DOI: 10.1038/s41598-018-24465-1.
- [36] L. Tacchetti, W. A. Serdijn, and V. Giagka, “An Ultrasonically Powered and Controlled Ultra-High-Frequency Biphasic Electrical Neurostimulator,” in *2018 IEEE Biomedical Circuits and Systems Conference (BioCAS)*, Oct. 2018, pp. 1–4. DOI: 10.1109/BIOCAS.2018.8584718.
- [37] D. K. Piech, B. C. Johnson, K. Shen, M. M. Ghanbari, K. Y. Li, R. M. Neely, J. E. Kay, J. M. Carmena, M. M. Maharbiz, and R. Muller, “A wireless millimetre-scale implantable neural stimulator with ultrasonically powered bidirectional communica-

- cation,” *Nat Biomed Eng*, vol. 4, no. 2, pp. 207–222, Feb. 2020. DOI: 10.1038/s41551-020-0518-9.
- [38] D. Seo, J. M. Carmena, J. M. Rabaey, E. Alon, and M. M. Mahabiz, “Neural Dust: An Ultrasonic, Low Power Solution for Chronic Brain-Machine Interfaces,” *arXiv:1307.2196 [physics, q-bio]*, Jul. 2013. arXiv: 1307.2196 [physics, q-bio]. [Online]. Available: <http://arxiv.org/abs/1307.2196>.
- [39] D. Seo, J. M. Carmena, J. M. Rabaey, M. M. Mahabiz, and E. Alon, “Model validation of untethered, ultrasonic neural dust motes for cortical recording,” *Journal of Neuroscience Methods*, Brain Computer Interfaces; Tribute to Greg A. Gerhardt, vol. 244, pp. 114–122, Apr. 2015. DOI: 10.1016/j.jneumeth.2014.07.025.
- [40] L. Jiang, Y. Yang, R. Chen, G. Lu, R. Li, J. Xing, K. K. Shung, M. S. Humayun, J. Zhu, Y. Chen, and Q. Zhou, “Ultrasound-Induced Wireless Energy Harvesting for Potential Retinal Electrical Stimulation Application,” *Advanced Functional Materials*, vol. 29, no. 33, p. 1902522, 2019. DOI: 10.1002/adfm.201902522.
- [41] FDA, “Marketing Clearance of Diagnostic Ultrasound Systems and Transducers,” Federal Drug & Food Administration, Tech. Rep. FDA-2017-D-5372, Jun. 2019, p. 64. [Online]. Available: <https://www.fda.gov/media/71100/download>.
- [42] J. Thimot and K. L. Shepard, “Bioelectronic devices: Wirelessly powered implants,” *Nat Biomed Eng*, vol. 1, no. 3, pp. 1–2, Mar. 2017. DOI: 10.1038/s41551-017-0051.
- [43] M. Seyedi, B. Kibret, D. T. H. Lai, and M. Faulkner, “A Survey on Intrabody Communications for Body Area Network Applications,” *IEEE Transactions on Biomedical Engineering*, vol. 60, no. 8, pp. 2067–2079, Aug. 2013. DOI: 10.1109/TBME.2013.2254714.
- [44] B. Jaafar, J. Luo, D. Firfilionis, A. Soltan, J. Neasham, and P. Degenaar, “Ultrasound Intra Body Multi Node Communication System for Bioelectronic Medicine,” *Sensors*, vol. 20, no. 1, p. 31, Jan. 2020. DOI: 10.3390/s20010031.
- [45] J. Heidemann, M. Stojanovic, and M. Zorzi, “Underwater sensor networks: Applications, advances and challenges,” *Philosophical Transactions of the Royal Society A: Mathematical, Physical and Engineering Sciences*, vol. 370, no. 1958, pp. 158–175, Jan. 2012. DOI: 10.1098/rsta.2011.0214.
- [46] L. Lanbo, Z. Shengli, and C. Jun-Hong, “Prospects and problems of wireless communication for underwater sensor networks,” *Wireless Communications and Mobile Computing*, vol. 8, no. 8, pp. 977–994, 2008. DOI: 10.1002/wcm.654.
- [47] J. Lloret, “Underwater Sensor Nodes and Networks,” *Sensors*, vol. 13, no. 9, pp. 11 782–11 796, Sep. 2013. DOI: 10.3390/s130911782.

- [48] J. Pearlman, S. Jirka, J. del Rio, E. Delory, L. Frommhold, S. Martinez, and T. O'Reilly, "Oceans of Tomorrow sensor interoperability for in-situ ocean monitoring," in *OCEANS 2016 MTS/IEEE Monterey*, Sep. 2016, pp. 1–8. DOI: 10.1109/OCEANS.2016.7761404.
- [49] M. Stojanovic, "On the relationship between capacity and distance in an underwater acoustic communication channel," *SIGMOBILE Mob. Comput. Commun. Rev.*, vol. 11, no. 4, pp. 34–43, Oct. 2007. DOI: 10.1145/1347364.1347373.
- [50] C. G. Lowe, K. N. Holland, and T. G. Wolcott, "A new acoustic tailbeat transmitter for fishes," *Fisheries Research*, vol. 36, no. 2, pp. 275–283, Jun. 1998. DOI: 10.1016/S0165-7836(98)00109-X.
- [51] M. Føre, J. A. Alfredsen, and A. Grønningsater, "Development of two telemetry-based systems for monitoring the feeding behaviour of Atlantic salmon (*Salmo salar* L.) in aquaculture sea-cages," *Computers and Electronics in Agriculture*, vol. 76, no. 2, pp. 240–251, May 2011. DOI: 10.1016/j.compag.2011.02.003.
- [52] H. Li, C. Tian, J. Lu, M. J. Myjak, J. J. Martinez, R. S. Brown, and Z. D. Deng, "An Energy Harvesting Underwater Acoustic Transmitter for Aquatic Animals," *Sci Rep*, vol. 6, no. 1, p. 33 804, Sep. 2016. DOI: 10.1038/srep33804.
- [53] L. Paull, S. Saeedi, M. Seto, and H. Li, "AUV Navigation and Localization: A Review," *IEEE Journal of Oceanic Engineering*, vol. 39, no. 1, pp. 131–149, Jan. 2014. DOI: 10.1109/JOE.2013.2278891.
- [54] E. Demirors, B. G. Shankar, G. E. Santagati, and T. Melodia, "SEANet: A Software-Defined Acoustic Networking Framework for Reconfigurable Underwater Networking," in *Proceedings of the 10th International Conference on Underwater Networks & Systems*, ser. WUWNET '15, New York, NY, USA: Association for Computing Machinery, Oct. 2015, pp. 1–8, ISBN: 978-1-4503-4036-6. DOI: 10.1145/2831296.2831316.
- [55] E. Demirors, J. Shi, R. Guida, and T. Melodia, "SEANet G2: Toward a high-data-rate software-defined underwater acoustic networking platform," in *Proceedings of the 11th ACM International Conference on Underwater Networks & Systems*, ser. WUWNet '16, New York, NY, USA: Association for Computing Machinery, Oct. 2016, pp. 1–8, ISBN: 978-1-4503-4637-5. DOI: 10.1145/2999504.3001112.
- [56] M. Jouhari, K. Ibrahimi, H. Tembine, and J. Ben-Othman, "Underwater Wireless Sensor Networks: A Survey on Enabling Technologies, Localization Protocols, and Internet of Underwater Things," *IEEE Access*, vol. 7, pp. 96 879–96 899, 2019. DOI: 10.1109/ACCESS.2019.2928876.

- [57] M. Jahanbakht, W. Xiang, L. Hanzo, and M. Rahimi Azghadi, “Internet of Underwater Things and Big Marine Data Analytics—A Comprehensive Survey,” *IEEE Communications Surveys Tutorials*, vol. 23, no. 2, pp. 904–956, Jan. 2021. DOI: 10.1109/COMST.2021.3053118.
- [58] R. Ghaffarivardavagh, S. S. Afzal, O. Rodriguez, and F. Adib, “Ultra-Wideband Underwater Backscatter via Piezoelectric Metamaterials,” in *Proceedings of the Annual Conference of the ACM Special Interest Group on Data Communication on the Applications, Technologies, Architectures, and Protocols for Computer Communication*, ser. SIGCOMM ’20, New York, NY, USA: Association for Computing Machinery, Jul. 2020, pp. 722–734, ISBN: 978-1-4503-7955-7. DOI: 10.1145/3387514.3405898.
- [59] R. Guida, E. Demirors, N. Dave, J. Rodowicz, and T. Melodia, “An Acoustically Powered Battery-less Internet of Underwater Things Platform,” in *2018 Fourth Underwater Communications and Networking Conference (UComms)*, Aug. 2018, pp. 1–5. DOI: 10.1109/UComms.2018.8493229.
- [60] C. Sugino, R. Gerbe, C. Reinke, M. Ruzzene, A. Erturk, and I. El-Kady, “Ultrasonic Communication through a Metallic Barrier: Transmission Modeling and Crosstalk Minimization,” in *2020 IEEE International Ultrasonics Symposium (IUS)*, Sep. 2020, pp. 1–3. DOI: 10.1109/IUS46767.2020.9251623.
- [61] D.-X. Yang, Z. Hu, H. Zhao, H.-F. Hu, Y.-Z. Sun, and B.-J. Hou, “Through-Metal-Wall Power Delivery and Data Transmission for Enclosed Sensors: A Review,” *Sensors*, vol. 15, no. 12, pp. 31 581–31 605, Dec. 2015. DOI: 10.3390/s151229870.
- [62] F. A. Duck, *Physical Properties of Tissues: A Comprehensive Reference Book*. Academic Press, Oct. 2013.
- [63] K. Ono, “A Comprehensive Report on Ultrasonic Attenuation of Engineering Materials, Including Metals, Ceramics, Polymers, Fiber-Reinforced Composites, Wood, and Rocks,” *Applied Sciences*, vol. 10, no. 7, p. 2230, Jan. 2020. DOI: 10.3390/app10072230.
- [64] L. E. Kinsler, Ed., *Fundamentals of Acoustics*, 4th ed. New York: Wiley, 2000, ISBN: 0-471-84789-5.
- [65] D. B. Christensen and S. Roundy, “Ultrasonically powered piezoelectric generators for bio-implantable sensors: Plate versus diaphragm,” *Journal of Intelligent Material Systems and Structures*, vol. 27, no. 8, pp. 1092–1105, 2015. DOI: 10.1177/1045389X15585897.

- [66] R. Krimholtz, D. A. Leedom, and G. L. Matthaei, “New equivalent circuits for elementary piezoelectric transducers,” *Electronics Letters*, vol. 6, no. 13, pp. 398–399, Jun. 1970. DOI: 10.1049/el:19700280.
- [67] A. Puttmer, P. Hauptmann, R. Lucklum, O. Krause, and B. Henning, “SPICE model for lossy piezoceramic transducers,” *IEEE Transactions on Ultrasonics, Ferroelectrics, and Frequency Control*, vol. 44, no. 1, pp. 60–66, Jan. 1997. DOI: 10.1109/58.585191.
- [68] S. Ozeri, D. Shmilovitz, S. Singer, and C.-C. Wang, “Ultrasonic transcutaneous energy transfer using a continuous wave 650kHz Gaussian shaded transmitter,” *Ultrasonics*, vol. 50, no. 7, pp. 666–674, Jun. 2010. DOI: 10.1016/j.ultras.2010.01.004.
- [69] S. H. Song, A. Kim, and B. Ziaie, “Omnidirectional Ultrasonic Powering for Millimeter - Scale Implantable Devices,” *IEEE Transactions on Biomedical Engineering*, vol. 62, no. 11, pp. 2717–2723, Nov. 2015. DOI: 10.1109/TBME.2015.2444854.
- [70] T. Chou, R. Subramanian, J. Park, and P. P. Mercier, “A miniaturized ultrasonic power delivery system,” in *2014 IEEE Biomedical Circuits and Systems Conference (BioCAS) Proceedings*, Oct. 2014, pp. 440–443. DOI: 10.1109/BioCAS.2014.6981757.
- [71] A. Denisov and E. Yeatman, “Ultrasonic vs. Inductive Power Delivery for Miniature Biomedical Implants,” in *2010 International Conference on Body Sensor Networks*, Jun. 2010, pp. 84–89. DOI: 10.1109/BSN.2010.27.
- [72] S. Shahab, M. Gray, and A. Erturk, “Ultrasonic power transfer from a spherical acoustic wave source to a free-free piezoelectric receiver: Modeling and experiment,” *Journal of Applied Physics*, vol. 117, no. 10, 2015. DOI: 10.1063/1.4914130.
- [73] ——, “An experimentally validated contactless acoustic energy transfer model with resistive-reactive electrical loading,” in *Active and Passive Smart Structures and Integrated Systems*, W.-H. Liao, Ed., vol. 9431, San Diego, Calif.: SPIE, 2015, p. 943 105, ISBN: 978-1-62841-534-6. DOI: 10.1117/12.2084361.
- [74] M. Gorostiaga, M. C. Wapler, and U. Wallrabe, “Analytic model for ultrasound energy receivers and their optimal electric loads II: Experimental validation,” *Smart Mater. Struct.*, vol. 26, no. 10, p. 105 021, 2017. DOI: 10.1088/1361-665X/aa86f6.
- [75] ——, “Analytic model for ultrasound energy receivers and their optimal electric loads,” *Smart Mater. Struct.*, vol. 26, no. 8, p. 085 003, 2017. DOI: 10.1088/1361-665X/aa61ea.

- [76] A. Allam, K. G. Sabra, and A. Erturk, “Aspect Ratio-Dependent Dynamics of Piezoelectric Transducers in Wireless Acoustic Power Transfer,” *IEEE Transactions on Ultrasonics, Ferroelectrics, and Frequency Control*, vol. 67, no. 5, pp. 984–996, May 2020. DOI: 10.1109/TUFFC.2019.2962711.
- [77] S. Sherrit, B. Doty, M. Badescu, X. Bao, Y. Bar-Cohen, J. Aldrich, and Z. Chang, “Studies of acoustic-electric feed-throughs for power transmission through structures,” in *Smart Structures and Materials 2006: Industrial and Commercial Applications of Smart Structures Technologies*, vol. 6171, International Society for Optics and Photonics, Mar. 2006, p. 617 102. DOI: 10.1117/12.657736.
- [78] X. Bao, B. J. Doty, S. Sherrit, M. Badescu, Y. Bar-Cohen, J. Aldrich, and Z. Chang, “Wireless piezoelectric acoustic-electric power feedthru,” in *Sensors and Smart Structures Technologies for Civil, Mechanical, and Aerospace Systems 2007*, vol. 6529, International Society for Optics and Photonics, Apr. 2007, p. 652 940. DOI: 10.1117/12.716429.
- [79] X. Bao, W. Biederman, S. Sherrit, M. Badescu, Y. Bar-Cohen, C. Jones, J. Aldrich, and Z. Chang, “High-power piezoelectric acoustic-electric power feedthru for metal walls,” in *Industrial and Commercial Applications of Smart Structures Technologies 2008*, vol. 6930, International Society for Optics and Photonics, Mar. 2008, 69300Z. DOI: 10.1117/12.776473.
- [80] D. A. Shoudy, G. J. Saulnier, H. A. Scarton, P. K. Das, S. Roa-Prada, J. D. Ashdown, and A. J. Gavens, “An Ultrasonic Through-Wall Communication System with Power Harvesting,” in *2007 IEEE Ultrasonics Symposium Proceedings*, Oct. 2007, pp. 1848–1853. DOI: 10.1109/ULTSYM.2007.465.
- [81] J. D. Ashdown, K. R. Wilt, T. J. Lawry, G. J. Saulnier, D. A. Shoudy, H. A. Scarton, and A. J. Gavens, “A full-duplex ultrasonic through-wall communication and power delivery system,” *IEEE Transactions on Ultrasonics, Ferroelectrics, and Frequency Control*, vol. 60, no. 3, pp. 587–595, Mar. 2013. DOI: 10.1109/TUFFC.2013.2600.
- [82] K. R. Wilt, H. A. Scarton, G. J. Saulnier, T. J. Lawry, and J. D. Ashdown, “High-Power Operation of Acoustic-Electric Power Feedthroughs Through Thick Metallic Barriers,” in *ASME 2012 International Mechanical Engineering Congress and Exposition*, American Society of Mechanical Engineers Digital Collection, Oct. 2013, pp. 475–482. DOI: 10.1115/IMECE2012-89496.
- [83] M. Kluge, J. Sabater, J. Schalk, L. V. Ngo, H. Seidel, and U. Schmid, “Wireless Sensing of Physical Parameters Inside Hermetically Enclosed Conductive Envelopes,” in *ASME 2007 International Design Engineering Technical Conferences and Computers and Information in Engineering Conference*, American Society of

Mechanical Engineers Digital Collection, Sep. 2007, pp. 353–359. DOI: 10.1115/DETC2007-35481.

- [84] O. Freychet, F. Frassati, S. Boisseau, N. Garraud, P. Gasnier, and G. Despesse, “Analytical optimization of piezoelectric acoustic power transfer systems,” *Eng. Res. Express*, vol. 2, no. 4, p. 045 022, Nov. 2020. DOI: 10.1088/2631-8695/abcb4a.
- [85] T. J. Winnard, “Theoretical Parametric Study of Through-Wall Acoustic Energy Transfer Systems,” Thesis, Virginia Tech, May 2021. [Online]. Available: <https://vttechworks.lib.vt.edu/handle/10919/103387>.
- [86] H. F. Leung and A. P. Hu, “Modeling the Contact Interface of Ultrasonic Power Transfer System based on Mechanical and Electrical Equivalence,” *IEEE Journal of Emerging and Selected Topics in Power Electronics*, vol. PP, no. 99, pp. 1–1, 2017. DOI: 10.1109/JESTPE.2017.2720852.
- [87] O. Freychet, S. Boisseau, F. Frassati, V. Josselin, P. Gasnier, N. Garraud, R. Gohier, D. Gibus, S. Brulais, and G. Despesse, “A Versatile Through-Metal-Wall Acoustic Power and Data Transfer Solution,” in *2019 19th International Conference on Micro and Nanotechnology for Power Generation and Energy Conversion Applications (PowerMEMS)*, Dec. 2019, pp. 1–6. DOI: 10.1109/PowerMEMS49317.2019.92321100357.
- [88] S. Moss, D. Science, and T. O. Division, *Modelling and experimental validation of the acoustic electric feedthrough technique*, Archived Website; Thesis, 2008. [Online]. Available: <https://trove.nla.gov.au/version/44687280>.
- [89] K. R. Wilt, T. J. Lawry, H. A. Scarton, and G. J. Saulnier, “One-dimensional pressure transfer models for acoustic–electric transmission channels,” *Journal of Sound and Vibration*, vol. 352, pp. 158–173, Sep. 2015. DOI: 10.1016/j.jsv.2015.04.031.
- [90] H. Yang, M. Wu, Z. Yu, and J. Yang, “An Ultrasonic Through-Metal-Wall Power Transfer System with Regulated DC Output,” *Applied Sciences*, vol. 8, no. 5, p. 692, May 2018. DOI: 10.3390/app8050692.
- [91] V. F.-G. Tseng, S. S. Bedair, and N. Lazarus, “Acoustic Power Transfer and Communication With a Wireless Sensor Embedded Within Metal,” *IEEE Sensors Journal*, vol. 18, no. 13, pp. 5550–5558, Jul. 2018. DOI: 10.1109/JSEN.2018.2839558.
- [92] S. Moss, J. Skippen, M. Konak, I. Powlesland, and S. Galea, “Detachable acoustic electric feedthrough,” in *Sensors and Smart Structures Technologies for Civil, Mechanical, and Aerospace Systems 2010*, vol. 7647, International Society for Optics and Photonics, Apr. 2010, p. 764 745. DOI: 10.1117/12.848901.

- [93] A. Allam, K. Sabra, and A. Erturk, “3D-Printed Gradient-Index Phononic Crystal Lens for Underwater Acoustic Wave Focusing,” *Phys. Rev. Applied*, vol. 13, no. 6, p. 064 064, Jun. 2020. DOI: 10.1103/PhysRevApplied.13.064064.
- [94] ——, “Sound energy harvesting by leveraging a 3D-printed phononic crystal lens,” *Appl. Phys. Lett.*, vol. 118, no. 10, p. 103 504, Mar. 2021. DOI: 10.1063/5.0030698.
- [95] M. I. Hussein, M. J. Leamy, and M. Ruzzene, “Dynamics of Phononic Materials and Structures: Historical Origins, Recent Progress, and Future Outlook,” *Appl. Mech. Rev.*, vol. 66, no. 4, pp. 040802-040802–38, May 2014. DOI: 10.1115/1.4026911.
- [96] Z. He, F. Cai, and Z. Liu, “Guiding acoustic waves with graded phononic crystals,” *Solid State Commun.*, vol. 148, no. 1, pp. 74–77, Oct. 2008. DOI: 10.1016/j.ssc.2008.07.007.
- [97] L.-Y. Wu and L.-W. Chen, “An acoustic bending waveguide designed by graded sonic crystals,” *Journal of Applied Physics*, vol. 110, no. 11, p. 114 507, Dec. 2011. DOI: 10.1063/1.3664856.
- [98] A. Colombi, D. Colquitt, P. Roux, S. Guenneau, and R. V. Craster, “A seismic metamaterial: The resonant metawedge,” *Scientific Reports*, vol. 6, p. 27 717, Jun. 2016. DOI: 10.1038/srep27717.
- [99] A. Colombi, V. Ageeva, R. J. Smith, A. Clare, R. Patel, M. Clark, D. Colquitt, P. Roux, S. Guenneau, and R. V. Craster, “Enhanced sensing and conversion of ultrasonic Rayleigh waves by elastic metasurfaces,” *Scientific Reports*, vol. 7, no. 1, p. 6750, Jul. 2017. DOI: 10.1038/s41598-017-07151-6.
- [100] S. Alan, A. Allam, and A. Erturk, “Programmable mode conversion and bandgap formation for surface acoustic waves using piezoelectric metamaterials,” *Appl. Phys. Lett.*, vol. 115, no. 9, p. 093 502, Aug. 2019. DOI: 10.1063/1.5110701.
- [101] S.-C. S. Lin, T. J. Huang, J.-H. Sun, and T.-T. Wu, “Gradient-index phononic crystals,” *Phys. Rev. B*, vol. 79, no. 9, p. 094 302, Mar. 2009. DOI: 10.1103/PhysRevB.79.094302.
- [102] A. Climente, D. Torrent, and J. Sánchez-Dehesa, “Sound focusing by gradient index sonic lenses,” *Appl. Phys. Lett.*, vol. 97, no. 10, p. 104 103, Sep. 2010. DOI: 10.1063/1.3488349.
- [103] T. P. Martin, M. Nicholas, G. J. Orris, L.-W. Cai, D. Torrent, and J. Sánchez-Dehesa, “Sonic gradient index lens for aqueous applications,” *Appl. Phys. Lett.*, vol. 97, no. 11, p. 113 503, Sep. 2010. DOI: 10.1063/1.3489373.

- [104] L. Zigoneanu, B.-I. Popa, A. F. Starr, and S. A. Cummer, “Design and measurements of a broadband two-dimensional acoustic metamaterial with anisotropic effective mass density,” *Journal of Applied Physics*, vol. 109, no. 5, p. 054 906, Mar. 2011. DOI: 10.1063/1.3552990.
- [105] Y. Li, G. Yu, B. Liang, X. Zou, G. Li, S. Cheng, and J. Cheng, “Three-dimensional Ultrathin Planar Lenses by Acoustic Metamaterials,” *Sci. Rep.*, vol. 4, p. 6830, Oct. 2014. DOI: 10.1038/srep06830.
- [106] A. Climente, D. Torrent, and J. Sánchez-Dehesa, “Gradient index lenses for flexural waves based on thickness variations,” *Appl. Phys. Lett.*, vol. 105, no. 6, p. 064 101, Aug. 2014. DOI: 10.1063/1.4893153.
- [107] J. Zhao, B. Bonello, R. Marchal, and O. Boyko, “Beam path and focusing of flexural Lamb waves within phononic crystal-based acoustic lenses,” *New J. Phys.*, vol. 16, no. 6, p. 063 031, 2014. DOI: 10.1088/1367-2630/16/6/063031.
- [108] Y. Chen, H. Liu, M. Reilly, H. Bae, and M. Yu, “Enhanced acoustic sensing through wave compression and pressure amplification in anisotropic metamaterials,” *Nature Communications*, vol. 5, p. 5247, Oct. 2014. DOI: 10.1038/ncomms6247.
- [109] Y.-J. Liang, L.-W. Chen, C.-C. Wang, and I.-L. Chang, “An acoustic absorber implemented by graded index phononic crystals,” *J. Appl. Phys.*, vol. 115, no. 24, p. 244 513, Jun. 2014. DOI: 10.1063/1.4885459.
- [110] N. Jiménez, V. Romero-García, A. Cebrecos, R. Picó, V. J. Sánchez-Morcillo, and L. M. Garcia-Raffi, “Broadband quasi perfect absorption using chirped multi-layer porous materials,” *AIP Adv.*, vol. 6, no. 12, p. 121 605, Dec. 2016. DOI: 10.1063/1.4971274.
- [111] X. H. Zhang, Z. G. Qu, X. C. He, and D. L. Lu, “Experimental study on the sound absorption characteristics of continuously graded phononic crystals,” *AIP Advances*, vol. 6, no. 10, p. 105 205, Oct. 2016. DOI: 10.1063/1.4965923.
- [112] R. Fleury and A. Alù, “Metamaterial buffer for broadband non-resonant impedance matching of obliquely incident acoustic waves,” *The Journal of the Acoustical Society of America*, vol. 136, no. 6, pp. 2935–2940, Dec. 2014. DOI: 10.1121/1.4900567.
- [113] Y. Fu, J. Li, Y. Xie, C. Shen, Y. Xu, H. Chen, and S. A. Cummer, “Compact acoustic retroreflector based on a mirrored Luneburg lens,” *Phys. Rev. Materials*, vol. 2, no. 10, p. 105 202, Oct. 2018. DOI: 10.1103/PhysRevMaterials.2.105202.

- [114] C. J. Naify, T. P. Martin, C. N. Layman, M. Nicholas, A. L. Thangawng, D. C. Calvo, and G. J. Orris, “Underwater acoustic omnidirectional absorber,” *Appl. Phys. Lett.*, vol. 104, no. 7, p. 073 505, Feb. 2014. DOI: 10.1063/1.4865480.
- [115] F. Ju, Y. Tian, Y. Cheng, and X. Liu, “Asymmetric acoustic transmission with a lossy gradient-index metasurface,” *Appl. Phys. Lett.*, vol. 113, no. 12, p. 121 901, Sep. 2018. DOI: 10.1063/1.5032263.
- [116] S. Tol, F. L. Degertekin, and A. Erturk, “Gradient-index phononic crystal lens-based enhancement of elastic wave energy harvesting,” *Appl. Phys. Lett.*, vol. 109, no. 6, p. 063 902, Aug. 2016. DOI: 10.1063/1.4960792.
- [117] ——, “Phononic crystal Luneburg lens for omnidirectional elastic wave focusing and energy harvesting,” *Appl. Phys. Lett.*, vol. 111, no. 1, p. 013 503, Jul. 2017. DOI: 10.1063/1.4991684.
- [118] ——, “3D-printed phononic crystal lens for elastic wave focusing and energy harvesting,” *Addit. Manuf.*, vol. 29, p. 100 780, Oct. 2019. DOI: 10.1016/j.addma.2019.100780.
- [119] J. Zhao, B. Bonello, and O. Boyko, “Focusing of the lowest-order antisymmetric Lamb mode behind a gradient-index acoustic metasurface with local resonators,” *Phys. Rev. B*, vol. 93, no. 17, p. 174 306, May 2016. DOI: 10.1103/PhysRevB.93.174306.
- [120] H. Y. Dong, Q. Cheng, G. Y. Song, W. X. Tang, J. Wang, and T. J. Cui, “Realization of broadband acoustic metamaterial lens with quasi-conformal mapping,” *Appl. Phys. Express*, vol. 10, no. 8, p. 087 202, Jul. 2017. DOI: 10.7567/APEX.10.087202.
- [121] X. Su, A. N. Norris, C. W. Cushing, M. R. Haberman, and P. S. Wilson, “Broadband focusing of underwater sound using a transparent pentamode lens,” *The Journal of the Acoustical Society of America*, vol. 141, no. 6, pp. 4408–4417, Jun. 2017. DOI: 10.1121/1.4985195.
- [122] R. Zhu, C. Ma, B. Zheng, M. Y. Musa, L. Jing, Y. Yang, H. Wang, S. Dehdashti, N. X. Fang, and H. Chen, “Bifunctional acoustic metamaterial lens designed with coordinate transformation,” *Appl. Phys. Lett.*, vol. 110, no. 11, p. 113 503, Mar. 2017. DOI: 10.1063/1.4978689.
- [123] C. M. Park and S. H. Lee, “Acoustic Luneburg lens using orifice-type metamaterial unit cells,” *Appl. Phys. Lett.*, vol. 112, no. 7, p. 074 101, Feb. 2018. DOI: 10.1063/1.5016477.

- [124] Y. Jin, R. Kumar, O. Poncelet, O. Mondain-Monval, and T. Brunet, “Flat acoustics with soft gradient-index metasurfaces,” *Nat. Commun.*, vol. 10, no. 1, p. 143, Jan. 2019. DOI: 10.1038/s41467-018-07990-5.
- [125] Y. Ruan, X. Liang, Z. Wang, T. Wang, Y. Deng, F. Qu, and J. Zhang, “3-D underwater acoustic wave focusing by periodic structure,” *Appl. Phys. Lett.*, vol. 114, no. 8, p. 081 908, Feb. 2019. DOI: 10.1063/1.5081661.
- [126] A. Sukhovich, L. Jing, and J. H. Page, “Negative refraction and focusing of ultrasound in two-dimensional phononic crystals,” *Phys. Rev. B*, vol. 77, no. 1, p. 014 301, Jan. 2008. DOI: 10.1103/PhysRevB.77.014301.
- [127] G. D’Aguanno, K. Q. Le, R. Trimm, A. Alù, N. Mattiucci, A. D. Mathias, N. Aközbek, and M. J. Bloemer, “Broadband metamaterial for nonresonant matching of acoustic waves,” *Sci. Rep.*, vol. 2, p. 340, Mar. 2012. DOI: 10.1038/srep00340.
- [128] A. Hladky-Hennion, C. Croenne, J. O. Vasseur, L. Haumesser, and A. N. Norris, “Focusing capability of a phononic crystal based on a hollow metallic structure,” *IEEE Trans. Ultrason., Ferroelectr., Freq. Control*, vol. 61, no. 8, pp. 1314–1321, Aug. 2014. DOI: 10.1109/TUFFC.2014.3038.
- [129] T. P. Martin, C. J. Naify, E. A. Skerritt, C. N. Layman, M. Nicholas, D. C. Calvo, G. J. Orris, D. Torrent, and J. Sánchez-Dehesa, “Transparent Gradient-Index Lens for Underwater Sound Based on Phase Advance,” *Phys. Rev. Applied*, vol. 4, no. 3, p. 034 003, Sep. 2015. DOI: 10.1103/PhysRevApplied.4.034003.
- [130] S. A. M. Tofail, E. P. Koumoulos, A. Bandyopadhyay, S. Bose, L. O’Donoghue, and C. Charitidis, “Additive manufacturing: Scientific and technological challenges, market uptake and opportunities,” *Mater. Today*, vol. 21, no. 1, pp. 22–37, Jan. 2018. DOI: 10.1016/j.mattod.2017.07.001.
- [131] Y. Xie, Y. Fu, Z. Jia, J. Li, C. Shen, Y. Xu, H. Chen, and S. A. Cummer, “Acoustic Imaging with Metamaterial Luneburg Lenses,” *Sci. Rep.*, vol. 8, no. 1, p. 16 188, Nov. 2018. DOI: 10.1038/s41598-018-34581-7.
- [132] M. G. L. Roes, M. A. M. Hendrix, and J. L. Duarte, “Contactless energy transfer through air by means of ultrasound,” in *IECON 2011 - 37th Annual Conference of the IEEE Industrial Electronics Society*, Nov. 2011, pp. 1238–1243. DOI: 10.1109/IECON.2011.6119486.
- [133] V. F. G. Tseng, S. S. Bedair, and N. Lazarus, “Acoustic wireless power transfer with receiver array for enhanced performance,” in *2017 IEEE Wireless Power Transfer Conference (WPTC)*, May 2017, pp. 1–4. DOI: 10.1109/WPT.2017.7953842.

- [134] ——, “Phased Array Focusing for Acoustic Wireless Power Transfer,” *IEEE Transactions on Ultrasonics, Ferroelectrics, and Frequency Control*, vol. 65, no. 1, pp. 39–49, Jan. 2018. DOI: 10.1109/TUFFC.2017.2771283.
- [135] J. Choi, I. Jung, and C.-Y. Kang, “A brief review of sound energy harvesting,” *Nano Energy*, vol. 56, pp. 169–183, Feb. 2019. DOI: 10.1016/j.nanoen.2018.11.036.
- [136] S. B. Horowitz, M. Sheplak, L. N. Cattafesta, and T. Nishida, “A MEMS acoustic energy harvester,” *J. Micromech. Microeng.*, vol. 16, no. 9, S174–S181, Aug. 2006. DOI: 10.1088/0960-1317/16/9/S02.
- [137] F. Liu, A. Phipps, S. Horowitz, K. Ngo, L. Cattafesta, T. Nishida, and M. Sheplak, “Acoustic energy harvesting using an electromechanical Helmholtz resonator,” *J. Acoust. Soc. Am.*, vol. 123, no. 4, pp. 1983–1990, Apr. 2008. DOI: 10.1121/1.2839000.
- [138] M. Yuan, Z. Cao, J. Luo, J. Zhang, and C. Chang, “An efficient low-frequency acoustic energy harvester,” *Sens. Actuators, A*, vol. 264, pp. 84–89, Sep. 2017. DOI: 10.1016/j.sna.2017.07.051.
- [139] G.-S. Liu, Y.-Y. Peng, M.-H. Liu, X.-Y. Zou, and J.-C. Cheng, “Broadband acoustic energy harvesting metasurface with coupled Helmholtz resonators,” *Appl. Phys. Lett.*, vol. 113, no. 15, p. 153 503, Oct. 2018. DOI: 10.1063/1.5041731.
- [140] B. Li, J. H. You, and Y.-J. Kim, “Low frequency acoustic energy harvesting using PZT piezoelectric plates in a straight tube resonator,” *Smart Mater. Struct.*, vol. 22, no. 5, p. 055 013, Apr. 2013. DOI: 10.1088/0964-1726/22/5/055013.
- [141] H. Guo, Y. Wang, X. Wang, and C. Xu, “Investigation on acoustic energy harvesting based on quarter-wavelength resonator phononic crystals,” *Advances in Mechanical Engineering*, vol. 10, no. 1, p. 1687814 017 748 077, Jan. 2018. DOI: 10.1177/1687814017748077.
- [142] L.-Y. Wu, L.-W. Chen, and C.-M. Liu, “Acoustic energy harvesting using resonant cavity of a sonic crystal,” *Appl. Phys. Lett.*, vol. 95, no. 1, p. 013 506, Jul. 2009. DOI: 10.1063/1.3176019.
- [143] W.-C. Wang, L.-Y. Wu, L.-W. Chen, and C.-M. Liu, “Acoustic energy harvesting by piezoelectric curved beams in the cavity of a sonic crystal,” *Smart Mater. Struct.*, vol. 19, no. 4, p. 045 016, Mar. 2010. DOI: 10.1088/0964-1726/19/4/045016.
- [144] M. Carrara, M. R. Cacan, J. Toussaint, M. J. Leamy, M. Ruzzene, and A. Erturk, “Metamaterial-inspired structures and concepts for elastoacoustic wave energy harvesting,” *Smart Mater. Struct.*, vol. 22, no. 6, p. 065 004, Apr. 2013. DOI: 10.1088/0964-1726/22/6/065004.

- [145] A. Yang, P. Li, Y. Wen, C. Lu, X. Peng, J. Zhang, and W. He, “Enhanced Acoustic Energy Harvesting Using Coupled Resonance Structure of Sonic Crystal and Helmholtz Resonator,” *Appl. Phys. Express*, vol. 6, no. 12, p. 127 101, Nov. 2013. DOI: 10.7567/APEX.6.127101.
- [146] S. Qi and B. Assouar, “Acoustic energy harvesting based on multilateral metasurfaces,” *Appl. Phys. Lett.*, vol. 111, no. 24, p. 243 506, Dec. 2017. DOI: 10.1063/1.5003299.
- [147] J. M. D. Ponti, A. Colombi, R. Ardito, F. Braghin, A. Corigliano, and R. V. Craster, “Graded elastic metasurface for enhanced energy harvesting,” *New J. Phys.*, vol. 22, no. 1, p. 013 013, Jan. 2020. DOI: 10.1088/1367-2630/ab6062.
- [148] Y. Jin, B. Djafari-Rouhani, and D. Torrent, “Gradient index phononic crystals and metamaterials,” *Nanophotonics*, vol. 8, no. 5, pp. 685–701, 2019. DOI: 10.1515/nanoph-2018-0227.
- [149] J. Hyun, C.-S. Park, J. Chang, W.-H. Cho, and M. Kim, “Gradient-index phononic crystals for omnidirectional acoustic wave focusing and energy harvesting,” *Appl. Phys. Lett.*, vol. 116, no. 23, p. 234 101, Jun. 2020. DOI: 10.1063/5.0008791.
- [150] M. Kluge, T. Becker, J. Schalk, and T. Otterpohl, “Remote acoustic powering and data transmission for sensors inside of conductive envelopes,” in *2008 IEEE SENSORS*, Oct. 2008, pp. 41–44. DOI: 10.1109/ICSENS.2008.4716378.
- [151] D. J. Graham, J. A. Neasham, and B. S. Sharif, “Investigation of Methods for Data Communication and Power Delivery Through Metals,” *IEEE Transactions on Industrial Electronics*, vol. 58, no. 10, pp. 4972–4980, Oct. 2011. DOI: 10.1109/TIE.2010.2103535.
- [152] T. J. Lawry, G. J. Saulnier, J. D. Ashdown, K. R. Wilt, H. A. Scarton, S. Pascarelle, and J. D. Pinezich, “Penetration-free system for transmission of data and power through solid metal barriers,” in *2011 - MILCOM 2011 Military Communications Conference*, Nov. 2011, pp. 389–395. DOI: 10.1109/MILCOM.2011.6127699.
- [153] X. Tang, M. Sameer, and S. Mandal, “Acoustic Wireless Power and Data Telemetry for Structural Health Monitoring,” in *2018 IEEE SENSORS*, Oct. 2018, pp. 1–4. DOI: 10.1109/ICSENS.2018.8589762.
- [154] S. Roa-Prada, H. A. Scarton, G. J. Saulnier, D. A. Shoudy, J. D. Ashdown, P. K. Das, and A. J. Gavens, “An Ultrasonic Through-Wall Communication (UTWC) System Model,” *Journal of Vibration and Acoustics*, vol. 135, no. 011004, Feb. 2013. DOI: 10.1115/1.4007565.

- [155] S. Ozeri and D. Shmilovitz, “Simultaneous backward data transmission and power harvesting in an ultrasonic transcutaneous energy transfer link employing acoustically dependent electric impedance modulation,” *Ultrasonics*, vol. 54, no. 7, pp. 1929–1937, Sep. 2014. DOI: 10.1016/j.ultras.2014.04.019.
- [156] V. L. Takahashi, A. C. Kubrusly, A. M. B. Braga, S. M. M. Quintero, S. W. O. Figueiredo, and A. B. Domingues, “Ultrasonic Power and Data Transfer through Multiple Curved Layers Applied to Pipe Instrumentation,” *Sensors*, vol. 19, no. 19, p. 4074, Jan. 2019. DOI: 10.3390/s19194074.
- [157] B. M. G. Rosa and G. Z. Yang, “Towards Integration of Ultrasonic-Powered Implantable Devices for Physiological Monitoring, Stimulation, and Imaging in Soft Tissues Using a Handheld Scanning Probe,” *IEEE Sensors Journal*, pp. 1–1, 2020. DOI: 10.1109/JSEN.2020.3026240.
- [158] S.-n. Suzuki, S. Kimura, T. Katane, H. Saotome, O. Saito, and K. Kobayashi, “Power and Interactive Information Transmission to Implanted Medical Device Using Ultrasonic,” *Jpn. J. Appl. Phys.*, vol. 41, no. 5S, p. 3600, May 2002. DOI: 10.1143/JJAP.41.3600.
- [159] H. Kawanabe, T. Katane, H. Saotome, O. Saito, and K. Kobayashi, “Power and Information Transmission to Implanted Medical Device Using Ultrasonic,” *Jpn. J. Appl. Phys.*, vol. 40, no. 5S, p. 3865, May 2001. DOI: 10.1143/JJAP.40.3865.
- [160] G. J. Saulnier, H. A. Scarton, A. J. Gavens, D. A. Shoudy, T. L. Murphy, M. Wetzel, S. Bard, S. Roa-Prada, and P. Das, “P1G-4 Through-Wall Communication of Low-Rate Digital Data Using Ultrasound,” in *2006 IEEE Ultrasonics Symposium*, Oct. 2006, pp. 1385–1389. DOI: 10.1109/ULTSYM.2006.358.
- [161] B. C. Johnson, K. Shen, D. Piech, M. M. Ghanbari, K. Y. Li, R. Neely, J. M. Carmena, M. M. Maharbiz, and R. Muller, “StimDust: A 6.5mm³, wireless ultrasonic peripheral nerve stimulator with 82% peak chip efficiency,” in *2018 IEEE Custom Integrated Circuits Conference (CICC)*, Apr. 2018, pp. 1–4. DOI: 10.1109/CICC.2018.8357047.
- [162] D. M. Pozar, *Microwave Engineering, 4th Edition*, 4th edition. Wiley, Dec. 2011.
- [163] M. Abom, “Measurement of the scattering-matrix of acoustical two-ports,” *Mech. Syst. Signal Pr.*, vol. 5, no. 2, pp. 89–104, Mar. 1991. DOI: 10.1016/0888-3270(91)90017-Y.
- [164] S. Nygård, “Low frequency modelling of complex duct networks,” Tech, Licent. Thesis, KTH, Marcus Wallenb. Lab. Sound Vib., 1999.

- [165] M. Shatalov, J. Marais, I. Fedotov, and M. J. Tenkam, “Longitudinal vibration of isotropic solid rods: From classical to modern theories,” in, InTech Open, Dec. 2011, ISBN: 978-953-307-173-2. [Online]. Available: <https://researchspace.csir.co.za/dspace/handle/10204/5739>.
- [166] H. F. Tiersten, “Hamilton’s principle for linear piezoelectric media,” *Proceedings of the IEEE*, vol. 55, no. 8, pp. 1523–1524, Aug. 1967. DOI: 10.1109/PROC.1967.5887.
- [167] C. L. Dym and I. H. Shames, *Solid Mechanics: A Variational Approach*, Augmented edition. New York: Springer Science+Business Media, 2013, ISBN: 978-1-4614-6033-6.
- [168] *COMSOL Multiphysics Reference Manual, version 5.4*. [Online]. Available: <http://www.comsol.com/>.
- [169] S. Jahn, M. Margraf, V. Habchi, and J. Raimund, *Qucs-Technical Papers*. [Online]. Available: <http://qucs.sourceforge.net/index.html>.
- [170] J. N. Coupland and D. J. McClements, “Physical properties of liquid edible oils,” *Journal of the American Oil Chemists’ Society*, vol. 74, no. 12, pp. 1559–1564, 1997. DOI: 10.1007/s11746-997-0077-1.
- [171] T. Nimura and Y. Watanabe, “Effect of a Finite Circular Baffle Board on Acoustic Radiation,” *The Journal of the Acoustical Society of America*, vol. 25, no. 1, pp. 76–80, Jan. 1953. DOI: 10.1121/1.1907012.
- [172] L. L. Beranek and T. J. Mellow, *Acoustics: Sound Fields and Transducers*, First edition. Amsterdam: Academic Press, and imprint of Elsevier, 2012, ISBN: 978-0-12-391421-7.
- [173] G. Kossoff, “The Effects of Backing and Matching on the Performance of Piezoelectric Ceramic Transducers,” *IEEE Transactions on Sonics and Ultrasonics*, vol. 13, no. 1, pp. 20–30, Mar. 1966. DOI: 10.1109/T-SU.1966.29370.
- [174] T. J. Lawry, K. R. Wilt, H. A. Scarton, and G. J. Saulnier, “Analytical modeling of a sandwiched plate piezoelectric transformer-based acoustic-electric transmission channel,” *IEEE Transactions on Ultrasonics, Ferroelectrics, and Frequency Control*, vol. 59, no. 11, pp. 2476–2486, Nov. 2012. DOI: 10.1109/TUFFC.2012.2480.
- [175] H. F. Leung and A. P. Hu, “Modeling and analysis of ultrasonic power transfer system with tightly coupled solid medium,” *Wireless Power Transfer*, vol. 4, no. 1, pp. 1–12, Mar. 2017. DOI: 10.1017/wpt.2016.9.

- [176] G. S. Kino, *Acoustic Waves: Devices, Imaging, and Analog Signal Processing*. Englewood Cliffs, N.J: Prentice Hall, Jan. 1987, ISBN: 978-0-13-003047-4.
- [177] W. P. Mason and H. J. McSkimin, “Attenuation and Scattering of High Frequency Sound Waves in Metals and Glasses,” *The Journal of the Acoustical Society of America*, vol. 19, no. 3, pp. 464–473, May 1947. DOI: 10.1121/1.1916504.
- [178] D. Frickey, “Conversions between S, Z, Y, H, ABCD, and T parameters which are valid for complex source and load impedances,” *IEEE Transactions on Microwave Theory and Techniques*, vol. 42, no. 2, pp. 205–211, Feb. 1994. DOI: 10.1109/22.275248.
- [179] Sophocles J. Orfanidis, *Electromagnetic Waves and Antennas*. [Online]. Available: <http://eceweb1.rutgers.edu/~orfanidi/ewa/>.
- [180] D. M. Pozar, *Microwave Engineering*, 3rd ed. Hoboken, NJ: J. Wiley, 2005, ISBN: 0-471-44878-8.
- [181] C. H. Sherman and J. L. Butler, *Transducers and Arrays for Underwater Sound*. New York, NY: Springer New York, 2007. DOI: 10.1007/978-0-387-33139-3.
- [182] D. Anderson, “Comparison of Spice Vs. Harmonic Balance Simulations,” in *55th ARFTG Conference Digest*, vol. 37, Jun. 2000, pp. 1–7. DOI: 10.1109/ARFTG.2000.327418.
- [183] H.-M. Lee and M. Ghovanloo, “An Integrated Power-Efficient Active Rectifier With Offset-Controlled High Speed Comparators for Inductively Powered Applications,” *IEEE Transactions on Circuits and Systems I: Regular Papers*, vol. 58, no. 8, pp. 1749–1760, Aug. 2011. DOI: 10.1109/TCSI.2010.2103172.
- [184] A. Ballo, M. Bottaro, and A. D. Grasso, “A Review of Power Management Integrated Circuits for Ultrasound-Based Energy Harvesting in Implantable Medical Devices,” *Applied Sciences*, vol. 11, no. 6, p. 2487, Jan. 2021. DOI: 10.3390/app11062487.
- [185] S. C. Cripps, *RF Power Amplifiers for Wireless Communications*, 2nd ed, ser. Artech House Microwave Library. Boston: Artech House, 2006, ISBN: 978-1-59693-018-6.
- [186] F. Raab, “Idealized operation of the class E tuned power amplifier,” *IEEE Transactions on Circuits and Systems*, vol. 24, no. 12, pp. 725–735, Dec. 1977. DOI: 10.1109/TCS.1977.1084296.

- [187] G. Kkelis, D. C. Yates, and P. D. Mitcheson, “Class-E Half-Wave Zero dv/dt Rectifiers for Inductive Power Transfer,” *IEEE Transactions on Power Electronics*, vol. 32, no. 11, pp. 8322–8337, Nov. 2017. DOI: 10.1109/TPEL.2016.2641260.
- [188] S. Aldhaher, P. C.-K. Luk, and J. F. Whidborne, “Tuning Class E Inverters Applied in Inductive Links Using Saturable Reactors,” *IEEE Transactions on Power Electronics*, vol. 29, no. 6, pp. 2969–2978, Jun. 2014. DOI: 10.1109/TPEL.2013.2272764.
- [189] S. Aldhaher, P. C.-K. Luk, A. Bati, and J. F. Whidborne, “Wireless Power Transfer Using Class E Inverter With Saturable DC-Feed Inductor,” *IEEE Transactions on Industry Applications*, vol. 50, no. 4, pp. 2710–2718, Jul. 2014. DOI: 10.1109/TIA.2014.2300200.
- [190] M. Hayati, S. Roshani, M. K. Kazimierczuk, and H. Sekiya, “Analysis and design of class E power amplifier considering MOSFET parasitic input and output capacitances,” *IET Circuits, Devices & Systems*, vol. 10, no. 5, pp. 433–440, Sep. 2016. DOI: 10.1049/iet-cds.2015.0271.
- [191] Y.-C. Weng, C.-C. Wu, E. L. Chang, and W.-H. Chieng, “Minimum Power Input Control for Class-E Amplifier Using Depletion-Mode Gallium Nitride High Electron Mobility Transistor,” *Energies*, vol. 14, no. 8, pp. 1–16, 2021. [Online]. Available: https://econpapers.repec.org/article/gamjeners/v_3a14_3ay_3a2021_3ai_3a8_3ap_3a2302-_3ad_3a539084.htm.
- [192] C.-Y. Liu, G.-B. Wang, C.-C. Wu, E. Y. Chang, S. Cheng, and W.-H. Chieng, “Derivation of the Resonance Mechanism for Wireless Power Transfer Using Class-E Amplifier,” *Energies*, vol. 14, no. 3, p. 632, Jan. 2021. DOI: 10.3390/en14030632.
- [193] F. Mazzilli and C. Dehollain, *Ultrasound Energy and Data Transfer for Medical Implants*. Springer, 2020.
- [194] J. Krautkrämer and H. Krautkrämer, *Ultrasonic Testing of Materials*, Fourth. Berlin Heidelberg: Springer-Verlag, 1990, ISBN: 978-3-662-10680-8. DOI: 10.1007/978-3-662-10680-8.
- [195] E. H. Carnevale, L. C. Lynnworth, and G. S. Larson, “Ultrasonic Measurement of Elastic Moduli at Elevated Temperatures, using Momentary Contact,” *The Journal of the Acoustical Society of America*, vol. 36, no. 9, pp. 1678–1684, Sep. 1964. DOI: 10.1121/1.1919264.
- [196] G. E. Goode and R. Lewis, “A momentary-contact system for ultrasonic testing of steel at temperatures up to 1 200°C,” *Non-Destructive Testing*, vol. 8, no. 6, pp. 313–319, Dec. 1975. DOI: 10.1016/0029-1021(75)90032-8.

- [197] G. Canella and F. Monti, “Ultrasonic inspection of hot thick steel products,” *NDT International*, vol. 13, no. 1, pp. 10–14, Feb. 1980. DOI: 10.1016/0308-9126(80)90119-4.
- [198] K. W. Andrews, “Ultrasonics in the steel industry,” *Physics in Technology*, vol. 5, no. 4, pp. 259–277, Jan. 1974. DOI: 10.1088/0305-4624/5/4/I04.
- [199] N. Bhadwal, M. Torabi Milani, T. Coyle, and A. Sinclair, “Dry Coupling of Ultrasonic Transducer Components for High Temperature Applications,” *Sensors*, vol. 19, no. 24, p. 5383, Jan. 2019. DOI: 10.3390/s19245383.
- [200] B. Drinkwater and P. Cawley, “An Ultrasonic Wheel Probe Alternative to Liquid Coupling,” in *Review of Progress in Quantitative Nondestructive Evaluation: Volume 14*, D. O. Thompson and D. E. Chimenti, Eds., Boston, MA: Springer US, 1995, pp. 983–989, ISBN: 978-1-4615-1987-4. DOI: 10.1007/978-1-4615-1987-4_124.
- [201] A. M. Robinson, B. W. Drinkwater, and J. Allin, “Dry-coupled low-frequency ultrasonic wheel probes: Application to adhesive bond inspection,” *NDT & E International*, vol. 36, no. 1, pp. 27–36, Jan. 2003. DOI: 10.1016/S0963-8695(02)00056-7.
- [202] P. B. Nagy, “Ultrasonic classification of imperfect interfaces,” *J Nondestruct Eval*, vol. 11, no. 3, pp. 127–139, Dec. 1992. DOI: 10.1007/BF00566404.
- [203] B. W. Drinkwater, R. S. Dwyer-Joyce, and P. Cawley, “A study of the interaction between ultrasound and a partially contacting solid—solid interface,” *Proceedings of the Royal Society of London. Series A: Mathematical, Physical and Engineering Sciences*, vol. 452, no. 1955, pp. 2613–2628, Jan. 1996. DOI: 10.1098/rspa.1996.0139.
- [204] R. S. Dwyer-Joyce, B. W. Drinkwater, and A. M. Quinn, “The Use of Ultrasound in the Investigation of Rough Surface Interfaces,” *Journal of Tribology*, vol. 123, no. 1, pp. 8–16, Sep. 2000. DOI: 10.1115/1.1330740.
- [205] A. Baltazar, S. I. Rokhlin, and C. Pecorari, “On the relationship between ultrasonic and micromechanical properties of contacting rough surfaces,” *Journal of the Mechanics and Physics of Solids*, vol. 50, no. 7, pp. 1397–1416, Jul. 2002. DOI: 10.1016/S0022-5096(01)00119-3.
- [206] R. Thomas, B. W. Drinkwater, and D. Liaptsis, “The reflection of ultrasound from partially contacting rough surfaces,” *The Journal of the Acoustical Society of America*, vol. 117, no. 2, pp. 638–645, Jan. 2005. DOI: 10.1121/1.1835505.
- [207] D. Liaptsis, B. W. Drinkwater, and R. Thomas, “The interaction of oblique incidence ultrasound with rough, partially contacting interfaces,” *Nondestructive Test-*

- ing and Evaluation*, vol. 21, no. 3-4, pp. 109–121, Sep. 2006. DOI: 10.1080/10589750601056920.
- [208] B. Drinkwater, R. Dwyer-Joyce, and P. Cawley, “A study of the transmission of ultrasound across solid–rubber interfaces,” *The Journal of the Acoustical Society of America*, vol. 101, no. 2, pp. 970–981, Feb. 1997. DOI: 10.1121/1.418055.
- [209] B. Drinkwater and P. Cawley, “Measurement of the frequency dependence of the ultrasonic reflection coefficient from thin interface layers and partially contacting interfaces,” *Ultrasonics*, vol. 35, no. 7, pp. 479–488, Nov. 1997. DOI: 10.1016/S0041-624X(97)00072-3.
- [210] N. Guo and M. C. Leu, “Additive manufacturing: Technology, applications and research needs,” *Front. Mech. Eng.*, vol. 8, no. 3, pp. 215–243, Sep. 2013. DOI: 10.1007/s11465-013-0248-8.
- [211] F. M. Guillot and D. H. Trivett, “Complete elastic characterization of viscoelastic materials by dynamic measurements of the complex bulk and Young’s moduli as a function of temperature and hydrostatic pressure,” *J SOUND VIB*, vol. 330, no. 14, pp. 3334–3351, Jul. 2011. DOI: 10.1016/j.jsv.2011.02.003.
- [212] T. Tancogne-Dejean, M. Diamantopoulou, M. B. Gorji, C. Bonatti, and D. Mohr, “3D Plate-Lattices: An Emerging Class of Low-Density Metamaterial Exhibiting Optimal Isotropic Stiffness,” *Advanced Materials*, vol. 30, no. 45, p. 1803 334, Nov. 2018. DOI: 10.1002/adma.201803334.
- [213] M. F. Daqaq, R. Masana, A. Erturk, and D. Dane Quinn, “On the Role of Nonlinearities in Vibratory Energy Harvesting: A Critical Review and Discussion,” *Applied Mechanics Reviews*, vol. 66, no. 4, May 2014. DOI: 10.1115/1.4026278.
- [214] V. T. Rathod, “A Review of Acoustic Impedance Matching Techniques for Piezoelectric Sensors and Transducers,” *Sensors*, vol. 20, no. 14, p. 4051, Jan. 2020. DOI: 10.3390/s20144051.
- [215] C. Poole and I. Darwazeh, *Microwave Active Circuit Analysis and Design*, C. Poole and I. Darwazeh, Eds. Oxford: Academic Press, Jan. 2016, ISBN: 978-0-12-407823-9. DOI: 10.1016/B978-0-12-407823-9.00004-4.
- [216] J. Goll and B. Auld, “Multilayer Impedance Matching Schemes for Broadbanding of Water Loaded Piezoelectric Transducers and High Q Electric Resonators,” *IEEE Transactions on Sonics and Ultrasonics*, vol. 22, no. 1, pp. 52–53, Jan. 1975. DOI: 10.1109/T-SU.1975.30776.
- [217] T. E. G. Alvarez-Arenas, “Acoustic impedance matching of piezoelectric transducers to the air,” *IEEE Transactions on Ultrasonics, Ferroelectrics, and Frequency Control*

Control, vol. 51, no. 5, pp. 624–633, May 2004. DOI: 10.1109/TUFFC.2004.1320834.

- [218] A. Selfridge, “Approximate Material Properties in Isotropic Materials,” *IEEE Transactions on Sonics and Ultrasonics*, vol. 32, no. 3, pp. 381–394, May 1985. DOI: 10.1109/T-SU.1985.31608.
- [219] K. G. Foote, “Discriminating between the nearfield and the farfield of acoustic transducers,” *JASA*, vol. 136, no. 4, pp. 1511–1517, Oct. 2014. DOI: 10.1121/1.4895701.
- [220] H.-W. Wang and L.-W. Chen, “A cylindrical optical black hole using graded index photonic crystals,” *Journal of Applied Physics*, vol. 109, no. 10, p. 103 104, May 2011. DOI: 10.1063/1.3590336.
- [221] C. Wei, Z. Wang, Z. Song, K. Wang, D. Wang, W. W. L. Au, and Y. Zhang, “Acoustic Property Reconstruction of a Neonate Yangtze Finless Porpoise’s (Neophocaena asiaeorientalis) Head Based on CT Imaging,” *PLOS ONE*, vol. 10, no. 4, e0121442, Apr. 2015. DOI: 10.1371/journal.pone.0121442.
- [222] Z. Song, W. Ou, E. Dong, J. Zhang, Q. Xie, C. Zhang, M. Bai, T. A. Mooney, and Y. Zhang, “Physical implementation of dolphin biosonar to facilitate ultrasound control,” *Appl. Phys. Lett.*, vol. 117, no. 17, p. 173 701, Oct. 2020. DOI: 10.1063/5.0025788.